UNIVERSIDADE DE LISBOA
FACULDADE DE CIÊNCIAS
DEPARTAMENTO DE GEOLOGIA

Relationship between dioritic magmatism and oxide ore forming processes in the Beja Igneous Complex, Portugal

Manuel Antunes Dias

Mestrado em Geologia
Especialização em Geodinâmica e Recursos Geológicos

Dissertação orientada por:
Doutora Ana Patrícia Marques de Jesus
Professor Doutor António Manuel Nunes Mateus

2024

À minha família

Agradecimentos

Apesar de aparecer só o meu nome como autor deste trabalho, o desenvolvimento do mesmo teria sido muito mais complicado sem a colaboração de várias pessoas a quem dedico os próximos parágrafos. Contudo, antes dos agradecimentos individuais, um obrigado ao projecto SEMACRET que, através da minha orientadora, financiou todos os custos e logística associada ao trabalho.

Um obrigado muito especial à minha orientadora, Doutora Ana Jesus, pela enorme ajuda durante todas as etapas da tese. A sua disponibilidade imediata em *n* situações para me esclarecer dúvidas no Zoom fez com que não ficasse preso em problemas durante demasiado tempo. O seu entusiasmo científico é contagiante e motivaram-me muitas vezes para manter o ritmo de trabalho. Agradeço todos os conselhos pessoais e científicos para um (possível) futuro académico, especialmente em tempos que se tornam cada vez mais incertos. Agradeço ainda e valorizo muito as várias discussões interessantes sobre a intrusão magmática mais marada que existe (Beja, para quem não saiba).

Um obrigado igualmente especial ao meu co-orientador, Professor António Mateus. Valorizo toda a ajuda, sabedoria, insistência e esforço físico durante o trabalho de campo no Torrão. Um especialíssimo obrigado pelas inúmeras vezes que, no meio dos seus próprios assuntos e projectos, me arranjou sempre um tempo no gabinete para esclarecer e discutir variadíssimas dúvidas que me apareciam. A sua ajuda foi essencial para o desenvolvimento desta tese, sobretudo nas fases iniciais em que andava meio perdido.

Um obrigado ao Bruno Bartolomeu e ao António Oliveira, membros da equipa SEMACRET. Por toda a ajuda e companhia durante o trabalho de campo, desde as várias fotografias que estão umas páginas mais abaixo, até à maior amostra que alguma vez foi colhida. Por toda a ajuda no processamento de amostras e muitas outras dúvidas que foram surgindo ao longo destes meses.

Um agradecimento à Sofia Rodrigues pela ajuda e companhia na cave durante possivelmente a fase mais monótona e física e mentalmente esgotante do trabalho: serrar, polir e moer rochas. Agradeço ainda por ter feito lâminas polidas tão bonitas que mereceram ser exaustivamente vistas e revistas. Um obrigado ao Pedro Rodrigues pela ajuda no manuseamento e aquisição de dados na microssonda.

Um obrigado muito especial aos meus colegas da sala 65, a Mariana Cândido, o Pedro Costa, a Ana Rita e, apesar de não estar na sala, mas sim no IPMA, o David Salvador. A sua companhia e amizade durante os últimos 2 ou 3 anos foi imprescindível e tornaram o dia-a-dia menos cansativo. Obrigado por todos os almoços, lanches e outras pausas que às vezes eram tão precisas. Gostaria ainda de agradecer aos meus colegas de licenciatura, David Vicente, Gonçalo Fevereiro, João Sérgio, Catarina Bastos e Nuno Duarte, além de outros já mencionados. Apesar de não ser a pessoa mais social, nunca me fizeram sentir de parte e a sua companhia motivou-me a continuar.

Um gigantesco obrigado à Mariana Cândido por todo o suporte pessoal nos últimos 2 anos. A sua ajuda e compreensão durante fases mais complicadas foram essenciais não só para o desenvolvimento "escrito" desta tese, mas também para a estabilidade emocional. Espero conseguir retribuir todo o carinho.

O maior obrigado à minha família, pais, irmãos e animais, por todo o apoio no decorrer deste trabalho e por toda a ajuda mútua nos últimos anos. Obrigado ainda pelo apoio financeiro e confiança em mim.

Acknowledgements

Despite only my name appearing as the author of this work, its development would have been much more complicated without the collaboration of several people to whom I dedicate the following paragraphs. However, before the ‘personal’ thanks, I would like to thank the SEMACRET project which, through my supervisor, financed all costs and logistics associated with the work.

A very special thank you to my supervisor, Dr Ana Jesus, for her enormous help during the work. Her immediate willingness to answer my questions on Zoom meant that I didn't get tangled up in problems for too long. Her scientific enthusiasm is contagious and has often motivated me to keep up my work pace. Thank you for all personal and scientific advice for a (possible) academic future, in times that are becoming increasingly uncertain. I also appreciate and value a lot the many interesting discussions about the craziest magmatic intrusion there is (Beja, for the unaware).

An equally special thank you to my co-supervisor, Professor António Mateus. I appreciate all his help, wisdom, insistence and physical effort during my fieldwork in Torrão. A very special thanks for making me time in his office to clarify and discuss the many questions I had, despite being in the midst of his own affairs and projects. His help was essential to the development of this thesis, especially in the early stages when I was a little lost.

To Bruno Bartolomeu and António Oliveira, members of the SEMACRET team, for all their help and companionship during the fieldwork. From the various photographs shown a few pages down below, to the largest rock ever sampled. Thank you also for all the help in processing the samples and the many questions that arose over these last few months.

Thanks to Sofia Rodrigues for all her help and company in the basement during possibly the most monotonous and physically and mentally exhausting phase of the work: sawing, polishing and grinding rocks. I'd also like to thank her for making polished thin sections so beautiful that they deserve to be looked at and revised exhaustively. Thanks to Pedro Rodrigues for his help in handling and acquiring data on the microprobe.

A very special thank you to my colleagues in room/laboratory 65, Mariana Cândido, Pedro Costa, Ana Rita and, despite not being in the room, but at IPMA, David Salvador. Your company and friendship over the last two or three years has been indispensable and has made everyday life less tiring. Thank you for all the lunches, snacks and other breaks that were sometimes so necessary. I would also like to thank my fellow undergraduates, David Vicente, Gonçalo Fevereiro, João Sérgio, Catarina Bastos and Nuno Duarte, as well as others already mentioned. Although I'm not the most social person, they never made me feel left out and their company motivated me to keep going.

A huge thank you to Mariana Cândido for all her personal support over the last two years. Her help and understanding during more complicated phases were essential not only for the ‘written’ development of this thesis, but also for my emotional stability. I hope I can repay all the affection and tenderness.

The biggest thank you goes to my family, parents, siblings and pets, for all their support throughout this work and for all the mutual help over the last few years. Thank you also for your financial support and trust.

Resumo

O Complexo Ígneo de Beja (CIB) situa-se no bordo SW da Zona de Ossa Morena (ZOM), onde afloram unidades lito-estratigráficas que integram secções de idade diversa, maioritariamente do Neoproterozóico ao Devónico. O CIB estende-se ao longo de uma faixa de direcção NW-SE por mais de 100 km e a sua instalação ocorreu durante as fases colisionais (pós-subducção) da orogenia Varisca, na transição Devónico-Carbónico (*ca.* 350 Ma). Processos de *slab break-off* seguidos por relaxamento do campo de tensões (desencadeando descompressão) das massas continentais terão promovido a geração de sucessivos eventos magmáticos no decorrer da orogénese. O CIB é composto por três unidades principais que documentam episódios magmáticos progressivamente mais evoluídos e recentes, nomeadamente: a Sequência Gabróica Bandada, o Complexo gabro-diorítico de Cuba-Alvito e os Pórfiros de Baleizão.

A Sequência Gabróica Bandada, que representa o membro mais primitivo do CIB, tem sido alvo de diversos estudos no passado, alguns orientados para a compreensão da génese das mineralizações de óxidos de Fe-Ti-V e sulfuretos que hospeda. A evolução da Sequência Gabróica Bandada caracteriza-se por um primeiro episódio magmático que deu origem às rochas mais primitivas (Fo_{88}), representadas por gabronoritos ricos em óxidos nas Soberanas, e evoluídas (Fo_{54}), patenteadas por diversos gabros com acumulações maciças de óxidos em Odivelas. Posteriormente, a recarga progressiva da câmara magmática deu origem às designadas Séries Monótonas, cujo nome advém do facto destas rochas não representarem magmas tão primitivos como os que deram origem aos gabros das Soberanas nem atingirem os graus de diferenciação característicos de Odivelas. Além do interesse económico da Sequência Gabróica Bandada, uma característica importante desta unidade é a ocorrência de corpos dioríticos na sua bordadura, os quais não estão atribuídos a nenhuma unidade do CIB. A transição entre gabros e dioritos nem sempre é clara e muitos dos contactos fazem-se através de falhas e zonas de cisalhamento de direcção WNW-ESSE a E-W e outros rearranjos estruturais, comuns na ZOM devido à sua evolução prolongada no tempo. Uma destas unidades dioríticas aflora no Torrão, situada a cerca de 10 km a Norte das rochas gabróicas das Soberanas. Estudos prévios sobre os dioritos do Torrão revelaram enriquecimentos em Fe e Ti, que se tornam de especial interesse tendo em conta o contexto mineralizante da Sequência Gabróica Bandada.

O essencial da cartografia do Torrão pode ser descrito por duas fácies dioríticas: dioritos e quartzo-dioritos, cujos contactos são graduais ou feitos através de estruturas tectónicas. Ambas as litologias têm a anfíbola e plagioclase (variavelmente zonada) como fases minerais silicatadas principais. Contudo, os quartzo-dioritos apresentam aumento gradual na proporção modal de quartzo e biotite. As fases minerais de óxidos são magnetite e ilmenite, sendo mais abundantes nos dioritos. No Torrão encontram-se ainda em abundância encraves de anfibolito no seio dos dioritos e quartzo-dioritos. Os encraves anfibolíticos ocorrem como blocos heterométricos variavelmente digeridos. São compostos por anfíbola e plagioclase dispostos numa matriz grano-nematoblástica. A granularidade dos encraves permite a distinção entre duas famílias de anfibolitos, uma mais fina e outra mais grosseira. Além destes critérios texturais, as suas características petrográficas são essencialmente iguais, sendo a maior diferença a abundância de magnetite, ilmenite e pirite nos anfibolitos mais finos. As amostras estudadas apresentam variáveis graus de alteração que se manifestam através de veios compostos por clorite, calcite, prehnite e epídoto.

As composições das anfíbolas primárias nos quartzo-dioritos revelam características que são tipicamente atribuídas a rochas mais evoluídas quando comparadas às dos dioritos, *i.e.* menos Ti, Al na posição tetraédrica e ocupação da posição dodecaédrica por Na e K. A plagioclase é geralmente mais cálcica nos dioritos do que nos quartzo-dioritos. Constata-se, contudo, que o zonamento dos cristais de plagioclase é tanto normal como inverso. As biotites primárias contêm quantidades significativas de Fe^{3+}, cujo

"excesso" é suficiente para ocupar a posição tetraédrica. A magnetite e ilmenite têm composições relativamente "puras", ambas aproximando-se das composições ideias tanto nos dioritos como nos quartzo-dioritos. As principais fases minerais dos anfibolitos têm composições que estão compreendidas entre os extremos definidos pelas fácies dioríticas.

De acordo com o referido em estudos anteriores referentes às rochas aflorantes no Torrão, os dioritos amostrados têm uma assinatura geoquímica semelhante aos 'gabros' das Soberanas, sendo enriquecida em $Fe_2O_3^T$ e TiO_2 (valores medianos, X, = 9.35 e 1.46 wt%, respectivamente), e com valores de SiO_2 em torno dos 50 wt%. Estas características levaram autores anteriores a designar estas rochas por dioritos 'high-Ti'. Por oposição, os quartzo-dioritos são mais enriquecidos em SiO_2 (X = 55.5 wt%) e empobrecidos em $Fe_2O_3^T$ e TiO_2, sendo designados de dioritos 'low-Ti'. Por terem teores baixos em $Fe_2O_3^T$ mas quantidades apreciáveis em MgO, os quartzo-dioritos caracterizam-se ainda por terem valores de Mg (Mg# = Mg/[Mg + Fe^{Total}]) superiores a 50. Padrões de Elementos Terra-Raras (ETR) normalizados ao condrito CN1 mostram que os quartzo-dioritos são mais enriquecidos que os dioritos em ETR leves ($X_{La/SmN}$ = 2.5 e 1.35, respectivamente), sem anomalias significativas em Eu. Os quartzo-dioritos estão também enriquecidos em Ni, Cr, Th, U, Zr e Hf em relação aos dioritos. Os dioritos apresentam ainda padrões comparáveis e graus de enriquecimento ligeiramente superiores em relação aos 'gabros' primitivos das Soberanas. Estas mesmas tendências confirmam-se ao nível de vários elementos incompatíveis, sendo a maior diferença enriquecimentos significativos em LILE nos dioritos. Os padrões de ETR e outros elementos incompatíveis permite a distinção entre as duas fácies anfibolíticas, sendo os anfibolitos mais finos ligeiramente mais enriquecidos e com padrões "lisos" com anomalias em Eu moderadas (Eu/Eu* = 0.72) em relação aos anfibolitos mais grosseiros, que apresentam ligeiros enriquecimentos em ETR leves. Os anfibolitos mais grosseiros têm anomalias marcadas em Nb e Ta que estão ausentes nos anfibolitos mais finos. As características composicionais dos anfibolitos finos e "grosseiros" são semelhantes a rochas metabasálticas neoproterozóicas aflorantes em Santiago do Escoural e metavulcanitos devónicos expostos na proximidade da Barragem de Odivelas, sugerindo a sua respectiva correlação.

Estimativas de variáveis intensivas (P, T, wt% H_2O) obtidas com base em calibrações empíricas de diversas fases minerais (anfíbola, plagioclase e biotite) para as fácies dioríticas fornecem pressões de instalação da câmara magmática a 4.5 kbar (*ca.* 13.5 km de profundidade); existem, porém, estimativas de 7-8 kbar (*ca.* 24 km de profundidade) obtidas para cristais grosseiros de anfíbola. As temperaturas de cristalização dos quartzo-dioritos (830-720 ºC) são mais baixas que as obtidas para os dioritos (830-770 ºC). Estimativas higrométricas indicam conteúdos em água dos magmas dioríticos de *ca*. 6 wt%, dentro do campo de estabilidade da anfíbola.

O Mg# dos quartzo-dioritos, juntamente com os seus conteúdos em Ni e Cr, sugerem que estes cristalizaram a partir de um magma mais primitivo que o que deu origem aos dioritos. Por outro lado, os enriquecimentos em Th, U, Zr e Hf sugerem a adição de componentes crustais. Simulações numéricas fazendo uso de modelos de mistura binária e de assimilação concomitante com cristalização fraccionada (AFC) revelam que é possível obter a composição de elementos maiores ($Fe_2O_3^T$, TiO_2 e Mg# incluídos), ETR e outros incompatíveis dos quartzo-dioritos através destes processos, tomando como composição inicial o gabronorito das Soberanas e diversas rochas aflorantes na OMZ como contaminantes. Considerando o mesmo ponto de partida, a cristalização fraccionada de uma associação mineral composta por clinopiroxena + olivina + espinela juntamente com pequenos graus de assimilação de rochas crustais, reproduz os padrões de ETR e outros elementos incompatíveis dos dioritos a fracções de *melt* residuais de 70% (F = 0.7). O envolvimento de rochas crustais é também denotado por dados isotópicos relatados em estudos anteriores que revelam assinaturas mais contaminadas nos dioritos relativamente à amostra de gabronorito das Soberanas. As estimativas de pressão mais elevadas para

anfíbola sugerem que este processo ocorreu em domínios crustais profundos. O enriquecimento em LILE dos dioritos relativamente aos gabros pode ser explicado por: 1) estes elementos se concentrarem em fracções mais ricas em água, como os dioritos, ou 2) assimilação de rochas crustais. A modelação inversa de H_2O sugere que os 'gabros' das Soberanas teriam conteúdos em água de *ca.* 4 wt%, assumindo que este composto se comportou como perfeitamente incompatível e que toda a água dos dioritos resultou da cristalização de minerais nominalmente anidros.

A evolução dos dioritos do Torrão pode ser então descrita como se segue. A fraccionação de magmas gabróicos hidratados, provavelmente em profundidade, levou a um enriquecimento em água dos magmas deles derivados. A extracção destes magmas terá sido promovida pela sua reduzida viscosidade tendo em conta os teores em água (> 4 wt%). Os primeiros magmas, mais primitivos, ao instalarem-se a *ca.* 13.5 km de profundidade, foram contaminados por diversas rochas crustais, levando ao enriquecimento destes em SiO_2, ETR leves, Th, U, Zr e Hf, e ficando mais empobrecidos em $Fe_2O_3^T$ e TiO_2. Ao cristalizarem, estes magmas deram origem aos quartzo-dioritos (ou dioritos 'low-Ti'). A recarga progressiva deste sistema levou à formação dos dioritos (ou dioritos 'high-Ti'), que, por serem menos contaminados, retiveram as suas características composicionais primárias, nomeadamente os enriquecimentos em $Fe_2O_3^T$ e TiO_2.

Palavras-chave: diorito, anfibolito, gabros de Beja, diferenciação, magmatismo

Abstract

The Layered Gabbroic Sequence (LGS) is the most primitive unit of the Beja Igneous Complex (BIC), emplaced during the collisional stages of the Variscan orogeny. The LGS hosts several occurrences of Fe-Ti-V oxide type mineralization. Furthermore, some diorite bodies, unaffiliated with any BIC unit, are recognized in the LGS northern-northeastern margin. This is the case with the Torrão dioritic suite, which features a unique geochemical signature due its Fe and Ti enrichments and incompatible elemental trends which are comparable to those of the most primitive LGS rocks.

At Torrão, diorites and quartz-diorites are recognized, both being composed of amphibole + plagioclase plus quartz + biotite in the latter. Several amphibolite enclaves are found within the dioritic rocks, providing evidence of the involvement of country rocks in this magmatic event. The diorites show enrichments in $Fe_2O_3^T$ and TiO_2. Conversely, the quartz-diorites are depleted in these elements but enriched in SiO_2, LREE, Th, U, Zr, Hf, Ni and Cr, as well as having relatively high Mg-number (> 50). Pressure, temperature and wt% H_2O estimates reveal a cooling episode from 830-720 ºC at *ca.* 13.5 km depth (4.5 kbar) and water contents of 6 wt%.

Numerical simulations using AFC, FC and binary mixing equations suggest that diorites might derive from hydrous LGS primitive magmas by fractional crystallization, probably at depth, of a mineral assemblage comprising clinopyroxene + olivine + spinel together with small degrees of crustal assimilation. This same process led to an enrichment in H_2O of the derived magmas. The compositional features of the quartz-diorites can be reproduced by significant assimilation of diverse crustal sources at the depth of emplacement. Therefore, the quartz-diorites represent more contaminated, albeit more primitive, magmas, whereas diorites represent compositionally more evolved but less contaminated magmas.

Keywords: diorite, amphibolite, Beja gabbro, differentiation, magmatism

Table of Contents

Acronyms and abbreviations

Geochemical Features			
Rare Earth Elements	REE	Large Ion Lithophile Elements	LILE
Light Rare Earth Elements	LREE	High Field Strength Elements	HFSE
Heavy Rare Earth Elements	HREE	CN1 Chondrite	CN1
Middle Rare Earth Elements	MREE	Primitive Mantle	PM
Minerals			
Amphibole	Amp	Olivine	Ol
Apatite	Ap	Spinel s.l.	Sp
Biotite	Bt	Epidote	Ep
Chlorite	Chl	Prehnite	Prh
Hematite	Hem	Rutile	Rut
Quartz	Qz	Plagioclase *s.l.*	Plg
Magnetite	Mgt	Muscovite	Ms
Ilmenite	Ilm	Zircon	Zrn
Pyrite	Py	Sulfides	Sulf
Clinopyroxene	Cpx	Phlogopite	Phl
Titanium-rich magnetite	Ti-mgt		
Geology – miscellaneous			
atoms per formula unit	apfu	Évora-Beja-Aracena Domain	EBAD
parts per million	ppm	Beja Igneous Complex	BIC
weight percent	wt%	Layered Gabbroic Sequence	LGS
Whole-Rock	WR	Soberanas Sector	SB
Parallel Nicols	PN	Odivelas Sector	ODV
Crossed Nicols	XN	Beringel Sector	BRG
Transmitted Light	TL	Border Group	BG
Reflected Light	RL	Anorthosite-Tonalite-Throndjemite Suite	ATT
Northwest	NW	Cuba-Alvito gabbro-dioritic Complex	CAC
Northeast	NE	Baleizão Porphyry Complex	BPC
North-Northwest	NNW	Beja-Acebuches Ophiolite Complex	BAOC
Southwest	SW	Central Iberian Zone	CIZ
South-Southeast	SSE	Southern Portuguese Zone	SPZ
West-Northwest	WNW	Pulo do Lobo Terrane	PLT
East-Southeast	ESE	Assimilation-Fractional Crystallization	AFC
Ossa-Morena Zone	OMZ	Fractional Crystallization	FC
Others			
sensu lato/broad sense	*s.l.*	*sensu strictu*/strict sense	*s.s.*
exempli gratia/example	*e.g.*	*id est*/this is	*i.e.*
circa/approximately	*c.a.*		

Figure Index

Table Index

I. Introduction

The Beja Igneous Complex (BIC) is a major geological entity of the SW Iberian Variscides, emplaced during the main collisional stages of the Variscan orogeny (Upper Devonian, *ca.* 355 – 345 Ma). The BIC extends along the southern border of the Ossa-Morena Zone (OMZ) for over *ca.* 100 km and includes several blocks of (siliciclastic and carbonate) metasedimentary and (mafic and felsic) metavolcanic rocks, also recognized across its boundaries, preserving sequences that document the OMZ evolution from Neoproterozoic to Ordovician (Silurian?) times (*e.g.,* Oliveira *et al.*, 1991). The BIC comprises three main units, corresponding to progressively younger and more evolved magmatic events, namely: the Layered Gabbroic Sequence (LGS), the Cuba-Alvito gabbro-dioritic Complex (CAC) and the Baleizão Porphyry Complex (BPC). Out of these units, the LGS has been a target for several studies in the past two decades due to its economic potential which stems from the Fe-Ti-V oxide mineralization it hosts (*e.g.,* Jesus, 2011; Jesus *et al.*, 2014). One other feature of this unit is the occurrence of several marginal diorite bodies which relationship to the LGS is not well understood due to the scarcity of detailed studies. That is the case of the diorite rocks cropping-out at Torrão, at *ca.* 10 km to the North of the most primitive rocks forming the LGS. Classification of the Torrão diorites varies according to several authors, ranging from gabbros and "gabbro-diorites" to diorites and tonalites. Despite ambiguities regarding their designation, one common feature among studies on this diorite suite concerns its Fe and Ti enrichment, which is distinct from the other BIC diorite suites (Caldeira *et al.*, 2007; Pin *et al.*, 2008).

Considering the proximity of the Torrão diorites to the LGS and their unique geochemical signature (in the BIC context), it is likely that at least some portion of the composition was inherited from their parental magmas, assumed to correspond to the LGS. Indeed, the available geochemical data for the Torrão diorites suggests that this may be the case, with fractional crystallization at depth from parental magmas like the LGS being the main process of differentiation (Jesus *et al.*, 2016). In this view, the assimilation of deep crustal amphibolite rocks is interpreted to have provided the necessary water to generate the hydrous diorite melts (Jesus *et al.*, 2016). Furthermore, the isotopic values for the Torrão diorites are rather primitive ($^{87}Sr/^{86}Sr = 0.7045$; $\varepsilon Nd_{350Ma} = +2.5 \pm 1$; Pin *et al.*, 2008) and overlap the LGS field, suggesting that these rocks derived from the same magma batches that produced the LGS. An additional way of explaining the genesis of the Torrão diorites is by crustal contamination. The development of marginal diorite facies by crustal contamination is a common feature in mafic plutons emplaced at upper crustal levels, where thermal gradients between the intruding magmatic body and the country-rocks promote their partial melting and assimilation, thus driving differentiation processes towards more evolved compositions. From SW to NE, the BIC sequence (excluding the BPC) evolves from gabbro to diorite, also considering the heterogeneous suites that form the CAC. Cartographic observations thus suggest the existence of a differentiation vector towards the NE of the main intrusion (the LGS), which in turn potentially indicates that crustal contamination could have played a pivotal role in differentiating the melts that formed the Torrão diorites and the other BIC diorite suites. Candidates for crustal contaminants would then likely be the Neoproterozoic – Devonic metasedimentary and metavolcanic sequences. Both interpretations are equally valid but rely on a very limited dataset.

Seeking to answer the many open questions regarding the processes behind the genesis of the Torrão diorites and the meaning of their distinct geochemical signature, the main objective of this work is to characterize these rocks in detail. A thorough study should also contribute to a better understanding of how intermediate magmatic suites develop in mafic plutons in other geological contexts. Furthermore, due to the economic potential of the LGS, assessing its relationship with the Torrão diorites is fundamental since these enriched diorite suites could be used as proxies to oxide accumulations that might have grade and tonnage attributes of orthomagmatic ore bodies.

II. Geological Setting

The Torrão diorites are part of the Beja Igneous Complex, a voluminous, composite magmatic intrusion located at the SW border of the Ossa-Morena Zone, extending across a significant area of the Évora-Beja-Aracena Domain (EBAD). Within the BIC, several kilometric-sized blocks of metasedimentary and metavolcanic rocks can be recognized, preserving sections of the Neoproterozoic to Ordovician (Silurian?) succession described in the EBAD. Some of the contacts between the BIC gabbros or diorites and these country rocks are intrusive, but those of tectonic nature prevail, namely via WNW-ESE to E-W left-lateral shear zones. Tectonic reworking possibly obliterates primary relationships useful to unravel dynamic rock/melt interactions during the emplacement of successive magma batches. These interactions are of prime importance because the assimilation of hosting rocks may regulate various geochemical and physical properties of melts. As such, a comprehensive characterization of the local geological setting that will accommodate the igneous body is necessary.

The Ossa-Morena Zone Southern border

The Ossa-Morena Zone (OMZ) is an internal continental segment representing a tectono-stratigraphic unit of the SW Iberian Variscides (*e.g.*, Ribeiro *et al.*, 2007; Figure II-1). To the north, the Tomar-Badajoz-Córdoba Shear Zone separates the OMZ from the Central-Iberian Zone (CIZ) and is interpreted as a Cadomian structure reworked during the Variscan orogeny (from Upper Devonian to the Carboniferous-Permian transition, *ca.* 370-299 Ma; Ribeiro *et al.*, 2007). So, the Ossa-Morena Zone evolution dates to Proterozoic times, followed by the OMZ-CIZ accretion during the Cadomian Orogeny (late Neoproterozoic, *ca.* 650-550 Ma), forming the Iberian Autochthonous Terrane. The OMZ can be divided into several sectors, according to stratigraphic criteria, regardless of their boundaries coinciding with tectonic contacts or not (following the definition of Oliveira *et al.*, 1991). From NE to SW, these sectors are labelled as Blastomylonitic Belt, Elvas - Alter do Chão, Estremoz-Barrancos and Montemor-Ficalho (Oliveira *et al.*, 1991; Figure II-2). In this framework, the combination of the Montemor-Ficalho sector, Beja Igneous Complex, Santa-Susana Odivelas sub-sector and Cabrela synclinal, corresponding to the SW portions of the OMZ, represent the EBAD (further details about each sector/sub-sector can be consulted in Oliveira *et al.*, 1991; Figure II-2). This section will mainly cover the stratigraphic Neoproteozoic to Ordovician (Silurian?) sequence of the EBAD and, although each sector has its own characteristics, general outlines regarding the geodynamic evolution of the OMZ can be made since the lithological sequences that characterize them are correlated.

Continental rifting episodes during the Neoproterozoic in SW Iberia generated conditions to the development of concurrent bimodal magmatism and siliciclastic sedimentation. The geological record of such processes is represented in the EBAD by several low- to high-grade metamorphic sequences, namely the Água de Peixes Formation, composed of black-schists, meta-greywackes and cherts, and the Escoural Formation, composed of mica-schists, gneisses and diverse metavolcanic rocks. Exposures of these sequences can be found in restricted domains within the BIC or adjoining its boundaries but are well-preserved in some NW portions of the EBAD (Figure II-3). For the sake of clarity, from here onwards these Neoproterozoic metavolcanic and metasedimentary sequences will be referred to by their common name 'Série Negra' (which in its strict meaning refers to the oldest exposed rocks throughout the OMZ).

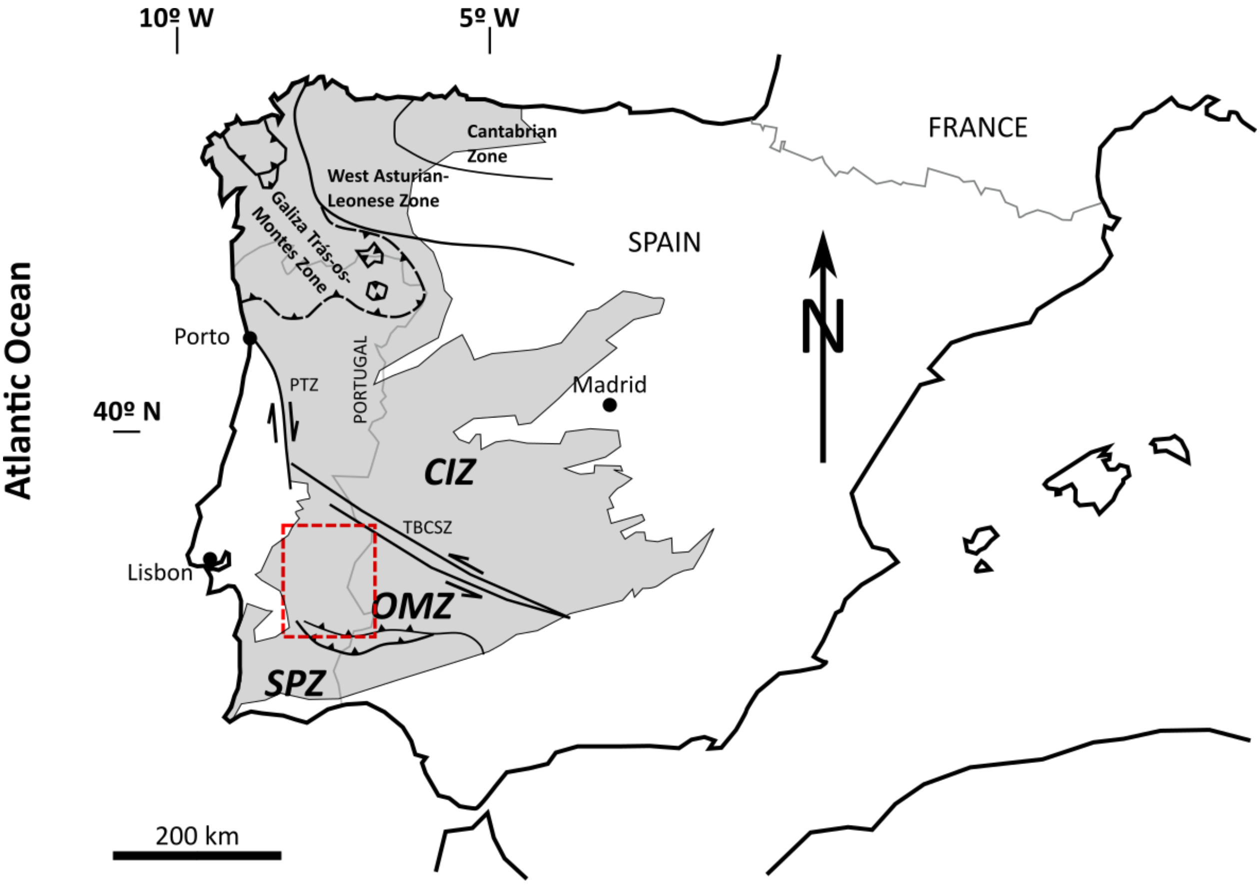

Figure II-1. Terrane map of the Iberian Peninsula. Red dashed line indicates the location of Figure II-2. Adapted from Ribeiro *et al.* (2007). SPZ – South Portuguese Zone, OMZ – Ossa-Morena Zone, CIZ – Central Iberian Zone.

An extensive carbonate, locally dolomitic, platform was developed during the Lower Cambrian (*ca.* 540 Ma), which onset was associated with significant bimodal volcanism. The geological record of this evolving stage is provided by the Montemor-Ficalho dolomitic meta-limestones and marbles (also called the “Dolomitic Formation”), along with minor bimodal volcanics, that crop-out in the Serpa anticline and along strips across the SE portions of the EBAD in Portugal, and in very restricted windows within the central EBAD (Figure II-3). After an emersion period of imprecise extent, a new cycle of carbonate deposition began, locally simultaneous with significant volcanic activity and/or fine-grained siliciclastic sedimentation. These processes generated the heterogeneous volcano-sedimentary piles that typify the Upper Cambrian (to Lower Ordovician?, *ca.* 500-470 Ma) geological record in the EBAD, well-represented by the Ficalho-Moura Vulcano-Sedimentary Complex which includes successions of marbles, schists and diverse metavolcanic rocks with variable thickness and internal arrangement (Oliveira *et al.*, 1991).

The Cambrian-Ordovician boundary marks the opening of the Rheic ocean. Afterwards, at the Ordovician-Silurian boundary (*ca.* 450-430 Ma), a new rifting episode started, driving the opening of the Paleothetys ocean and splitting Armorica (and Finisterra) from the rest of Iberia (Ribeiro *et al.*, 2007). A siliciclastic platform was established during the Silurian, leading to the accumulation of monotonous fine-grained sediments locally accompanied by manifestations of magmatic activity, now represented by the Moura Schists, a major litho-stratigraphic unit of the EBAD (Figure II-3).

Closure of the Rheic and Paleothetys oceans had already begun during Silurian-Devonian times (*ca.* 425-410 Ma), but the onset of oblique continental collision took place in the Lower to Middle Devonian period (*ca.* 390-370 Ma; Ribeiro *et al.*, 2007). The onset of a magmatic arc growth during Devonian times remains somewhat controversial, but bimodal (meta-)volcanic sequences associated with carbonate sedimentary sequences, exposed near the Odivelas dam, are interpreted to represent a subduction-related magmatic arc (da Silva, 2011). The obduction of an ephemeral back-arc basin related to the opening of Paleothetys is documented by the Beja-Acebuches Ophiolite Complex (BAOC) and associated accretionary wedge, the Pulo do Lobo Terrane (PLT; *e.g.*, Quesada *et al*, 1994; Ribeiro *et al.*, 2007). These exotic terranes occur along tectonic contacts to the South of the BIC and trace the boundary between the Ossa Morena and the South Portuguese zones. Slivers of the Rheic oceanic basement are preserved within the Internal Ossa-Morena Zone Ophiolite Sequences, namely in tectonic stackings involving the Moura schists and, in some places, within older lithostratigraphic sequences (Fonseca *et al.*, 1999).

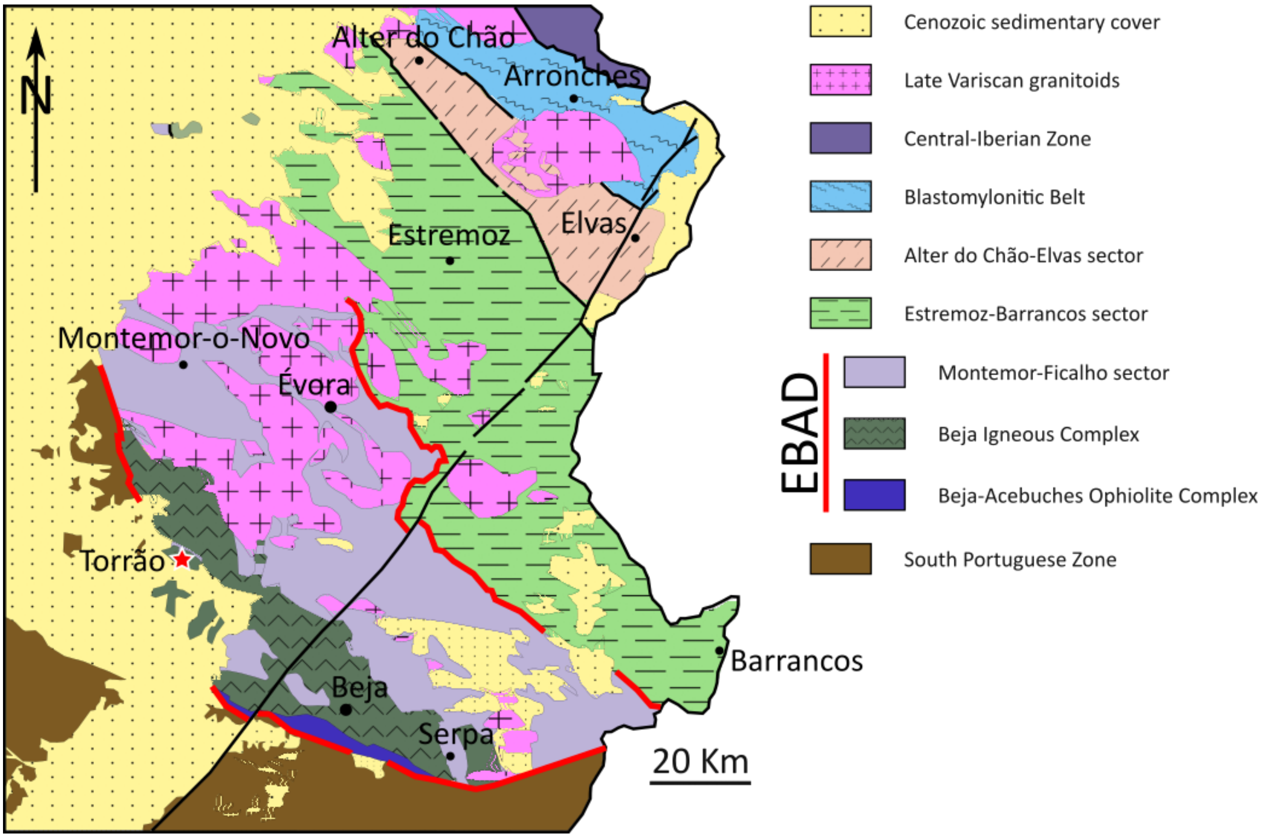

Figure II-2. OMZ division into stratigraphic sectors. Adapted from Oliveira *et al.* (1991).

Variscan tectono-metamorphic constraints in the Évora-Beja-Aracena Domain

The tectono-metamorphic evolution of the EBAD during subduction and subsequent continental collision during the Variscan orogeny can be divided into three deformation phases; their main characteristics can be outlined as follows:

i) D_1: The first deformation phase follows a HP-LT (High Pressure-Low Temperature) path during which blueschist/eclogite facies rocks developed (*e.g.*, Safira, Viana do Alentejo, Vidigueira-Vila de Frades), concurrently with the subduction/obduction of the back-arc basin (Moita *et al.*, 2005a; Fonseca *et al.*, 1999). Structures formed during this phase display a preferred WNW-ESE strike and vergence to the S-SW. The eclogite rocks define a clockwise P-T path that peaks at 16-18 kbar and 600-650 ºC; Sm/Nd whole rock-garnet age date the eclogites at 371 ± 17 Ma, whereas $^{40}Ar/^{39}Ar$ in late amphibole date exhumation and cooling below 550-500 ºC at 360 ± 4 Ma (Moita *et al.*, 2005a).

ii) D_2: The second deformation phase is coeval with the development of widespread magmatic activity in the EBAD, triggered by underplating, leading to a transition from HP-LT to LP-HT metamorphism, that peaked at amphibolite facies conditions (Dallmeyer *et al.*, 1993).

This phase is diachronic from SW to NE and usually sub-divided into D_{2a} and D_{2b}. Structures formed during D_2 display a N (D_{2a}) to NW (D_{2b}) vergence, indicating an anti-clockwise rotation of the stress field (*e.g.*, Fonseca, 1995). Available geochronological data from OMZ metamorphic rocks date the LP-HT event at 358 ± 11 Ma (Rosas *et al.*, 2008; based on K/Ar on muscovite, yielding the minimum age) and suggest that it lasted *ca.* 30 Ma (Dallmeyer *et al.*, 1993; Castro *et al.*, 1999).

iii) D_3: The third deformation phase marks the waning stages of collision achieved after voluminous crustal melting processes caused by the extensive post-D2 decompression at *ca.* 325-320 Ma, to which many peraluminous granites are associated (*e.g.*, Évora Massif, located immediately to the North of BIC). The D_3 phase is synchronous of metamorphic retrogression towards LT conditions (*e.g.,* Fonseca, 1995). Structures formed during this phase display a preferred NW-SE strike. Other subsidiary WNW-ESE shear zones developed during this deformation phase acted as the main conduits for focused fluid flow which led to strong carbonate-siliceous metasomatism within the BAOC and BIC (Mateus *et al.*, 1999). Post-collisional granites in the EBAD were dated at 298 ± 3 Ma and provide the youngest age estimate for D_3 (Moita, 2005b).

The Beja Igneous Complex

The BIC is a major geological feature of the SW Iberian Variscides, extending along the OMZ southern border in Portugal for over *ca.* 100 km (Figure II-2). This complex comprises three main units which document progressively younger and more evolved magmatic episodes, namely the Layered Gabbroic Sequence, the Cuba-Alvito gabbro-diorite Complex and the Baleizão Porphyry Complex (Figure II-3). Geochronological data for each unit will be presented afterwards.

Layered Gabbroic Sequence (LGS)

The Layered Gabbroic Sequence (LGS) is the most primitive unit and has been a target for several studies (*e.g.*, Jesus, 2011; Jesus *et al*., 2003a, 2003b, 2007, 2014, 2016). A noticeable feature of the LGS, as its name implies, is its uncommon – given the collisional context (*e.g.*, Parsons, 2013) – layered character, which strikes from NNW-SSE to WNW-ESE and dips 25º to the S-SW (*e.g.*, Jesus, 2011). The regional Messejana strike-slip fault zone separates the LGS into an eastern and western compartment, the latter comprising four main sectors, from NW to SE: Soberanas, Odivelas, Ventoso and Ferreira-Beringel (Jesus, 2011; Figure II-3).

Compiling evidence preserved in sectors forming the LGS western compartment show that the gabbroic rocks develop distinct magmatic Series portraying specific layering features and mineralogical and geochemical affinities. These Series were labelled as Soberanas (SB) I and II, Odivelas (ODV) I, II and III (the third Series is exposed at Ventoso), and Beringel (BRG) I and II (*e.g.*, Jesus *et al*., 2016; Figure II-3). The SB I Series comprises mostly troctolite and wehrlite rocks within olivine leucogabbros. Based on mineral chemistry, the SB I series is used as a proxy for LGS parental magmas, *i.e.*, high alumina, low-K, primitive basalts (Jesus *et al*., 2014). Further North, the SB I series contacts with SB II through a WNW-ESE shear zone. The SB II Series is primarily composed of oxide-rich gabbronorites which marginal position, fine-grained texture and geochemical features have been interpreted as representing the LGS chilled margins (Jesus, 2011). Representative samples of SB II display the most primitive (less contaminated) Nd-Sr isotopic values for the LGS ($^{86}Sr/^{87}Sr_{350Ma}$ = 0.7031; εNd_{350Ma} = +6.0; Jesus *et al*., 2016). To the SE, the ODV I Series marks the peak of the Fe, Ti and V enrichment trend set by the SB I → SB II → ODV I sequence. This sequence follows a tholeiitic path, leading to the formation of massive Fe-Ti-V oxide ores (Ti-maghemite after magnetite + ilmenite; Jesus *et al*., 2003) within ODV I Series olivine leucogabbros, wehrlite and olivine clinopyroxenite. This sequence is interpreted as a major differentiation path (Fo_{88-54}) within an upper magmatic chamber with very limited replenishment. Subsequently emplaced Series (ODV II and III, BRG I and II) encompass several types of gabbroic rocks and never differentiated enough to reach the levels of Fe enrichment that characterize ODV I, thus following a calc-alkaline trend (*e.g.*, Jesus, 2011; Jesus *et al*., 2014). This shift in geochemical behavior can be explained by recurrent magma replenishment processes, assisted by periodic opening of the magma chamber, which in turn was favored by the tectonic regime operating at that time (Jesus, 2011). Other mineralization types include sulfide veins (pyrrhotite + pyrite + chalcopyrite) hosted in metasomatic haloes superimposed on ODV III Series, and intercumulus to massive Ni-Cu-Co rich sulfides (pyrrhotite + pentlandite + chalcopyrite ± pyrite) hosted in clinopyroxenites of BRG II Series. Additionally, an eighth suite of rocks can be recognized, labelled the Border Group (BG), rimming the Ferreira-Beringel sector. The BG comprises heterogenous anorthosites that enclose troctolite xenoliths identical to those included in SB I (Jesus, 2011). Isotopic data for the LGS shows a clear correlation between magmatic differentiation and Nd-Sr enrichment, suggesting the progression of Assimilation-Fractional Crystallization processes (AFC; DePaolo, 1981).

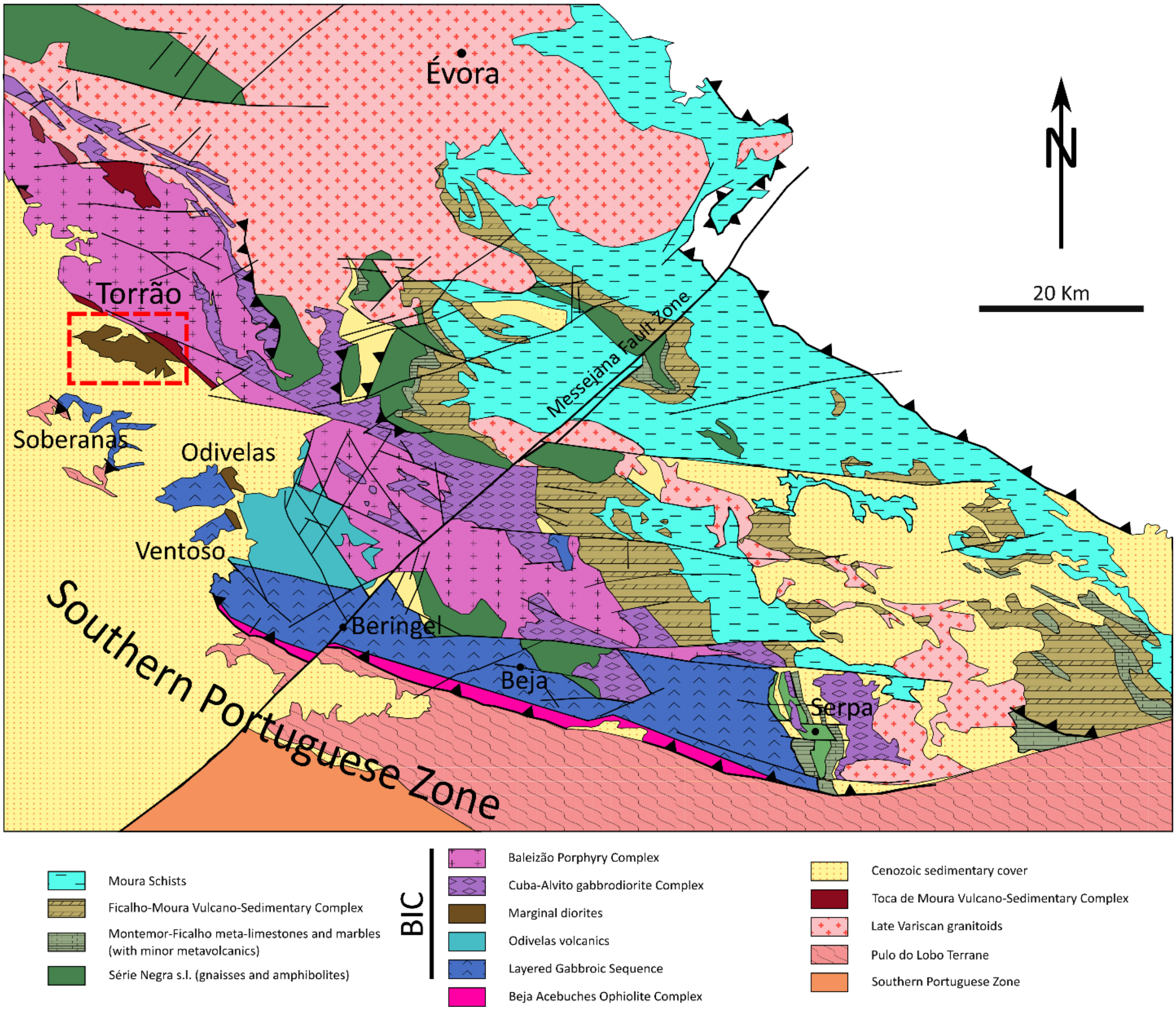

Figure II-3. Schematic geologic map of the EBAD. Red dashed line indicates the study area, Torrão. The "unaffiliated diorites" were included in the CAC. Adapted from Jesus *et al.* (2016) and the 1:500 000 geological map of Portugal provided by LNEG (Laboratório Nacional de Energia e Geologia, available at https://geoportal.lneg.pt/).

Four additional types of evolved rocks document the multiphase magmatic evolution of the BIC: the Anorthosite-Tonalite-Trondhjemite (ATT) suite, pegmatoid dykes, marginal diorites, and felsic (high-K) dykes and sills (*e.g.*, Jesus *et al*., 2016). The ATT suite develops dyke-swarms enveloping the

BG which emplacement is controlled by NW-SE shear zones, postdating the LGS and possibly the adjoining diorite domains. The pegmatoid dykes that intrude the ODV III Series are of centimetric thickness and comprise Mg-hornblende (replaced by actinolite) + albite + quartz. These dykes result from late events that progressed under magmatic-to-hydrothermal conditions, entangling contributions from siliceous melts (Jesus, 2011). The marginal diorites crop-out to the North of the Odivelas and Soberanas sectors; in the former sector, an aureole of amphibolitic gabbros marks the transition between the ODV I series and diorites. Late intruding high-K felsic dykes and sills are interpreted as the roots of the Baleizão Porphyry Complex.

Cuba-Alvito gabbro-dioritic Complex (CAC)

The Cuba-Alvito gabbro-dioritic Complex (CAC) comprises several intrusions of diorite, gabbro, a mix of both, tonalite and granodiorite (Andrade, 1983; Caldeira *et al*., 2007). This complex develops an extensive margin to the North of the Baleizão Porphyry Complex and intrudes older metasedimentary sequences (Figure II-3), locally developing Fe-skarns (such as those in Vila Nova de Baronia, Vila de Frades and Herdade da Louzeira). The compositional nature of CAC rocks ranges from tholeiitic (gabbroic rocks) to calc-alkaline, falling in the medium-K to high-K calc-alkaline fields in a K_2O *vs.* SiO_2 diagram (SiO_2 concentrations around 55 wt%; Caldeira *et al*., 2007; Andrade, 1983, 1984). In general, the CAC is interpreted to have resulted from magma mixing and contamination at the BIC margin (Andrade, 1983). Chondrite and primitive mantle-normalized concentrations of Rare Earth Elements (hereafter, REE) and selected incompatible elements for the CAC "gabbrodiorites", Torrão diorites (discussed below) and SB II series are shown in Figure II-4. The normalized incompatible elements trend displays a somewhat similar pattern to the SB II and the Torrão diorites, the main difference being higher Cs and Rb values. Conversely, the normalized-REE trend for the CAC shows marked LREE enrichments and a flat HREE pattern, reflecting the abundance of mineral phases that incorporate LREE, such as apatite.

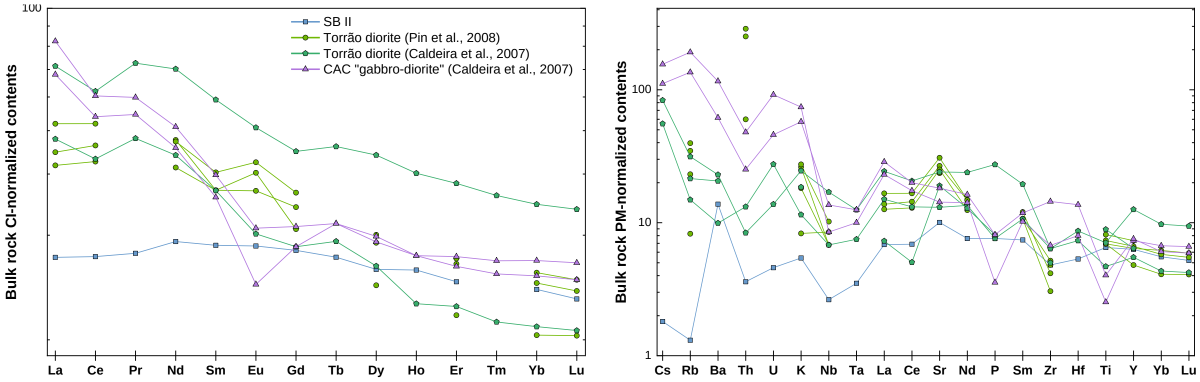

Figure II-4. Chondrite-normalized patterns for REE and Primitive Mantle-normalized patterns for selected incompatible elements, including data for the SB II series, Torrão diorites and a median of the CAC rocks. Data from Caldeira *et al.* (2007) and Pin *et al.* (2008)

Baleizão Porphyry Complex

The most evolved and youngest member of the BIC is the Baleizão Porphyry Complex, composed of several epizonal granitoid bodies. It extends over the largest exposure area out of all the BIC units, suggesting a multistage emplacement of consecutive magma pulses (Figure II-3). The most typical rocks are dacites and porphyry rhyolites, displaying calc-alkaline affinities (Andrade, 1983). This unit is interpreted to have derived from the same magmas that gave rise to the CAC with significant crustal contributions, due to their Th and U enrichments (Caldeira *et al*., 2007).

“Unaffiliated diorites”

Other diorite-bearing units crop-out within the BIC, namely the “Dioritos de Casa Branca” and “Dioritos de Monte Novo”, which were included in the “unaffiliated diorites” (Jesus, 2011). According to Ferreira *et al*. (2014), gabbroic rocks also occur in the Monte Novo diorite unit. The Monte Novo diorites comprise plagioclase, amphibole, pyroxene, quartz, and biotite as the main mineral assemblage; the gabbros have a similar mineral assemblage but higher amphibole-pyroxene/plagioclase proportions. No major, minor or trace element contents are available, but diagrams reported in Ferreira *et al*. (2014) show that these diorites have silica concentrations in the range of 55-60 wt% whereas the nearby gabbros have < 52 wt% SiO_2, thus allowing their distinction. All these rocks display calc-alkaline affinities (Ferreira *et al*., 2014).

Geochronological constraints

A summary of the most relevant geochronological data concerning the BIC and adjoining units is shown in Table II-1; the compiled data does not represent all available geochronological data for an area of such large extension but provides a representative overview on the average ages.

Available U-Pb (ID-TIMS) geochronological data for the ‘Beja gabbroic complex’ (which is assumed to correlate to the LGS; Pin *et al.*, 1999) is restricted to two samples collected at Serpa and Torrão, and date the complex at 350 ± 4 Ma and 352 ± 4 Ma, respectively[1]. This age is interpreted as the crystallization/emplacement age of gabbroic rocks, based on the >900 ºC closure temperature of the U-Pb system in zircon (Lee *et al.*, 1997). Furthermore, Pin *et al.* (2008) dated two samples using U-Pb (ID-TIMS) on zircons from a leuco-diorite from Serpa (CAC), a tonalite from Torrão and a granodiorite from São Pedro (assumed to have been collected at an exposure of the CAC in São Pedro de Pomares, to the N of Baleizão), indicating crystallization/emplacement ages of 350 ± 2 Ma, 352 ± 2 Ma and 353 ± 4 Ma, respectively. Ages obtained for Variscan intrusives in Spain along the NW-SE alignment of the BIC point towards a later ~340 Ma major magmatic event (Table II-1). The 355-345 Ma interval is thus interpreted as a first collision-related tectono-magmatic event, coeval with D_{2a} and the development of widespread magmatic activity (Jesus, 2011).

The $^{40}Ar/^{39}Ar$ dating of amphibole concentrates extracted from samples collected in the LGS (340 ± 1; 338 ± 1 Ma), BAOC (347 ± 3; 343 ± 1; 342 ± 1 Ma) and Série Negra (337 ± 2; 341 ± 1 Ma) are reported in Dallmeyer *et al*. (1993; Table II-1). Assuming a reasonable 500-550 ºC closure temperature for amphibole, these ages around ~340 Ma are interpreted to represent the regional cooling period, following moderate to rapid crustal uplift (Dallmeyer *et al*., 1993; Pin *et al*., 2008). This event also provides an estimate for the transition between the D_{2a} and D_{2b} phases of Variscan deformation (Jesus *et al*., 2007). The Ar-Ar ages indicated for Série Negra samples therefore imply the overprinting and resetting experienced by these rocks during regional Variscan tectono-metamorphic events, their ages corresponding to regional cooling below the 500-550 ºC isotherm. The average U-Pb (SHRIMP) zircon age of 342 ± 9 Ma for the amphibole-bearing pegmatoid dykes that crosscut the LGS (ODV III Series) dates the crystallization/emplacement of hydrous melts during the regional retrogression metamorphic path from amphibolite to greenschist facies conditions, in agreement with the previous data (Jesus *et al*., 2007). Dating of the Baleizão Porphyry Complex, the youngest BIC unit, yields an age of 324 +8/-5 Ma (Priem *et al*., 1976) which is interpreted as the last stage of the LP-HT regime, coeval with development of crustal-derived melts (Jesus, 2011).

---

[1] Note that these ‘gabbroic’ samples were collected at Serpa and Torrão, where units other than the LGS crop-out (namely, the CAC at Serpa and, of course, the diorites at Torrão). Having this in mind, care should be taken when interpreting these ages since the lack of petrographic data and precise location of sampling makes it difficult to correlate them to the BIC units.

Table II-1. Summary of selected geochronological data for the OMZ southern border, its Spanish counterpart and exotic terranes. WR – Whole rock; Amp – Amphibole; Ms – Muscovite; Zrn – Zircon; Bt – Biotite; Sulf – Sulfides; Phl – Phlogopite. References: 1 – Pin *et al.* (1999); 2 – Pin *et al.* (2008); 3 – Dallmeyer *et al.* (1993); 4 – Rosas (2003); 5 – Jesus *et al.* (2007); 6 – Gomes (2000); 7 – Ruffet (1990); 8 – Priem *et al.* (1976); 9 – Giese *et al.* (1994); 10 – Azor *et al.* (2008); 11 – Castro *et al.* (2008); 12 – Spiering *et al.* (2005); 13 – Romeo *et al.* (2006); 14 – Tornos *et al.* (2006); 15 – Moita *et al.* (2005a).

Domain	Age (Ma)	Method	Mineral/WR	Rock type	Area	Reference (caption)
OMZ southern border (Portugal)	371 ± 17	Sm-Nd	Garnet-WR	Eclogite	Safira	15
	360 ± 4	$^{40}Ar/^{39}Ar$	Amp	Eclogite	Safira	15
	352.6 ± 4.4	U-Pb	Zrn	Granodiorite	São Pedro	2
	352 ± 4	U-Pb	Zrn	Gabbro	Torrão	1
	351.7 ± 2.1	U-Pb	Zrn	Tonalite	Torrão	2
	350.4 ± 2.3	U-Pb	Zrn	Leucodiorite	Serpa	2
	350 ± 4	U-Pb	Zrn	Gabbro	Serpa	1
	345.2 ± 2.1	U-Pb	Zrn	Felsic dyke	Vau de Cima	2
	342 ± 9	U-Pb	Zrn	Pegmatoid dykes	Ventoso	5
	339.5 ± 1.0	$^{40}Ar/^{39}Ar$	Amp	Gabbro	Odivelas	3
	337.9 ± 1.0	$^{40}Ar/^{39}Ar$	Amp	Gabbro	Odivelas	3
	336.4 ± 0.8	$^{40}Ar/^{39}Ar$	Amp	Gabbro	Beja	7
	334 (+8/-5)	K-Ar	Ms	Porphyry	Alcáçovas	8
	331 ± 7	K-Ar	Amp	Diorite	Alvito	6
	325 ± 10	K-Ar	Amp	Gabbro-diorite	Viana-Alvito	4
	298 ± 3	Rb-Sr	Bt-WR	Granite	Sesmarias	15
Exotic terranes (Portugal)	342.6 ± 1.4	$^{40}Ar/^{39}Ar$	Amp	Amphibolite	BAOC	3
	342.6 ± 0.6	$^{40}Ar/^{39}Ar$	Amp	Amphibolite	BAOC	11
	342.0 ± 0.8	$^{40}Ar/^{39}Ar$	Amp	Amphibolite	BAOC	3
	340 ± 4	U-Pb	Zrn	Amphibolite	BAOC	10
	337 ± 5	U-Pb	Zrn	Amphibolite	BAOC	10
Santa Olalla Pluton (Spain)	347 ± 3.4	U-Pb	Zrn	Granodiorite	Minor facies	12
	344 ± 2.1	U-Pb	Zrn	Mineralized gabbro	Aguablanca stock	12
	338.6 ± 0.8	U-Pb	Zrn	Diorite dikes	Aguablanca stock	13
	338.2 ± 3	$^{40}Ar/^{39}Ar$	Phl	Brecia pipe rocks	Aguablanca stock	14
	335 ± 2	$^{40}Ar/^{39}Ar$	Phl	Brecia pipe rocks	Aguablanca stock	14

Geodynamic evolution

Reported geochemical and isotopic data (Pin *et al.*, 2008; Jesus *et al.*, 2014) support an asthenospheric mantle source for the LGS and associated mesocratic rocks, with variable contributions from lower and upper crustal components (Jesus *et al.*, 2016). LGS rocks display a complex geobarometric history, ranging from 9 to 4 kbar (from *ca.* 27 to 12 km depth). The maximum barometric estimates suggest that the primary locus of magmatic emplacement was the Moho, whereas minimum estimates place the magmatic chamber at the upper crust (Jesus *et al.*, 2016). High emplacement temperatures (>900 ºC) reported in Jesus *et al.* (2016) explain the lack of regional amphibolite facies metamorphism that affected the OMZ autochthonous rocks at *ca.* 350 Ma and the well-preserved igneous mineral assemblage of the LGS. Crustal uplift following slab-breakoff at *ca.* 345 Ma is argued to have promoted regional cooling to temperatures below 500-550 ºC (Jesus *et al.*¸ 2007; Pin *et al.*, 2008; Ribeiro *et al.*, 2010).

According to Jesus (2011), the BIC evolution can be envisaged as the result of a Deep Crustal Hot Zone (DCHZ). Following the definition of Annen *et al*. (2006), repeated intrusions in the deep crust will stall and generate a zone where magma, heat and volatiles accumulate. Incomplete crystallization of basaltic magma, remelting of older intrusions and partial melting of older crust are the main processes whereby intermediate and silicic melts generate (Annen *et al*., 2006). Geobarometric data (Jesus *et al*., 2016) is consistent with magma underplating and stalling at the lower crust, further supporting the DCHZ model for the BIC. Extraction of magma from the DCHZ to an upper crustal chamber was favored by the tectonically active regime present at the time. The SB I → SB II → ODV I series represent a major differentiation event driven by low-pressure fractionation (after magma extraction from the DCHZ to the upper crustal chamber), peaking with the development of massive Fe-Ti oxides. The evolution of subsequently emplaced series (ODV II → ODV III → BRG I → BRG II) resulted from repeated magma replenishments (Jesus *et al*., 2016). As for the more evolved melts of the LGS, assimilation of isotopically similar amphibolitic rocks within the lower crust is proposed in Jesus *et al*. (2016) to have provided the necessary water to generate the diorite rocks that outcrop in the LGS margins. The genesis of the ATT suite and pegmatoid dykes required a more significant contribution from isotopically contrasting crustal rocks, argued to be represented by the metasedimentary pile above the granulitic lower crust (Jesus *et al*., 2016).

III. Local Geology

The Torrão diorites crop-out at *ca.* 10 km to the North of the SB II series within a small window (*ca.* 20 km^2) imbedded in Cenozoic sediments, which northern limit corresponds to the late NW-SE strike-slip Torrão fault zone that places these rocks in contact with the Carboniferous Toca de Moura volcano-sedimentary complex and the Baleizão Porphyry Complex (Figure II-3). Studies concerning the Torrão diorites are scarce and mainly report geochemical and isotopic data with very limited petrographic information (Pin *et al*., 2008; Caldeira *et al*., 2007). Together with the diorites exposed in the Odivelas and Ventoso sectors, the Torrão diorites define a marginal NW-SE alignment along the northern border of the western compartment of the LGS (Figure II-3).

Before reviewing further information regarding the rocks exposed at Torrão, clarification regarding their classification in the literature is necessary. Reported petrographic data indicates that the Torrão rocks comprise mostly clinopyroxene, amphibole, plagioclase, magnetite and ilmenite (Caldeira *et al.*, 2007). Secondary minerals include apatite, biotite, titanite and quartz. There is no additional information relative to the proportions of the mineral assemblages nor of any intra-granular textural features. Classification of these rocks varies according to authors; for example, Caldeira *et al.* (2007) classify them as gabbros, based on a total alkali (K_2O + Na_2O wt%) – silica diagram (Cox *et al.*, 1979). However, according to the IUGS (International Union of Geological Sciences) this diagram should be used to classify aphanitic and glassy rock types, not being appropriate to categorize phaneritic rocks such as gabbros or diorites. Following the same IUGS recommendations, a QAPF diagram (Q- Quartz, A- Alkali feldspar, P- Plagioclase, F- Feldspathoids; Le Maitre, 1989) should be used to plot phaneritic, magmatic rock types that contain > 10 modal% Q + A + P + F, such as diorites. In this diagram, the Torrão rocks plot near the P point, along the P-Q line, on the Gabbro/Diorite field. Distinction between these two lithologies is made based on the anorthite molecule content of plagioclase: gabbros have An% > 50% and diorites have < 50%. Mineral chemistry data from Caldeira *et al.* (2007) reveals that half of the analyzed plagioclase grains show An% above 50. This data makes classification of the Torrão rocks somewhat difficult. Nonetheless, a diorite classification should be favored since these rocks are distinct from the gabbros forming the LGS, and pyroxene is not a major constituting mineral, as shown by petrographic data (discussed below).

The Torrão diorites are also termed as the 'high-Ti diorites' in Jesus (2011) based on their Ti and Fe enrichment relative to the 'low-Ti diorites' preserved in domains to the North of the ODV I series. Reported geochemical data for the Torrão diorites by Caldeira *et al.* (2007) is very similar to the high-Ti diorites and as such, will be included in this group from here onwards[2]. Other diorite rocks from Torrão are also classified as low-Ti, but these are described as 'microgranular enclaves', 'microdiorite enclaves' and 'Hbl-diorites' by Pin *et al.* (2008) and consequently will not be considered as part of the "true" Torrão diorites; this same work reports the occurrence of tonalites in the Torrão area.

Additional geochemical features for the Torrão diorites include restricted low silica (47.09-49.60 wt%) – distinctively lower than the values indicated for the Monte Novo diorites and CAC gabbro-diorites – and low Ni and Zr contents. Compared to the low-Ti diorites, the diorites at Torrão display mild LILE (Large-Ion Lithophile Elements) enrichment in comparison with HFSE (High Field Strength Elements). Like the LGS suite, the Torrão diorites display a somewhat transient character between tholeiitic and calc-alkaline affinities (Jesus, 2011, including data from Pin *et al.*, 2008; Caldeira *et al.*, 2007): in a FeO^T/MgO vs SiO_2 diagram, the Torrão diorites plot on the high-Fe tholeiitic field (from Arculus, 2003), whereas in a K_2O vs SiO_2 diagram they plot on the medium-K calc-alkaline field (from Miyashiro, 1947). Such diagrams should be interpreted carefully since these diorites are enriched in Fe, which strongly influences deviations towards the reference field of tholeiitic affinity, and the K_2O concentrations can be related to late superimposition of HT(-alkaline) metasomatic processes or heterogeneous interactions with evolved melts, like those involved in the multistage development of the BPC.

As noted previously, the relationship between the Torrão diorites and other BIC units is still uncertain and constitutes the motivation for this work. The REE and selected incompatible element normalized patterns suggest that Torrão diorites may be related to the SB II series by concurrent fractionation along with possible assimilation, due to LREE + Th enrichment (the Th enrichment is absent from the data reported by Caldeira *et al.*, 2007; Figure II-4), and slight discrepancies in the patterns (*e.g.*, Jesus *et al.*, 2016)[3]; it should be noted that the LREE enrichment could also be caused by the abundance of apatite, as described in Caldeira *et al.* (2007). Indeed, Santos *et al.* (1990) described diorites to the North of the Soberanas sector, before cropping out again in Torrão, suggesting a gradual transition between these two units. Available Sr-Nd isotopic data for the LGS (Jesus *et al.*, 2014, 2016; Pin *et al.*, 2008) overlaps the field where the diorites plot ($^{87}Sr/^{86}Sr_{350Ma} = 0.7045$; $\varepsilon Nd_{350Ma} = +2.5 \pm 1$; Pin *et al.*, 2008), which, combined with geochemical data, reinforces the interpretation that the Torrão diorites derive from the same magma batch that gave rise to the LGS. Furthermore, Jesus *et al.* (2016) suggest the contribution from a deep crustal amphibolitic source to explain the genesis of such hydrous and isotopically primitive magmas; the geodynamic meaning behind this process will be addressed below.

---

[2] Data published by Caldeira et al. (2007) was not used in Jesus (2011) and therefore, not included in the high-Ti designation.

[3] The data set used by Jesus *et al.* (2016) and their interpretation does not include the geochemical data reported by Caldeira *et al.* (2007). However, the same conclusions apply since the samples 39D-1 and 39D-8 (reported in Caldeira *et al.*, 2007) display broadly similar patterns to the SB II, albeit with some discrepancies (Figure II-4 includes the expanded dataset).

IV. Methodologies

Mapping and sampling

To fulfil the initially proposed objective, a mapping and sampling campaign was designed to ensure the overall representativity of the rocks cropping out at Torrão. Fieldwork was mainly carried out to the North of the Torrão village and along the Xarrama river, where well-preserved exposures allowed a detailed analysis of several facies, besides their features and mutual relationships. Mapping was done on tracing paper over an aerial photograph of the area surrounding the Torrão village at a scale of around 1:15,000. Structural features were measured using a compass and the FieldMove Clino application (Petroleum Experts Ltd); measurements are in azimuth notation, following the standard ‘right-hand rule’ (strike, dip), and their plotting was performed using the Stereonet software (https://www.rickallmendinger.net/stereonet). Field observations were subsequently processed in ArcGIS Pro, allowing the production of a geological map of the study area (Figure IV-1). A schematic stratigraphic column was made based, considering field relationships and other attributes (see below) to reconstruct the architecture of the magmatic chamber. The following criteria were used during field work to distinguish different facies:

i) Mineralogy, namely the proportions of felsic and mafic minerals, mainly plagioclase and amphibole; mineral proportions contribute to the color index (leuco- and melano-) used.
ii) Textural features, such as grain size, layering and dominant crystal habits.
iii) Magnetic intensity, assessed with hand magnet.

Following these criteria, several facies were identified and a total of 20 samples were collected (Table IV-1). Nine of the samples were picked at the abandoned Torrão quarry (for location, see Fig. 2 ‘**Q**’ spot on the map), which exposures provided a better characterization of facies relationships. In addition, four samples (SEM-II1-R2, SEM-II2-R3, SEM-II2-R4 and SEM-I10-R12), corresponding to amphibolite (with variable degrees of metasomatism) and marble rocks, were collected near the Beja airport during additional fieldwork carried out in the broader scope of the Horizon Europe SEMACRET project (https://semacret.eu).

Table IV-1. Collected samples and their respective facies and location. Coordinates are given in the WGS 84 system.

Ref	Facies	Long. Coordinate	Lat. Coordinate
SEM-TOR-1	Melanocratic enclave (fine-grained amphibolite) w/ leucocratic injections	-8.23213	38.30076
SEM-TOR-2	Melanocratic enclave (fine-grained amphibolite) w/ leucocratic injections	-8.23197	38.30081
SEM-TOR-3	Melanocratic enclave (amphibolite) within a quartz-diorite	-8.23176	38.30080
SEM-TOR-4	Acicular-textured diorite	-8.23146	38.30070
SEM-TOR-5	Quartz-diorite	-8.23131	38.30056
SEM-TOR-6	Melanocratic (amphibolite) enclave	-8.23222	38.30072
SEM-TOR-7	Sulfide-rich injection	-8.23096	38.30032
SEM-TOR-8	Digested enclave	-8.23097	38.30044
SEM-TOR-9	Partly digested enclave within acicular-textured diorite	-8.23160	38.30079
SEM-TOR-10	Quartz-diorite	-8.23433	38.29912
SEM-TOR-11	Metasomatized quartz-diorite	-8.23373	38.29907
SEM-TOR-12	Diorite	-8.23291	38.29864
SEM-TOR-13	Acicular-textured diorite	-8.23184	38.29846
SEM-TOR-14	Quartz-diorite	-8.23402	38.29992
SEM-TOR-15	Melanocratic enclave (amphibolite) within diorite	-8.23096	38.30087
SEM-TOR-16	Pegmatoidal domain	-8.23459	38.30001
SEM-TOR-17	Quartz-diorite	-8.23639	38.29851
SEM-TOR-18	Metasomatized diorite	-8.23646	38.29869
SEM-TOR-19	Strongly metasomatized diorite with a cataclasite-like domain	-8.22948	38.29881
SEM-TOR-20	Acicular-textured diorite	-8.23066	38.30263
SEM-II1-R2	Amphibolite	-7.93710	38.06722
SEM-II2-R3	Amphibolite	-7.94056	38.07066
SEM-II2-R4	Amphibolite	-7.94133	38.07111
SEM-I10-R12	Marble	-7.94904	38.07615

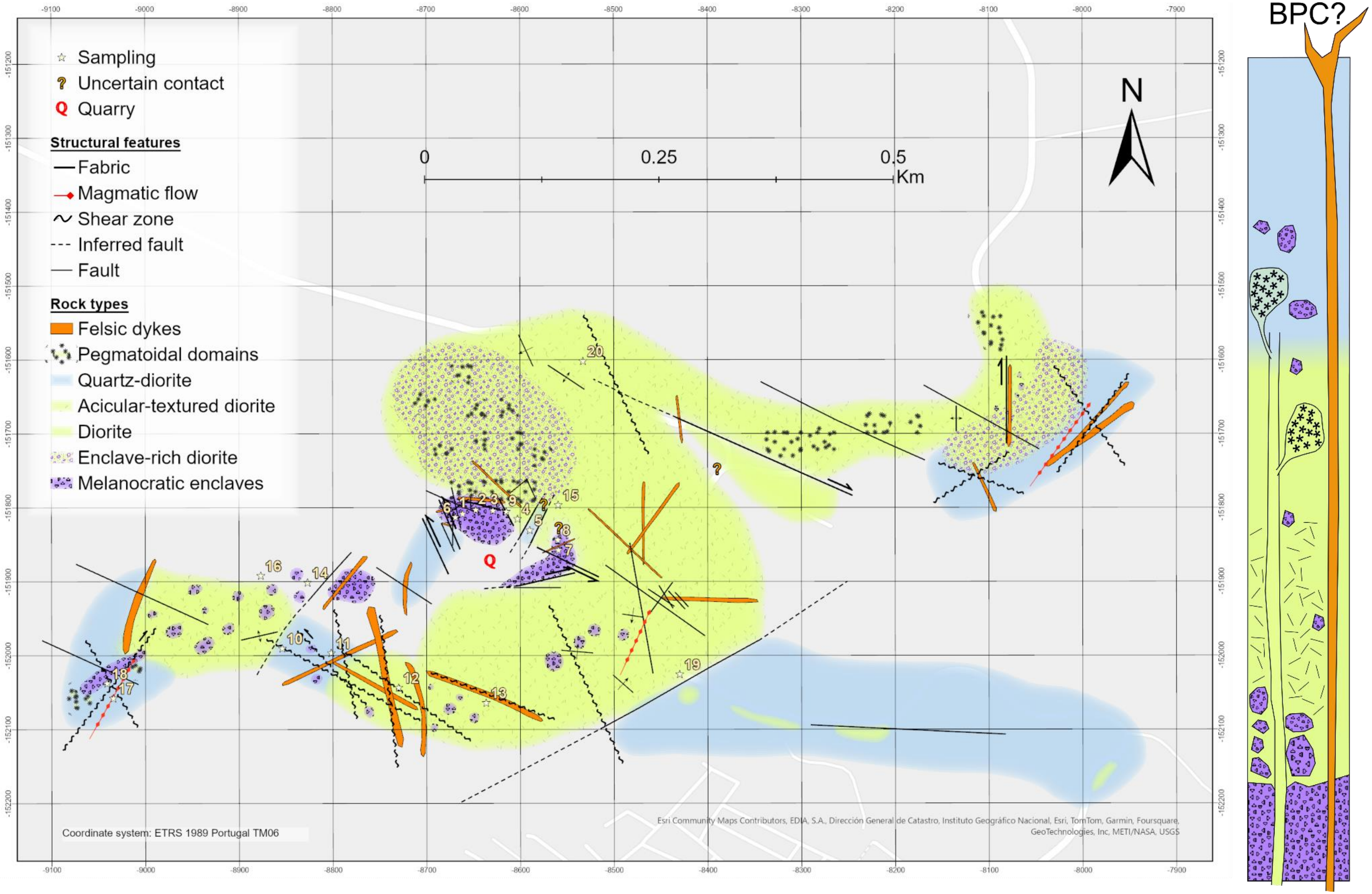

Esri Community Maps Contributors, EDIA, S.A., Dirección General de Catastro, Instituto Geográfico Nacional, Esri, TomTom, Garmin, Foursquare, GeoTechnologies, Inc, METI/NASA, USGS

Figure IV-1. Geological map of the study area (made solely based on observations) and schematic interpretative *log*.

Petrography and mineral chemistry

Laboratorial processing of samples was carried out at the Geology Department of the University of Lisbon. Samples were cut using a diamond wheel saw from which slabs were obtained and photographed. Selected domains of the slabs were cut using a smaller diamond wheel saw to make a total of 29 billets with ~2 cm height which were subsequently abraded to make polished thin sections of 30 µm. The number of polished thin sections is higher than the total number of collected samples because some of these display significant mineralogy and texture variability or specific features requiring detailed characterization. The polished thin sections were analyzed under transmitted and reflected light microscopy with detailed and quantitative record of observations. Identification of the mineral assemblages and textural features that typify each rock facies were done to support their classification. Selected features within the polished thin sections were documented and (micro-) photographed.

The most relevant features within a total of 28 polished thin sections were selected for further mineral chemistry analysis. Electron probe microanalysis (EPMA) was performed at the Geology Department of the University of Lisbon using a JEOL-JXA 8200 equipped with four WDS spectrometers, six crystal analyzers (LIF, LIFH, PET, PETH, TAP, LDE2) and secondary and backscattered electron detectors, coupled with a dispersive energy spectrometer (EDS). The analyses were carried out using a 5 µm diameter beam, 25 nA, 15 kV acceleration potential and acquisition times of 20 seconds for peaks and 5 seconds for background radiation. The full database, as well as the used standards and detections limits are reported in Supplementary Data 1.

Whole-rock geochemistry

A total of 25 samples were analyzed for major, minor and trace elements. The number of samples selected for whole-rock geochemical analysis is higher than the total number of collected samples because some of these comprise more than one facies (for example, a melanocratic enclave within a diorite), which were analyzed separately.

The samples were prepared at the Geology Department of the University of Lisbon. Slabs were cut using a diamond saw wheel from which the obtained fragments were abraded with emery to remove saw metal contaminants. Coarse splitting of these fragments was done using a RETSCH BB 200 jaw crusher. The resulting materials were then pulverized in an agate ring mill. In all samples material was thoroughly cleansed with compressed air and alcohol and, when possible, the mills were pre-contaminated with a portion of the sample.

A minimum of 50 g of rock pulp material per sample was sent to Activation Laboratories Ltd. (ActLabs) in Canada for whole-rock geochemical analysis. At ActLabs, samples were analyzed by ICP-MS following lithium metaborate/tetraborate fusion (package code 4Lithoresearch); additionally, samples were subjected to further analysis for selected elements (Cd, Cu, Ni, S and Zn) by multi-acid digestion, ensuring smaller analytical errors (package code 4B1; details on the analytical procedures are provided at https://actlabs.com). The full dataset, standards and detection limits are reported in Supplementary Data 2.

V. Field relations

Within the studied area, four main rock types were identified: diorites, melanocratic enclaves, leucocratic injections and felsic dykes. No felsic dyke samples were collected since their analysis is out-of-scope, considering the proposed objective; these are interpreted to represent the roots of the Baleizão Porphyry Complex, which crops-out at *ca.* 2 km to the north of Torrão.

A striking feature which had not yet been reported for this region is the sheer abundance of melanocratic enclaves. These enclaves occur throughout the studied area as heterometric, blocky fragments within the diorites (Figure V-1A). Dense swarms of small to medium-sized fragments (up to 1 meter) can also be locally found in areas exhibiting strong focused magmatic flow features (Figure V-1B). Exposures at the Torrão quarry allowed assessing the size of some of the larger enclaves, which can reach the decametric scale.

Macroscopic lithological observations

Macroscopic observations of the diorites allowed the identification of plagioclase and amphibole as their main mineral constituents; accessory minerals could only be recognized under the microscope. Although quartz was only observed in a few samples in small quantities, the modal abundance of this mineral, inferred from microscopic observations (discussed below), justified the classification of some samples as quartz-diorites (Table IV-1). This mineral assemblage, and the lack of pyroxene as a major phase, justify a diorite classification. Plagioclase and amphibole modal proportions remain uniform and equivalent in most of the diorite facies, granting them their mesocratic appearance; sample **SEM-TOR-20** is an exception, corresponding to an acicular-textured diorite where the mafic minerals are more abundant.

The diorites exhibit considerable textural variety, which is a feature of prime importance in distinguishing the several diorite facies. Quartz-diorites display phaneritic texture with medium-sized grains (~1 to 3 mm) and isotropic mineral distribution (Figure V-1C). Acicular-textured diorites preserve layering features (Figure V-1E) and have well-developed acicular amphibole crystals, which are often strongly aligned along a preferential direction, defining a magmatic fabric (Figure V-1C). These two facies have the largest cartographic expression out of all the dioritic facies (Figure IV-1). Additionally, they develop local pegmatoidal domains characterized by abundant plagioclase and coarse-grained amphibole crystals, which are interpreted as representing “squeezed” domains within the magma chamber where volatiles (primarily water) and other amphibole-constituting elements concentrated (Figure V-1F). The (non-acicular textured) diorites and quartz-diorites are rather similar macroscopically, but in the latter rock type both plagioclase and amphibole can occur as medium-grained, globular-shaped crystals (Figure V-1G). Sample **SEM-TOR-20**, although being classified as an acicular-textured diorite, shows amphibole crystals that are slightly larger and isotropic in distribution (Figure V-1H). Sample **SEM-TOR-7** was collected at the top of the Torrão quarry and does not fit into any of the aforementioned facies. This sample corresponds to a sulfide-rich melanocratic injection with coarse amphibole grains within a fine-grained amphibolite (discussed in more detail below; Figure V-2A). The contact between the injection and the amphibolite enclave is marked by an amphibole-rich domain.

The melanocratic enclaves correspond to fine-grained amphibolites and are macroscopically similar to those included in the OMZ Neoproterozoic sequences. Textural criteria allow distinguishing two different amphibolite facies based on a slightly coarser-grained texture for one of them. Besides amphibole, only pyrite and pyrrhotite are observed in the amphibolites, occurring as fine disseminations or local millimetric aggregates (Figure V-2B); in the slightly coarser amphibolite, plagioclase can also be distinguished macroscopically. The amphibolite enclaves exhibit varying degrees of digestion by the diorites but are well-preserved in most cases. Reaction rims between the diorites and the amphibolite enclaves are limited to their contacts, where chemical reactions developed metasomatic haloes composed predominantly of plagioclase and a late-developed amphibole (Figure V-1A). A very incipient (primary?) fabric can also be identified in some of the amphibolite enclaves (Figure V-2C); in the enclave “swarm” domains (Figure V-1B), the orientation of plagioclase grains within amphibolite coincides with that of the magmatic flow.

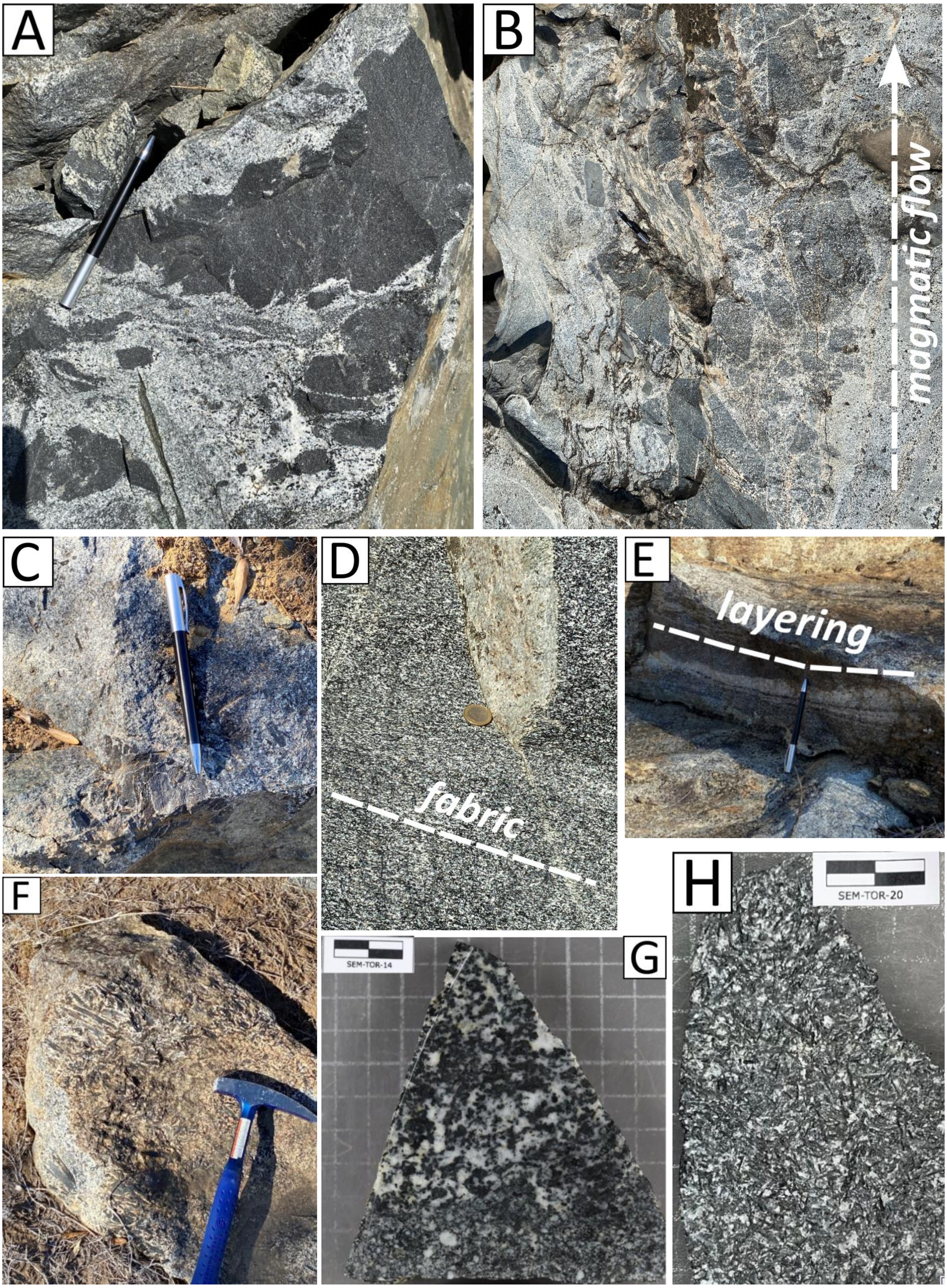

Figure V-1. Selected field and hand-sample photographs: (A) Typical appearance of the melanocratic enclaves within the diorites and the leucocratic rims developed during melt – enclave interaction (Torrão quarry). (B) Top-down look at dense breccia enclave swarms aligned with the direction of magmatic flow. (C) Typical appearance of a quartz-diorite and an enclave preserved within it. (D) Well-defined magmatic fabric and (E) layering features on the acicular-textured diorites. (F) Pegmatoidal domains within a diorite. (G) and (H) Typical appearance of a coarser-grained diorite and the isotropic acicular-textured diorite (samples **SEM-TOR-14** and **SEM-TOR-20**, respectively).

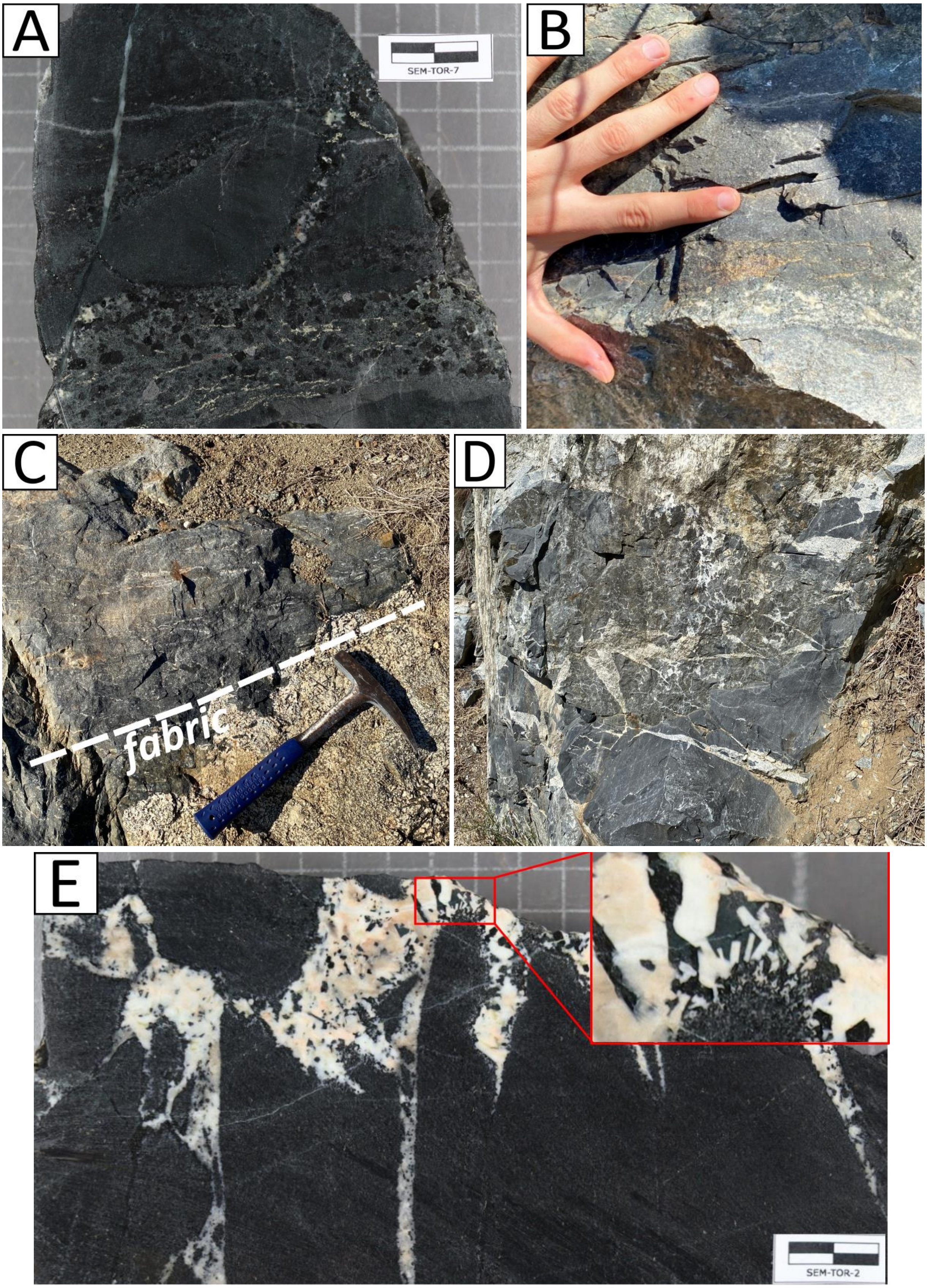

Figure V-2. Selected field and hand-sample photographs: (A) Sulfide-rich melanocratic injection within an amphibolite (**SEM-TOR-7**). (B) Pyrrhotite-rich aggregates within the fine-grained amphibolite. (C) Incipient fabric in the fine-grained amphibolite. (D) Leucocratic injections on a metric-scale amphibolite enclave. (E) Macroscopic features of the enclaves in (D), with reaction rims developing euhedral plagioclase crystals and a late amphibole.

Evolved leucocratic injections are often found in close association with the amphibolite enclaves. These are composed of plagioclase and late-developed amphibole, being macroscopically similar to those in the reaction rims of the enclaves developed during melt – enclave interaction. A distinction between the two can be made on the basis of the extent of reaction; the reactions rims are well-developed and form centimetric metasomatic haloes with permeated, mingling textures, whereas the leucocratic injections establish sharp contacts with the enclaves and their reactions are limited to a few millimeters off the contact (Figure V-2D and Figure V-2E). This contrast in the reactional physical-chemical behavior is interpreted to have resulted from the lower thermal (and/or chemical) contrast between the later-developed leucocratic injections and the amphibolite enclaves.

Structural features

Several faults and shear zones were identified throughout the study area, affecting all the mapped diorite facies; these structures account for many cartographic contacts between the several facies (Figure IV-1). Most fault and shear zones are sub-vertical and as such, rose diagrams were used to depict their orientation (Figure V-3). Both types of structures display similar trends, having a preferred NW-SE strike and predominant sinistral component of displacement; the fault zones define an additional N-S group (Figure V-3) which, in some cases, has strong associated metasomatism, generating a mineral assemblage composed of epidote + actinolite affecting the wall-rocks (Figure V-4A). Calcite infillings of fractures (typically subsidiary structures to a fault zone of larger dimensions) were also identified locally, strongly digesting the melanocratic enclaves they crosscut. Many fault zones exhibit brittle deformation arrangements, not affecting primary magmatic features such as the well-defined fabric displayed by the acicular-textured diorites. Evidence of ductile deformation is preserved by very local *en échelon* domains of more evolved, leucocratic diorite melts (within the diorites themselves; Figure V-4B), magmatic flow bands which direction is controlled by the conjugate NE-SW planes of shear zones, and sigmoid figures in melanocratic enclaves, which are found in association with pyrrhotite aggregates (only observed in an exposure at the top of the Torrão Quarry).

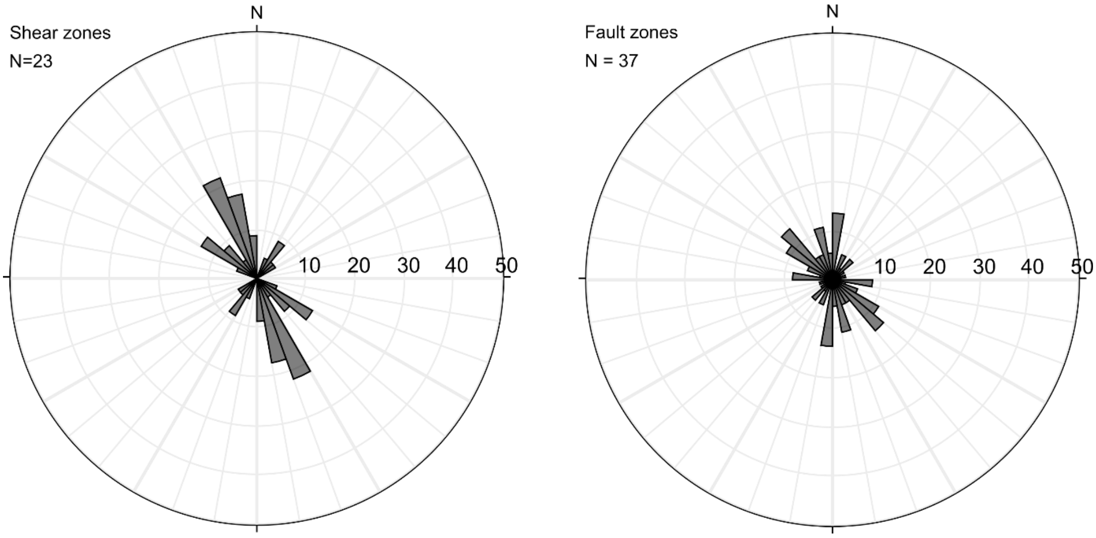

Figure V-3. Rose diagram projection of measurements of shear and fault zones.

Interpretation

The preferred NW-SE direction displayed by fault and shear zones is broadly coincident with the EBAD southern border to the SW of Torrão, suggesting a significant tectonic influence induced by the same stress field (σ_1 = NE-SW, where σ_1 corresponds to the maximum stress). This evidence allows correlating deformation in the Torrão area with the D_2 tectono-metamorphic phase of Variscan deformation, in agreement with the development of magmatic activity in the EBAD. Both brittle and ductile structures show the same mean direction, suggesting that the emplacement and crystallization of the Torrão diorites occurred under the same stress field and that the N-S brittle fault zones and fractures were developed subsequently. Development of these structures originated structural weaknesses and other smaller structural discontinuities which were later resumed by felsic dykes, presumably during development of the Baleizão Porphyry Complex dated at *ca.* 324 Ma by Priem *et al.* (1976).

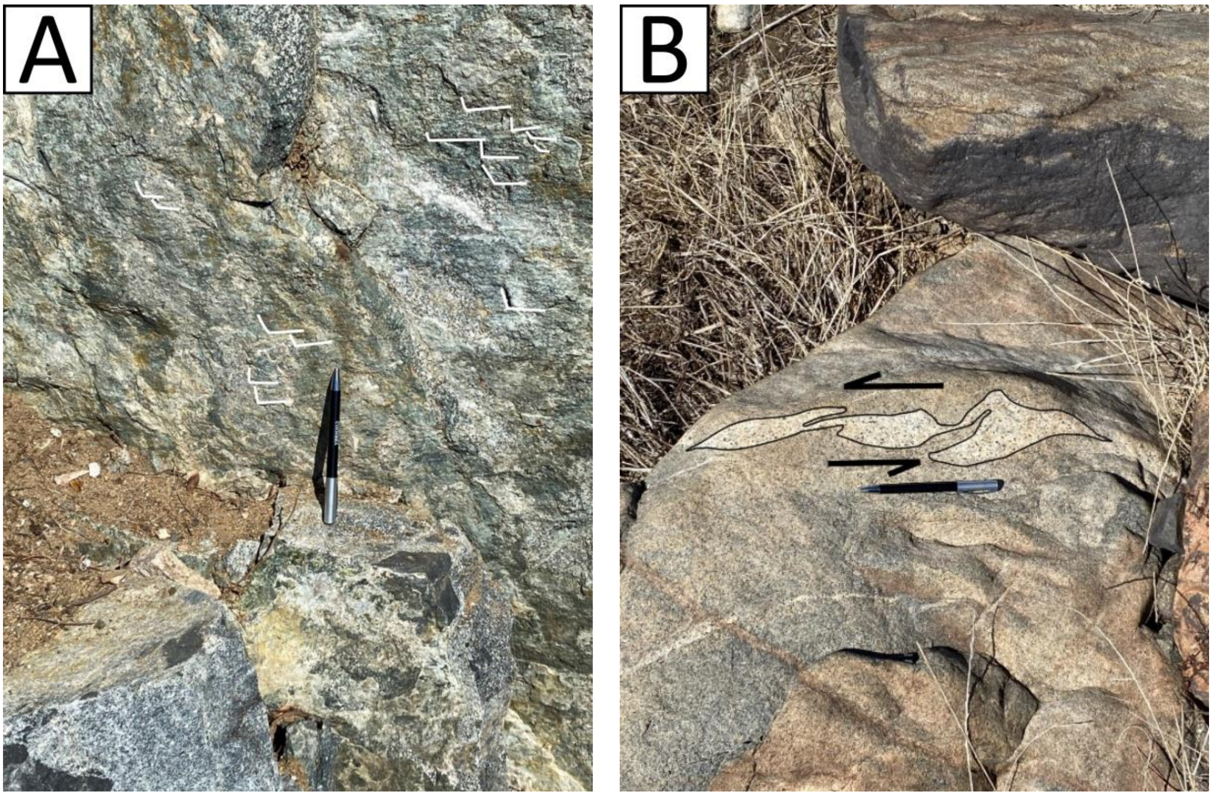

Figure V-4. Selected field photographs: (A) Low-temperature mineral assemblage (ep + act) developed from late fluid circulation within a fault zone. White lines delineate fault scratch marks, indicating right-lateral and downdip displacement. (B) *En échelon* vein of a more evolved leucocratic diorite melt within a quartz-diorite, indicating left-lateral displacement.

VI. Petrography

Despite the importance and validity of the macroscopic observations discussed in the previous chapter, some of the fundamental differences between the various dioritic facies and other rock types can only be characterized under the microscope. Compiled petrographic data enabled the classification of these rocks as diorite, quartz-diorite, amphibolite and leucocratic injections. Other lithologies, which are not as well represented and can only be observed in restricted domains of selected samples, will be addressed separately; these include gabbroic enclaves (preserved in sample **SEM-TOR-9** and digested in sample **SEM-TOR-8**), pegmatoidal domains (sample **SEM-TOR-16** and part of **SEM-TOR-18**), and a sulfide-rich injection (sample **SEM-TOR-7**). Strongly altered diorites (samples **SEM-TOR-19** and **SEM-TOR-11**) are not accounted for.

Mineral mode estimations were made based on qualitative assessments during petrographic observations and are shown in Figure VI-1 for samples representing amphibolite, diorite, quartz-diorite and leucocratic injections; values obtained through this methodology were used to support the classification of every lithological group following the IUGS recommendations (Le Maitre, 1989).

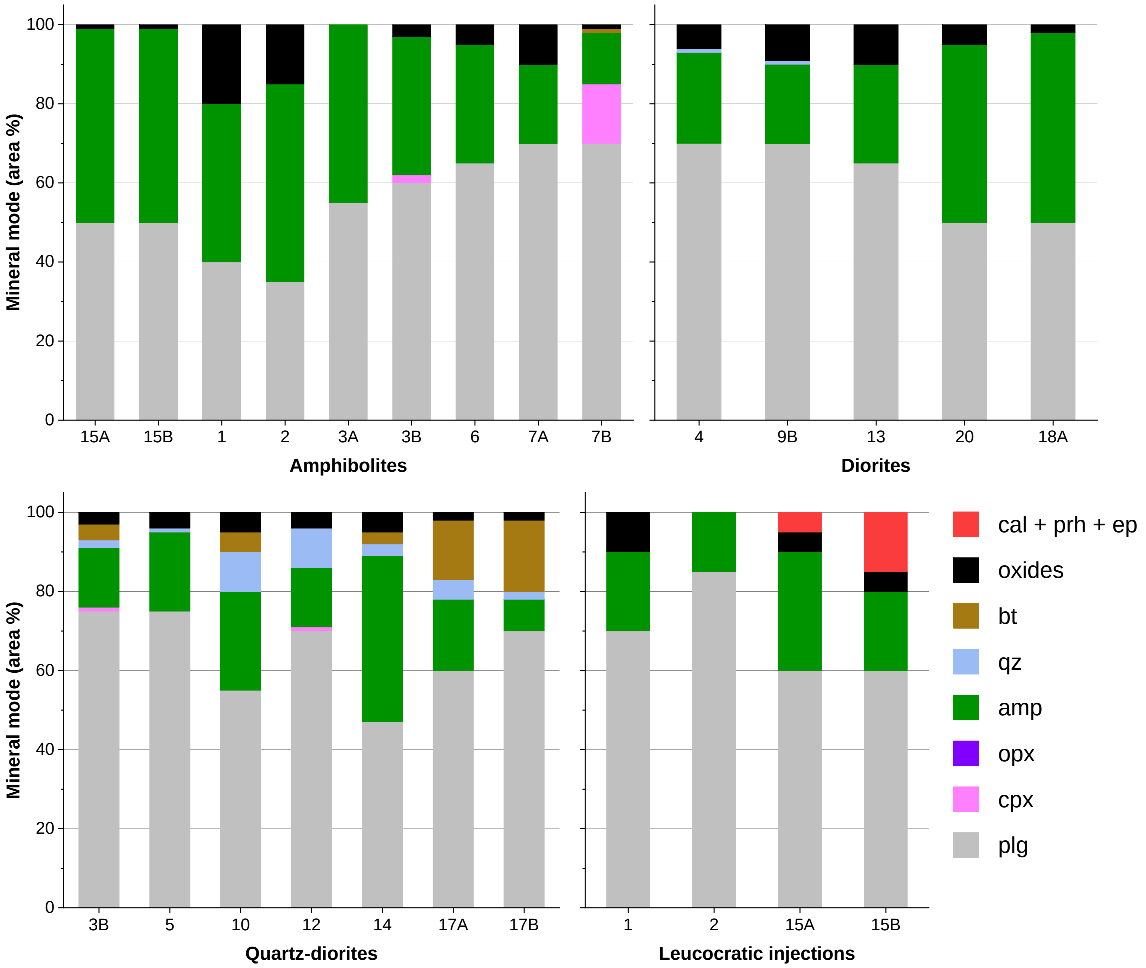

Figure VI-1. Mineral mode estimations for samples included in the amphibolite, diorite, quartz-diorite and leucocratic injection groups. The sample prefix 'SEM-TOR-‘ is omitted for clarity.

Diorites

A schematic representation of the inferred crystallization sequence for the diorites and quartz-diorites is shown in Figure VI-2.

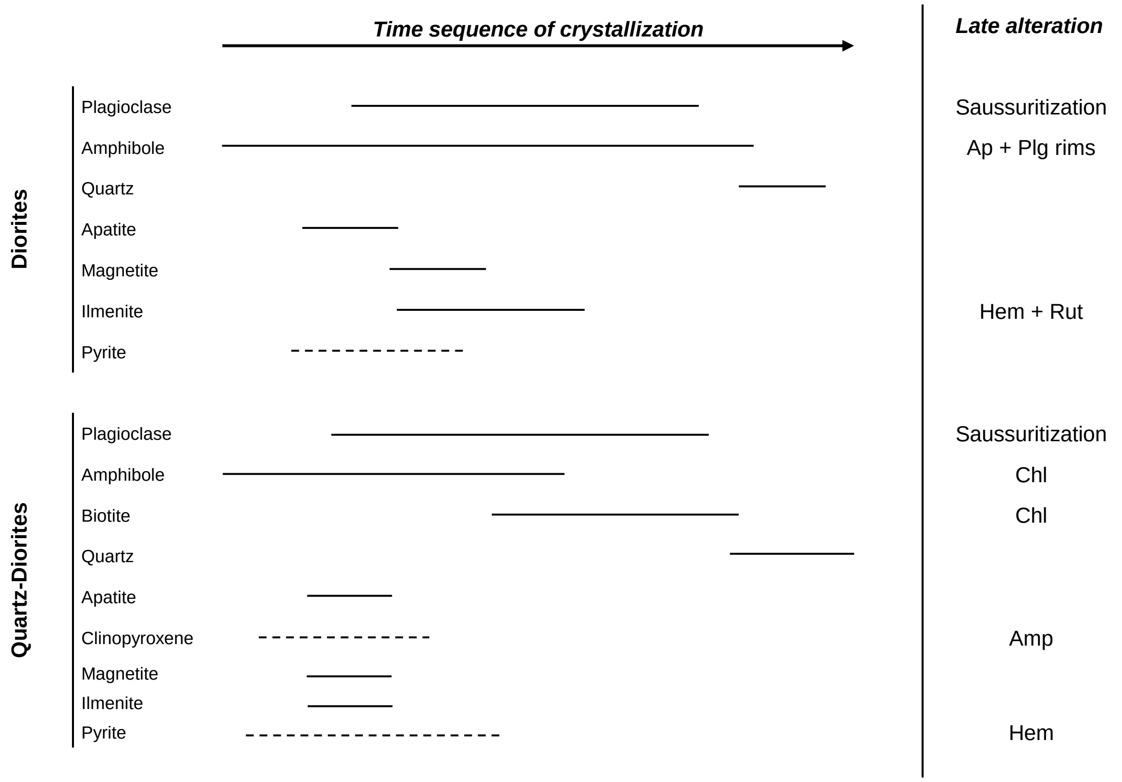

Figure VI-2. Schematic representation of the inferred crystallization sequence for diorite- and quartz-diorite- based on petrographic observations. Dashed lines indicate uncertain extent of crystallization.

Diorite rocks have equigranular, medium (1-5 mm) to coarse-grained (> 5 mm), phaneritic texture. Plagioclase is the most abundant mineral phase and occurs as medium-grained, subhedral to euhedral, tabular crystals. Saussuritization[4] primarily affects the cores of plagioclase grains and its intensity is variable (Figure VI-3A). Amphibole shows different optical properties, occurring as: (1) zoned, medium to coarse-grained, euhedral, light brown (core) to dark-green (border) phenocrysts, which cores have a “ripple” texture and the rims have numerous inclusions of fine-grained plagioclase + apatite (Figure VI-3B); (2) coarse-grained, brown, subhedral to anhedral, acicular crystals, often displaying a preferential direction (Figure VI-3C) and (3) fine-grained (0.2-1 mm), anhedral, brown-green crystals (Figure VI-3D). The second type of amphibole is characteristic of the acicular-textured diorites whereas the third type is abundant in all samples. When present, quartz occurs in subordinate amounts as interstitial crystals within the plagioclase and amphibole framework. Accessory mineral phases include apatite and titanite, the former occurring as fine-grained euhedral inclusions in plagioclase and amphibole, and the latter as small, interstitial domains.

Oxide mineral phases comprise variable proportions of magnetite and ilmenite. These mineral phases occur either as isolated, homogeneous single grains or as mixed grains with both phases clearly separated (Figure VI-3E). Both types of grains are found as inclusions in amphibole or at the contact between amphibole and plagioclase. Magnetite grains often exhibit irregular domains that are completely replaced by a fine-grained mixture of silicate minerals (Figure VI-3E).

---

[4] This term is used here to describe a heterogeneous mixture of carbonate minerals, calcite (and related carbonate brown-colored aggregates), epidote, zoisite and sericite, which under transmitted light microscopy and plane-polarized light, appear often as irregular, microcrystalline brown patches.

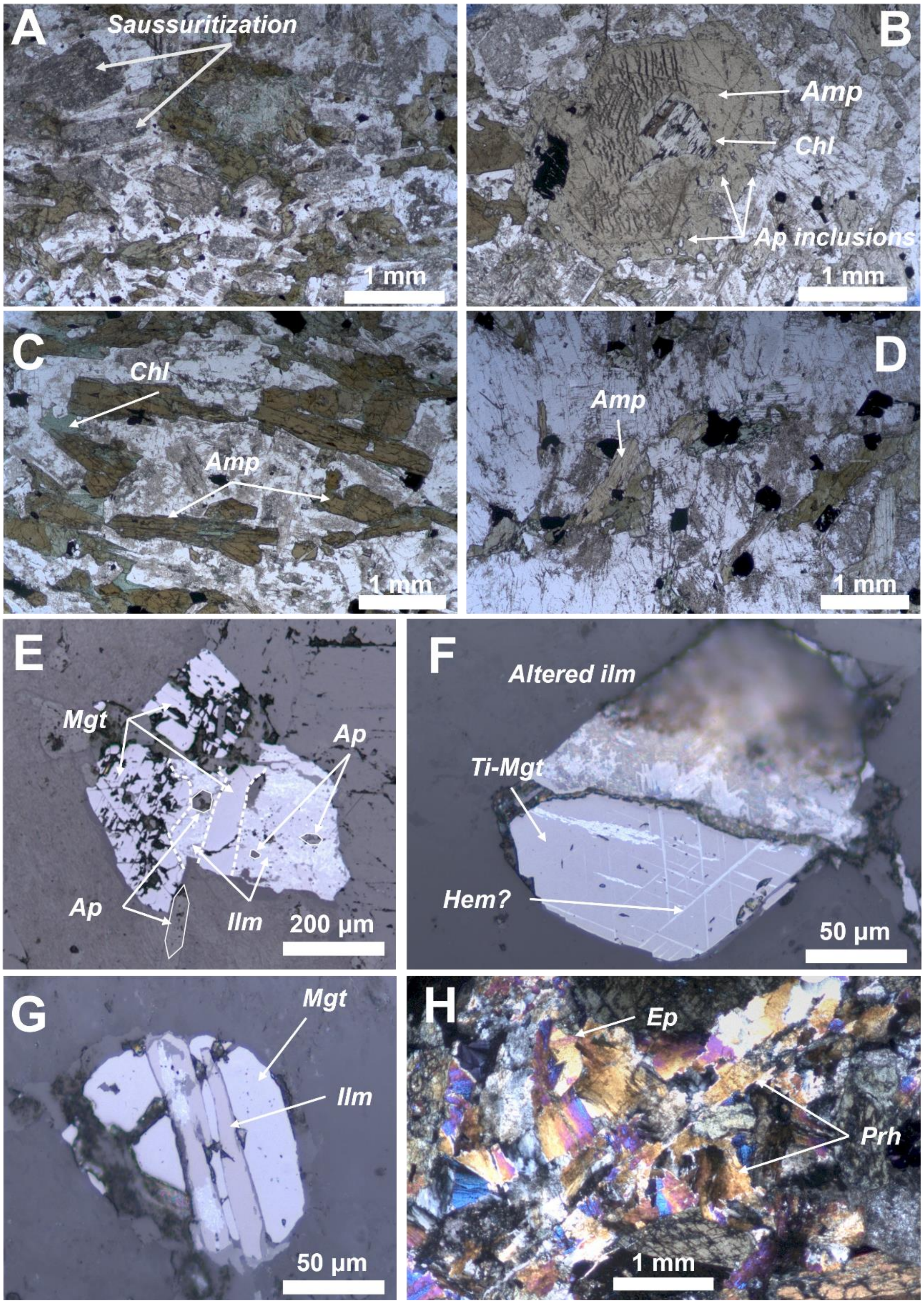

Figure VI-3. Microphotographs of the typical appearance and features of the diorites. (A) Saussuritized plagioclase grains (TL PN). (B) Coarse amphibole with a chloritized core and apatite inclusions in the rims. Note the “ripple” marks near the core. (C) Acicular amphibole and chloritization features in the acicular-textured diorites (TL PN). (D) The third and most common type of amphibole; note the oxide distribution in amphibole and in the contact between amphibole and plagioclase (TL PN). (E) Mixed magnetite-ilmenite grain with euhedral apatite inclusions (RL PN). (F) Fine hematite? oxy-exsolutions in the Ti-magnetite portion of a magnetite-ilmenite mixed grain; the (most likely) ilmenite portion (at the top) has been completely replaced by hematite + maghemite? (RL PN). (G) Ilmenite sandwich type ‘exsolutions’ (RL PN). (H) Thick prehnite + epidote vein (TL XN). TL – Transmitted Light; RL – Reflected Light; PN – Parallel Nicols; XN – Crossed Nicols.

Intragranular textures are relatively rare in magnetite and include oriented fine ilmenite or hematite oxy-exsolutions and thick sandwich exsolution lamellae (Buddington & Lindsley, 1964; Haggerty, 1991; Figure VI-3F and G). All occurrences of ilmenite (either as exsolutions or as single/mixed grains) are often significantly oxidized, showing irregular alteration textures composed of hematite and rutile, following the reaction: Ilm + O_2 → Hem + Rut (Buddington & Lindsley, 1964; Hagerty, 1991; Figure VI-4). Occasionally, ilmenite grains in contact with silicates (mostly amphibole) develop titanite rims. These textural arrangements of oxide phases are common throughout most of all diorite and quartz-diorite samples. Sulfides are accessory mineral phases and comprise pyrite and trace amounts of chalcopyrite. Pyrite occurs primarily as fine-grained disseminations with no specific association with any mineral type. Chalcopyrite is only present in samples **SEM-TOR-4** and **20**, and is found either in close association with late chlorite alteration or as irregular, fine-grained blebs.

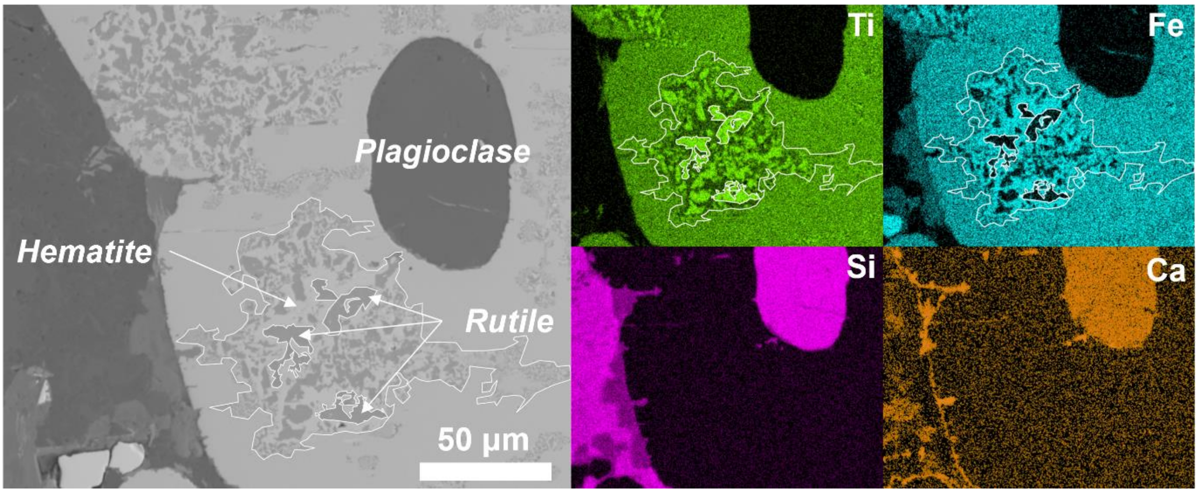

Figure VI-4. Back Scattered Electron (BSE) and Energy Dispersive X-Ray mapping for relevant elements highlighting hematite + rutile alteration/oxidation patches and a plagioclase inclusion in ilmenite; dark gray spots = rutile and bright gray spots = hematite.

Evidence of late hydrothermal alteration and low-temperature mineral neoformation is observed in a small number of diorite samples, being preserved as fine- to medium-grained calcite + prehnite + epidote + chlorite + silica veinlets (Figure VI-3H). Strain accommodation by diorite rocks is recorded by plagioclase mechanical wedge twinning and bent plagioclase crystals. Samples **SEM-TOR-4**, **9**, **13** and **20** correspond to the acicular-textured diorites and display evident linear fabrics outlined by acicular amphiboles (Figure VI-3C), which are interpreted to have resulted from magmatic flow.

Quartz-diorites

Only three out of the seven quartz-diorite thin sections show modal quartz ≥ 5% (using a QAPF diagram, this is the requirement for the prefix '-quartz'; Le Maitre, 2002) whereas the remaining have slightly less (3 to 4%). However, because these samples share many characteristics which are distinct from the diorites, like the occurrence of quartz and biotite (and identical geochemical features, as will be seen below in Chapter VIII.), they will be considered as part of the same group.

Quartz-diorites are characterized by the presence of quartz and biotite as major constituting mineral phases alongside plagioclase and green amphibole (Figure VI-5A). Quartz-diorites have a fine to medium-grained, isotropic, phaneritic to intergranular texture, the latter being characteristic of sample **SEM-TOR-5**, where amphibole, quartz and biotite occur as interstitial minerals within a plagioclase framework. Plagioclase is the most abundant mineral and typically occurs as optically zoned, medium-grained, subhedral laths (Figure VI-5B).

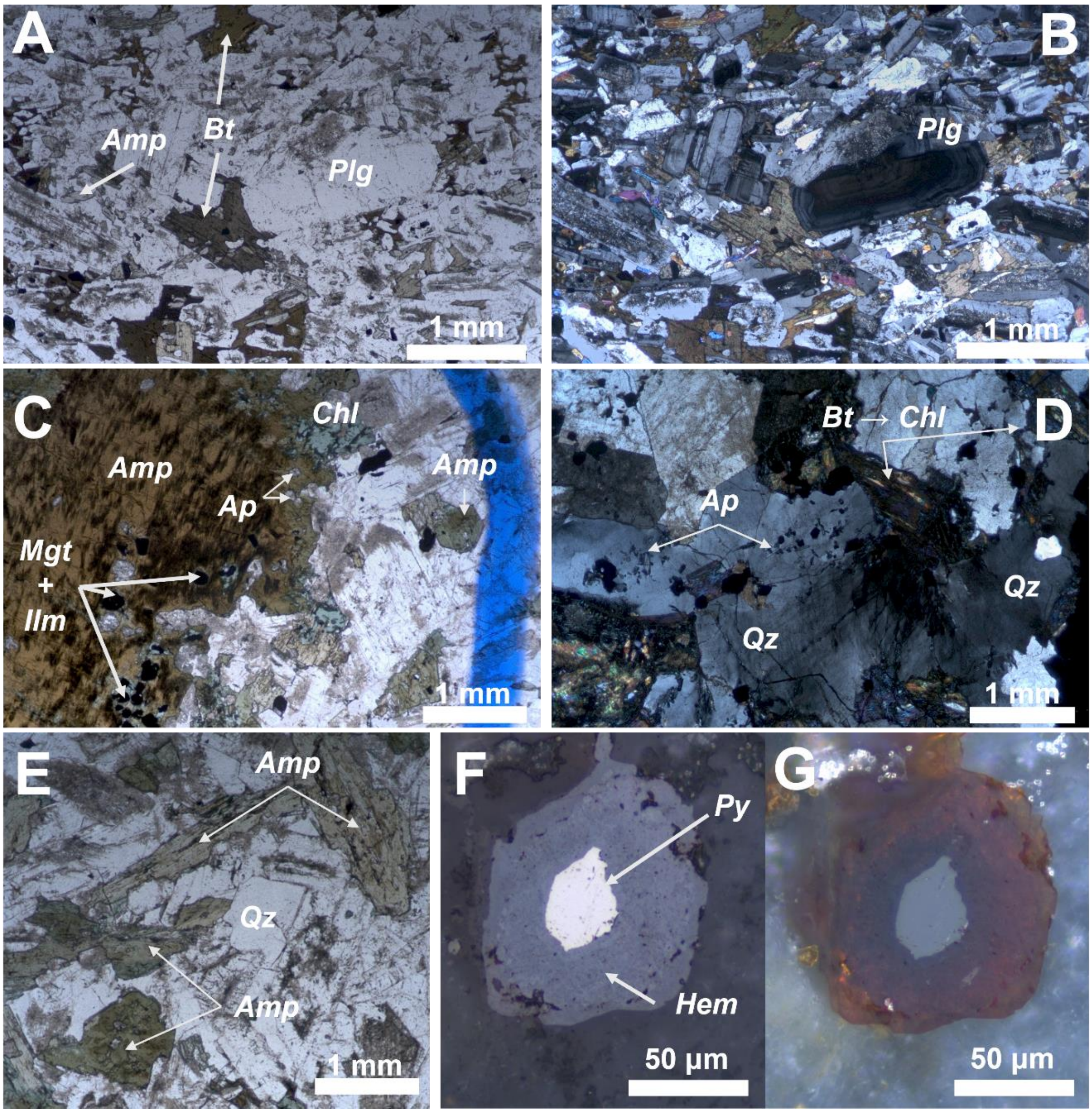

Figure VI-5. Microphotographs of the typical appearance and features of quartz-diorite rocks under the microscope. (A) Biotite plates and fine-grained/microcrystalline pale-green amphibole crystals (TL PN) and (B) same section showing complex oscillatory zoning in plagioclase and an incipient fabric (TL XN). (C) Coarse-grained brown amphibole with mgt + ilm + ap + chl inclusions in its rims (TL PN). (D) Coarse-grained interstitial quartz with apatite inclusions and chloritized biotite (TL XN). (E) Interstitial quartz and the typical appearance of type II amphibole (TL PN). (F-G) Pyrite grain with strongly oxidized borders composed of hematite (left – RL PN; right – RL XN).

Plagioclase grain cores are often affected by moderate saussuritization whereas the borders are well preserved. Rarely, plagioclase grains are oriented along a preferential direction, outlining a magmatic fabric (Figure VI-5B). Amphibole occurs as: (1) coarse-grained, brown phenocrysts which rims are replaced by a mineral assemblage composed of chlorite + magnetite + ilmenite + plagioclase + apatite (Figure VI-5C) – this amphibole type is only present in sample **SEM-TOR-5** and is very similar to the first type of amphiboles in the diorites – and (2) green (and pale-green varieties, which will be addressed in Chapter VII.) crystals with dark-green cores, either forming the matrix as fine-grained, acicular crystals or as smaller, interstitial grains. Amphibole grains are relatively well preserved, their cores and borders being only occasionally replaced by chlorite and biotite, which in turn is also partially replaced by chlorite. Primary biotite occurs as medium-grained, platy anhedral crystals, being often partially replaced by chlorite. Quartz occurs exclusively as fine to medium-grained (locally, coarse-grained) interstitial crystals within the plagioclase, amphibole and/or biotite framework (Figure VI-5D and E). Accessory minerals include apatite, zircon and epidote; the first two occurring in the same context as in the diorites whilst epidote forms small, irregular-shaped interstitial grains. Pyroxene is only observed in samples **SEM-TOR-3B** and **SEM-TOR-12**, where it occurs as fine-grained, anhedral crystals. Estimating the original proportion of clinopyroxene is difficult because some grains may be completely replaced by amphibole resulting in optically indistinguishable grains relative to primary amphibole.

Oxide phases are relatively scarcer in the quartz-diorites and comprise variable proportions of fine-grained magnetite and ilmenite mixed grains. The characteristics of these oxide phases are very similar to those described for the diorites, the main difference being the more altered appearance of ilmenite. Sulfide phases mostly comprise pyrite with trace amounts of chalcopyrite. Both are accessory mineral phases and occur either as fine matrix disseminations in association with amphibole or as local aggregates comprising euhedral grains. Pyrite grains are well preserved but are occasionally found replaced by hematite at the rims (Figure VI-5F and G).

Late alteration and focused fluid circulation is recorded by small (~0.05 mm thick), silica + albite + carbonate veinlets that establish sharp contacts and induce strong saussuritization of plagioclase grains they cut across, whereas amphibole either remains rather unaffected or is completely replaced by chlorite. Deformation in quartz-diorite rocks is recorded by plagioclase wedge twinning, quartz wavy extinction and longitudinal biotite sections that sometimes reveal a bent cleavage.

Amphibolite enclaves

As noted in Chapter V. , two distinct amphibolite facies can be separated macroscopically based on grain size. This division is not as clear under the microscope, where grain size variation across amphibolite samples is more gradual than bimodal (Figure VI-6A, B and C). Nevertheless, samples **SEM-TOR-1** and **2** – which represent the finer-grained endmember of all amphibolite samples – show some distinct mineralogical and textural features that will be considered below.

Amphibolite enclaves have a homogeneous, microcrystalline (0.1-0.2 mm) to fine-grained, grano-nematoblastic texture. Plagioclase and amphibole are the main mineral constituents alongside considerable amounts of oxides in the finer-grained varieties. Plagioclase typically occurs as microcrystalline to fine-grained, anhedral to subhedral, granular to tabular crystals which are moderately affected by saussuritization. Modal proportions of plagioclase are the lowest in the finer-grained amphibolite portions. Amphibole occurs as microcrystalline to fine-grained, granular, anhedral crystals and its color varies significantly across studied samples, ranging from dark-green to green and brown to pale-green/yellow. In sample **SEM-TOR-6**, a pale-yellow amphibole megacryst is found with a core partially replaced by biotite and rims replaced by clinopyroxene (Figure VI-6D). Amphibole grains are generally well preserved in all samples, being only replaced in minor amounts by chlorite. Clinopyroxene is only present in samples **SEM-TOR-7B** and **3B**, where it occurs as fine-grained, anhedral crystals, partially replaced by amphibole and chlorite. Apatite is the only accessory mineral phase and occurs as fine-grained inclusions in plagioclase.

Oxide mineral phases in the amphibolite enclaves comprise variable proportions of magnetite and ilmenite; in sample **SEM-TOR-15**, the most coarse-grained amphibolite, hematite is also a major oxide phase. Magnetite and ilmenite both occur as microcrystalline to fine-grained, single and mixed grains. Magnetite rarely shows intragranular ilmenite oxy-exsolutions and the thicker sandwich-type exsolutions whereas ilmenite appears fresh and homogenous.

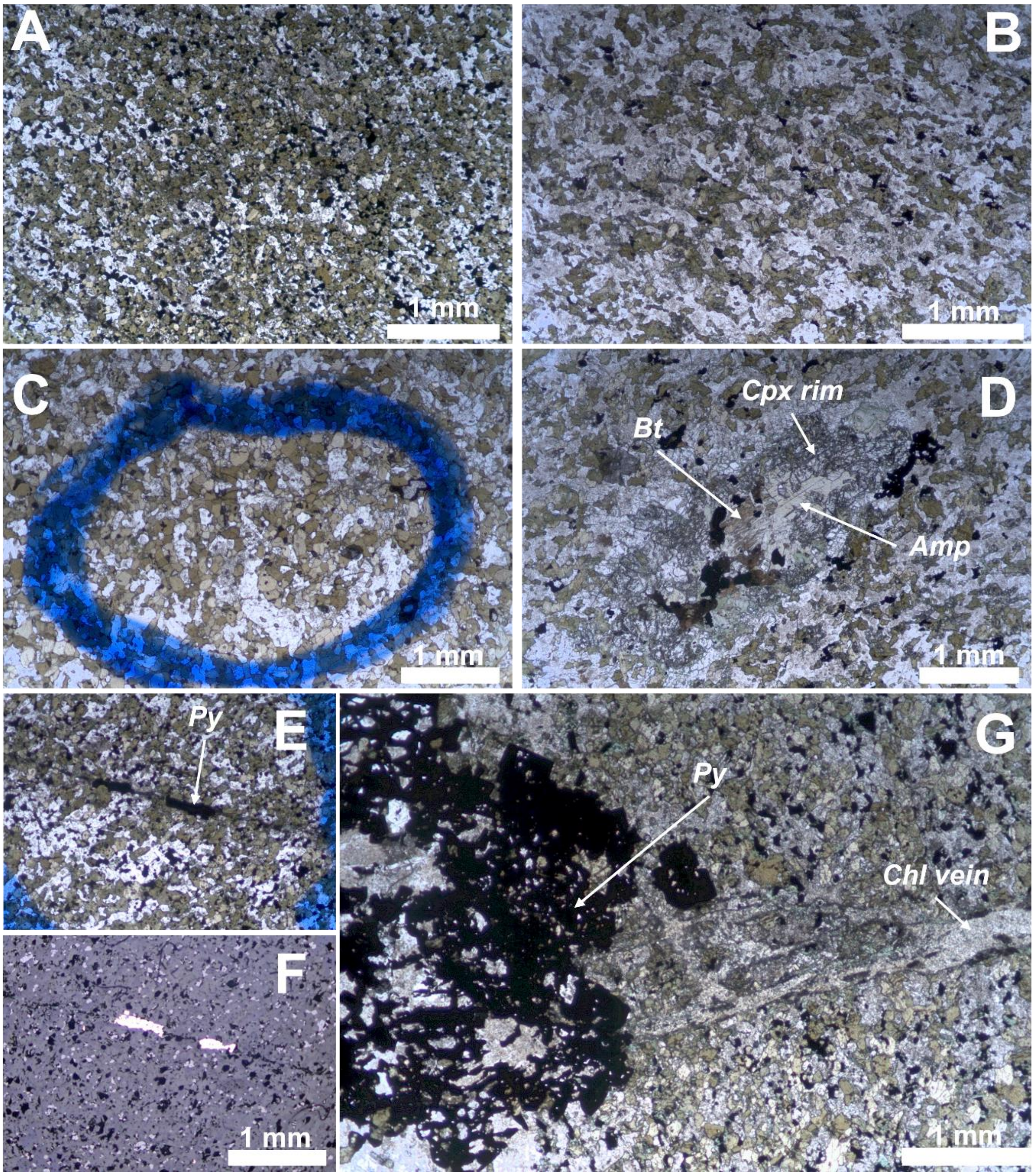

Figure VI-6. Microphotographs of the typical appearance and features of the amphibolite enclaves under the microscope. (A), (B) and (C) document the textural and mineralogical variety across the amphibolite enclaves: (A) Fine-grained amphibolite with dark-green amphibole (sample **SEM-TOR-1**); note the relative abundance of opaque minerals (mostly oxides; TL PN). (B) Slightly coarser-grained amphibolite with higher modal proportions of plagioclase and a fabric denoted by oriented amphibole grains (sample **SEM-TOR-6**; TL PN). (C) The most coarse-grained amphibolite (sample **SEM-TOR-15**). Note the browner amphibole colors (TL PN). (D) Preserved core of an amphibole phenocryst (partially replaced by biotite) with clinopyroxene rims, within sample **SEM-TOR-6** (see B; TL PN). (E) Microcrystalline chlorite + pyrite vein with subhedral pyrite grains in TL PN and (F) TL XN. (G) Extension of the chlorite + pyrite vein from (E) and (F) which broadens near the contact between the amphibolite and a leucocratic injection, resulting in the formation of a coarse-grained aggregate of pyrite.

Sulfides are common in all amphibolite samples, being more abundant in the finer-grained varieties, and include pyrite and chalcopyrite, which occur either as micrometric disseminations or as irregular, fine aggregates randomly dispersed in the rock matrix. Both pyrite and chalcopyrite are also found in association with late chlorite veinlets (Figure VI-6E and F).

Late alteration in the amphibolite enclaves is preserved as crypto- (< 0.1 mm) to microcrystalline chlorite + pyrite, epidote + prehnite + chlorite + brown carbonate aggregates and albite veinlets. The alteration adjoining these veinlets affects both plagioclase and amphibole, being most intense in the finer-grained amphibolite portions – likely because of their close spatial relation with the leucocratic injections. In sample **SEM-TOR-2**, a chlorite + pyrite vein cuts across the amphibolite enclave and develops a coarse pyrite aggregate in the contact with the leucocratic injection (Figure VI-6G). Amphibole, tabular plagioclase grains and oxides often show a preferred orientation, developing plano-linear fabrics. The interpretation of this feature depends heavily on the geological context of the sampling location and may be interpreted as the result of: (1) (micro-) shear zones affecting the amphibolite rocks; (2) imprinted textures resulting from the stress caused by the magmatic flow of the surrounding dioritic melt; or (3) the same tectono-thermal processes which modified the protolith.

Leucocratic injections

Leucocratic injections are found in close spatial association with amphibolite enclaves. The characteristics of this lithological group differ slightly between samples, which can simply be the result of observing small portions of a relatively coarse-grained (not in strict terms) lithology. Nevertheless, leucocratic injections have inequigranular, medium-grained (on the higher end of the mineral length interval which brackets this designation) texture which is highlighted by the abundance of plagioclase and amphibole. Plagioclase occurs as medium-grained, subhedral, tabular crystals; grain size for **SEM-TOR-15** is slightly smaller. Other features, such as optical zoning, are obscured by the advanced state of alteration of plagioclase. Amphibole occurs as dark-green, fine to medium-grained, anhedral, prismatic crystals (Figure VI-7A and B). Amphibole crystals from sample **SEM-TOR-15** share the same textural characteristics but have a yellower/browner color (Figure VI-7C). Chloritization of amphibole is moderate to strong across all samples. Interstitial pockets of calcite + prehnite + epidote infillings are present in all samples and are major constituents of sample **SEM-TOR-15** (Figure VI-1 and Figure VI-7D). Apatite and titanite are the only accessory minerals phases; the former occurs as fine-grained, euhedral crystals with no apparent preferential association with any silicate phase and the latter as irregular domains.

Oxide phases comprise variable proportions of magnetite and ilmenite, which features are in every way alike of the previously described lithologies. Sulfide phases are only present in sample **SEM-TOR-1** where irregular, fine-grained pyrite occurs as inclusions in plagioclase.

Alteration is observed as microcrystalline epidote + prehnite + chlorite and calcite + prehnite + epidote + silica veinlets, which effect on the grains they cut across is difficult to assess because of the advanced state of alteration in which this lithology is found. There is no evidence of ductile deformation.

Reactions between diorites, amphibolite enclaves and leucocratic injections

Reactions involving amphibolite enclaves and diorites, as well as amphibolite and leucocratic injections, are rather monotonous and similar across studied samples. The contacts between these lithologies are typically sharp to semi-diffuse and originate domains characterized by a framework of interlocking medium-grained, polygonal, dark-green amphibole crystals (Figure VI-7E). These domains are relatively thin (4 mm across at most). The sections corresponding to diorites and amphibolite enclaves, in contact with each other or with the leucocratic injections, are well preserved.

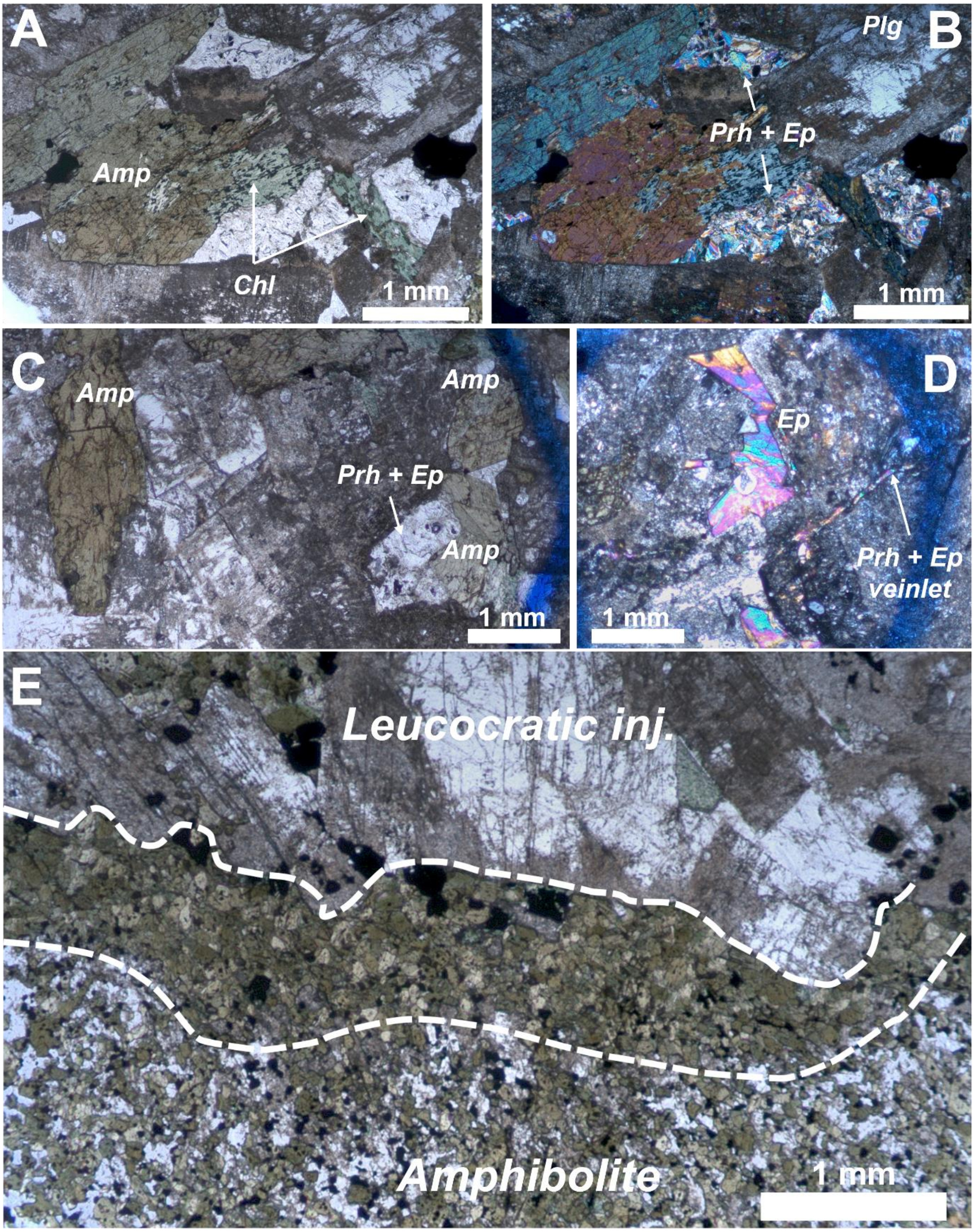

Figure VI-7. Microphotographs of typical features displayed by leucocratic injections (A, B, C and D) and reaction rims (E) under the microscope. (A) Medium-grained amphibole crystals partially replaced by chlorite (TL PN) and (B) same section but in XN, highlighting the interstitial prehnite + epidote pockets (sample **SEM-TOR-1**). (C) Yellower/browner amphibole crystals and prehnite + epidote interstitial pockets in sample **SEM-TOR-15**. (D) Interstitial epidote and a microcrystalline prehnite + epidote veinlet. (E) Reaction rim (in between the dashed lines) between a fine-grained amphibole and a leucocratic injection, originating a polygonal, amphibole-rich domain. Reactions between amphibolite enclaves and diorites have the same features.

Other lithologies

Gabbroic enclaves

Gabbroic enclaves were observed in samples **SEM-TOR-9** and **SEM-TOR-8** being well preserved in the former and digested in the latter. During macroscopic observations, sample **SEM-TOR-9** was described as a partly digested, fine-grained amphibolite enclave within an acicular-textured diorite matrix. However, the preserved portions of the enclave reveal a mineral assemblage and textural features which are rather characteristic of gabbroic rocks. The enclave has an equigranular, fine-grained, phaneritic texture. Plagioclase is the most abundant mineral, making up around 70% of the sample, and occurs as fine-grained, subhedral, tabular grains (Figure VI-8A and B). Both ortho- and clinopyroxene are present up to ~10% (with orthopyroxene being slightly more abundant) and occur as fine-grained, anhedral, granular crystals (Figure VI-8A and B); it is likely that some clinopyroxene grains have been completely replaced by amphibole, as suggested by preserved clinopyroxene cores surrounded by amphibole. Orthopyroxene shows intense alteration induced by a network of parallel chlorite + amphibole? veinlets. The proportions of amphibole are difficult to assess owing to the diffuse contact between the diorite and the enclave but there is no amphibole in the core of the enclave. Accessory minerals include apatite which occurs as numerous, fine-grained, euhedral inclusions in plagioclase.

Magnetite and ilmenite occur as fine-grained (within the grain size of both types of pyroxene), single and mixed grains. Oxide phases are found partly included at the margins of ortho- and clinopyroxene (Figure VI-8A). Magnetite frequently shows fine-grained ilmenite oxy-exsolutions. The hematite + rutile patches, which are diagnostic of alteration and oxidation in ilmenite grains, are rare. Sulfide phases are also rare and comprise fine-grained, irregular pyrite aggregates.

Evidence for late alteration is preserved as a network of parallel microcrystalline chlorite veinlets which induce strong alteration on ortho- and clinopyroxene, as well as amphibole. Plagioclase grains show mechanical wedge twinning and slightly bent crystals; these features are absent from the diorite counterpart and thus account for evidence of ductile deformation within the gabbroic enclave before gabbro – diorite melt interaction.

Pegmatoidal domains[5]

Under the microscope, the pegmatoidal domains are characterized by having subhedral, acicular amphibole crystals which maximum size cannot be measured because part of these extend out of the thin section, being at least 8 mm in diameter (Figure VI-8C). Amphibole grains are affected by moderate chloritization and have brown cores with light green/pale-yellow borders. Plagioclase is a secondary mineral phase and occurs as anhedral to subhedral, granular to tabular grains recording strong saussuritization. Calcite, prehnite and epidote interstitial pockets make up the remainder of the pegmatoidal domains. Late alteration is preserved in the form of fine-grained white mica + prehnite and chlorite + calcite veinlets (Figure VI-8D).

Sulfide-rich injection

The sulfide-rich injection has a medium to coarse-grained texture and is composed primarily of amphibole, quartz, clinopyroxene and pyrite. Amphibole has brown cores and green borders, and occurs as subhedral to euhedral, coarse-grained crystals (Figure VI-8E). Amphibole grains are well preserved, being only locally replaced by chlorite and calcite. Clinopyroxene occurs as numerous fine to medium-

---

[5] The pegmatoidal domains are here discussed separately from the diorites and quartz-diorites because they have a more limited expression, both cartographically and in the number of polished thin sections. Nevertheless, it should be reminded that these domains are closely related to both the diorites and quartz-diorites, meaning that their interpretation in a petrogenetic sense should be done in the same context of the latter rock types. For this reason, they will be included together with the diorites and quartz-diorites in a broader 'dioritic rocks' group from here onwards, unless stated otherwise.

grained, granular crystals, either in interstices of the amphibole framework, or as inclusions in it (Figure VI-8E). A qualitative assessment on the way in which these pyroxene grains occur, *i.e.*, as rounded, small granular grains, suggests that these could have been transported with the injection instead of having crystallized directly from it. Quartz is a secondary mineral phase and occurs as interstitial crystals. Lastly, subhedral pyrite aggregates are arranged in a soft-wall veins (Barnes *et al.*, 2017), possibly indicating the flow direction of the injection (Figure VI-8F).

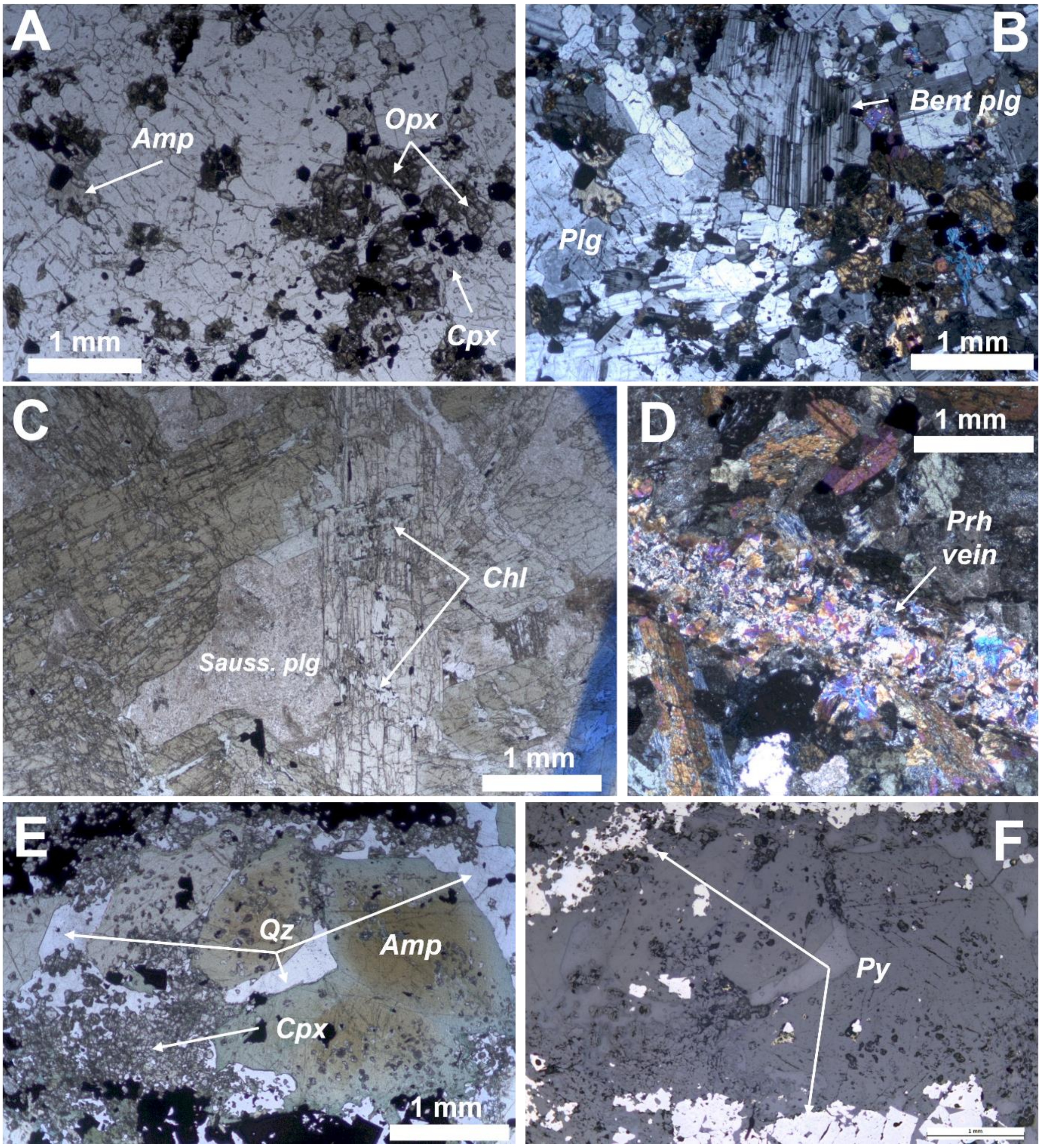

Figure VI-8. Microphotographs of the main features displayed by gabbroic enclaves (A and B), pegmatoidal domains (C and D) and leucocratic injections (E and F). (A) Gabbroic enclave, note the altered appearance of ortho- and clinopyroxene and the association of opaque (oxide) minerals with the mafic silicates (TL PN). (B) Same section in TL XN, illustrating the slightly bent plagioclase mechanical twinning. (C) Coarse-grained green and pale amphibole crystals, characteristic of the pegmatoidal domains (TL PN). (D) Prehnite vein crisscrossing the pegmatoidal domain (TL XN). (E) Zoned amphibole crystals in the sulfide-rich injection; note the fine-grained, rounded clinopyroxene crystals and the interstitial quartz (TL PN), and (F) same section in RL PN, highlighting the vein-like structure of the pyrite aggregates.

VII. Mineral chemistry

In this chapter, the compositional variations displayed by the main mineral phases forming the rock types cropping out at Torrão are reported by order of decreasing abundance; oxide minerals are presented separately. The complete analytical dataset can be found in Supplementary Data 1.

Amphibole

To document the compositional variation of magmatic, metamorphic and (magmatic-) hydrothermal amphiboles, a total of 344 quantitative electron probe micro-analyses were performed in 28 polished thin-sections representing the Torrão diorites and their enclaves. Structural formulae, Fe^{3+} estimation based on site occupancies and stoichiometric limits, and classification of amphiboles were done following the criteria in Leake *et al.* (1997) on the basis of 23 oxygens per formula unit, where the sum of cations is allowed to vary between 15 and 16. It should be noted, however, that *most* of the analysed grains from sample **SEM-TOR-17** do not follow the last constraint and will not be considered below. The general formula of amphibole is $A_{0-1}B_2C_5{}^{VI}T_8{}^{IV}O_{22}(OH, F, Cl)_2$, where: A = Na^+ and K^+; B = Mg^{2+}, Fe^{2+}, Mn^{2+}, Ca^{2+} and Na^+; C = Al^{3+}, Ti^{4+}, Fe^{3+}, Cr^{3+}, Mg^{2+}, Fe^{2+} and Mn^{2+}, and T = Si^{4+} and Al^{3+}.

Amphiboles show significant compositional variation between and within lithologies. Based on the predominant cation occupying the B-site, most amphiboles are calcic and plot in the Mg-hornblende field (Figure VII-1). A few analyses plot in the pargasite, edenite and tschermakite compositional fields, reflecting a wide compositional range (Figure VII-1). In addition, amphiboles in the gabbroic enclave and the pale-green amphiboles from sample **SEM-TOR-17** belong to the Mg-Fe-Mn-Li group, being classified as cummingtonite and ferro-anthophyllite (ortho-amphibole), respectively.

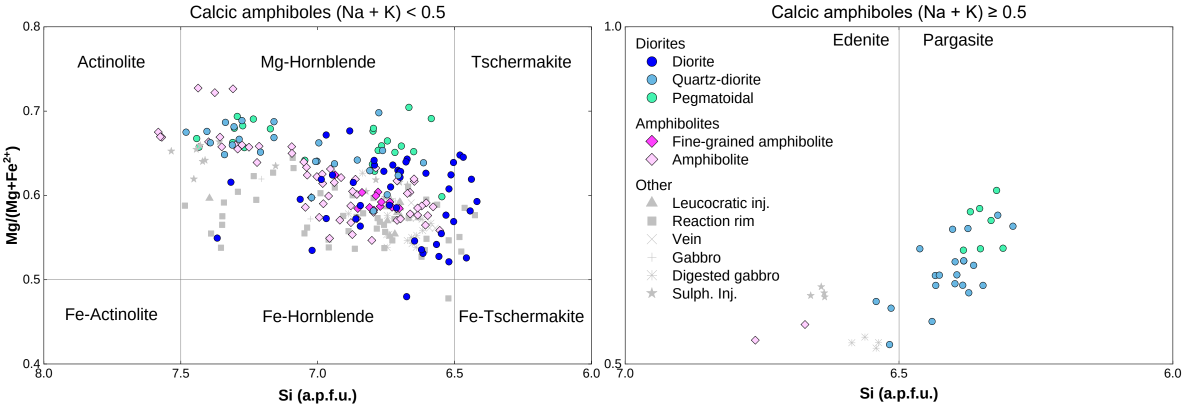

Figure VII-1. Amphibole classification diagrams for calcic amphiboles based on the proposal of Leake *et al.* (1997).

Overall, amphibole Mg-number [Mg# = 100 * $Mg/(Mg+Fe^{2+})$] ranges from 44.2 to 75.5 mol%. Despite the obtained spread, the Mg-number of amphiboles included in diorites is slightly lower relative to those found in quartz-diorites (median values, X, of 61.11 and 63.55 mol%, respectively; Figure VII-2A). The lowest Mg-number values typify the ortho-amphiboles, which show considerable enrichment in Fe. The A-site occupancy [$(Na+K)^A$] ranges from 0.008 (associated with an ortho-amphibole) to 0.65 a.p.f.u. and is generally higher in the diorites than in the quartz-diorites (X_{diorites} = 0.43, $X_{\text{qz-diorites}}$ = 0.22; Figure VII-2A). Titanium contents range from 0.03 to 0.45 a.p.f.u. and, like A-site occupancy, are higher in the diorites relative to the quartz-diorites (X = 0.27 and 0.14, respectively; Figure VII-2B). There is a strong correlation between Al^{IV} and Ti contents, suggesting that the temperature-dependent Ti-Tschermak exchange (see Gilbert *et al.*, 1982; Equation VII-1) was the main process through which Ti was incorporated into the amphibole structure, having played a significant role during the amphibole crystallization (Figure VII-2B). Analyses that deviate from this trend correspond to the Mg-Fe-Mn-Li amphiboles, having low Ti and Al^{IV} contents.

Equation VII-1

$$(\mathrm{Mg, Fe^{2+}})^{\mathrm{VI}}2\mathrm{Si}^{\mathrm{IV}} \rightleftharpoons \mathrm{Ti}^{\mathrm{VI}}2\mathrm{Al}^{\mathrm{IV}}$$

Conversely, the Al^{IV} contents show a poor correlation with those of Al^{VI}, implying that the pressure-dependent Al-Tschermak exchange (see Gilbert *et al.*, 1982; Equation VII-2) was not significant during the amphibole crystallization path (Figure VII-2C).

Equation VII-2

$$(\mathrm{Mg, Fe^{2+}})^{\mathrm{VI}}\mathrm{Si}^{\mathrm{IV}} \rightleftharpoons \mathrm{Al}^{\mathrm{VI}}\mathrm{Al}^{\mathrm{IV}}$$

Ferric iron ratios, here defined as $Fe^{3+}/(Fe^{3+}+Fe^{2+})$, range from 0.04 (~0.0 in the ortho-amphiboles) to 0.34, considering only the diorites and quartz-diorites. There is a well-defined negative correlation between the ferric iron ratio and Al^{IV} contents in diorites (Figure VII-2D), which is lacking in amphiboles forming the quartz-diorites.

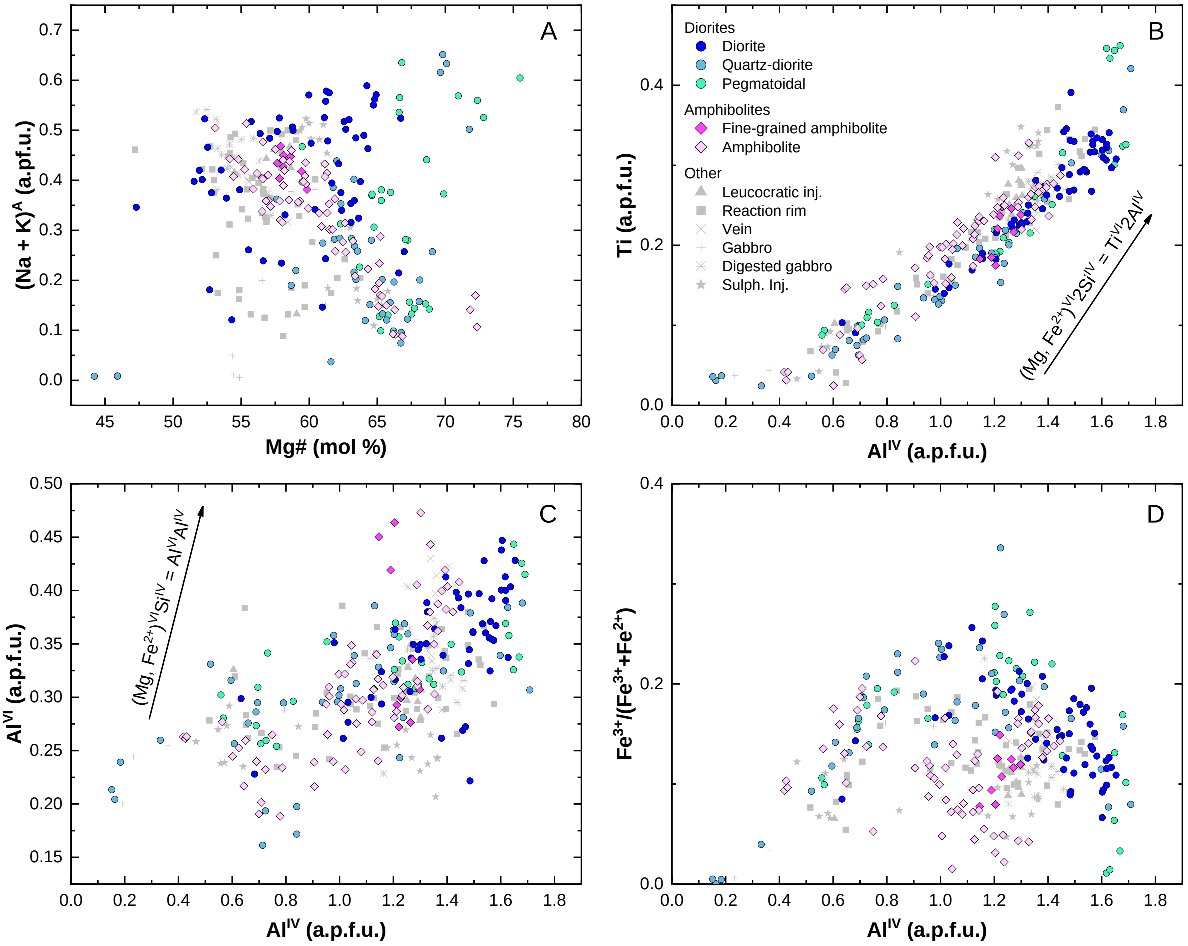

Figure VII-2. Main compositional characteristics of amphibole. (A) Mg-number (Mg#) *vs.* $(Na+K)^A$ contents; note the peculiar Mg-number increase of amphibole with A-site occupancy indicating decreasing temperature/differentiation. (B) Al^{IV} *vs.* Ti contents, highlighting the prominent role of the temperature-dependent Ti-Tschermak exchange vector during differentiation. (C) Lack of correlation between Al^{IV} and Al^{VI} contents, indicating that the pressure-dependent Al-Tschermak exchange did not play a significant role during crystallization. (D) Ferric iron ratios $[Fe^{3+}/(Fe^{3+}+Fe^{2+})]$ vs. Al^{IV}, indirectly denoting the ratio variation as a function of decreasing temperature; note the negative slope trend for amphiboles in the diorites.

An interesting feature of amphibole in diorites and quartz-diorites is the distribution of Na between the A and B site (Figure VII-3A). The Na^A concentration has a strong positive correlation with temperature (*e.g.*, Blundy & Holland, 1990), whereas Na^B is mainly a function of the CaAl-NaSi exchange between amphibole and plagioclase, increasing consistently with the anorthite molecular content [An% = 100 * Ca/(Ca+Na+K)] of coexisting plagioclase (Blundy & Holland, 1990). Amphiboles in diorites and quartz-diorites show distinct trends: the former displays a tendency for a negative Na^A-Na^B slope, whereas the latter have a positively sloping trend. To test the validity of the CaAl-NaSi exchange between amphibole and plagioclase, the Na contents of amphibole in the B-site were plotted against the anorthite molecular content of coexisting plagioclase (Figure VII-3B). Data in this cross-plot shows considerable scatter, meaning that there is very little (if any) correlation between Na^B and An%.

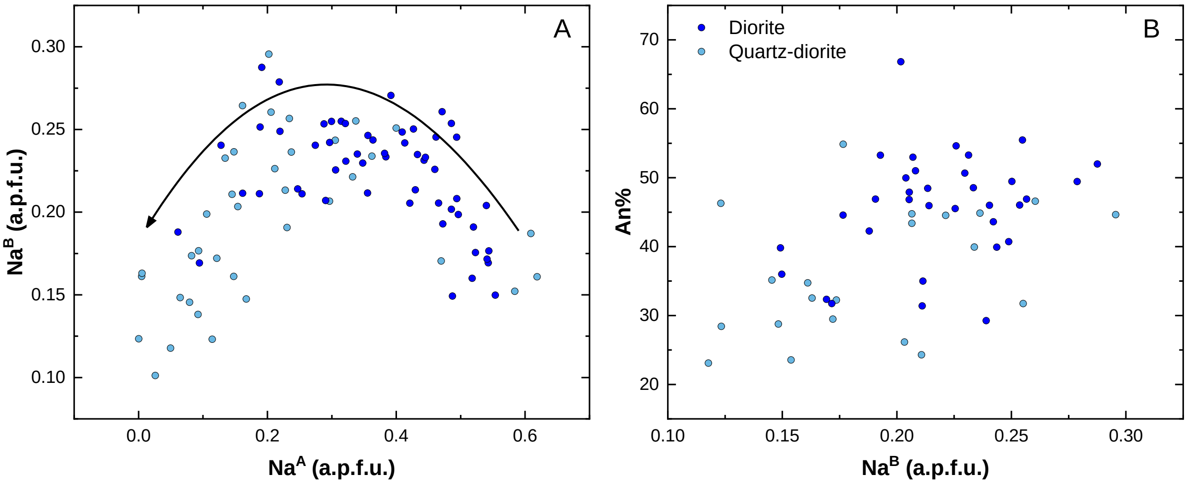

Figure VII-3. (A) Evolving trend in the partitioning of Na between the A and B-site of amphibole, from a negative to a positive correlation. (B) Lack of correlation between Na^B and An molecular content of plagioclase coexisting with amphibole, implying that plagioclase composition did not (at least, significantly) buffer Na^B contents.

Amphiboles in the remaining rock types generally have Mg-number and Ti, $(Na+K)^A$ and Al^{VI} contents bracketed between the aforementioned limits defined by the diorites and quartz-diorites. Amphiboles in the pegmatoidal domains record high Al^{IV} and Ti contents as well as high A-site occupancy. Furthermore, they have restricted Mg-number (~67 mol%) which does not vary significantly with decreasing Ti contents and A-site occupancy. Amphiboles in the amphibolite enclaves show a wide compositional range with well-defined trends in the $(Na+K)^A$ *vs.* Mg# and Ti *vs.* Al^{IV} cross-plots. There is no compositional distinction between amphiboles in the fine-grained amphibolite enclaves and those in the coarser-grained ones. Other lithologies show no remarkable compositional features.

Fluorine and chlorine concentrations are variable and show no correlation with any specific compositional feature in each rock type. Many analyses have F concentrations below the detection limit of the analytical method used.

Plagioclase

Plagioclase is the most abundant mineral phase in the examined rock types and a total of 275 quantitative micro-analyses were performed in 28 polished thin sections. Structural formulae were calculated using 32 oxygens per formula unit as reference and assuming all iron as ferric. This is a reasonable assumption because Fe^{3+} is more readily incorporated into plagioclase (in tetrahedral coordination positions) than Fe^{2+}, which only enters the plagioclase structure in more anorthitic ($An_{>90}$) compositions where it substitutes for Ca^{2+} (Hofmeister & Rossman, 1984).

Plagioclase compositions are variable, ranging from $An_{66.8}$ to $An_{18.8}$. Despite this wide compositional variation, intermediate to high An contents tend to typify the plagioclase in diorites, andesine (An_{50-30}) to oligoclase compositions (An_{30-10}) are usual in plagioclase found in quartz-diorites and albite is only present in the pegmatoidal domains (Figure VII-4A). Orthoclase molecular contents [Or% = 100 * K/(Ca+Na+K)] are always low, reaching a maximum of 2.98% in all analyses, except one from a pegmatoidal sample that records the highest (9.09%) Or contents. In addition, orthoclase contents increase slightly with decreasing An contents.

Iron concentrations, albeit somewhat similar, are generally lower in the quartz-diorites and show a positive correlation with An values, reflecting a decrease of the availability of Fe^{3+} to enter the plagioclase crystal structure (Figure VII-4B). The SrO and BaO concentrations are low (averages of 0.08 and 0.02 wt%, respectively) and for a considerable number of analyses they are below the detection limit of the analytical method used; there is no specific range of Sr or Ba contents in plagioclase forming each rock type.

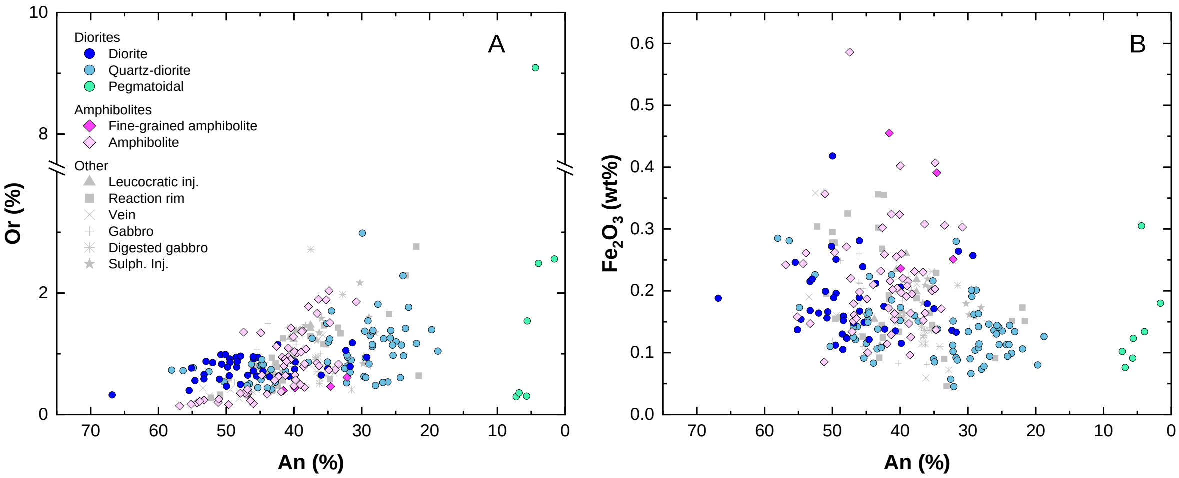

Figure VII-4. Main compositional features of plagioclase. (A) Slight positive correlation between An and Or molecular contents across every lithology. (B) Very rough negative correlation between Fe_2O_3 and An molecular contents.

Intragranular compositional disparity is evident from the highly variable shift in An contents from core to border within plagioclase grains. Decreasing An contents towards the border of plagioclase grains (*i.e.*, normal zoning) are expected in the course of a common fractionation path; however, the conspicuous reverse zoning and its variability, especially in the diorites and quartz-diorites, warrants further explanation.

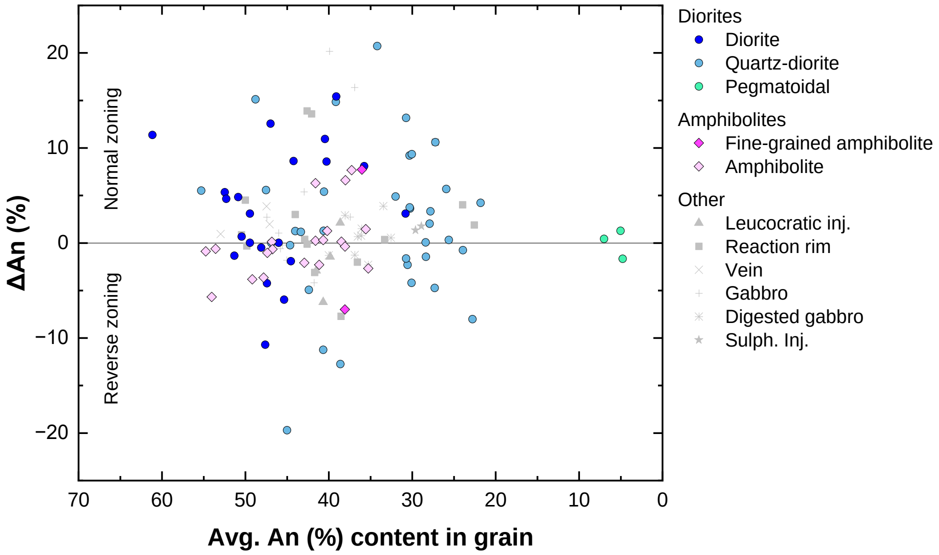

Figure VII-5. Shift in An molecular contents between core and border of each analysed grain (ΔAn) as a function of the average An molecular content in the same grain.

Phyllosilicates

Biotite

Biotite is modally significant in quartz-diorites and in the digested gabbroic enclave. A total of 56 quantitative electron probe microanalyses were performed on primary biotite grains across 7 polished thin sections to characterize its compositional variation. Seventeen analyses from various samples have total oxide contents well below (< 90 wt%) what is expected for biotite. Despite each analysis being taken at the most well-preserved spot of each grain, it is possible that some of these were already partially altered to chlorite, which could explain the lower bulk analytical totals. Therefore, to discriminate between preserved and altered biotite, a somewhat arbitrary minimum threshold of 93.0 total wt% was set based on the average minimum bulk oxide concentrations of biotite analyses (Deer *et al.*, 2013). Consequently, most valid biotite analyses from quartz-diorites were collected in sample **SEM-TOR-17**, which could generate some bias to the dataset.

In a MgO-10*TiO_2-FeO^T diagram, used to discriminate between magmatic, re-equilibrated and new-formed biotite, as proposed by Nachit *et al.* (2005), most of the analysed biotite plot on the primary magmatic field (Figure VII-6). Calculation of structural formulae, based on 22 oxygens per formula unit and assuming all iron as ferrous (Fe^{2+}), yields octahedral-site occupations exceeding the maximum of 6 a.p.f.u. The most likely cause for this discrepancy is an overestimation of Fe resulting from the assumption that all Fe is ferrous, meaning that a significant amount of the total iron is, in fact, ferric. Structural formulae were then recalculated following Li *et al.* (2020) using the MagMin_PT software (Gündüz & Asan, 2023), which allows an estimation of ferric iron contents. Results obtained through this method show reasonable octahedral site occupancies and considerable amounts of Fe^{3+} in both the octahedral and tetrahedral sites. Accordingly, the general formula of biotite can be written as $(R^{+})^{XII}(R^{2+})^{VI}_{6-4}(R^{3+}; R^{4+})^{VI}_{0-2}\,(Si^{4+}_{6-5}R^{3+}_{2-3})^{IV}O_{20}(OH, F)_4$, where: $R^+ = K^+$; $R^{2+} = Mg^{2+}$ and Fe^{2+}; $R^{3+} = Al^{3+}$ and Fe^{3+}; $R^{4+} = Ti^{4+}$.

Biotite from both rock types plot close to the trioctahedral mica join in a $R^+ + R^{2+} + R^{4+} + (Si^{IV} - 3)$ *vs.* R^{3+}_{Total} diagram (Figure VII-7A). The biotite from quartz-diorites shows slight deviations towards the dioctahedral join, reflecting the incorporation of tri- and tetravalent cations into the octahedral sites, which originates vacancies in the octahedral layer to retain charge balance. Most biotite classifies as annite, with only one analysis plotting in the phlogopite compositional field (Figure VII-7B). The $Fe^{2+}/(Mg + Fe^{2+})$ ratio clearly discriminates biotite from quartz-diorites and digested gabbro, the former being richer in Fe. Other elements also highlight the compositional difference between these two lithologies: Mn is higher in the quartz-diorites, whereas Na, Cl and Ba are lower. Fluorine concentrations are variable within each lithology (up to 0.20 wt%), standing below the detection limit of the analytical method used in 20 analyses. There is no specific correlation between F concentrations and lithology, sample, sector and whether the analyzed spot was taken at the core or border of the grain.

The TiO_2 concentrations in biotite are relatively high in both lithologies, ranging from 3.31 to 5.18 wt%. Titanium can be incorporated into the biotite structure through many different mechanisms; such an example is shown in Figure VII-7C, highlighting the role of the Ti-Tschermak exchange, following Equation VII-3:

Equation VII-3

$$(R^{2+})^{VI}2Si^{IV} \rightleftharpoons Ti^{VI}2Al^{IV}$$

As stated above, ferric iron contents in all the analyzed biotite plates are high; approximately one third of the total iron is in the form of Fe^{3+} across all analyses. Ferric iron in octahedral positions can proxy for Al^{IV} via a ferri-Tschermak substitution, following Equation VII-4 (Figure VII-7D):

Equation VII-4

$$(\mathrm{R}^{2+})^{\mathrm{VI}}\mathrm{Si}^{\mathrm{IV}} \rightleftharpoons (\mathrm{Fe}^{3+})^{\mathrm{VI}}\mathrm{Al}^{\mathrm{IV}}$$

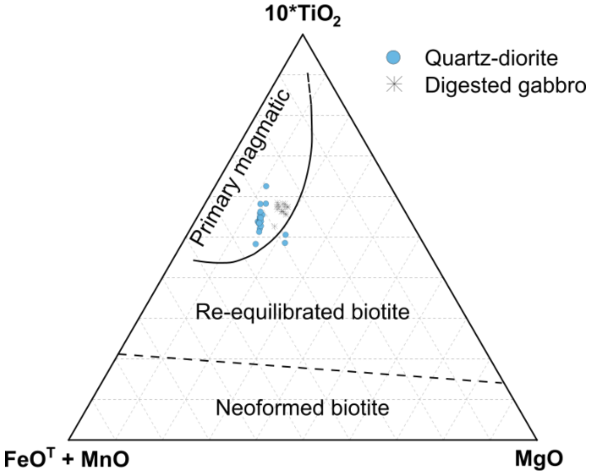

Figure VII-6. Discriminating diagram for primary (magmatic), re-equilibrated and new-formed biotite, adapted from Nachit *et al.* (2005).

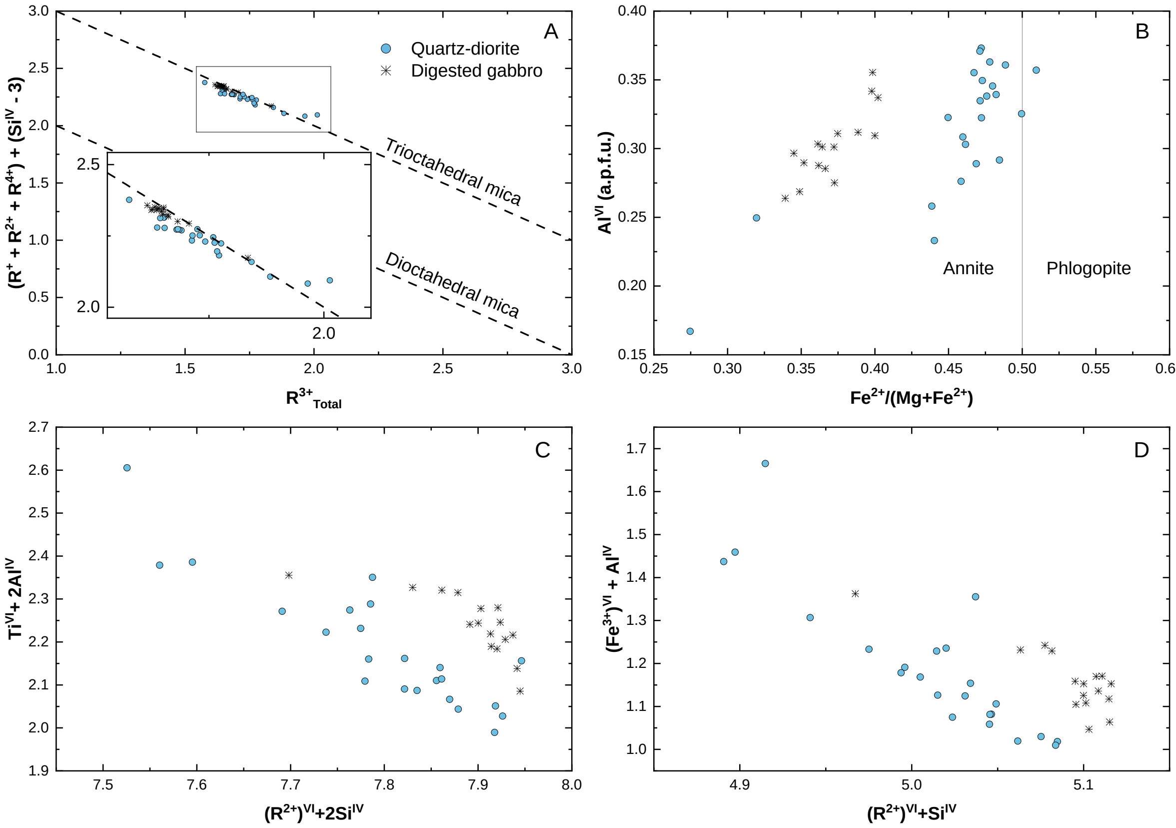

Figure VII-7. Main compositional features of biotite. (A) Cross-plot of total trivalent cationic contents (R^{3+}) *vs.* ($R^{+} + R^{2+} + R^{4+}$) + (Si^{IV}-3), illustrating the proximity of the analyzed biotite to the ideal trioctahedral mica join and slight deviations towards the dioctahedral mica join in the quartz-diorites. (B) Classification of biotite based on $Fe^{2+}/(Fe^{2+} + Mg)$ *vs.* Al^{VI} values. (C) Negative correlation between $(R^{2+})^{VI} + 2Si^{IV}$ and $Ti^{VI} + 2Al^{IV}$, suggesting the Ti-Tschermak exchange. (D) Negative correlation between $(R^{2+})^{VI} + Si^{IV}$ and $(Fe^{3+})^{VI} + Al^{IV}$, reflecting the ferri-Tschermak exchange.

Chlorite

Chlorite represents the most common alteration mineral affecting the ferro-magnesian silicates (amphibole and biotite) and is also found as new-formed infillings of late veinlets. Despite only being present in minor amounts, a total of 71 quantitative electron probe micro-analyses were performed across 20 polished thin sections to characterize the main compositional features of chlorite. Structural formulae were calculated based on 14 oxygens per formula unit. The general formula of chlorite is given by $(R^{2+}, R^{3+})^{VI}{}_6(Si^{4+}{}_{4\text{-}x}R^{3+})^{IV}O_{10}(OH)_8$, where: $R^{2+} = Mg^{2+}, Fe^{2+}, Ni^{2+}$ and Zn^{2+}, and $R^{3+} = Al^{3+}, Fe^{3+}$ and Cr^{3+}.

In a Fe^{2+} *vs.* Mg+Mn cross-plot, which documents the common Fe ⇌ (Mg, Mn) exchange, most of the analyses fall close to the chamosite-clinochlore join. Analogous to biotite, deviations from this trend can be assigned to the presence of other exchange mechanisms involving di- and trivalent cations (Figure VII-8). Regarding compositional variations between lithologies, the most evident feature is the iron-enriched character of chlorite in late veins. Chlorites from quartz-diorites and pegmatoidal domains have higher Mg and Mn concentrations relative to those from the diorites. This is not surprising because chlorite composition could be significantly influenced by local chemical gradients, thus mimicking the main features of amphiboles from the quartz-diorites, which have higher Mg-number when compared to those from the diorites. In a R^{2+} *vs.* Si^{IV} contents cross-plot, distinction between the various lithologies is less clear, with every analysis plotting near the middle of the Amesite-Al-free chlorite join (Figure VII-8B). Furthermore, it should be noted that analyses falling outside the polygon defined by the several compositional joins were most likely affected by late alteration process (leading to the formation of mixed layered phyllosilicates) and do not represent a chlorite solid solution.

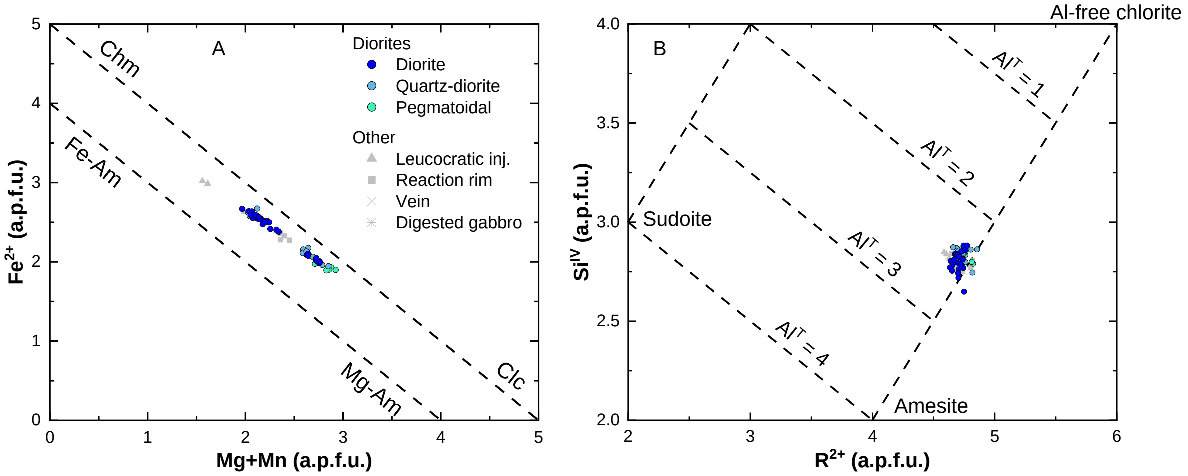

Figure VII-8. (A) Cross-plot of Mg+Mn contents *vs.* Fe^{2+} and the respective solid solution space, showing the possible incorporation of other di- and trivalent cations. Chm – chamosite, Clc – Chlinoclore, Fe-Am – Fe-amesite, Mg-Am – Mg-amosite. (B) Cross-plot of total R^{2+} contents *vs.* Si^{IV}; Sudoite = $(Mg_2Al_3)(Si_3Al)O_{10}(OH)_8$, Amesite = $(Mg_4Al_2)(Si_2Al_2)O_{10}(OH)_8$, Al-free chlorite = $(Mg_6)(Si_4)O_{10}(OH)_8$.

Apatite

Apatite is an accessory but ubiquitous mineral in all the examined samples, representing the only phosphate mineral phase. To characterize the main compositional features of apatite, a total of 102 quantitative electron probe microanalyses were performed in 26 polished thin sections. Structural formulae were recalculated on the basis of 25 oxygens per formula unit, which is ideally described as $A_5{}^{VII\text{-}IX}(XO_4)^{IV}{}_3Z$, where: A = Ca^{2+}, Mn^{2+}, Fe^{2+}, Na^{+} and trivalent Rare-Earth Elements; X = P^{5+} and Si^{4+}, and Z = F^-, Cl^- and OH^-.

All apatite analyses have considerable (and rather similar) concentrations of Cl (median = 0.66 wt%), which, when related to the other Z-site anions, F^- and OH^-, in a ternary diagram, shows proportions of 15-20%[6] (Figure VII-9A). In this same diagram, it is evident that most of the Z-site is occupied with F, indicating a fluorapatite composition. In the Ca-Mn-Fe compositional space, most analyses are distributed along the Ca-Fe join, plotting close to the Ca point (Figure VII-9B). Manganese concentrations are always low and Mn/Fe ratios increase from 0.44 to 0.64 in silica-rich lithologies, as denoted by the rock types in which these analyses were performed. In a Ca *vs.* P cross-plot, a significant deviation from the ideal proportions is observed for many of the analyzed apatite grains (Figure VII-9C). This deviation likely reflects the incorporation of other mono-, di- and trivalent cation in the A-site. Indeed, there is a negative correlation between $R^+ + R^{2+} + R^{3+}$ and Ca contents (Figure VII-9D). However, the sum of all A-site cations does not equal the ideal 10 a.p.f.u., meaning that there are other substitution mechanisms which were not account for and/or elements that were not reported. Likewise, X-site occupancy is systematically below the ideal 6 a.p.f.u. and every analysis reports SiO_2 concentrations below the detection limit of the analytical method used, implying that other non-reported elements which can be incorporated into the X-site (such as S^{6+}, As^{5+} or V^{5+}) have somewhat significant concentrations. These possibilities must be investigated in subsequent studies[7].

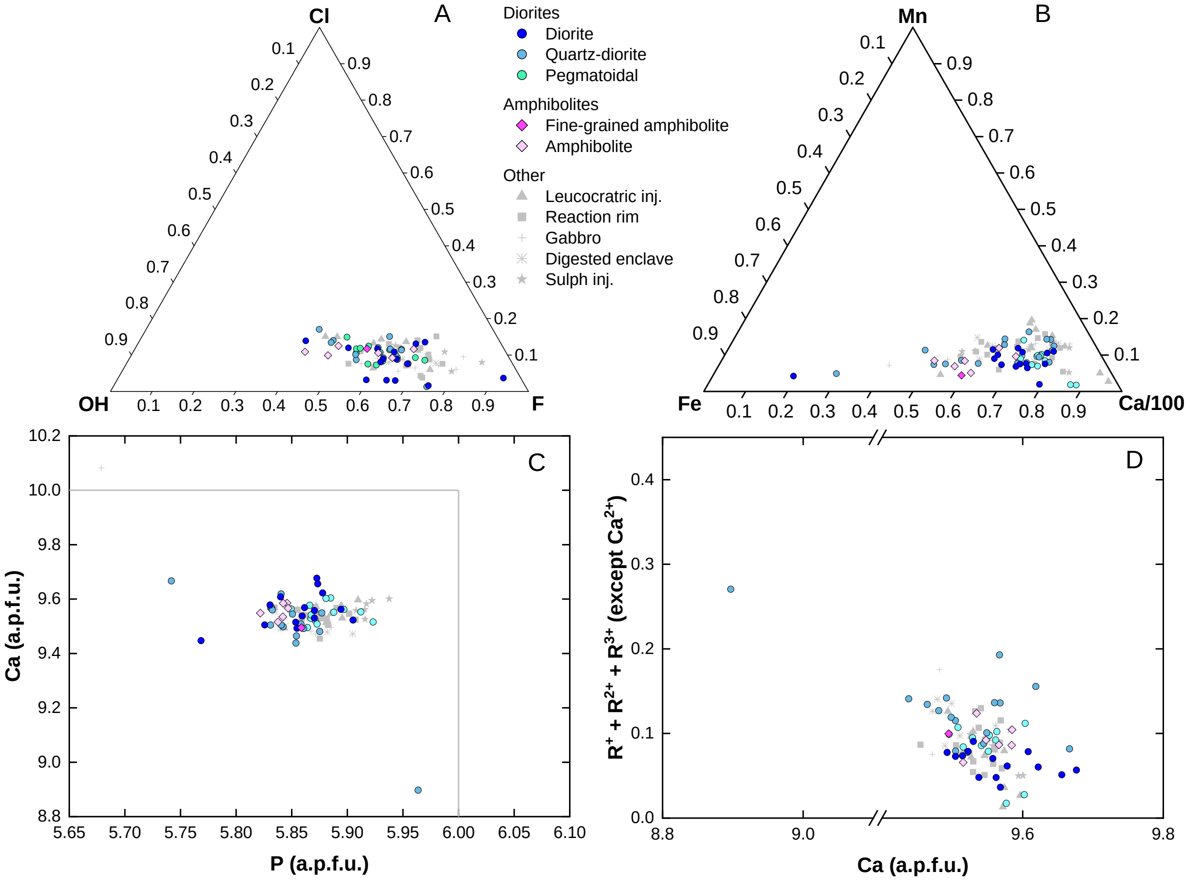

Figure VII-9. Main compositional features of apatite. (A) Ternary F-Cl-OH diagram, showing the relative proportions of the anions incorporated into the Z-site. (B) Ca/100-Mn-Fe ternary diagram, illustrating the substitution of Ca for Fe or Mn. (C) Deviation of analyzed apatite grains from the ideal 6 P and 10 Ca a.p.f.u. proportions. (D) Slight negative correlation between Ca and $R^+ + R^{2+} + R^{3+}$ (except Ca^{2+}), highlighting the possible incorporation of other mono-, di- and trivalent cations at the expense of Ca.

---

[6] Note that in such diagrams, values are normalized so that their sum equals 1 (or 100%), therefore, the values presented merely reflect the proportions of each element with respect to each other and not their absolute concentrations.

[7] It should be noted that there is no reason to doubt the calibration used for the EPMA analyses. The standards used are reported in Supplementary Data 1.

Pyroxene

Pyroxene only occurs in a few samples and its compositional variation was inspected using 40 analyses performed in 5 polished thin sections. Structural formulae were calculated on the basis of 6 oxygens per formula unit which is ideally expressed as $[(M2)(M1)]^{VI}(Si, Al)^{IV}{}_2O_6$, where: M2 = Mg^{2+}, Fe^{2+}, Ca^{2+} and Na^+; M1 = Al^{3+}, Fe^{3+}, Ti^{4+}, Cr^{3+}, V^{3+}, Zn^{2+}, Mg^{2+} and Fe^{2+}. Several analyses of pyroxene in quartz-diorites, digested gabbro and amphibolite enclaves show total oxide contents averaging 97%. Even though there is no convincing petrographic evidence of replacement processes, it is possible that these grains were already somewhat protonated, hydrated or incipiently replaced by amphibole (at the micrometric scale)[8].

Clinopyroxene from quartz-diorite and digested gabbro samples have similar compositions and plot in the (clino-)enstatite and pigeonite fields (Figure VII-10). This similarity could be the result of the interaction between the quartz-dioritic melts and the gabbroic enclave. However, following this same interpretation, it is uncertain whether: (1) clinopyroxene from the gabbroic enclave was compositionally re-equilibrated during quartz-diorite melt – gabbro interaction; or (2) clinopyroxene formed from the quartz-diorite melt. Orthopyroxene from the preserved gabbroic portion plots in the enstatite field but has considerable amounts of the ferrosilite component, averaging Fs_{43}. The most Ca rich (and Mn poor) clinopyroxenes are associated with the sulfide-rich injection.

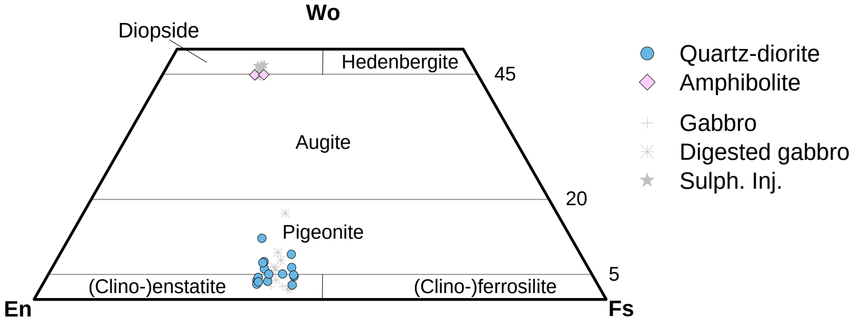

Figure VII-10. Pyroxene quadrilateral diagram, showing the relative proportions of the ferrosilite (Fs), wollastonite (Wo) and enstatite (En) components.

Oxides

Magnetite

Magnetite is present in all studied samples, occurring as one of the major oxide mineral phases along with ilmenite (discussed below). To describe its compositional variability, 169 analyses were performed across 28 polished thin sections. Structural formulae were calculated based on 32 oxygens per formula unit and Fe^{3+} was estimated by iteration using the $Fe^{3+} = 8*(2-2Ti/8)-R^{3+}$ approach. After Fe^{3+} estimation, oxide bulk concentrations were recalculated to account for Fe_2O_3. The general formula of magnetite (and normal spinel *s.l.*) is ideally expressed as $(R^{2+})_8{}^{IV}(R^{3+})_{16}{}^{VI}O_{32}$, where: R^{2+} = Fe^{2+}, Ni^{2+}, Co^{2+}, Zn^{2+}, Mg^{2+}, Mn^{2+} and Ca^{2+}; R^{3+} = Fe^{3+}, Al^{3+}, Cr^{3+} and V^{3+}.

Most of the major compositional variation in magnetite can be ascribed to the solid solution series between magnetite and ulvöspinel (Fe_2TiO_4). In a Fe^{3+}-Ti-Fe^{2+} diagram, it is evident that, regardless of lithology, most analyzed grains plot close to the proportions of $2Fe^{3+}:1Fe^{2+}$ that describe the ideal magnetite composition (Figure VII-11). As such, apart from six outliers, median ulvöspinel molecular contents [Usp% = $100 * (Fe^{2+}+Ti/2)/(Al+Mg+Mn+V+Ti/2+Zn+Ni+Fe^{2+}+Fe^{3+}+Cr)$] across

---

[8] For this reason, no pyroxene thermobarometry was attempted (see Chapter IX. below).

every lithology are relatively low, with a median value of 34.67%[9]. Magnetite in both the diorite and quartz-diorite shows similar median TiO_2 concentrations, 0.26 and 0.23 wt%, respectively. There is no distinction in TiO_2 concentrations between single and mixed magnetite-ilmenite grains, suggesting that exchange between adjoining magnetite and ilmenite grains was likely not significant (Figure VII-12); otherwise, magnetite in contact with ilmenite would tend to have lower TiO_2 concentrations in comparison with single grains.

Other compositional changes in magnetite can be explained by the incorporation of minor elements, the most significant of which V, Cr, Al, Mn, and Mg, by decreasing concentration. Because many analyses have MnO and MgO concentrations below the detection limit of EPMA, most minor compositional variation results in trivalent cation enrichment. In addition, incorporation of these cations explains the small compositional shift away from the ideal Fe^{3+}/Fe^{2+} proportions, unnoticeable in the ternary diagram. Vanadium contents are variable both in the diorite and quartz-diorite rocks, ranging from 0.03 to 0.38 a.p.f.u. (Figure VII-13A). Conversely, V contents in the amphibolite enclaves (including the fine-grained variety) are more restricted, ranging from 0.15 to 0.30 a.p.f.u. Chromium contents are clustered around 0.1 a.p.f.u. for every lithology apart from four analyses belonging to an amphibolite sample (**SEM-TOR-3**) that record the highest bulk Cr_2O_3 concentrations, ranging from 6.3 to 7.6 wt% (Figure VII-13B); these analyses correspond to fine magnetite grains that occur as numerous inclusions within an amphibole aggregate. Aluminum contents show a well-defined negative correlation with Fe^{3+}/Fe^{2+}, spanning from 0 to 0.5 a.p.f.u. for most analyses (Figure VII-13C). The MnO and MgO concentrations (for analyses above the detection limit) do not co-vary with Fe^{3+}/Fe^{2+}.

Thus, although magnetite is an abundant oxide mineral phase in every lithology, its composition remains rather constant and close to the ideal one throughout all the sampled rock types. For diorite, quartz-diorite and pegmatoidal domains, this is in good agreement with the expected composition of magnetite in felsic plutonic rocks, approaching pure Fe_3O_4 due to extensive *sub-solidus* re-equilibration which can potentially be enhanced by the presence of immiscible aqueous fluids (Frost & Lindsley, 1991).

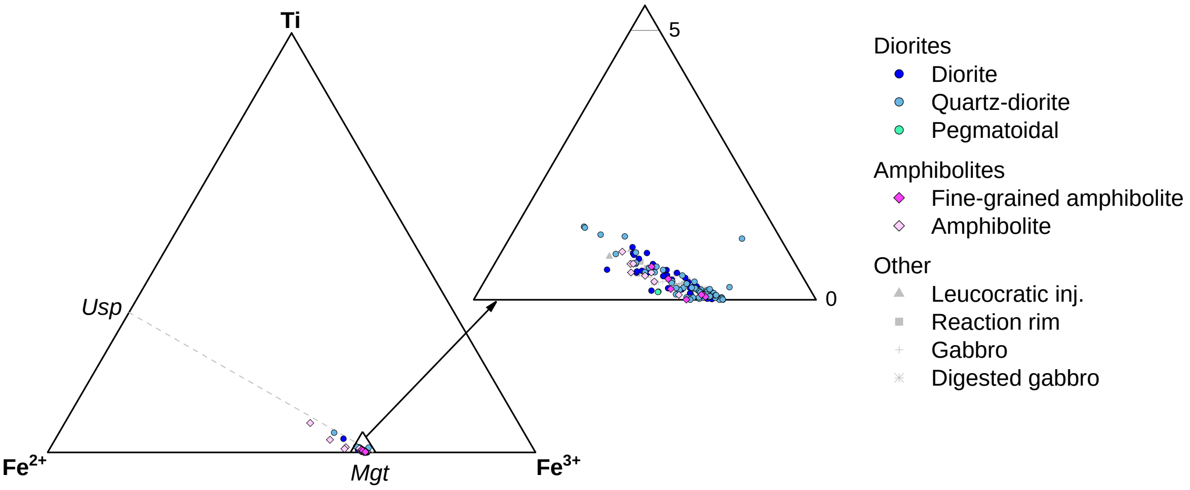

Figure VII-11. Major compositional variation of magnetite in the ternary Fe^{3+}-Ti-Fe^{2+} diagram. The dashed line corresponds to the ulvöspinel-magnetite solid solution join. The labels ‘0’ and ‘5’ in the amplified diagram indicate Ti% proportions relative to Fe^{3+} and Fe^{2+}.

---

[9] Although this value may seem higher than expected, at least upon closer inspection of Figure VII-11, it should be kept in mind that following the adopted expression to determine Usp%, a pure magnetite has 33.33 Usp%. This is a direct consequence arising from the fact that both magnetite and ulvöspinel have Fe^{2+}.

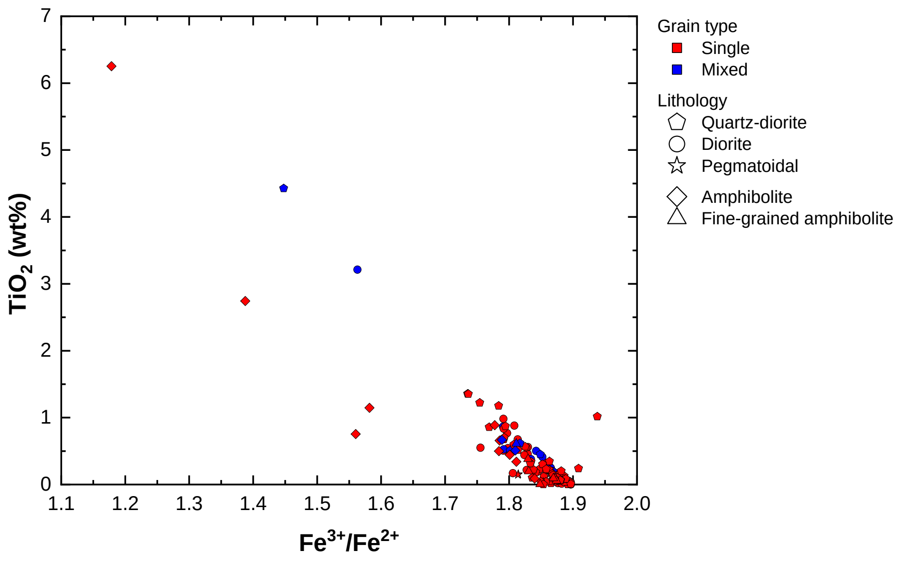

Figure VII-12. Single and mixed grains in a Fe^{3+}/Fe^{2+} *vs.* TiO_2 projection, showing that there is no correlation between grain type and TiO_2 concentration.

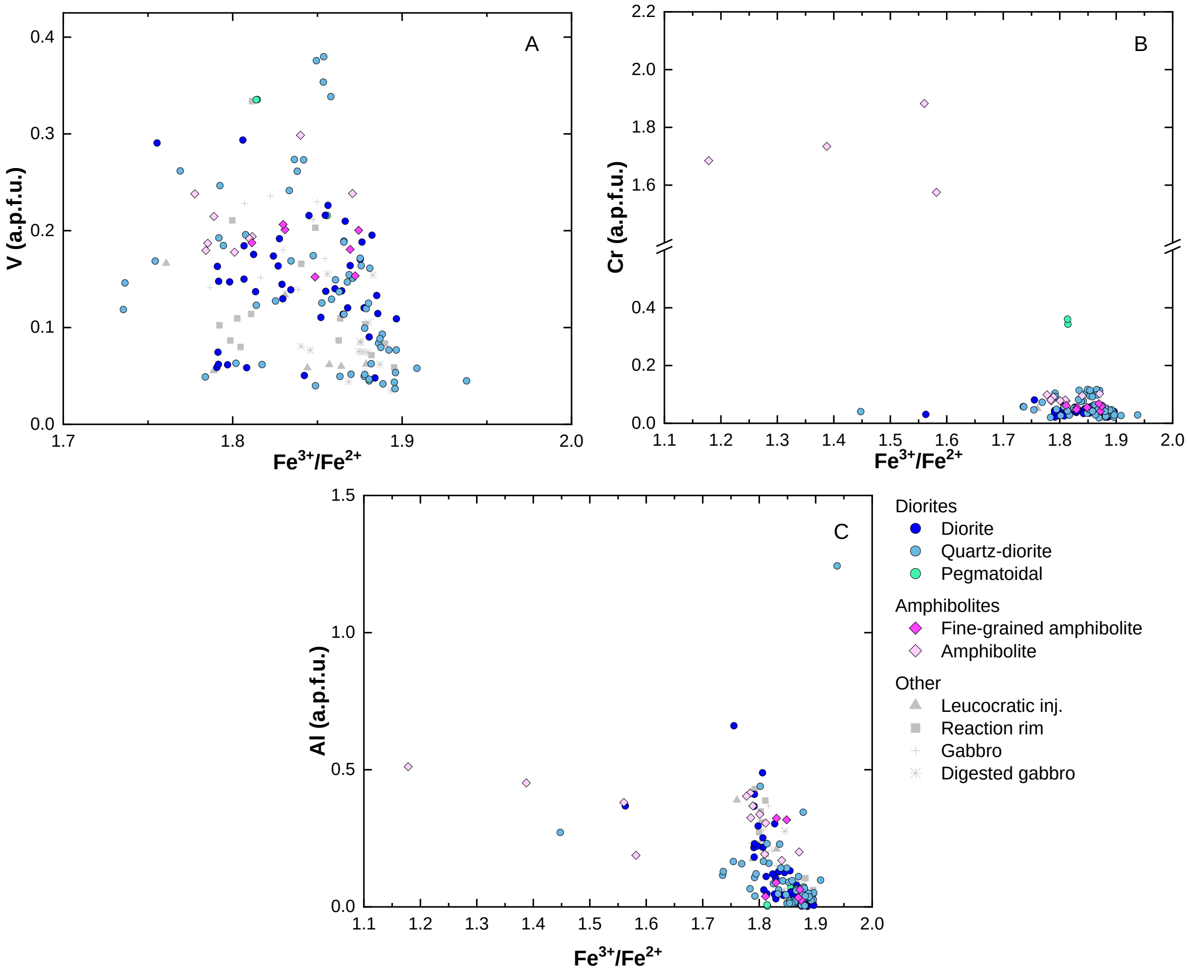

Figure VII-13. Minor element compositional variation of magnetite. (A) Negative correlation and relative spread in the relationship between Fe^{3+}/Fe^{2+} and V contents; magnetite analyses in amphibolite with low Fe^{3+}/Fe^{2+} were omitted for clarity, having V contents around 0.1 a.p.f.u. (B) Fe^{3+}/Fe^{2+} *vs.* Cr contents cross-plot, showing the cluster of analyses from every lithology around the same value and the high Cr contents of amphibolite sample **SEM-TOR-3**. (C) Negative co-variation between Fe^{3+}/Fe^{2+} and Al contents in magnetite from different rock types.

Ilmenite

Ilmenite from plutonic rocks may form either by direct crystallization or by oxy-exsolution from titanomagnetite (Buddington & Lindsley, 1964). Because the latter process is rarely observed in the studied samples, most analyses focused on homogenous and isolated grains. This view is supported by the fact that both single and mixed grains of ilmenite have similar TiO_2 concentrations. As such, in the following description, all the analysed ilmenite grains will be interpreted as direct products of crystallization.

Like magnetite, ilmenite is an abundant oxide mineral phase across most of the examined rock types. To describe its compositional variability, a total of 215 quantitative electron probe micro-analyses were performed in 28 polished thin sections. Structural formulae were calculated using 3 oxygens as reference, thus implying an ideal composition of A_2O_3, where: A = Fe^{2+}, Ti^{4+}, Mg^{2+}, Mn^{2+}, Fe^{3+}, Cr^{3+}, V^{3+} and Al^{3+}.

Major compositional variation in ilmenite can be explained by the solid solution series between ilmenite and hematite (Fe_2O_3). In the Fe^{3+}-Ti-Fe^{3+} compositional space, most ilmenite is relatively poor in Fe^{3+}, plotting close to the ideal ilmenite proportions. Hematite molecular contents, defined as in ILMAT (Lepage, 2003), range from 0 to 27%, with a median of 4% (Figure VII-14).

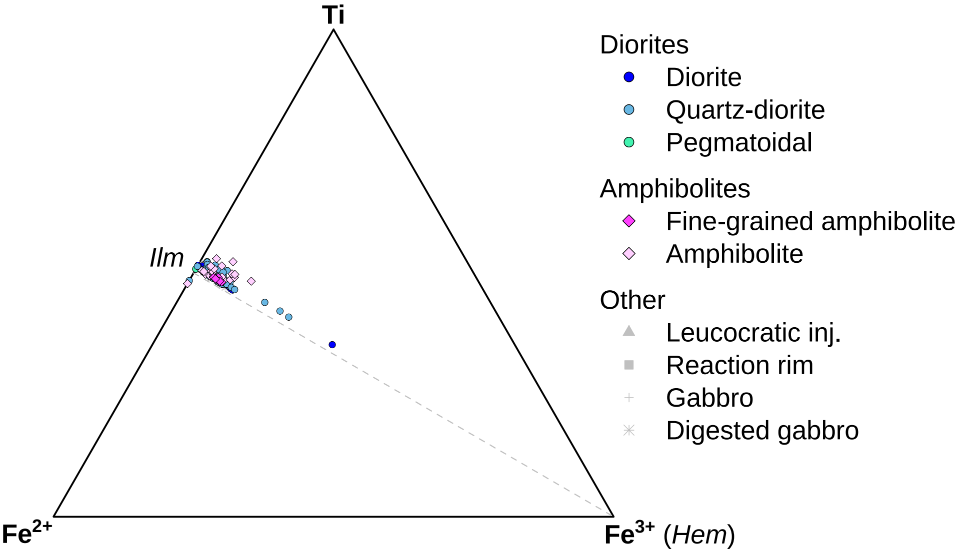

Figure VII-14. Major compositional variation of ilmenite in the ternary Fe^{3+}-Ti-Fe^{2+} diagram. The dashed line corresponds to the ilmenite-hematite solid solution join.

Minor element incorporation accounts for some compositional variation in ilmenite and small shifts away from the ideal Ilm-Hem join. The most significant elements are Mn, V and Mg, ordered by decreasing concentration values. Manganese contents have a negative correlation with Fe^{2+} and range from 0.028 to 0.11 a.p.f.u. in diorite and quartz-diorite samples (Figure VII-15A). Ilmenite from these rocks show similar MnO concentrations, with median values of 2.11 and 2.19 wt%, respectively. These values are well within those typically found in felsic plutonic rocks and, although the difference is not significant, data shows that MnO concentrations in ilmenite are indeed higher in more evolved rocks (Frost & Lindsley, 1991). Magnesium contents are rather similar across every lithology (X = 0.002 a.p.f.u.), except for some outliers associated with ilmenite grains within amphibolite enclaves, for which the Mn contents may reach 0.0046 a.p.f.u. (Figure VII-15B). In addition, there is no correlation of any kind between Mg and Fe^{2+} contents. As shown in Figure VII-15C, V is incorporated at the expense of Ti. Vanadium contents are clustered from 0 to 0.005 a.p.f.u. across every lithology. Despite the lack of a relationship between V enrichment and lithology, ilmenite from the pegmatoidal domains is systematically in the higher end of the clustered analyses. Irrespective of lithology, a considerable number of analyses have Al_2O_3 concentrations below the detection limit of EPMA.

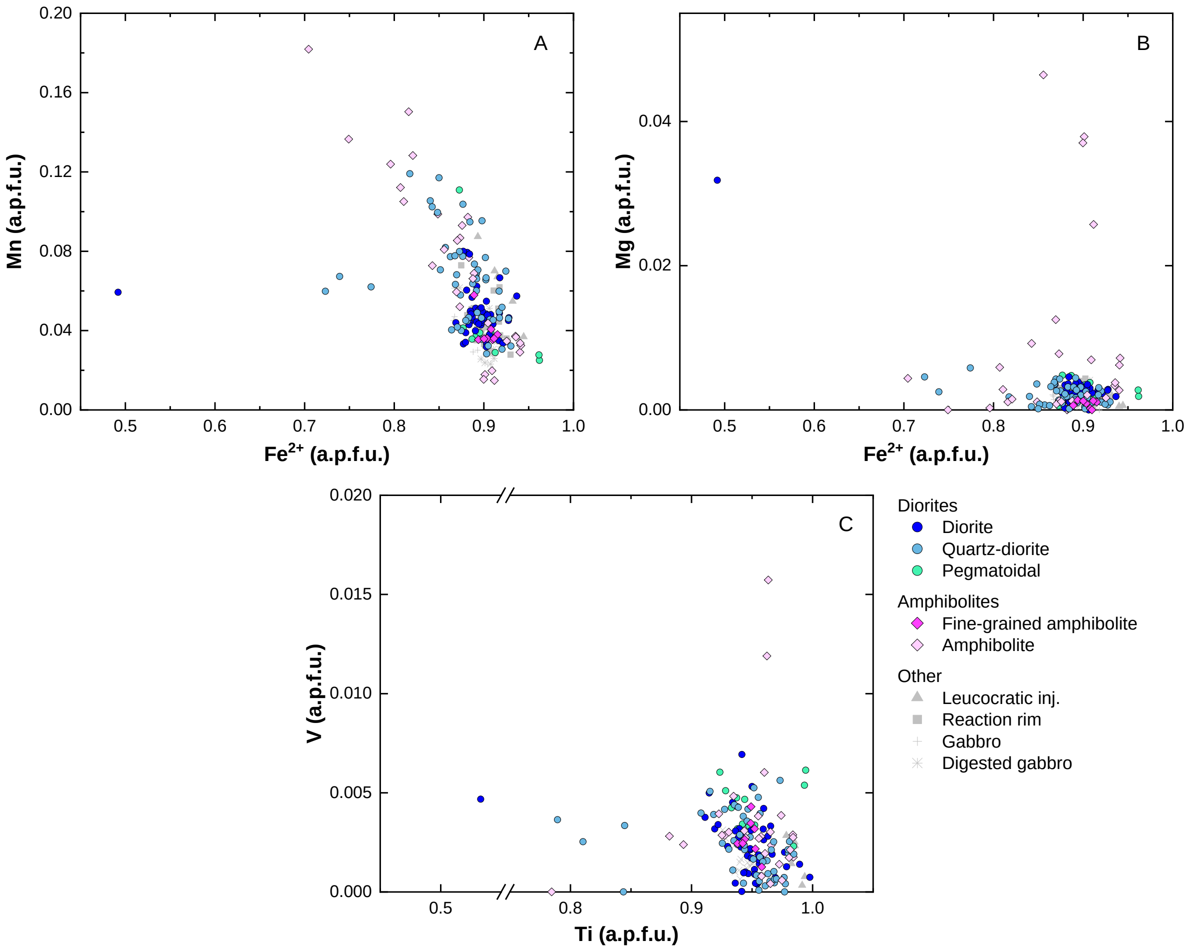

Figure VII-15. Minor compositional variation of ilmenite. (A) Negative correlation between Fe^{2+} and Mn contents. (B) Clustered (and low) Mg contents in ilmenite. (C) Negative correlation between Ti and V contents; note that the pegmatoidal domains have systematically (relatively) high V contents.

VIII. Whole-rock geochemistry

In addition to the major, minor and trace elemental data obtained from this work for the several rock types cropping out at Torrão, the following datasets were used for reference and are reported in Supplementary Data 2: representative analyses of the LGS and associated mesocratic rocks (Jesus, 2011; Jesus *et al.*, 2016), high-Ti diorites (Jesus *et al.*, 2016 using the expanded dataset from Caldeira *et al.*, 2007), 'metabasalts' belonging to the Escoural Formation (Chichorro, 2006) and other 'metavolcanic'[10] rocks cropping out near the Odivelas dam (da Silva, 2011). It should be noted that, as the name implies, metavolcanic rocks are not amphibolites. Particularly, whereas the amphibolites reported in this work show an amphibolite facies metamorphic mineral assemblage, the Odivelas metavolcanics show variable degrees of greenschist facies metamorphism features which coexist in disequilibrium with magmatic minerals (da Silva, 2011). Conversely, the metabasalts reported in Chichorro (2006) show a typical amphibolite facies metamorphic mineral assemblage. Nevertheless, as will be shown below, their usage as a compositional analogy of mafic volcanic rocks affected by different degrees of metamorphism is valid. To better understand the characteristics and compositional trends of each rock type, information provided by the compositional variations of the two main lithologies (*i.e.*, dioritic and amphibolite rocks) will be discussed separately.

---

[10] 'Metabasalt' and 'metavolcanic' are the terms used in the respective works.

Major elements

Major element concentrations represented in Figure VIII-1 and throughout this chapter were recalculated in an anhydrous basis with total iron as $Fe_2O_3^T$. As noted previously, classification of plutonic rocks according to the IUGS recommendations is done using a QAPF diagram, which considers mineral modal abundances (Le Maitre, 2002). Plotting the diorite samples in the TAS (Total Alkalis *vs.* Silica) diagram for plutonic rocks shows that many of them fall in the reference fields of their more mafic equivalents. Most diorites and high-Ti diorites plot in the gabbro field whereas the quartz-diorites plot in the diorite field. The leucocratic, pegmatoidal and sulfide-rich rock samples have intermediate compositions which lie in the middle of these two compositional fields. Nonetheless, the analyzed rock types do not have mineralogical features typical of gabbroic rocks, such as considerable amounts of olivine and pyroxene; in fact, the abundance of amphibole and andesine/oligoclase feldspar in these rocks is quite characteristic of diorites (and other granitoid rocks). Furthermore, the anorthite molecular contents of plagioclase are not strictly higher than 50% in every single diorite sample. Therefore, classification using the QAPF diagram is preferred and will be used throughout this chapter because it accounts for mineralogical variations and their relative proportions, which, in this case, reflect more accurately the nature of these rocks. Nevertheless, the TAS diagram does indicate that the diorite rocks of Torrão are considerably more silica depleted than the numerous other diorites and quartz-diorites used for calibration of this diagram, so much so that they are comparable to gabbros, such as those from the LGS.

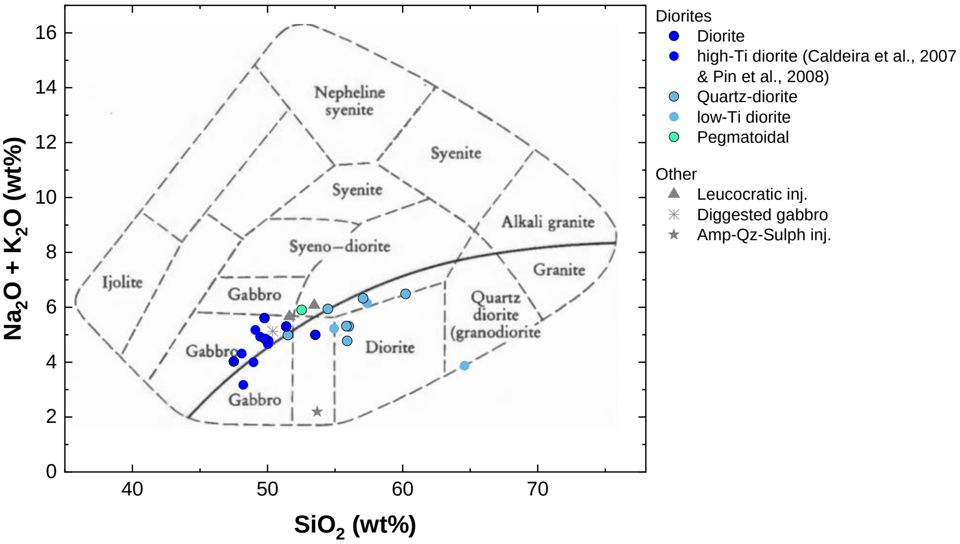

Figure VIII-1. TAS diagram (Total Alkalis *vs.* Silica) for discrimination and classification of igneous plutonic rocks. Adapted by Wilson (1989) for plutonic rocks based on the work of Cox *et al.* (1979). The curved solid line subdivides the alkalic from subalkalic rocks.

Previous studies on the diorites

As noted above, previous studies concerning the diorites exposed at Torrão (Caldeira *et al.*, 2007; Pin *et al.*, 2008) provide insufficient data on their petrographic characteristics, resulting in difficulties regarding their classification or meaning. However, both studies provide whole-rock geochemical data which, assuming that sampling was carried out at (or near) the study area, could present some similarities to that of the rocks examined in this work, thus enabling a direct correlation. Indeed, as will be clearer below, the diorite samples here presented share many similarities with the high-Ti diorites (Jesus *et al.*, 2016; Caldeira *et al.*, 2007), showing elemental enrichments in both $Fe_2O_3^T$ and TiO_2 (median values of 9.5 and 1.5 wt%, respectively). Other compositional characteristics of the high-Ti diorites, such as their low Mg-number and silica plus other features addressed below (Ni and Zr concentrations and normalized incompatible element trends), are also comparable to those of the diorites sampled in this work. As such, to make use of a larger dataset, the whole-rock geochemical data from Caldeira *et al.* (2007) and Pin *et al.* (2008) will be interpreted and presented together with the diorite data from this work. Despite sharing many compositional features, the term 'high-Ti' will be omitted during this chapter when referring to the diorites for the sake of preserving the nomenclature used up to this point. Nevertheless, this term seems appropriate to describe the sampled diorite *s.s.* rocks and should be used as such in a broader context (making use of the now expanded dataset). In addition, the quartz-diorites share some of the features highlighted for the low-Ti diorites, namely similar silica, Fe, Ti and Zr contents, mild LILE enrichments relative to HFSE and strong LREE (Light REE) fractionation relative to HREE (Heavy REE). For this reason, the low-Ti diorite geochemical data reported in Jesus *et al.* (2016) will be interpreted together with the quartz-diorites.

Dioritic rocks

The major element signatures for diorites and quartz-diorites enable a clear distinction between these two lithologies. As expected, the silica-saturated quartz-diorites have higher SiO_2 concentrations (54.5 to 60.2 wt%) compared to the diorites (47.5 to 53.5 wt%). Alumina concentrations are similar between diorites and quartz-diorites (Figure VIII-2A), which reflects the balance between increasing Al contents in plagioclase but decreasing in amphibole. Both lithologies display similar MgO concentrations (around 4 wt%) but the diorites are $Fe_2O_3^T$-richer, with values ranging from 8.17 to 11.5 wt% (Figure VIII-2B and C), mainly due to higher modal abundances of Fe-Ti oxide mineral phases. These differences result in slightly higher Mg-numbers for the quartz-diorites in comparison with those obtained for diorites ($X_{Mg\#}$ = 51.8 and 48.7, respectively). Higher TiO_2 concentrations in the diorites are related to the abundance of oxide mineral phases, particularly ilmenite (Figure VIII-2F), the quartz-diorite sample **SEM-TOR-14** being the exception and recording 2.63 TiO_2 wt%. Calcium oxide concentrations are lower in the quartz-diorites (X = 4.4 wt%) relative to the diorites (X = 8.5 wt%; Figure VIII-2D) which can be caused by the higher anorthite molecular contents of plagioclase in the latter. Conversely, higher Na_2O contents in the quartz-diorites should reflect the more sodic plagioclase characterizing this lithology (Figure VIII-2E). The data on K_2O and P_2O_5 is relatively spread out, showing no correlation with each lithology (Figure VIII-2G and H). The lower K_2O in quartz-diorites is somewhat unexpected considering the modal abundance of biotite, which would result in higher K_2O concentrations. It should be noted, however, that variation in K_2O contents may also be related to superimposition of post-magmatic alkaline metasomatic processes, like those macroscopically documented by samples **SEM-TOR-11**, **12**, **16** and **18**.

Apart from having the highest MgO concentration of all dioritic samples, the pegmatoidal domain shows no other remarkable compositional distinctive features, displaying an intermediate composition between diorites and quartz-diorites in all other major elements. The same remarks can be made about the leucocratic injections, which composition lies consistently between that of the diorites and quartz-diorites, apart from their lower MgO concentrations. Compared to the diorites, both the leucocratic injections and pegmatoidal domains have higher SiO_2 and Na_2O but lower $Fe_2O_3^T$, CaO and TiO_2. Sulphur contents are similar in all dioritic samples (X = 0.027 wt%), but, as expected, the sulfide injection has considerable sulfur concentrations (2.44 wt%). Excluding samples **SEM-TOR-10** and **17**, all the analyzed dioritic rocks are metaluminous [$Al_2O_3 < (CaO + Na_2O + K_2O)$ but $Al_2O_3 > (Na_2O + K_2O)$] (Figure VIII-3).

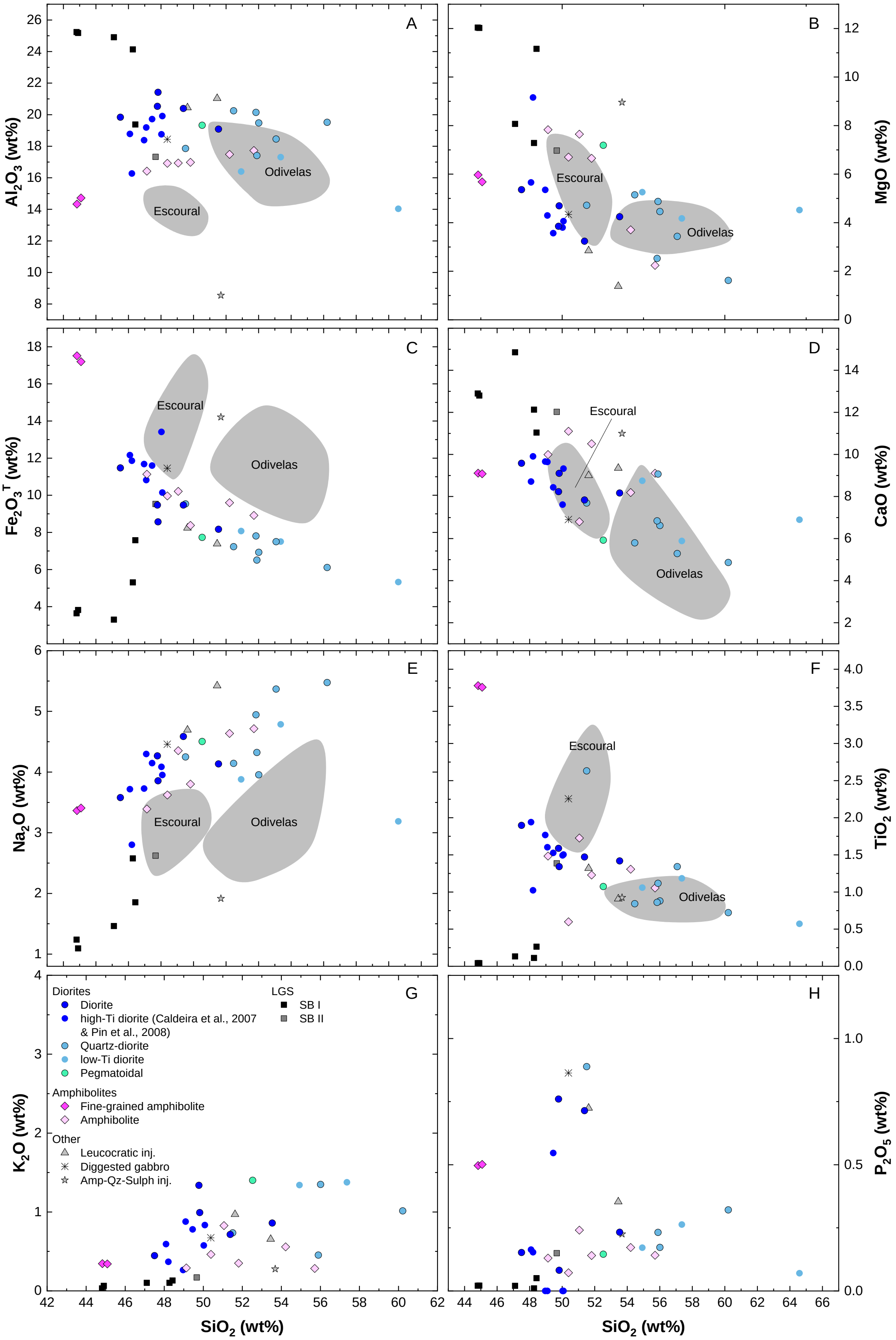

Figure VIII-2. Major element geochemistry of the rocks cropping out at Torrão, gabbroic samples from the LGS (Jesus, 2011) and high-Ti diorite samples from Caldeira *et al.* (2007) and Pin *et al.* (2008). The compositional fields refer to the data of metabasalt samples in the Escoural formation reported in Chichorro (2006) and metavolcanics cropping out near the Odivelas dam (da Silva, 2011); K$_2$O and P$_2$O$_5$ fields for the latter datasets are not represented for clarity due to their higher dispersion.

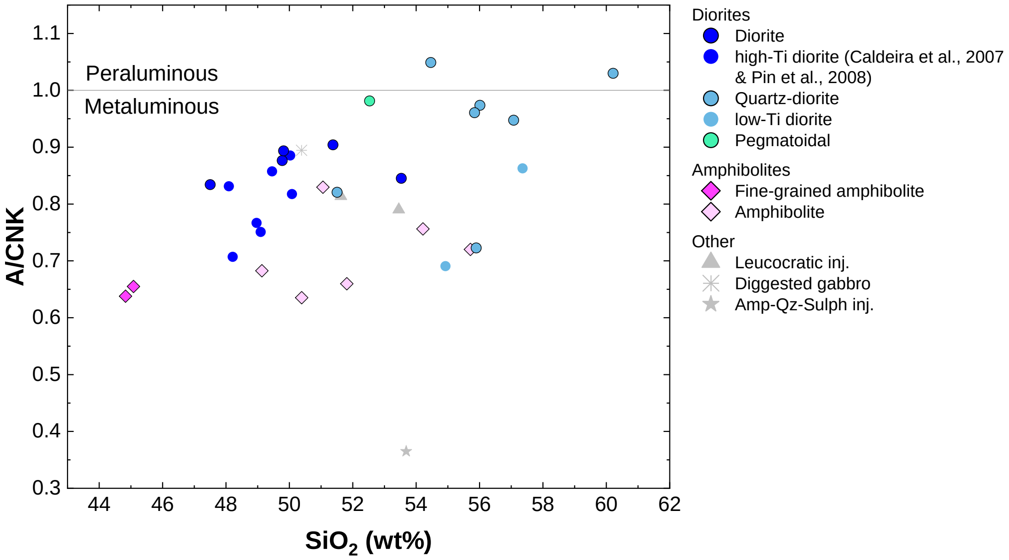

Figure VIII-3. Division between the metaluminous and peraluminous character of the dioritic and amphibolitic rocks.

A convenient way to examine how mineral compositions and abundances influence the whole-rock composition is by using general element ratios diagrams (as described in Stanley, 2020). The main advantage of using this type of diagram is that it has a molar format and is normalized to a common element, so that variations in the rock composition are projected in terms of material transfers. Another advantage is that it is relatively simple to compare rock compositions to those of their constituting minerals, enabling a direct assessment on mineral modal abundance and their influence on the bulk composition. More information on this and other methods of whole-rock analysis is summarized in Stanley (2020), however, the premise is that the element in the denominator must be incorporated into the major constituting minerals and be conservative, *i.e.*, its concentration should not change significantly across a set of samples. Similarly, the elements on the numerator should also be incorporated into the major constituting minerals of the considered rocks. A basic projection of this type is shown in Figure VIII-4 with the purpose of comparing rock compositions in terms of their three main constituting minerals: amphibole, plagioclase and biotite, and their respective Ti contents. The dataset plots close to, and somewhat parallel to the amphibole-plagioclase join, indicating that these are the main minerals controlling the composition of these rocks. The quartz-diorites plot closer to the median plagioclase node and have slightly higher K/Al, thus being slightly shifted towards the median biotite node. With exception of sample **SEM-TOR-14** (quartz-diorite), higher Ti contents are related to the diorites and, accordingly, plot close to the amphibole node.

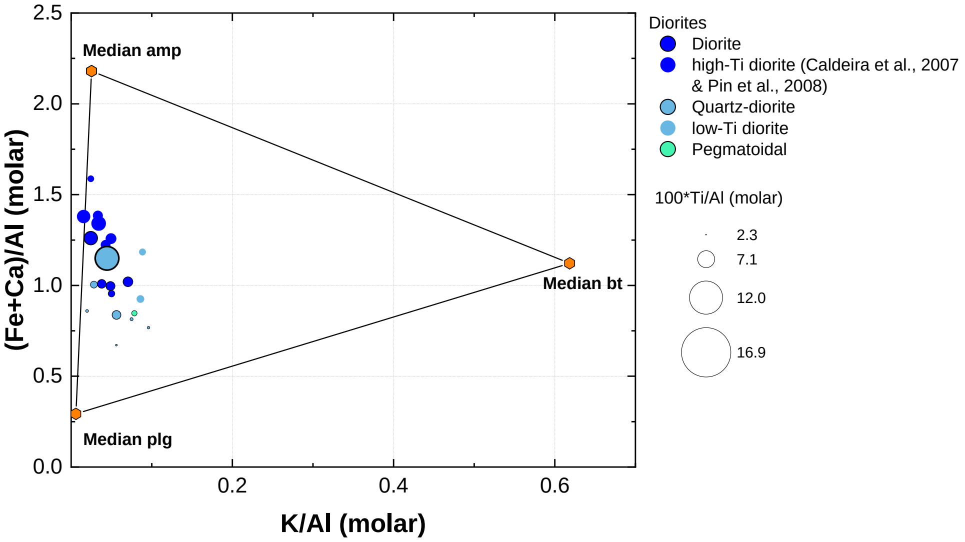

Figure VIII-4. General elemental ratio diagram for the dioritic rocks in terms of their K/Al and (Fe+Ca)/Al molar contents and their Ti enrichment (also normalised to aluminium). Median mineral molar contents were calculated using only grains from the diorites and quartz-diorites.

Regarding geochemical affinities, all diorite and high-Ti diorite samples plot on the tholeiitic reference field in a SiO_2 *vs.* FeO^T/MgO (FeO^T calculated from $Fe_2O_3^T$: $FeO^T = 0.8998 * Fe_2O_3^T$) cross-plot (following Miyashiro, 1984), whereas quartz-diorites and low-Ti diorites show a transitional character between tholeiitic and calc-alkaline affinities (Figure VIII-5A). For comparison, in a typical AFM (A – Na_2O+K_2O; F – FeO^T; M – MgO) diagram most diorite and quartz-diorite samples (as well as their equivalents from the literature) plot on the calc-alkaline reference field (following Irvine & Baragar, 1971; Figure VIII-5B). Such diagrams should be used cautiously, especially when making use of a limited dataset because local variations or accumulation of Fe-rich oxide minerals can shift samples towards the tholeiitic reference field, like the diorites. However, the rocks samples in question are neither cumulates nor are particularly altered (except for some metasomatized samples), meaning that this approach should be valid.

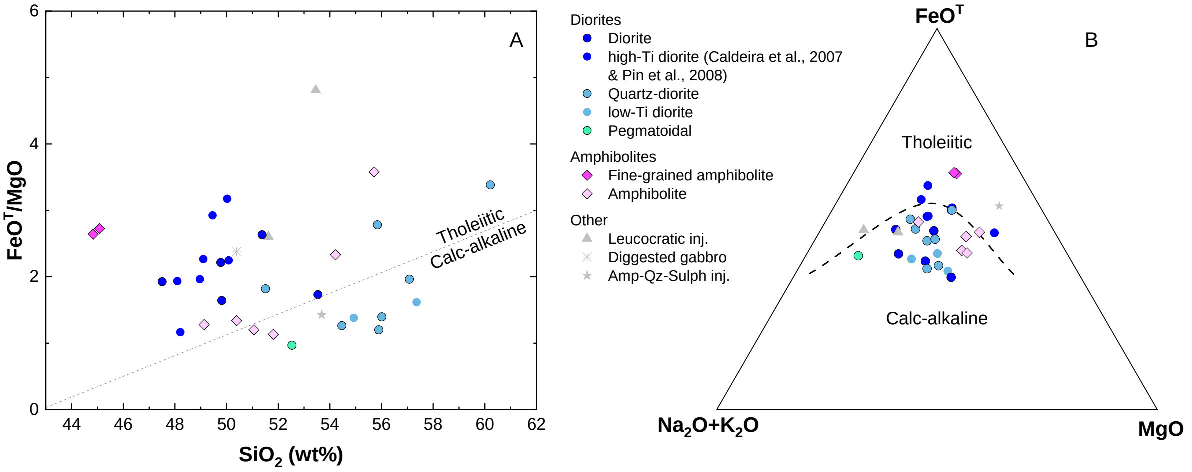

Figure VIII-5. Tholeiitic and calc-alkaline affinity discriminative diagrams. (A) SiO_2 *vs.* FeO^T/MgO cross-plot highlighting the transitional character between tholeiitic and calc-alkaline affinities of the diorite, quartz-diorite and amphibolite rocks, and the predominant tholeiitic affinity of the fine-grained amphibolite enclaves; (B) AFM plot showing mostly the same features as the diagram to the left albeit with a stronger calc-alkaline affinity for all samples. Reference fields from Miyashiro (1984) and Irvine & Baragar (1971), respectively.

Amphibolites

The compositional fields represented in Figure VIII-2 were gathered from the literature (Chichorro, 2006; da Silva, 2011) to compare and correlate the amphibolite samples from the present work with others of similar nature cropping out in the region. For this purpose, six Neoproterozoic metabasalt samples from the Escoural Formation (Chichorro, 2006) and eleven metavolcanic samples cropping out near the Odivelas dam (da Silva, 2011) were used[11]. The correlation between all four groups of amphibolites is not clear based on their major element compositions (Figure VIII-2). However, their minor and trace element geochemical signatures do support that there may exist correlations between these geological units (see below). Finally, it is worth reminding that the amphibolite *s.s.* group also includes the three samples collected near the Beja airport (*ca.* 36 km SE from Torrão).

As evidenced by Figure VIII-2, the Torrão fine-grained amphibolite enclaves represent a small data cluster, whereas the coarser-grained amphibolite enclaves define an evolving compositional trend for most elements at increasing silica contents. The compositional cluster defined by the fine-grained amphibolite enclaves likely reflects their proximity in the field whereas the coarser-grained amphibolites were sampled at several locations of the study area and their trends should bear some petrogenetic meaning.

The major element geochemistry of the amphibolites *s.l.* enables a distinction between the fine and coarser-grained varieties. The fine-grained amphibolite enclaves are distinguished by having lower silica (~45 wt%) and very significant enrichments in $Fe_2O_3^T$ and TiO_2 (17.5 and 3.7 wt%, respectively) due to the presence of Fe-Ti oxides, which are abundant in this rock type. Conversely, the coarser-grained amphibolite enclaves show intermediate $Fe_2O_3^T$ and TiO_2 concentrations which have a negative correlation with silica. Because MgO is slightly higher in the coarser-grained amphibolites, these have higher Mg-number (ranging from 43 to 61) in comparison to the fine-grained ones ($\bar{X}$ = 39.5). Alumina concentrations are slightly lower in the fine-grained amphibolites and, in the coarser-grained ones, increase slightly with increasing silica. These differences are likely related to amphibole composition since plagioclase is more sodic (hence less aluminous) in the fine-grained amphibolite enclaves. Calcium oxide contents in the coarser-grained amphibolites are variable, ranging from 6.8 to 11.1 wt% and show a faint negative correlation with increasing silica. Like alumina, Na_2O concentrations are slightly higher in the coarser-grained amphibolites and show a positive correlation with silica. The K_2O and P_2O_5 concentrations are similar for both lithologies, the latter being slightly higher in the fine-grained variety.

The amphibolite groups also display distinct trends in tholeiitic *vs.* calc-alkaline discriminant diagrams (Figure VIII-5). Although the sampled amphibolites appear well-preserved in both macro- and microscopical observations, it should not be excluded that some degree of chemical modification occurred during melt – enclave interaction. For this reason, some caution should be taken when interpreting these rocks as representative of their protoliths. The fine-grained amphibolites plot well within the tholeiitic reference field in both diagrams due to their elemental enrichments in Fe (Figure VIII-5A and B) and the coarser-grained ones show a transitional character between tholeiitic and calc-alkaline affinities. It should be noted that the amphibolites sampled near the Odivelas dam, with which the coarser-grained amphibolites share many compositional similarities, as will be seen below, plot consistently in the tholeiitic reference field (da Silva, 2011).

---

[11] The work carried out by da Silva (2011) also reports the occurrence of felsic metavolcanic rocks, which were not used for comparison.

Rare earth elements

Rare-Earth Elements (REE) shown in Figure VIII-6 and Figure VIII-7 were normalized to the chondrite ‘CNI’ elemental concentrations reported in Palme & O’Neill (2003).

Dioritic rocks

Chondrite-normalized distributions for the studied Torrão diorites are very similar to the high-Ti diorites, showing the same flat patterns with no anomalies and bulk enrichments ranging from *ca.* 20 to 40 × CN1 and slight LREE enrichments over HREE (median La/Sm = 1.35; Figure VIII-6A). Conversely, the Torrão quartz-diorites display normalized trends like those of the low-Ti diorites (Jesus, 2011), having higher bulk enrichments (30 to 70 × CN1) relative to the diorites and significantly higher LREE fractionation over HREE (median La/Sm = 2.5), resulting in a characteristic steep LREE segment for this lithology (Figure VIII-6B). Middle (MREE) and Heavy REE enrichment and trends are similar between the two dioritic rock types (Figure VIII-6C), showing the same gently negatively sloping pattern ($X_{\mathrm{Dy/Lu}}$ = 1.36 and 1.14, for the diorites and quartz-diorites, respectively). On the contrary, sample **SEM-TOR-17** displays strong HREE enrichments over MREE (Dy/Lu = 0.64). LREE enrichments over HREE can be ascribed to high modal abundances of minerals like apatite, which concentrate these elements (Fujimaki, 1989). Similarly, HREE enrichments may be explained by the occurrence of zircon, which displays high bulk distribution coefficients for HREE in andesites and diorites (Fujimaki, 1989). In addition, the quartz-diorites display slight positive or negative Eu anomalies, which are likely caused by higher and lower modal abundances of plagioclase. Finally, the leucocratic, pegmatoidal and sulfide rock samples display chondrite-normalized REE distributions like those of the diorites, the main difference being a marked Eu negative anomaly in the sulfide-rich injection (Eu/Eu* = 0.62; Figure VIII-6D).

Amphibolites

Both fine and coarse-grained amphibolites display similar REE distribution patterns but the former have considerably higher bulk enrichments (60.2 and 26.21 × CN1, for the fine-grained and coarser-grained amphibolites, respectively). The fine-grained amphibolites have flat LREE patterns with moderate Eu negative anomalies ($X_{\mathrm{Eu/Eu^*}}$ = 0.72) and gentle, negative sloping MREE and HREE patterns (Dy/Lu = 1.31). Such patterns are similar to those displayed by the Escoural metabasalts (Figure VIII-7A). The coarser-grained amphibolites display moderate LREE fractionation over HREE (median La/Sm = 1.44) and relatively flat MREE to HREE trends (median Dy/Lu = 1.06; Figure VIII-7B). Sample **SEM-TOR-15** is the exception, displaying a positive slope on LREE (La/Sm = 0.76). Despite the reported number of REE being limited for the Odivelas metavolcanic rocks (da Silva, 2011), their compositional trends and elemental enrichment degrees are like those displayed by the Torrão amphibolites in the available elements.

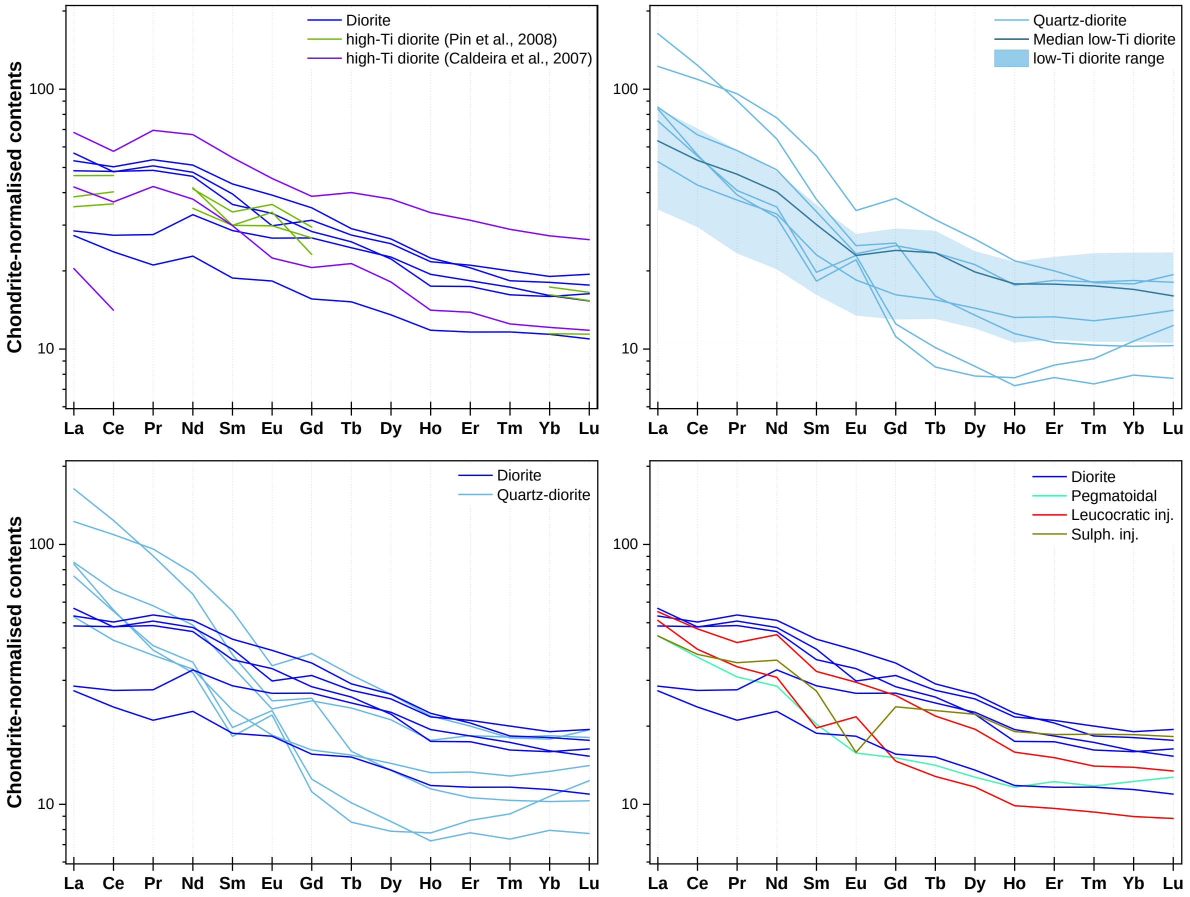

Figure VIII-6. Chondrite-normalized Rare-Earth elemental trends for the dioritic rocks. (A) Distribution of REE in the diorites and high-Ti diorites. (B) Compositional range and median values of normalized REE for the low-Ti diorites in comparison to the quartz-diorites. (C) Contrasting REE patterns between the diorites and quartz-diorites, the latter showing considerably higher degrees of LREE fractionation over HREE. (D) REE patterns for the leucocratic injections, pegmatoidal domains and sulfide-rich injection, all being alike of diorites. Broken line segments in the data of Pin *et al.* (2008) and Caldeira *et al.* (2007) results from incomplete REE analysis.

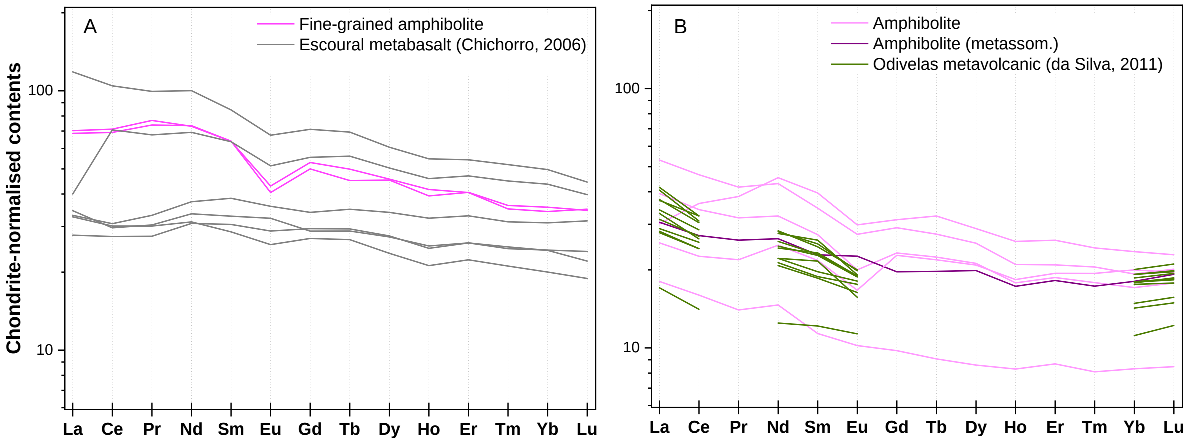

Figure VIII-7. Chondrite-normalized Rare-Earth elemental trends for the amphibolites *s.l.*. (A) Distribution of REE in the fine-grained amphibolites and metabasalts from the Escoural formation. (B) Distribution of REE in the coarser-grained amphibolites and metavolcanic rocks cropping out near the Odivelas dam. Broken line segments in the data of da Silva (2011) results from incomplete REE analysis.

Minor, trace and selected incompatible elements

Selected incompatible elements shown in Figure VIII-9, 8 and 9 were normalized to the primitive mantle elemental concentrations reported in Palme & O'Neill (2003).

Dioritic rocks

As noted above, Ni and Zr contents in the Torrão diorites are comparable to those in the high-Ti diorites reported in the literature. Nickel contents in the diorites range from 1 to 10 ppm whereas Zr varies between 49 and 86 ppm (reference Ni and Zr concentration ranges for the high-Ti diorites are 2-12[12] ppm and 33-69 ppm, respectively). The quartz-diorites display higher Ni (2-29 ppm; median = 25 ppm) and Zr contents (78-445 ppm; median = 94 ppm). The leucocratic injections show Ni and Zr contents which are within the range of the diorites (3-5 and 48-59 ppm, respectively). All diorite samples have Cr contents below the detection limit of 20 ppm, whereas in the quartz-diorites Cr contents range from 30 to 70 ppm (excluding three samples with Cr abundances below the detection limit). The Zr enrichment in the quartz-diorites is related to the higher modal abundance of zircon, even though the higher Ni and Cr values relative to the diorites suggest the involvement of a more primitive melt source.

Zirconium displays a positive linear correlation with silica in the diorites *s.l.* up to the SiO_2 concentrations that characterize the quartz-diorites (around 55 wt%), at which point Zr increases abruptly (Figure VIII-8A); this difference between the two main dioritic suites implies a significantly different chemical evolution. Regardless of absolute concentrations, the ratio between two immobile incompatible elements should remain constant throughout a typical fractionation path, unless a mineral phase preferentially incorporating one element over the other starts to crystallize, assuming a closed system evolution. Hafnium, the "geochemical twin" of Zr due their analogous behavior in geological systems – mainly due to their similarities in ionic radius and electronic charge – displays a positive linear correlation with Zr but variable ratios that deviate from canonical chondritic ratios in each lithology. The Zr/Hf values increase with increasing Zr, ranging from 26.5 to 52.3, showing distinctive median Zr/Hf for diorite (31.3) and quartz-diorite (42.1) samples. A value of 34.2 is typically used as representative of chondritic Zr/Hf ratios (Weyer *et al.*, 2003), meaning that the diorites have sub-chondritic Zr/Hf whereas the quartz-diorites display supra-chondritic Zr/Hf ratios (Figure VIII-8B). Variations in Zr/Hf ratios within the same suite can be explained by metasomatic processes or fractionation of minerals that preferentially incorporate Hf over Zr ($D_{Hf} > D_{Zr}$), for example clinopyroxene, amphibole and titanite (*e.g.,* Linnen & Keppler, 2002). Indeed, Sc, which strongly concentrates in pyroxene, displays a negative correlation with Zr/Hf, suggesting that crystallization of this mineral is possibly related to Zr and Hf fractionation (Figure VIII-8C). Similarly to Zr/Hf relationships, the ratio between Nb and Ta is also often used to infer the evolution of the crust-mantle system (*e.g.,* Weyer *et al.*, 2003). Most diorite samples from Torrão have sub-chondritic Nb/Ta ratios (reference value for chondritic and primitive mantle Nb/Ta is 17.6; Weyer *et al.*, 2002) and show values ranging from 8.5 to 20 (Figure VIII-8D). Contrarily to Zr/Hf relationships, there is no correlation between lithology and Nb/Ta values. It has been shown that Nb/Ta ratios vary greatly in granitic rocks, showing values as low as 4 and as high as 25 (Green, 1995). Significant variation in Nb/Ta may point to crystallization of a mineral phase that preferentially incorporates one element over the other, such as Ti-rich minerals (ilmenite, Ti-magnetite, rutile and titanite) and clinopyroxene (Green, 1995; Weyer *et al.*, 2003). There is a very weak (if any) correlation between Nb/Ta and Sc in the diorites but a moderate one in the quartz-diorites, meaning that in the latter clinopyroxene may have played a significant role in fractionating Nb and Ta (Figure VIII-8E).

---

[12] One high-Ti diorite sample from Caldeira *et al.* (2008) has 220 ppm of Zr.

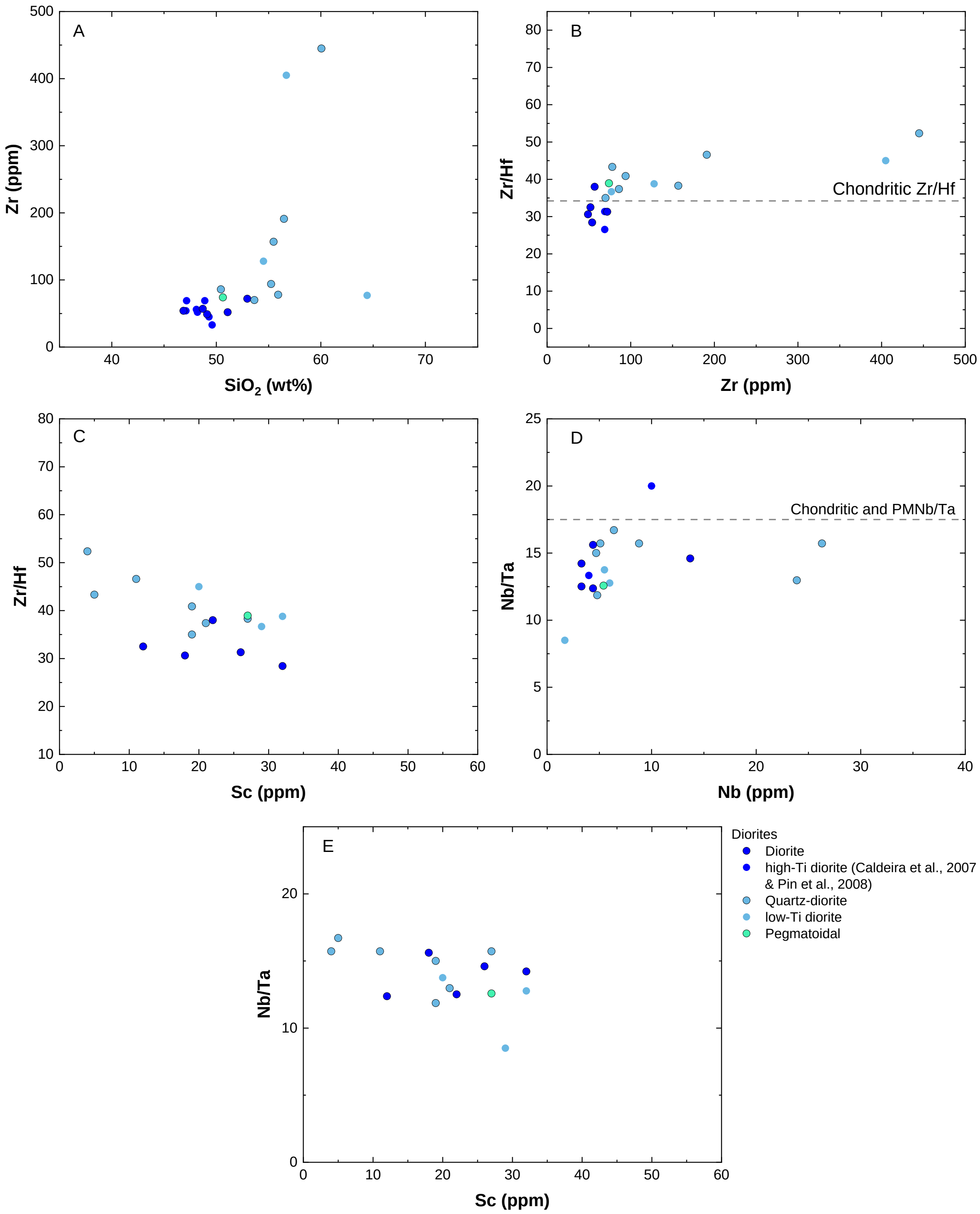

Figure VIII-8. Diagrams of relevant incompatible high field strength elements for dioritic rocks of Torrão and LGS. Some points are not displayed for the high-Ti diorites due to lack of data. (A) Relationship between SiO_2 and Zr, displaying a positive correlation that increases significantly at silica values around 55 wt%. (B) Ratio between Zr and Hf as a function of Zr contents, displaying a positive correlation. Chondritic Zr/Hf reference value from Weyer *et al.* (2003). (C) Negative correlation between Zr/Hf and Sc, suggesting that clinopyroxene crystallization was the main mineral controlling Zr-Hf fractionation. (D) Nb/Ta variation as a function of Nb contents. (E) Weak correlation between Nb/Ta and Sc, meaning that clinopyroxene did not significantly fractionated Nb and Ta.

Except for sample **SEM-TOR-9**, all diorites display broadly parallel patterns on normalized multi-elemental diagrams (Figure VIII-9A). The incompatible elemental signatures for the diorites closely resemble those of the high-Ti diorites in many regards, namely similar LILE enrichments, positive spikes in K and Sr (the latter suggesting minor plagioclase accumulation), and very similar patterns in the La-Ce-Sr-Nd segments. The immobile HFSE Zr, Hf, Ti, Y, Yb and Lu show similar degrees of enrichment and flat patterns. Phosphorus is the most variable element, which is primarily controlled by the modal abundance of apatite in each sample. Sample **SEM-TOR-9** shows a characteristic pattern, being relatively more enriched in Th and U and, unlike other diorite samples, is lacking a trough in Nb and Ta (Figure VIII-9A). Another noteworthy feature is that both leucocratic injections and pegmatoidal domains show normalized patterns that closely match those of the diorites, the only difference being the relatively lower Cs concentrations in the leucocratic injections (Figure VIII-9B). The resemblance in the normalized patterns can be explained by the similar major, minor and accessory mineralogy in these lithologies. In addition, the sulfide-rich injection, despite sharing many similarities in the normalized patterns to the diorites, shows significant enrichments in Th and U and depletion in Rb and Sr, the latter being likely related to the previous fractionation of plagioclase.

The SB II series of the LGS displays normalized incompatible element patterns parallel to those of the diorites (Figure VIII-9C), the major difference between both rock suites is the significant enrichment in mobile LILE Cs and Rb for the diorites. Jesus (2011) had already noticed the similarity in the patterns between the most primitive member of the LGS and the diorites cropping out at Torrão (with data reported in Pin *et al.*, 2008), however, these relied on a limited number of samples and elements.

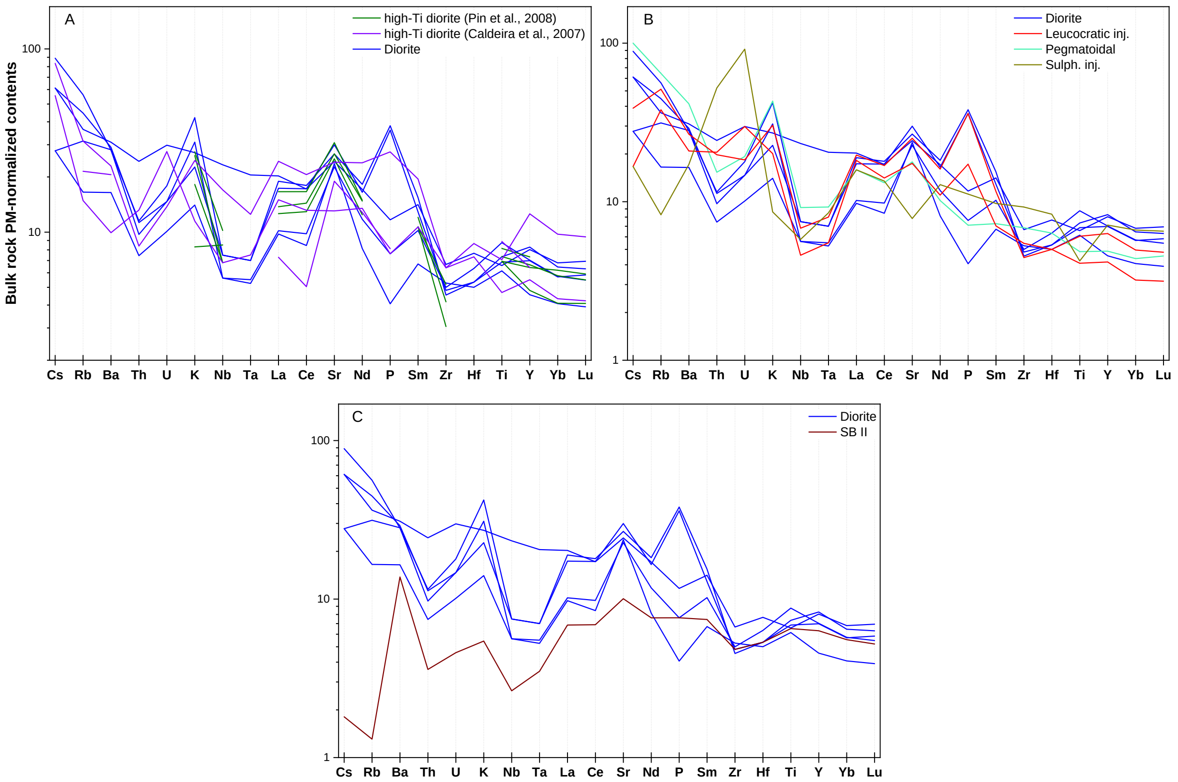

Figure VIII-9. Primitive mantle-normalized incompatible elements for the diorites, high-Ti diorites (Caldeira *et al.*, 2007; Pin *et al.*, 2008), leucocratic injections, pegmatoidal domains and SB II series of the LGS. (A) Comparison between normalized patterns of the diorites and high-Ti diorites; the patterns of both suites are parallel, as noted by Jesus (2011). (B) Normalized patterns between the diorites, leucocratic injections and pegmatoidal domains. (C) Broadly parallel patterns between the diorites and SB II.

The normalized incompatible elemental trends for some quartz-diorite samples are characteristically distinct from those of the diorites, displaying overall higher but more variable bulk enrichments (Figure VIII-10A). Samples **SEM-TOR-12**, **17** and **II2-R3** are significantly more enriched in Th, U, Zr and Hf (*ca.* 5× more enriched for each element). Furthermore, samples **SEM-TOR-12** and **14** display concave patterns in the Nb-Ta-La-Ce segment, which differs significantly from the trough in

Nb-Ta that characterizes most diorite and quartz-diorite samples. Despite these differences, the quartz-diorites display similar degrees of enrichment and normalized patterns that are parallel to the diorites in LILE (Cs, Rb and Ba) and some immobile HFSE (Ti, Y, Yb and Lu). In addition, the most enriched quartz-diorites display normalized patterns comparable to the low-Ti diorites (Figure VIII-10B).

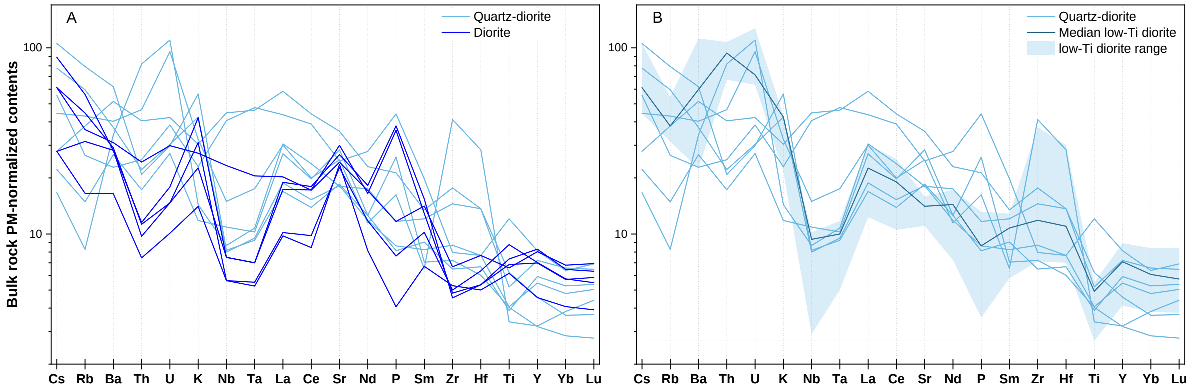

Figure VIII-10. Primitive mantle-normalized incompatible elements for the quartz-diorites, low-Ti diorites and diorites. (A) Comparison between normalized trends of the quartz-diorites and diorites. (B) Normalized trends for the quartz-diorites and low-Ti diorites.

Amphibolites

The fine and coarse-grained amphibolite enclaves display normalized incompatible elemental patterns that, despite being somewhat similar, have fundamental differences in some key elements (Figure VIII-11A). As noted above, because both fine-grained amphibolite samples were collected near each other, their patterns are identical, displaying positive anomalies in Ba and U and slight negative anomalies in Rb, Th and Sr, the latter being indicative of previous fractionation of plagioclase. Furthermore, all REE are enriched relative to LILE and HFSE. The coarse-grained amphibolite enclaves are significantly depleted in Nb and Ta (*ca.* 10× less enriched) relative to the fine-grained amphibolites. Furthermore, the coarser-grained amphibolites show a conspicuous spike in Ba which is also present in the finer-grained variety, albeit to a lesser extent. The immobile HFSE Hf, Ti, Y, Yb and Lu display the same flat segments in both amphibolite types but are more enriched in the finer-grained variety. Finally, the metasomatized amphibolite sample collected near the Beja airport displays similar patterns to those that typify the amphibolite enclaves, the main difference being a slightly more enriched elemental signature in Th and U.

Compared to the metabasalts of the Escoural formation, the fine-grained amphibolites display degrees of enrichment that are in the range of those reported in Chichorro (2006) for every element except Cs, Sr and Ti; the differences, however, are not significant: *ca.* 2× more enriched in the Torrão fine-grained amphibolites for each element (Figure VIII-11B). Notable similarities between the Escoural metabasalts and the amphibolites include the same relatively flat patterns and identical spikes and troughs in the Rb-Ba-Th and Ta-La-Ce-Sr segments. Compared to the median composition of the Escoural metabasalts, the fine-grained amphibolites have similar LILE enrichments and slightly higher HFSE.

The normalized patterns that characterize the coarser-grained amphibolites are comparable to the mafic metavolcanic rocks cropping out near the Odivelas dam (da Silva, 2011; Figure VIII-11C). The patterns are very similar, displaying the same degrees of enrichment for LILE and HFSE across the whole array of elements. The main differences between the Torrão amphibolite enclaves and the Odivelas metavolcanic rocks is a more significant Rb enrichment and Sr depletion in the latter. In addition, one sample from the Odivelas metavolcanics is significantly depleted in Zr compared to other rocks from the same group.

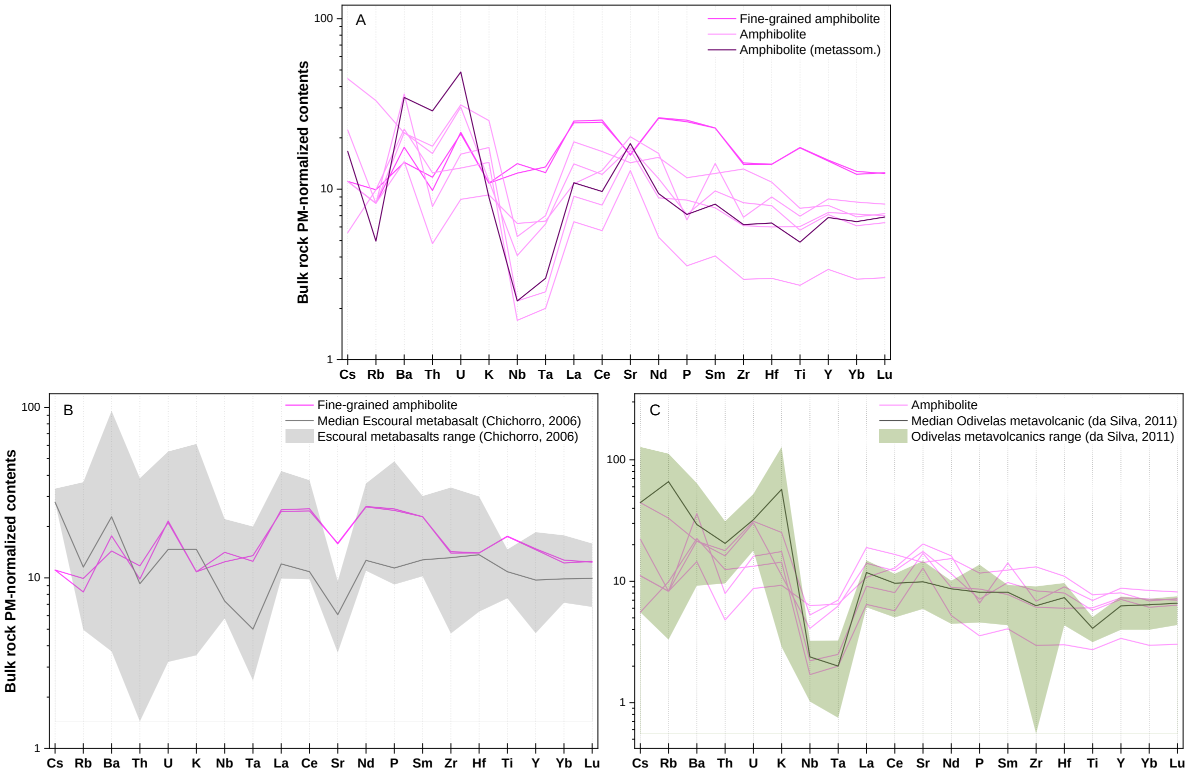

Figure VIII-11. Primitive mantle-normalized incompatible elemental patterns for the amphibolites *s.l.*, metabasalts from the Escoural formation (Chichorro, 2006) and mafic metavolcanic rocks from Odivelas (da Silva, 2011). (A) Comparison between the normalized patterns of the amphibolites and their finer-grained variety. (B) Compositional range and median values of normalized incompatible elements for the Escoural formation metabasalts in comparison to the fine-grained amphibolites. (C) Compositional range and median values of normalized incompatible elements for the Odivelas metabasalts in comparison to the amphibolites.

IX. Intensive variables estimation

The main purpose of this chapter is to draw a connection between the data presented in previous chapters in subsequent interpretation a broader context. Temperature and pressure estimates here presented were obtained based on different closure temperatures for relevant mineral species and whole-rock geochemical data. This approach allows to systematically test and compare different methods. Although there are many different lithologies, special attention will be given to those of unambiguous magmatic (diorites and quartz-diorites) and metamorphic (amphibolites) nature.

Methodology

Amphibole thermometry

A first qualitative approach on the temperature dependence of amphibole composition can be made using its Al^{IV} and Ti contents, A-site occupancy and Mg-number. Aluminum concentrations in the tetrahedral site, Ti contents and A-site occupancy will typically decrease with decreasing crystallization temperature whereas Mg-number increases, contrary to the typical trend of most ferro-magnesian silicate minerals (*e.g.*, Blundy & Holland, 1990). Such behavior can be ascribed to the dependence of Mg-number on oxygen fugacity (fO_2), being higher in more oxidizing conditions (Spear, 1981). As such, based on the median contents of temperature-sensitive variables (see Chapter VII.), amphiboles from the diorites crystallized at higher temperatures relative to those found in the quartz-diorites, in good agreement with the data presented below. In addition, the pegmatoidal domains record the highest-temperature signatures across every variable (*i.e.*, high Al^{IV}, Ti and A-site occupancy).

The coarse-grained, brown amphiboles and the acicular, green amphiboles discussed in Chapter VI. for the diorites and quartz-diorites are not readily discriminated when temperature-sensitive variables are used. Browner colors in amphibole are typically caused by higher concentrations of Ti whereas greener amphiboles have lower concentrations of this element (Deer *et al.*, 2013). Indeed, the brown amphiboles record the highest temperature signatures between the two types, but the difference is not significant: 0.03 a.p.f.u., or 0.7 wt%, between the Ti-richer brown and green amphiboles. Furthermore, there is a gradual shift in composition towards the acicular, green amphiboles. This suggests that the coarse-grained, brown amphiboles represent early formed amphibole which growth was concomitant with a decrease in temperature, gradually evolving in composition and approaching the chemical features that characterize the green amphiboles.

Quantitative temperature estimates based on amphibole-only thermometry were calculated using Equation 8 of the empirical geothermometer reported in Putirka (2016). All amphibole types except those belonging to the Mg-Mn-Fe-Li group fall within the wide recommended compositional range of usage for this thermometer. This calibration has an associated error of ± 47º C and a slight pressure dependency, for which a value of 5 kbar was used based on the average pressure estimates for the LGS (Jesus *et al.*, 2016). Considering the spatial association between the LGS and the Torrão diorites, as well as their similar ages (Pin *et al.*, 1999, 2008), this should be a reasonable assumption.

Pressure estimates relying solely on amphibole composition based on the work of Putirka (2016) are only possible if the melt composition is known. Often, the melt composition is difficult to estimate in plutonic rocks due to their long-lived evolution. Nevertheless, it is possible to test if the bulk-rock composition is an adequate approximation to that of the melt with which amphibole equilibrated, using the Fe-Mg exchange coefficient between amphibole and melt (herein, K_D). Expected K_D values are 0.28±11 in cases where amphibole and liquid are in equilibrium. However, obtained K_D values fall well outside this range, averaging around 0.70 for both the diorites and quartz-diorites, meaning that the bulk-rock composition is a very rough estimate for the liquid composition. As such, no pressure estimates were obtained through amphibole-only methods.

Amphibole-plagioclase thermobarometry

For geothermometry based on amphibole-plagioclase equilibria three methods were tested, namely equations A (Edenite-Tremolite) and B (Edenite-Richterite) from Holland & Blundy (1994) and equation B2 from Molina *et al.* (2021). Only the borders of grains were used when establishing amphibole-plagioclase pairs. These geothermometers are only valid for a set range of temperatures and amphibole-plagioclase pairs which compositions are in line with those used for calibration; such constraints are listed as follows:

1) Eq. A from Holland & Blundy (1994) is calibrated in the T range of 400-900º C for amphiboles that have $Na^A > 0.02$ a.p.f.u., $Al^{VI} < 1.8$ a.p.f.u. and Si in the range of 6.0-7.7 a.p.f.u, and plagioclase with An < 90%. Unlike Eq. B, this equation is not suitable for silica-undersaturated systems;
2) Eq. B from Holland & Blundy (1994) is calibrated in the range of 500-900º C, An contents in plagioclase from 10 to 90%, and amphiboles with $Na^B > 0.03$, $Al^{VI} < 1.8$ a.p.f.u. and Si in the range of 6.0-7.7 a.p.f.u.;
3) Eq. B2 from Molina *et al.* (2021) requires amphibole compositions with Na^B contents between 0.06 and 0.5 a.p.f.u., Ca > 1.2 a.p.f.u. Ti < 0.4 a.p.f.u., K < 0.25 a.p.f.u. and tremolite phase component < 0.34 (see Table 1 of Molina *et al.*, 2021 for the definition of this parameter). The An contents of plagioclase must be > 18% and Or contents < 11%. In addition, accuracy using this method is lower when Na^B in amphibole is constrained to < 0.30 a.p.f.u. and An contents of plagioclase are < 80%.

Temperature estimates obtained from the thermometer of Holland & Blundy (1994) have associated errors of ± 35-40º C, whereas those obtained through the calibration of Molina *et al.* (2021) are around ± 25-30º C. A comparison between the three methods is shown in Supplementary Data 3. The results are relatively similar. Equation A from Holland & Blundy (1994) shows the most variable temperature ranges and medians compared to the other two equations. Equation B2 from Molina *et al.* (2021) shows median temperatures which, although are within error, are systematically higher compared to equation B from Holland & Blundy (1994). Because of the more constrained compositional range and smaller associated error, only the temperature estimates obtained through equation B2 will be considered for discussion purposes.

Median temperatures obtained through the amphibole-only method are *ca.* 30º C higher than those obtained through amphibole-plagioclase for both the diorites and quartz-diorites. Molina *et al.* (2021) reported similar temperature discrepancies between their calibration and others relying on amphibole-only, which were attributed to inaccuracies reported in the amphibole-only expressions.

For pressure estimates based on amphibole-plagioclase equilibria, the geobarometer of Molina *et al.* (2015) was used. This method has a precision of ± 1.5 to 2.3 kbar and a slight dependence on temperature, for which the results obtained beforehand through equation B2 of Molina *et al.* (2021) were used.

Although there are many other amphibole-only geothermobarometers available (*e.g.*, Ridolfi *et al*, 2010; Ridolfi, 2021; Mutch *et al*., 2016), an exhaustive assessment of every method available is beyond the scope of this work. Every method has an associated error within which the temperature estimates from other calibrations are often found, thus providing no additional information except an expression of the different compositional dependencies of each method.

Biotite thermometry

Temperature estimates for biotite-only were obtained following Henry *et al.* (2005). This calibration has an estimated precision ranging from ± 12 to 24º C and can be applied to rocks that equilibrated between 4 and 6 kbar. This is a valid assumption for the considered rock suites, as can be seen from the pressure estimates obtained from amphibole-plagioclase geobarometry (see below) and the average LGS pressure estimates (Jesus *et al.*, 2016). In addition, Ti contents of biotite are constrained to values between 0 and 0.6 a.p.f.u. and Mg-number[13] between *ca.* 0.3 and 1.

Biotite-only geobarometry was tested following the method proposed in Uchida *et al.* (2007). Results obtained through this method yield values that are substantially different from those obtained through amphibole-plagioclase geobarometry, averaging 1.4 kbar. This calibration only considers the total Al content of biotite, meaning that small changes in the Al concentration result in significant temperature differences. As noted in Chapter VII. , the analyzed biotite grains have considerable amounts of Fe in both tetrahedral and octahedral positions, which results in lower total Al contents. This means that there is a significant underestimation of pressure through this method.

Apatite saturation temperature

Unlike the previously mentioned methods, temperature estimates for apatite saturation take the bulk-rock composition into account. For this reason, only one temperature estimate for each sample can be obtained. Apatite saturation temperatures were estimated by deriving the expression found in Harrison & Watson (1984) and solving for temperature. Other methods, such as those proposed by

---

[13] Mg-number in the work of Henry *et al.* (2005) is calculated assuming that all iron is ferrous. As seen in Chapter VII. , this is not a valid assumption for the biotites in question. As such, only Fe^{2+} was used for calculation purposes when using this method.

Pichavant *et al.* (1992) and Bea *et al.* (1992) were not considered because these were calibrated with peraluminous rocks.

A note on biotite-apatite equilibria

Two independent methods were tested for biotite-apatite geothermometry, namely the calibrations proposed by Ludington (1978) and Zhu & Sverjensky (1992). Both methods rely on the F-OH partitioning between coexisting biotite and apatite. Therefore, only biotite analyses with F concentrations above the detection limit were used. As noted by Zhu & Sverjensky (1992), the application of this method in igneous rocks poses some problems, the most important of which being the fact that these two mineral phases can crystallize at different temperatures. Indeed, there is no petrographic evidence that apatite only crystallized simultaneously with biotite, since the former occurs almost exclusively as inclusions in every mineral phase. Nevertheless, both methods were tested. The results show considerable spread on estimated temperatures, which, in a first approach, could simply be the result of the limited number of biotite-apatite pairs. The calibration of Ludington (1978) shows temperatures ranging from 539 to 1039º C for the quartz-diorites. This wide range most likely results from the distinct biotite composition, which shows variable F concentrations (see Chapter VII.). As noted in Ludington (1978), this calibration is very sensitive to changes in the F/OH. Furthermore, the method proposed in this same work for estimating the mole fractions of the endmembers of biotite yields negative values for the annite component. Temperature estimates obtained from the calibration of Zhu & Sverjensky (1992) show a smaller, albeit still very significant, range of temperatures, from 523 to 795º C. A comparison between the two methods is reported in Supplementary Data 3. Given that both methods show temperature ranges too wide to be valid as representative of equilibrium between biotite and apatite, it is likely that: (1) the analyzed biotite has compositions that fall well outside those used for calibration, and/or (2) the analyzed biotite-apatite pairs did not crystallize simultaneously. As such, none of these estimates will be considered.

Magnetite-ilmenite thermometry and oxybarometry

Temperature and oxygen fugacity constraints using magnetite-ilmenite equilibria were retrieved using the QUILF software (Andersen *et al.*, 1993). A median pressure estimate obtained through amphibole-plagioclase equilibria (Molina *et al.*, 2015) was used when determining temperature and oxygen fugacity conditions through this method. Magnetite and ilmenite compositional parameters were determined beforehand in ILMAT (following version 1.20h; Lepage, 2003).

Amphibole hygrometry

Water contents of the melt based on amphibole composition were estimated following Ridolfi *et al.* (2021). This method retrieves H_2O contents in the melt with an associated error of ± 14%. Water contents were estimated only for the diorites because the presence of biotite in the quartz-diorites (which is not accounted for using amphibole-only methods) implies that the water contents of these melts were higher . Furthermore, as will be demonstrated in the following chapter, the quartz-diorite melts have significant contributions of external components which may have added H_2O to the system. Therefore, it is not clear whether none, some, or all amphibole from the quartz-dioritic melts crystallized prior, during or after contamination.

Results

A summary of the obtained temperature and pressure estimates using every method is shown in Table IX-1and in Figure IX-1.

Table IX-1. Temperature estimates obtained using amphibole-only, amphibole-plagioclase equilibria, biotite-only, apatite and magnetite-ilmenite equilibria. [1]Putirka *et al.* (2016); [2]Molina *et al.* (2021); [3]Henry *et al.* (2005); [4]Derived from Harrison & Watson (1984); [5]Andersen *et al.* (1993). *Average is 808º C when considering two outliers which temperature estimates are 648 and 623º C; *[1]Standard deviation is 132º C when considering the outliers; *[2] Median is 850º C when considering the outliers.

	Diorites				Quartz-diorites				Amphibolites			
	Average	Std. Dev.	Median	N	Average	Std. Dev.	Median	N	Average	Std. Dev.	Median	N
Amp-only[1]	831	46	831	42	802	55	798	26	800	26	799	60
Amp-Plg[2]	809	47	813	38	789	44	789	16	798	49	796	45
Bt[3]	-	-	-	-	726	10	725	21	-	-	-	-
Ap saturation[4]	895*	61*[1]	913*[2]	6	863	68	877	6	-	-	-	-
Mgt-Ilm[5]	482	43	489	26	470	47	463	30	-	-	-	-

Apatite saturation temperatures are the highest of all considered calibrations, which is consistent with its occurrence as inclusions in every mineral phase, indicating early crystallization. The temperature estimates obtained from amphibole-plagioclase equilibrium show a positive correlation with the anorthite contents of the plagioclase grain used for each pair. The highest temperature estimates obtained from amphibole-only are associated with the cores of dark-green acicular and brown, coarse-grained amphibole grains. Conversely, the lowest temperature estimates using the same method are associated with interstitial, green amphibole. Biotite temperatures are rather restricted which is likely the result of some bias in the dataset arising from the fact that most biotite analyses were taken on the same sample.

Temperature estimates obtained for the diorites and quartz-diorites indicate cooling conditions ranging from ~830 to 725 ºC. Amphibole-only and amphibole-plagioclase equilibrium temperature estimates for the diorites are generally higher than those obtained for the quartz-diorites. Amphibole-only temperature estimates for the amphibolites are restricted within their 25-75% range. Temperature estimates obtained from magnetite-ilmenite equilibria are the lowest of all mineral systems.

Pressure estimates are broadly similar between the diorites and quartz-diorites, yielding a median value of *ca.* 4.5 kbar. The median pressure estimate for the amphibolites is around 6 kbar, showing a wide pressure range that ranges from *ca*. 8 to 2 kbar, comparable to that obtained for the diorites.

Oxygen fugacity estimates were normalized to the Fayalite-Magnetite-Quartz buffer ($\Delta FMQ \equiv \Delta \log(fO_2)_{FMQ} = \log(fO_2)_{sample} - \log(fO_2)_{FMQ}$). Estimated fO_2 values range from +0.63 to +7.46 ΔFMQ at the median temperature estimated through this method (*ca.* 450 ºC). It is worth noting, however, that the obtained T-fO_2 curve follows the ilmenite isopleths which, contrary to petrographic observations, suggests that ilmenite is considerably more abundant (> 90% modal abundance) than magnetite (Frost *et al.*, 1988).

Median water contents of the diorite melts were estimated to be about 6 wt%.

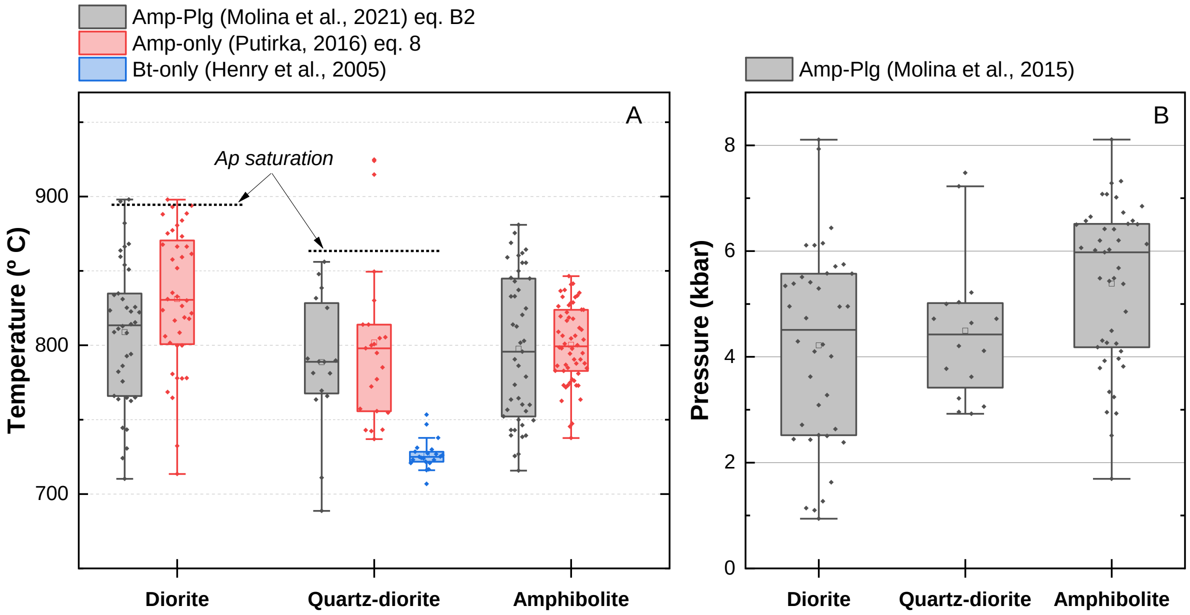

Figure IX-1. Temperature and pressure estimation for the examined rock types in a box chart diagram. Individual points represent each mineral or pair of minerals, box range is 25-75%, the small square represents the mean value and the line shows the median. (A) Temperature estimates obtained based on amphibole-plagioclase equilibria (Molina *et al.*, 2021), amphibole-only (Putirka, 2016) and biotite-only (Henry *et al.* 2005) calibrations. (B) Pressure estimations obtained through amphibole-plagioclase equilibria (Molina *et al.*, 2015).

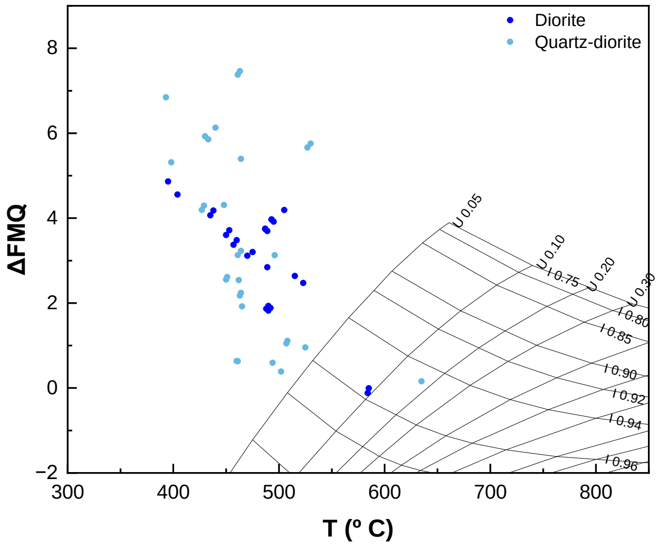

Figure IX-2. T-*f*O2 cross-plot for magnetite-ilmenite pairs, obtained using the QUILF software (Andersen *et al.*, 1993). Magnetite (U = Usp) and ilmenite (I = Ilm) isopleths were constructed by letting QUILF run through the idealized pairs of coexisting oxides at the pressure of interest (4500 bar, as estimated by amphibole-plagioclase geobarometry). The trend closely follows the ilmenite isopleth of I = 0.96.

X. Discussion

The following discussion seeks to answer the questions encompassed in this work's main objectives by compiling and interpreting previously reported data. A few notes regarding field and microscopic observations are first considered. Following these considerations, the magmatic processes and conditions that generated the Torrão dioritic suite will be discussed at a local scale, with emphasis on the generation of the quartz-diorites, and at a regional scale, seeking for contributions to the understanding of processes that might relate diorites to the LGS.

Implications from field and petrographic data

Field considerations

Most contacts between diorites and quartz-diorites take place via faults, shear zones and other minor structural rearrangements. Assuming that both dioritic lithologies are genetically related, their prevalent tectonic contacts must bear some petrogenetic significance on the timing of the intrusion and the development of both lithologies. Their field relationships can be interpreted as the result of either a gradual magmatic event that was structurally reworked after cooling, or a two-stage magmatic event with the (semi-) discreet development of diorites and quartz-diorites. The occasional occurrence of diorite ‘lenses’ within the quartz-diorites supports the first scenario.

The pegmatoidal domains are frequently found within the dioritic rocks, suggesting that these should derive from the same source of the diorites. Conversely, the leucocratic injections are found in close spatial association with the fine-grained amphibolite enclaves, implying that the genesis of these injections is dependent on the interaction between the dioritic melts and amphibolite rocks. These hypotheses will be explored in more detail below.

The most prominent feature of the exposures at Torrão is the abundance of amphibolite enclaves found within the dioritic rocks. Their occurrence as heterometric, blocky fragments is taken as evidence of the activity of a once dynamic magmatic environment that evolved under open system conditions. Medium-sized volumes where dense enclave swarms occur (the ‘enclave-rich diorites’) are interpreted to represent strong magmatic flow currents, analogous to convection currents, possibly close to the feeding zones of the magma chamber. Perhaps the most important question that arises from these observations and interpretations is whether other lithologies that form the Évora-Beja-Aracena Domain Neoproterozoic to Devonian sequences could have been involved in this magmatic event. The absence of enclaves corresponding to these other lithologies can be explained by their total digestion, considering the melting temperature of these rock types, which is well below those required by amphibolites. The following section will mainly explore the processes through which the Torrão dioritic rocks (and other diorite suites) may have formed, with particular emphasis being given to contamination/assimilation and fractional crystallization. As such, the following considerations must be kept in mind, namely:

i) The crustal arrangement at the depth of emplacement. Considering the protracted geological history of the host rocks (*ca.* 300 Ma, ranging from the Neoproterozoic to Devonian) and the fact that this evolution was subjected to various tectonic events, it is expectable that the stratigraphic sequence that hosted the intrusion may not follow the typical oldest at the bottom, newest at the top order. Indeed, the OMZ basement (*i.e.*, excluding Variscan magmatic bodies) is intensely folded and several thrust systems are identified (*e.g.*, Araújo *et al.*, 2006); in some sectors thick tectonic stackings developed and were displaced by regional shear zones. In addition, these geological units have lateral variations, contributing to the complexity of their spatial arrangement.

ii) Post-magmatic structural displacements. Many of the contacts between the BIC gabbros and diorites are made through WNW-ESE to E-W left-lateral shear zones. It is possible that the Torrão diorites (and other units within the BIC) are no longer in their original position, having been displaced to the West. Therefore, the country-rocks with which the diorite magmas may have interacted are not restricted to those exposed in the proximity of Torrão.

iii) The absence of good and continuous exposures throughout the Alentejo peneplain. The current understanding about some of the metasedimentary and metavolcanic sequences that form the OMZ basement as well as their inferred extent and contacts with other units is often extrapolated from sequences in other sectors.

iv) Scarcity of data. The available geochemical, petrographic or isotopic data for most formations or units in the EBAD is severely limited; this fact is in part a direct consequence of the previous point.

All the above considerations converge towards the controversy related to any event that involved the Cadomian and Variscan sequences forming the OMZ. As such, interpretations regarding the dioritic suites are affected by considerable uncertainty if all the possible scenarios are not considered.

Petrographic data

The mineral assemblage that characterizes the examined diorite and quartz-diorite samples shows a gradual increase in the modal abundance of quartz, biotite and zircon. This mineralogical variation further supports the scenario postulated above where the diorites and quartz-diorites document a gradual magmatic evolution, rather than a discreet two-stage magmatic event. Significantly, the petrographic characteristics described in Chapter VI. for the digested gabbroic samples (**SEM-TOR-8** and **9**), *e.g.*, their mineral assemblage and bent plagioclase crystals with mechanical wedge twinning, are very similar to those described for the rocks of the SB II series (Jesus, 2011). The gabbroic enclaves can, however, also correspond to deformed metagabbros, such as those forming the tectonic slivers of the Beja-Acebuches Ophiolite Complex (Pin *et al.*, 2008), or other deep gabbroic cumulates. Unfortunately, it was not possible to process the gabbroic part of this sample for bulk geochemical analysis and, therefore, its correlation to other units remains unclear. Considering the timing of the Torrão intrusion (at *ca.* 350 Ma), these plagioclase crystals were likely deformed before D_2 (which is synchronous with the LGS and Torrão magmatic events), meaning that their deformation occurred during or before the subduction-related deformation phase, D_1.

Some petrographic features related to late alteration processes, such as variable degrees of plagioclase saussuritization and amphibole chloritization when no (chlorite- and/or carbonate-rich) veinlets are present, are interpreted to have resulted from auto-metamorphic processes, *i.e.*, alteration that was promoted by the exsolution of volatiles from the melt during cooling. This is a reasonable assumption since the magma related to these diorites had, at the very least, moderate amounts of water – as evidenced by the abundance of amphibole. Nevertheless, the pervasive nature of carbonate-rich mineral veinlets and ‘pockets’ (calcite/carbonate aggregates, epidote and prehnite) likely reflects the effect of late external, moderately significant aqueous-carbonic fluids in Torrão.

The alteration and digestion state in which the amphibolite enclaves are found is a fundamental feature to understand their relationship with the dioritic rocks. The original mineral assemblages and textures of the fine-grained amphibolites are well-preserved, indicating that assimilation of this lithology was likely negligible, probably due to thermal constraints. Conversely, the coarser-grained amphibolite enclaves show variable degrees of digestion. This may have been locally promoted by temperature and/or chemical gradients, meaning that this amphibolite type could have been assimilated by the dioritic melts and compositionally modified them.

Temperature, pressure and oxygen fugacity constraints

Assuming a 1 kbar/3 km barometric gradient, the geobarometric constraints obtained for the diorites and quartz-diorites (X = 4.5 kbar) place the Torrão magmatic chamber at *ca.* 13.5 km depth. These estimates are identical to those reported for the LGS (Jesus *et al.*, 2016). The highest barometric estimates for diorites and quartz-diorites (from 6 to 8 kbar, corresponding to *ca.* 18-24 km depth) are related to the coarse-grained brown amphiboles, meaning that these could represent primocrysts grown at depth in an earlier magmatic evolution stage. Significantly, the Fe-Mg coefficient exchange values of the coarse-grained brown amphiboles are not different from those obtained for the “normal” green amphibole grains within the same thin section. This implies that the melt with which the coarse-grained brown amphiboles equilibrated was not significantly different from later derived liquids from which the green amphiboles crystallized, at least regarding the proportions between Fe and Mg. The estimated pressure range obtained for quartz-diorite samples is significantly lower than that of the diorites. Considering the number of amphibole-plagioclase pairs used for this estimation ($N_{diorites} = 38$, $N_{qz\text{-}diorites} = 16$), it is conceivable that the restricted range of pressure estimates for quartz-diorites results from a bias in dataset. However, this difference in the pressure range can also be explained by faster cooling of the quartz-diorites, which limited the degree to which amphibole and plagioclase could have re-equilibrated. The coarse and fine-grained amphibolite enclaves show pressure estimates ranging from ~1.7 to 8 kbar. Due to metamorphic nature of this rock type, the meaning behind the wide pressure range is difficult to ascribe to a single process; metamorphism of the mafic protolith and/or chemical re-equilibration with the dioritic melts are the most likely causes. According to the magnetotelluric survey carried out by Muñoz *et al.* (2008) and assuming a median 13.5 km depth for the primary locus of magma emplacement, the magmas that originated the dioritic rocks were emplaced and evolved onto a metasedimentary pile that extends to *ca.* 20 km depth. This metasedimentary pile, that in some sections was potentially enriched in metavolcanic rocks, is underlain by a granulitic basement which upper portion corresponds to the Iberian Reflective Body, at *ca.* 20 km depth (Simancas *et al.*, 2003).

Cooling temperatures of ~800-750 ºC obtained for the diorites are considerably above the regional thermal peak (*ca.* 500-700 ºC) and explain the lack of metamorphic imprint in the Torrão dioritic rocks. The wide range of temperatures obtained from amphibole-plagioclase equilibrium reflects the variable anorthite content in plagioclase and/or variations in amphibole composition. The temperature range obtained for the quartz-diorites and amphibolites through amphibole-only is rather restricted. The narrow range of temperature estimates obtained for the quartz-diorites are likely related to a shorter-lived cooling episode, whereas for the amphibolites it may be explained by chemical re-equilibration during melt-enclave interaction.

High fO_2 estimates (reaching as high as +7.5 ΔFMQ) at low temperature conditions retrieved from magnetite-ilmenite equilibrium fall outside the calibrated range (Scaillet & Evans, 1999). The same authors determined that for oxygen fugacity conditions > +1.5 ΔNNO (for reference, the oxygen fugacity values here obtained correspond to ~+6.5 ΔNNO), the values should be corrected to be about 1 log unit below the estimation. Nevertheless, the oxygen fugacity values remain high when applying a similar correction. Both temperature and oxygen fugacity values obtained through this method likely indicate extensive *sub-solidus* re-equilibration of H_2O-rich magmas which may increase fO_2 by liberation of free O_2 during amphibole crystallization (Mason, 1978).

Petrogenesis of low-Ti diorites and minor lithologies

The diorites and quartz-diorites show many similarities in their normalized incompatible elemental patterns and display overlapping Zr/Hf ratio values, as well as identical mineral compositions. Together with their spatial association, these features are taken as evidence that the diorites and quartz-diorites derived from the same magmatic source. The smooth major element trends displayed by the diorites and quartz-diorites with increasing silica could suggest that these rocks are linked by simple crystal fractionation. Indeed, except for K_2O, which variation can be related to late metasomatic processes, all the remaining elements show a behavior compatible with the fractionation of ferro-magnesian silicates and Fe-Ti oxide minerals, *i.e.*, increasing SiO_2 and Na_2O, and decreasing $Fe_2O_3^T$, MgO, TiO_2 and CaO. However, LREE fractionation over HREE and conspicuous elemental enrichments in Th, U, Zr and Hf in the quartz-diorites suggest that these rocks cannot be linked to the diorites by simple crystal fractionation and that an external component must be involved in their genesis. It should be noted that, although apatite may fractionate LREE over HREE, its presence as an accessory mineral phase and the systematically similar modal abundances in both lithologies suggest that accumulation of this phosphate phase should not be the main cause for the REE patterns that characterize the quartz-diorites. Decisively, the quartz-diorites have higher Mg-number and Cr and Ni contents relative to the diorites, indicating that they derive from a more primitive magma source; this directly implies that the quartz-diorites cannot represent melts derived from those that crystallized the diorites by fractional crystallization. If both diorites lithologies originated from the same magmatic source, this means that the quartz-diorites likely correspond to an earlier and more primitive magma batch that was significantly contaminated upon emplacement, whereas the diorites are associated with later emplaced, more evolved but less contaminated magmas. Compiled isotopic data reported in Jesus *et al.* (2016) shows that, compared to the high-Ti diorites, the low-Ti diorites (compositionally analogous to the quartz-diorites) have higher $^{87}Sr/^{86}Sr_{350Ma}$ ratios at similar εNd_{350Ma}, thus further supporting a scenario where the external addition of crustal components played a significant role. In addition, repeated assimilation by magmas can account for the variably zone plagioclase crystals. Similar ideas regarding the genesis of the low-Ti diorites were already proposed by Jesus *et al.* (2016) but relied on a limited dataset. Due to their similar compositional characteristics, from here onwards the petrogenetic discussion regarding the quartz-diorites and diorites will be expanded to the low-Ti and high-Ti diorites, respectively.

To test the feasibility of assimilation processes playing a fundamental role on the genesis of the low-Ti diorites, simple mixing simulations were performed using the SB II gabbronorite as the starting composition. Binary mixing models can be described as purely theoretical, meaning that they simulate ideal ‘endmember’ processes which are rarely observed in nature. However, the process of assimilation can be compared to magma mixing processes where reactions between hot magma and wall-rock can generate a partial melt (depending on the *solidus* temperature of the wall-rock) which is mixed with the more primitive magma. In addition, this simulation assumes that the uncontaminated low-Ti diorites can be represented by the SB II melts. Note, however, that perhaps a more correct way of expressing the uncontaminated low-Ti diorites melts would be a hydrous and possibly more evolved SB II-like gabbroic/dioritic magma. The reasoning behind this is that both uncontaminated and contaminated dioritic facies are spatially associated, which, together with deep (*ca.* 24 km depth) geobarometric estimates for amphibole, suggests that these magmas were already hydrated, or dioritic, prior to emplacement and contamination at *ca.* 13.5 km depth. Because of this conceptual difference, Assimilation-Fractional Crystallization models (AFC; DePaolo, 1981) were not considered here but will be explored further below. Finally, the processes through which H_2O enrichment was attained warrant further explanation which will be provided below when addressing the petrogenesis of the high-Ti diorites.

The choice for crustal representative contaminants was primarily performed by assessing the main compositional differences between the SB II (and by compositional analogy, the high-Ti diorites) and low-Ti diorites. The SiO_2, Th, U, Zr and Hf enriched character of the low-Ti diorites strongly suggests that siliciclastic and/or felsic metaigneous rocks were the main contaminants. However, other rock types must also be considered due to the possible tectonic dismembered structural arrangement at the depth of emplacement and the fact that those lithologies are spatially associated with other rock types. Meta-greywacke, quartz-phyllite and paragneiss samples from the Série Negra and Lower Cambrian sequences, as well as samples from the Moura Schists unit, reported in Chichorro (2006), were chosen to represent siliciclastic rocks. Felsic metaigneous rock samples (orthogneisses) exposed at Santiago do Escoural, reported in Chichorro (2006), were selected as representative of this rock type. In addition, the Torrão coarse-grained amphibolites as well as the Odivelas metavolcanics (da Silva, 2011) were used to represent meta-igneous mafic rocks. Finally, because these lithologies are often spatially associated with carbonate rocks of Lower Cambrian age, the marble sample collected at Trigaches (near the Beja airport) was also considered. The contribution of siliciclastic, felsic metaigneous, mafic meta-igneous and carbonate rocks to the final contaminant were distributed according to proportions of 35/35/15/15, respectively, using the median composition of each rock type.

The proportions of each rock type in the contaminant can be somewhat arbitrary. Of course, as argued above, the siliciclastic/felsic metaigneous component will have to be the most significant because it is required to explain most of the essential compositional features. However, assessing the realistic proportions of the remaining rock types is difficult because of the considerations listed above. Nevertheless, it is beyond the scope of this work to determine the effects of small adjustments to each component and, as such, the proportions used for each rock type were primarily determined to ensure that their assimilation played a role in the final composition (*i.e.*, the best simulated approach to a compositional match). Figure X-1 and Figure X-2 show the result of this binary mixing as an analogy for assimilation for major and trace elements, respectively, following Equation X-1:

Equation X-1

$$C_m = X(C_a - C_b) + C_b$$

where C_a, C_b and C_m are the concentration of an element in magma a, b and in the magma resulting from magma mixing, respectively, and X is the degree of mixing; when $X = 1$ there is no mixing and when $X = 0$ there is complete mixing and the resulting magma composition equals that of the contaminant (this is the case because C_a was chosen as the starting composition and C_b the contaminant).

Table X-1. Mixing results using the SB II gabbronorite as the starting composition and a rock mixture comprising siliciclastic, felsic and mafic meta-igneous rocks in proportions of 40/20/20, respectively, for all major elements at mixing degrees $X = 0.65$. Elemental oxide values are given in wt%. The difference refers to the absolute deviation between the result of mixing and the median low-Ti diorite composition (N = 10).

	SiO_2	**Al_2O_3**	**$Fe_2O_3^T$**	**MnO**	**MgO**	**CaO**	**Na_2O**	**K_2O**	**TiO_2**	**P_2O_5**
Starting comp.	49.82	17.38	9.56	0.16	6.99	12.06	2.63	0.17	1.39	0.15
Contaminant	66.99	14.83	4.69	0.05	1.60	1.87	3.28	3.21	0.57	0.11
Result	55.83	16.49	7.85	0.12	5.10	8.49	2.86	1.23	1.10	0.14
Difference	0.13	1.39	0.58	0.02	0.65	1.80	1.37	0.25	0.14	0.11

For the major element simulation, the marble composition was not considered because this sample was only analyzed for trace elements. The proportions of siliciclastic, felsic meta-igneous and mafic meta-igneous rocks were accordingly adjusted to 40/40/20, respectively. In spite of this, the results show that ~30-40% mixing of SB II magmas with diverse rock types can explain some of the major element features of the low-Ti diorites (Figure X-1; Table X-1). $Fe_2O_3^T$, MnO, TiO_2 and, significantly, SiO_2 contents correlate well to those of the low-Ti diorites at moderate mixing degrees. However, Al_2O_3, Na_2O and CaO concentrations of the mixing line show considerable differences compared to the low-Ti diorites. Such differences suggest that the low-Ti diorites magmas were compositionally distinct from those represented by the SB II prior to crustal contamination, suggesting fractionation of ferro-magnesian silicates by the precursor gabbroic magmas. A noteworthy feature is that the Mg-number of the binary mixing model (Mg-number = 56) is within the range of the low-Ti diorites.

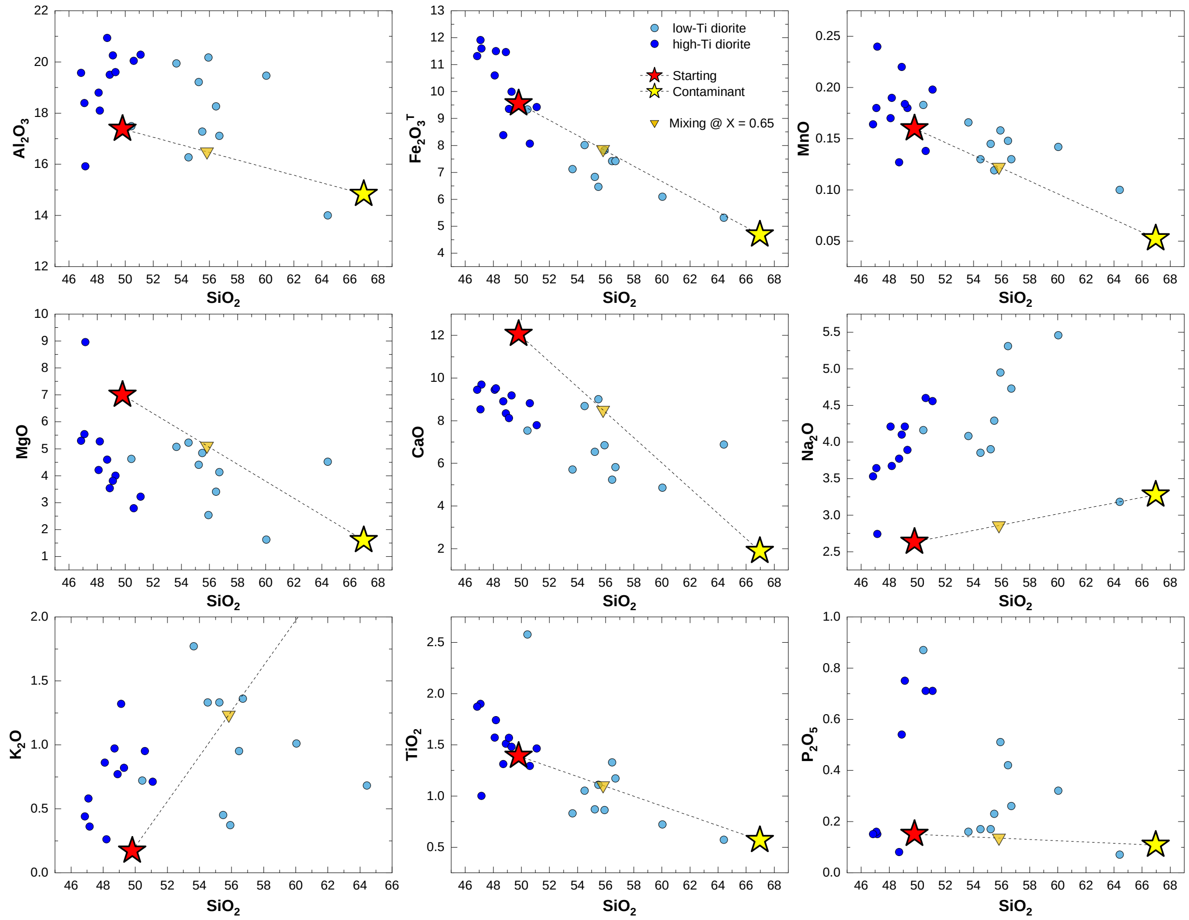

Figure X-1. Mixing simulation of melts represented by the SB II gabbronorite with siliciclastic, felsic and mafic meta-igneous rocks in proportions of 40/20/20, respectively, for all major elements. High-Ti diorite samples are shown for reference. Oxide values are in wt% (not shown to avoid visual clutter).

The multi-elemental incompatible patterns are much more sensitive to the contaminant composition. Mixing SB II magmas with the rock mixture described above (now, also considering the marble sample) is a viable way to obtain the LREE fractionation over HREE pattern that characterized the low-Ti diorites (Figure X-2). Nonetheless, the low-Ti diorites display steeper REE patterns, possibly indicating a larger contribution of carbonate rocks, which are significantly REE depleted and show high fractionation of LREE over HREE. Regarding extended incompatible elements, as suggested above, the addition of a crustal component seems required to obtain some of the fundamental compositional features of the low-Ti diorites, namely their enrichments in Zr, Hf, U and Th. Accordingly, the mixing simulation accurately predicts the incompatible elemental trends that characterize the low-Ti diorites (Figure X-2).

It should be noted that the required degree of assimilation (here represented as magma mixing) for both major and trace elements is relatively high (> 30%). Under typical circumstances involving hydrous intermediate magmas, such high amounts of assimilation would not be possible, especially when assuming that the contaminant rocks were completely digested. A way to circumvent this problem is via partial melting of the country-rocks, which would require significantly lower degrees of melting to attain the same degree of enrichment in several incompatible elements. However, this process requires knowing the mineral assemblage of the contaminant rocks, which is not always available for the considered rocks. For this reason, no geochemical simulations were performed using this method, but it likely represents a more realistic scenario relative to one where the contaminants were fully digested. Furthermore, continuous fractionation of uncontaminated low-Ti dioritic melts could have raised the temperature by latent heat of crystallization, hence promoting partial melting of country rocks.

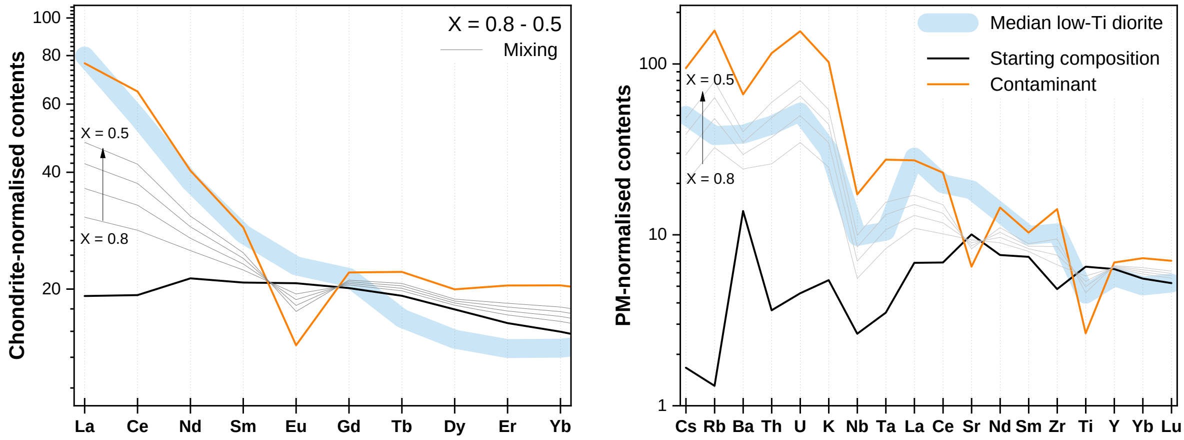

Figure X-2. Mixing simulation of melts represented by the SB II with siliciclastic, felsic meta-igneous, mafic meta-igneous and marble rocks in proportions of 35/35/15/15, respectively, for REE and selected incompatible elements, at mixing degrees of 0.5, 0.6, 0.7 and 0.8. Not every REE and incompatible element of those shown in previous chapters is shown due to insufficient data.

The main take-away note from these mixing simulations is that crustal contributions are necessary in order to generate the low-Ti diorites. However, the total digestion and assimilation of the contaminants by hydrous SB II-like magmas implied by binary mixing simulations is unlikely. Furthermore, differences in Al_2O_3, Na_2O, CaO and other elements warrant further explanation and suggest that the uncontaminated low-Ti diorite melts were probably more evolved than those represented by the SB II gabbronorite. Also, the increasing co-variation of Na_2O and SiO_2 suggests a more significant contribution of felsic meta-igneous rocks or other contaminants which are not accounted for. In fact, rising the proportions of felsic meta-igneous component would fail to replicate some of the other compositional features of the low-Ti diorites. The good agreement between the predicted Mg-number and those of the low-Ti diorites suggest that this compositional feature was attained during assimilation/contamination. Similarly, the predicted ‘low’ TiO_2 contents of the mixing model also suggest that this essential compositional feature was likely acquired during contamination of hydrated gabbroic melts.

The main compositional characteristics of the low-Ti diorites, *i.e.*, high SiO_2, LILE, LREE and Mg-number, as well as low TiO_2 and HREE, are fundamental features shared by high-Mg (Mg-number > 0.5) andesites, which are commonly found in continental arcs (Kelemen *et al.*, 2003). There are several processes that may explain the genesis of high-Mg andesites, among which the reaction of partial melts of eclogite/granulite-facies sediments and/or basalt with the overlying mantle-wedge is the most plausible one (Kelemen *et al.*, 2003). It has been shown that crustal contamination was likely the most relevant process in determining the main compositional features of the low-Ti diorites. Despite showing LREE fractionation over HREE, the low-Ti diorites have low to intermediate (~1-1.3) chondrite-normalized Dy/Yb values relative to those displayed by primary[14] high-Mg andesites (1-4; Kelemen *et al.*, 2003), meaning that melting of a garnet-bearing source can be excluded as the cause for the negatively sloping REE patterns of the low-Ti diorites. Furthermore, even if the low-Ti diorites represent primary partial melts, the source could not have been plagioclase-poor (such as eclogite facies rocks) due to intermediate Sr/Nd values (X = 23.3 compared to values > 100 shown by high-Mg andesites; Figure X-3). Other studies have shown that it is possible to yield high-Mg signatures by contamination of dioritic *s.l.* magmas (*e.g.*, Barnes *et al.*, 2004; Qian & Hermann, 2010).

---

[14] Following the definition of Kelemen *et al.* (2003), ‘primary’ refers to magmas and/or melts derived by melting a specific, homogeneous source.

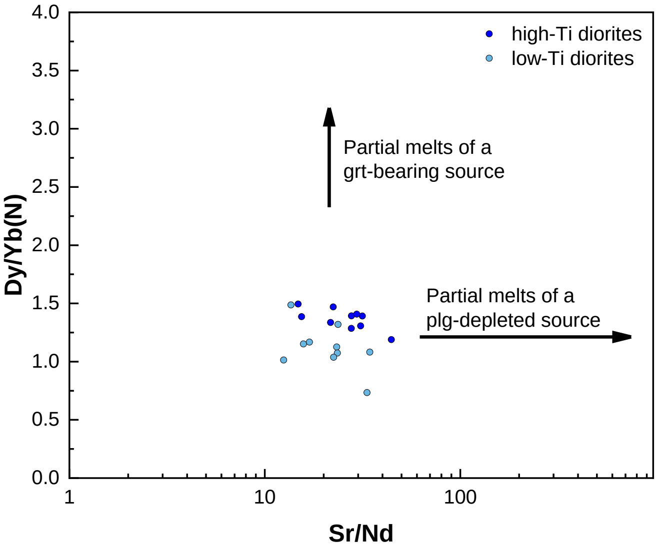

Figure X-3. Cross-plot of Sr/Nd contents *vs.* normalized Dy/Yb for the high-Ti and low-Ti diorites. Partial melts of a garnet-bearing source will tend to higher Dy/Yb values because HREE (in this case, Yb) behave as compatible elements in the presence of garnet. Likewise, partial melts of a plagioclase depleted source will generate partial melts with high (*ca.* > 100) Sr/Nd ratio values because Sr behaves as an incompatible element in the absence of plagioclase.

Considering the abundance of H_2O-rich mineral phases in siliciclastic rocks, mainly mica, the assimilation and dehydration melting of these rocks could efficiently increase the amount of water available in the system. Amphibole is abundant in both high-Ti and low-Ti diorites, however, biotite contains higher molar contents of water relative to amphibole and is only present in the more silica-enriched and contaminated rocks, *i.e.*, the low-Ti diorites. This is in good agreement with the lower crystallization temperature estimates obtained for the low-Ti diorites, which result from increased P_{H2O} (Winter, 2014).

The low-Ti diorites likely represent variably contaminated hydrous melts similar to the SB II instead of primary high-Mg magmas derived from partial melting of deep crustal sources, as many other diorites with similar composition (*e.g.*, Kelemen *et al.*, 2003). Despite the uncertainties regarding crustal contaminants, the results here presented are consistent with field, petrographic and mineral chemistry data. Assimilation of rocks compositionally identical to those used in numerical simulations of mixing with dioritic melts is therefore a plausible process to explain some of the fundamental compositional features displayed by the low-Ti diorites. Nevertheless, other processes not predictable under a simple mixing model might have played a significant role in determining the composition of the low-Ti diorites.

Minor rock types

As noted in Chapter VIII. , pegmatoidal, leucocratic and sulfide-rich rocks display normalized REE and selected incompatible elemental trends that are parallel to those of the diorites, meaning that they likely derive from a common magmatic source.

The occurrence of pegmatoidal domains within the diorites suggests that their coarse-grained textures should not be the result of slow cooling rates, which would affect their surroundings. The presence of an H_2O-rich phase allows chemical species to migrate readily, favoring the rapid growth of mineral phases (Winter, 2014). The prevalence of hydrous minerals in the dioritic rocks suggests that significant quantities of water existed in the magma chamber and, therefore, separation of an H_2O-rich phase might have been possible. Dynamic and turbulent magmatic could promote the exsolution of H_2O-rich melts, as evidenced by the abundance of pegmatoidal domains in 'enclave-swarm' zones. Finally, the lack of elemental enrichments in U, Th, Zr and Hf, as well as LILE, typically concentrated in fluid phases, implies that the pegmatoidal domains did not form by assimilation of country-rocks.

Despite being spatially associated with the fine-grained amphibolite enclaves, the leucocratic injections do not show evidence of contamination by this rock type. This is consistent with the well-preserved nature of the fine-grained amphibolite enclaves where only their rims show evidence of digestion. In addition, the sharp (macroscopic) contacts they establish with leucocratic injections further suggest that this lithology was not significantly digested and assimilated. Like the pegmatoidal domains, the leucocratic injections may have been formed by increased activity of H_2O, as suggested by common abundance of coarse-grained amphibole crystals.

The sulfide-rich injection shows a unique composition mainly due to its high sulfur contents and evidence of external contributions, emphasized by spikes in Th and U contents. Considering the similar REE and incompatible elemental patterns, the sulfide-rich injection likely derives from a source like the diorites. However, compared to the sulfide-rich injection, the diorites are notably S-poor. Therefore, external addition of sulfur is required to generate this lithology. A metasedimentary siliciclastic contaminant could have supplied the necessary sulfur, silica and Th and U contents that characterize the sulfide-rich injection. The fine-grained amphibolite enclaves have considerable amounts of sulfides, and their partial melting could have also supplied the required sulfur but not the measured Th and U contents.

Petrogenesis of high-Ti diorites

The Torrão high-Ti diorites represent the least contaminated rocks in the dioritic suite. Their LILE enrichments and Nb and Ta anomalies are indicative of crustal contamination and/or post-subduction magmatic processes, in good agreement with the inferred geodynamic setting of the Beja Igneous Complex. The sub-parallel normalized incompatible element patterns between SB II and the Torrão diorites strongly suggests that these two suites are cogenetic. Consequently, the ratio between most of the incompatible elements is identical, as is the case of the Zr/Hf ratio in Figure X-4, which also includes the expanded LGS and ATT suite dataset for LGS provided in Jesus (2011) and Jesus *et al.* (2016).

The absence of significant enrichments in elements 'proxy' of crustal contamination, such as Th, U, Zr, Hf and LREE, implies that assimilation did not play a significant role in the genesis of the high-Ti diorites, unlike their low-Ti counterpart. Major element trends for high-Ti diorites and SB II are also relatively similar, differing in the higher MgO and CaO contents and lower Al_2O_3 and Na_2O in SB II. The LILE enrichment in the high-Ti diorites relative to the SB II does not require crustal assimilation since these elements are mobile and can concentrate in residual, hydrous silicate melts. These features suggest that the high-Ti diorites derive from the SB II gabbroic melts by fractional crystallization in near closed-system conditions. The conspicuous Sr enrichments in the high-Ti diorites (~500 ppm) and lack of significant Eu anomalies imply that the initial gabbroic *s.l.* melts did not fractionate significant amounts of plagioclase. Suppressing crystallization of plagioclase explains the higher Al_2O_3 and Na_2O contents of the high-Ti diorites. The relationship of MgO with Zr/Hf and Sc (negative with Zr/Hf and positive with Sc) strongly suggest that pyroxene was the main fractionating mineral phase (Figure X-5). Furthermore, the lower Ni and Cr contents of the high-Ti diorites relative to SB II, suggest that, in addition to clinopyroxene, olivine could also have fractionated in relevant proportions. Following the same reasoning, small quantities of spinel must also have fractionated in order to 'control' the degree of Ti enrichment in derived melts.

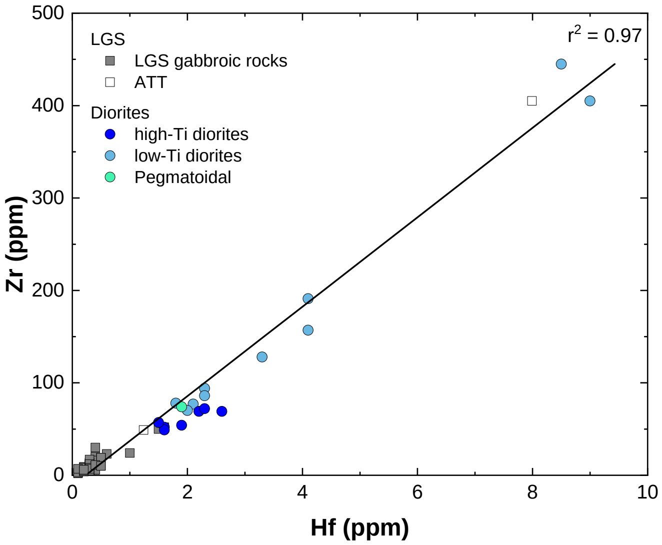

Figure X-4. Correlation between Hf and Zr for every sample from the LGS, ATT and Torrão dioritic rocks. Data from this work, Jesus (2011), Jesus *et al.* (2014, 2016), Caldeira *et al.* (2007) and Pin *et al.* (2008).

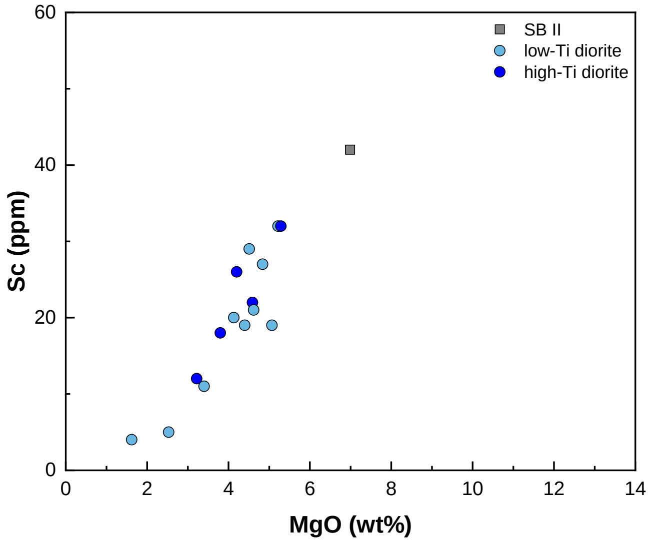

Figure X-5. Positive correlation between MgO and Sc contents for the SB II and high-Ti diorites (low-Ti diorites shown for reference), suggesting that pyroxene was the main fractionated mineral phase, assuming a fractional crystallization relationship between the SB II gabbronorite and high-Ti diorites.

Geochemical modelling based on thermodynamic calculations is precluded by the absence of algorithms suitable for hydrous melts. One such example is the MELTS algorithm (Gualda *et al.*, 2012), which, as stated on the MELTS homepage (https://melts.ofm-research.org), "[is not] suitable for intermediate composition liquids whose phase assemblages are dominated by the presence of hornblende or biotite"[15]. To circumvent this, the relationship between the trace element geochemistry of the SB II gabbronorite and high-Ti diorites was investigated by simple fractional crystallization and assimilation-fractional crystallization simulations following Equation X-2 and Equation X-3, respectively:

Equation X-2

$$C_l = C_0 F^{(D-1)}$$

---

[15] See also Nandedkar *et al.* (2014) for an example on how the MELTS algorithm fails to predict several compositional features of hydrous melts.

Equation X-3

$$C_l^{AFC} = C_0\left[F^{-z} + \left(\frac{r}{r-1}\right)\frac{C_a}{zC_0}(1 - F^{-z})\right]$$

where C_l is the concentration of an element in the remaining melt during fractional crystallization, C_0 is the concentration of an element in the starting melts, F is the fraction of the remaining melt, D is the bulk partition coefficient of the fractionating mineral phases, r expresses the relative ratio of assimilated material to crystallized material and z is expressed by $z = \frac{r+D-1}{r-1}$.

The bulk partition coefficients for the considered mineral phases are as reported in Ersoy & Helvacı (2010) for basic magmas (Supplementary Data 4).

The results show that in order to obtain the degrees of trace element enrichment of the high-Ti diorites, approximately 60% (F = 0.4) simple fractional crystallization of a mineral assemblage comprising 80% clinopyroxene, 15% olivine and 5% spinel from a melt represented by the SB II gabbronorite is required. However, such an extensive crystallization event of ferro-magnesian silicates would have significant implications on the major element geochemistry of the SB II-derived melts, resulting in silica-rich (> 55 wt%) magmas with other important compositional differences (see, for example, similar crystallization simulations in Chiaradia *et al.*, 2011). Concurrent assimilation of the rock mixture used above by SB II melts and fractional crystallization enables obtaining the high-Ti diorite compositions at a more reasonable melt fraction of 0.7-0.75 (AFC; DePaolo, 1981). At an assimilation/crystallization ratio (*r*) of 0.2, the patterns are comparable to those of the high-Ti diorites, whereas to obtain the low-Ti geochemical features, an *r* value of *ca.* 0.4 is required. Although the AFC model is a possible way to generate the low-Ti diorites, this model implies that assimilation and fractional crystallization of gabbroic melts occurred simultaneously at the depth of emplacement. There is, however, no evidence for gabbroic magmas at Torrão apart from rare xenoliths.

Evidence thus suggests that the high-Ti diorites are the result of fractional crystallization of a plagioclase-free gabbroic assemblage compositionally identical to the SB II gabbronorite. Nevertheless, these processes did not occur under strictly closed system conditions as implied by the AFC model and the isotopic signature of the high-Ti diorites (Pin *et al.*, 2008; Jesus *et al.*, 2016).

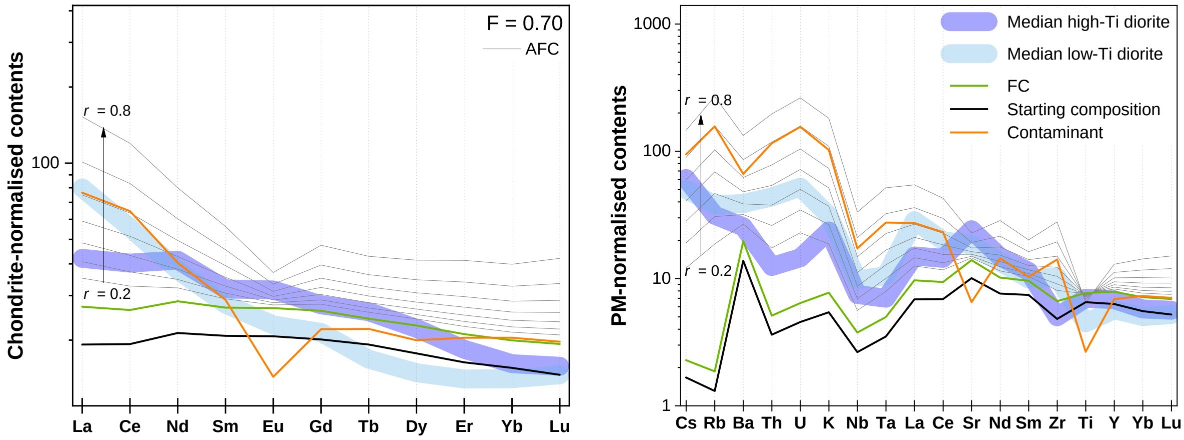

Figure X-6. Assimilation-fractional crystallization (AFC) simulation of a mineral assemblage composed of 80% clinopyroxene, 15% olivine and 5% spinel, starting from a melt compositionally analogous to SB II gabbronorite. The contaminant comprises a rock mixture composed of siliciclastic, felsic meta-igneous, mafic meta-igneous and marble rocks in proportions of 35/35/15/15, respectively. Results are shown for REE and selected incompatible elements. The obtained patterns at F = 0.7 and *r* = 0.2 correlate fairly well to those displayed by the high-Ti diorites.

Deep fractionation and the source of water

Should there be a genetic link between the LGS and the Torrão dioritic rocks, the source of water remains an uncertainty. Jesus *et al.* (2016) proposed that dehydration melting of lower crustal amphibolite units – isotopically identical to OMZ mafic amphibolite rocks (Casquet *et al.*, 2001; Schäfer, 1990) – and mingling with LGS primitive melts provided the necessary water to generate the diorites. Presently, field observations strongly support the idea that amphibolite rocks were involved in this magmatic event. However, they do not derive from the lower crust; rather, they likely represent mid-crustal pre-Variscan and Variscan amphibolites and metavolcanic rocks (compositionally similar to those reported in Chichorro, 2006 and da Silva, 2011). Furthermore, the size of some enclaves reaches the decametric scale, suggesting that they represent country-rocks intruded by dioritic magmas rather than xenoliths transported from the lower crust for more than 10 km. The role of the Torrão fine-grained amphibolite enclaves is seemingly minor as supported by their pristine mineralogy and absence of restite assemblages. The study area encompassed by the SEMACRET team (up to Serpa) abounds with examples of variably digested coarse-grained amphibolitic country-rocks. These feature do not rule out the involvement of deeper crustal amphibolite reservoirs as a source for water; indeed, maximum geobarometric estimates related to amphibole primocrysts record an evolution as deep as 24 km, well within the lower crust. As such, these melts must have been at least somewhat hydrated before their emplacement at *ca.* 13.5 km depth.

Differentiation driven primarily by fractional crystallization at depth has been a widely studied topic based on experimental (*e.g.*, Ulmer, 2007; Whitaker *et al*., 2007; Nandekar *et al*., 2014; Marxer *et al*., 2022; Hürlimann *et al*., 2016) and numerical methods (*e.g.*, Annen *et al*., 2006; Jackson *et al*., 2018; Solano *et al*., 2018), the latter all being based on the Deep Crustal Hot Zone (DCHZ) model. A common feature of all these models is the ability to differentiate basaltic magmas at depth to generate intermediate and felsic compositions through fractional crystallization alone. Assimilation of deep crustal rocks or previously emplaced intrusions and further homogenization are other mechanisms which can drive differentiation in the DCHZ, being a viable process to generate tonalitic and dioritic melts (see Otamendi *et al*., 2009). Although most of the mechanisms investigated in these studies are based on rather hydrous parental magmas (from ~3 to 10 wt% H_2O), typical of subduction settings, the same principles can be applied to other geodynamic contexts (Annen *et al.*, 2006). Depending on the depth of magma emplacement and initial H_2O contents, residual melts can become efficiently H_2O enriched. From Annen *et al*. (2006): 65% crystallization of a basalt with 2.5 wt% H_2O will yield an andesitic melt with 7 wt% H_2O. The primitive LGS magmas are thought to have contained at least minor amounts of water (> 0.3 wt% H_2O) due to their origin in a metasomatized astenospheric mantle, related to a post-subduction geodynamic context (Jesus *et al.*, 2016). Subduction-related magmas can reach H_2O contents as high as 10 wt% (Grove *et al.*, 2002). The common occurrence of late magmatic amphibole in the LGS provides further evidence for considerable amounts of water in the LGS parental magmas (*e.g.*, Jesus, 2011). Assuming a bulk partition coefficient of H_2O near zero during crystallization, the SB II melts would need to have *ca.* 4 wt% H_2O to attain the water contents of the high-Ti diorites (*ca.* 5.9 wt%) with a residual melt fraction of 0.7. Under the reasonable assumption that the H_2O/Ce ratio remains constant throughout mantle melting (Kovalenko *et al.*, 2007), these results imply that the astenospheric mantle from which the LGS Deep Crustal Hot Zone originated had H_2O/Ce ratios of 1918. Values of this range are rather high relative to the several mantle reservoirs (*e.g.*, Kovalenko *et al.*, 2007) but are chiefly comparable to those estimated for several Large Igneous Provinces (*e.g.*, Liu *et al.*, 2017).

Amphibole is stable in melts with H_2O contents above 4 wt% and temperatures below *ca.* 1050 ºC (*e.g.*, Eggler, 1972; Müntener *et al.*, 2001). The estimated water contents of 5.9 wt% and amphibole crystallization temperatures around 831 ºC for the high-Ti diorites are therefore well within the required conditions. In addition, fractional crystallization of an olivine + clinopyroxene assemblage at depth has been shown to be an effective mechanism to generate melts with characteristics alike of those displayed by the Torrão diorites, *i.e.*, low SiO_2 and compatible elements (Ni and Mg-number ~0.36-0.48), and high Al_2O_3 and Sr (meaning suppressed crystallization of plagioclase; Chiaradia *et al.*, 2011). An interesting feature of this process is the ability to differentiate primary magmas without significant SiO_2

enrichment and to shift compositions to follow a tholeiitic trend towards higher H_2O contents, like the high-Ti diorites. Addition of H_2O or its residual enrichment by closed-system processes can result in reduced plagioclase stability relative to ferromagnesian silicate minerals such as olivine, clinopyroxene and amphibole (*e.g.*, Kushiro *et al.*, 1968; Feig *et al.*, 2006; Koepke *et al.*, 2009), in good agreement with the simulations made above. Finally, residual magmas enriched in Fe and Ti have been produced by crystallization of an olivine tholeiite at elevated pressures (*ca.* 9 kbar). Note, however, that these experiments were performed in 'dry' conditions, not constraining the role of H_2O in such processes (Whitaker *et al.*, 2007)

The depth at which crystal fractionation primarily took place is uncertain. The occurrence of coarse-grained amphibole crystals which pressure estimates are consistently above 6-7 kbar, supports that fractional crystallization started in deep crustal domains. Furthermore, the spatial association of diorites and quartz-diorites implies that these magmas were already dioritic upon emplacement and could not have attained some of their geochemical features at the upper crust. Currently, the proposed model for the LGS (Jesus *et al.*, 2016) suggests magma storage in mid-crustal levels (*ca.* 20 km) was responsible for the formation of the ATT suite, but there is no evidence that the same applies for the Torrão diorites. Extraction of dioritic melts directly from the DCHZ could have been promoted by their lower viscosity, given their H_2O contents (*e.g.*, Annen *et al.*, 2006).

General model

Considering field and petrographic observations, mineral chemistry and geochemical data, and the above discussion as well as previous works regarding the Torrão diorites (Caldeira *et al.*, 2007; Pin *et al.*, 2008; Jesus *et al.*, 2016), the genesis and evolution of the Torrão diorite suite can be summarized as follows (Figure X-7).

Development of the Beja Igneous Complex Deep Crustal Hot Zone took place near the Moho discontinuity, at *ca.* 30 km depth (Figure X-7A; Jesus *et al.*, 2016). Given the (post-)subduction-related geodynamic setting of the LGS, the mantle source that fed the DCHZ likely contained at least 3-4 wt% H_2O. The first extracted magmas from the DCHZ are represented by the Soberanas gabbroic rocks. Continuous evolution of SB II-like magmas progressed by crystallization of a mineral assemblage composed of clinopyroxene + olivine + spinel, promoting the development of hydrous intermediate melts which did not become significantly enriched in silica (Figure X-7B). The dioritic magmas were emplaced at meso-crustal levels, around 13.5 km depth. The first magmas to arrive were likely hotter and, upon emplacement, were contaminated by the host rocks (Figure X-7B). In addition to the magma temperature, the heat required for assimilation/contamination may have been supplied by latent heat of crystallization of the low-Ti dioritic magmas. Given the tectonically dismembered structure of the Ossa-Morena Zone southern border, and the variety of autochthonous lithologies, several potential contaminants could be envisaged to explain the geochemical signature of the first emplaced dioritic melts. Assimilation of diverse rock types led to enrichments in SiO_2, Th, U, Zr, Hf, LREE and, possibly H_2O, and depletion in $Fe_2O_3^T$ and TiO_2. These contaminated magmas are now represented by the low-Ti diorites. The amphibolite enclaves, abundant in the study area, likely represent the host rocks which melting temperature was not significantly lower than that of the dioritic magmas, thus not allowing for significant assimilation. Gradual recharge of the Torrão magmatic chamber by slightly more evolved and cooler magmas (lower Mg-number and Ni and Cr contents) led to the formation of the high-Ti diorites (Figure X-7C). Due to their lower temperature, as well as being possibly insulated from the host rocks by the crystallized low-Ti diorites, the later emplaced high-Ti melts were not as extensively contaminated. Therefore, the Torrão high-Ti diorites are related to the LGS Fe-Ti oxide mineralization in the same sense of the SB II gabbroic rocks. Both rock suites represent Fe and Ti-rich magmas which, under certain conditions (like in the Odivelas sector), may develop massive accumulations of oxide mineral phases.

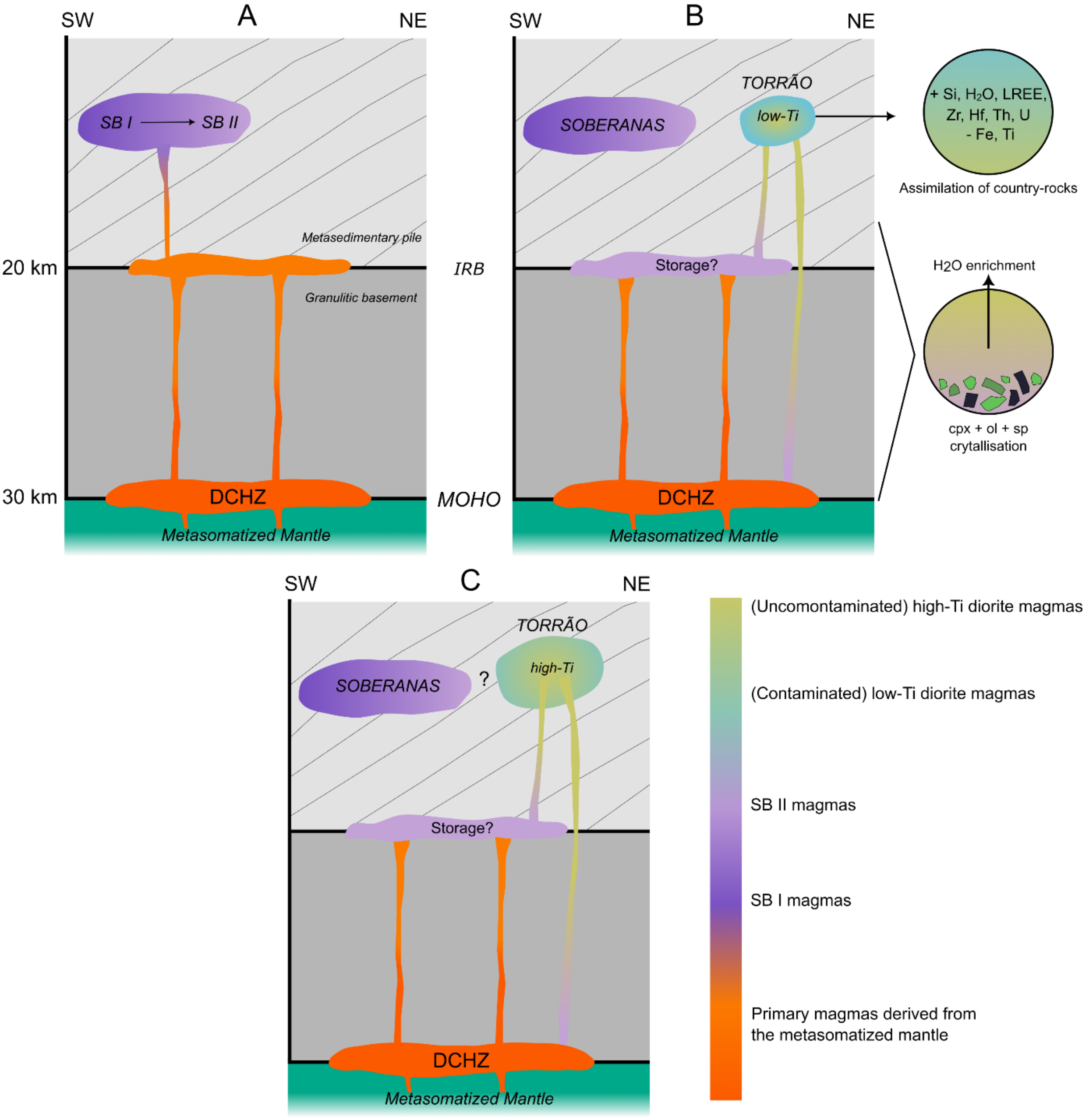

Figure X-7.Conceptual model for the formation of the Torrão dioritic suite. (A) Development of the LGS Deep Crustal Hot Zone and generation of a mid-crustal magmatic storage zone with subsequent extraction of the magmas that generated the Soberanas gabbroic rocks (according to the model of Jesus, 2011; Jesus *et al.*, 2016). (B) Water enrichment of SB II-like melts by crystal fractionation concurrent with minor degrees of assimilation. Significant assimilation of country-rocks by these magmas generated the low-Ti diorites. (C) Continuous recharge of the Torrão magma chamber by low temperature melts generated the high-Ti diorites. Due to their lower temperature, these magmas likely did not assimilate significant amounts of country-rocks, retaining a geochemical signature like that of the SB II gabbronorite.

Final remarks

Nd-Sr-Hf-Pb isotopic data will be acquired for representative diorite, quartz-diorite and amphibolite samples. Because these geochemical systems are much more sensitive to assimilation processes than incompatible elements, this new data will hopefully allow for a more comprehensive understanding of the genesis of the Torrão dioritic suite. Furthermore, the mixing simulations do not consider the thermodynamic constraints associated with the assimilation of several rock types, nor the possible variations triggered by different degrees of partial melting experienced by them when subjected to identical P-T conditions. The numerical simulations here described represent a preliminary approach to investigate whether assimilation processes are valid or not from a thermal and bulk compositional perspective.

XI. Conclusions

Several dioritic lithologies can be recognized at Torrão that document the evolution of a dynamic magmatic system that involved primary basaltic magmas as well as country rocks of diverse nature. Diorites and quartz-diorites are the most abundant rock types and represent most of the petrographic and geochemical variety found within the Torrão dioritic suite. The diorites are more enriched in Fe and Ti relative to the quartz-diorites, which motivated the usage of the ‘high-Ti’ and ‘low-Ti’ designation adopted in previous studies. These dioritic rock types include abundant enclaves of amphibolites rocks.

The petrographic features of the high-Ti and low-Ti diorites reveal a gradual increase in the modal proportions of quartz and biotite, as well as accessory mineral phases, such as zircon. Compositional variation of the main mineral constituents of both dioritic lithologies indicates typically more evolved compositions for the low-Ti diorites relative to the high-Ti diorites. Temperature estimates based on mineral composition for the dioritic rocks further support this idea, indicating crystallization temperatures which are *ca.* 50 ºC lower in the low-Ti diorites compared to their high-Ti counterpart. Geobarometric estimates based on amphibole-plagioclase equilibria are similar in dioritic rocks and indicate pressures ranging from *ca.* 7 to 4.5 kbar, which broadly correspond to depths around 13.5 km.

The low-Ti and high-Ti diorites found at Torrão are cogenetic due to their close spatial association and similar REE and incompatible element trends. The low-Ti diorites show significant enrichments in SiO_2, LREE, Th, U, Zr and Hf, suggesting assimilation of crustal rocks. However, these rocks also have higher Mg-number (> 50) and Ni and Cr contents relative to the high-Ti diorites, implying that they derive from a more primitive, albeit similar, magmatic source. Binary mixing simulations reveal that 35% of assimilation of meta-siliciclastic, metaigneous mafic and felsic and marble rocks by the melts represented by the SB II gabbronorite can explain most of the major, REE and other incompatible trace element compositional features of the low-Ti diorites. Assimilation-fractional crystallization simulations of SB II magmas performed at assimilation/crystallization ratios (*r*) of 0.3-0.4 show that this is also a viable process to generate the low-Ti diorites. Partial melting of the contaminant rocks rather than their total digestion was not modelled; however, it likely represents a scenario which is thermodynamically more realistic because the required melting degrees of the country-rocks are lower.

A genetic link between the Torrão dioritic suite and the nearby Layered Gabbroic Sequence (LGS) can be made through the high-Ti diorites, which represent the least contaminated rocks found at Torrão. Similar enrichments in incompatible elements, as well as parallel trends, suggest that the gabbroic and dioritic rocks may be related by fractional crystallization concurrent with minor crustal contamination. The products obtained by fractional crystallization of a mineral assemblage composed of clinopyroxene + olivine + spinel starting from a melt represented by the most primitive LGS rocks, and assimilation of crustal rocks, replicate the REE and other incompatible trace element compositional features of the high-Ti diorites at melt fractions of 70% (30% crystallization) and *r* values of 0.2. The process, however, requires that the primary basaltic magmas were already rather hydrous. Inverse fractional crystallization modelling of the high-Ti diorites, using the amphibole-only hygrometer estimates of *ca.* 6 wt% H_2O for the high-Ti dioritic melts and assuming $K_D^{H2O} = 0$, means that the LGS magmas from which the diorites originated had around 4 wt% H_2O. The depth at which this process occurred is uncertain, however, the occurrence of coarse-grained amphibole primocrysts from which the highest barometric estimates were obtained (*ca.* 8 kbar), suggests that fractional crystallization started in deep crustal domains. Therefore, the Fe and Ti enriched signature of the high-Ti diorites are a primary magmatic feature, inherited by fractional crystallization of hydrous, basaltic melts compositionally comparable to those of the LGS. This process, however, was not closed to mass exchange as denoted by the slightly contaminated isotopic signature of the high-Ti diorites, reported in previous studies.

Isotopic data is under acquisition for the high-Ti and low-Ti diorite samples, as well as amphibolite enclaves, which will elucidate on the processes involved in the genesis of these rocks. Further refinements of numerical approaches should support the development of thermodynamic modelling for contamination processes, which might also clarify to which extent assimilation was possible.

XII. References

Andersen, D. J., Lindsley, D. H., & Davidson, P. M. (1993). QUILF: A pascal program to assess equilibria among Fe-Mg-Mn-Ti oxides, pyroxenes, olivine, and quartz. *Computers & Geosciences*, 19(9), 1333-1350.

Andrade, A.S. (1983). Contribuition à la analyse de la suture Hercyniènne de Beja (Portugal), perspectives metallogéniques. University of Nancy (PhD Thesis).

Andrade, A.S. (1984). Sobre a originalidade (ou talvez não) de maciço de Beja no sudoeste peninsular. Memórias e notícias. *Publicações do Museu e Laboratório mineralógico e geológico da Universidade de Coimbra*, (97), 115-132.

Annen, C., Blundy, J. D., & Sparks, R. S. J. (2006). The genesis of intermediate and silicic magmas in deep crustal hot zones. *Journal of Petrology*, 47(3), 505-539.

Antunes, M. T., Pais, J., Gonçalves, F., & Oliveira, J. T. (1991). Folha 39-D Torrão, Carta Geológica de Portugal na escala 1: 50 000. *Serviços Geológicos de Portugal*, Lisboa.

Araújo, A. A., Almeida, J. P., Borrego, J., Pedro, J., & Oliveira, T. (2006). As regiões central e sul da Zona de Ossa-Morena.

Arculus, R. J. (2003). Use and abuse of the terms calcalkaline and calcalkalic. *Journal of Petrology*, 44(5), 929-935.

Azor, A., Rubatto, D., Simancas, J. F., González Lodeiro, F., Martínez Poyatos, D., Martín Parra, L. M., & Matas, J. (2008). Rheic Ocean ophiolitic remnants in southern Iberia questioned by SHRIMP U-Pb zircon ages on the Beja-Acebuches amphibolites. *Tectonics*, 27(5).

Barnes, C. G., Dumond, G., Yoshinobu, A. S., & Prestvik, T. (2004). Assimilation and crystal accumulation in a mid-crustal magma chamber: the Sausfjellet pluton, north-central Norway. *Lithos*, *75*(3-4), 389-412.

Barnes, S. J., Holwell, D. A., & Le Vaillant, M. (2017). Magmatic sulfide ore deposits. *Elements*, 13(2), 89-95.

Bea, F., Fershtater, G., & Corretgé, L. G. (1992). The geochemistry of phosphorus in granite rocks and the effect of aluminium. *Lithos*, 29(1-2), 43-56.

Bourdelle, F., Parra, T., Chopin, C., & Beyssac, O. (2013). A new chlorite geothermometer for diagenetic to low-grade metamorphic conditions. *Contributions to Mineralogy and Petrology*, 165, 723-735.

Buddington, A. F., & Lindsley, D. H. (1964). Iron-titanium oxide minerals and synthetic equivalents. *Journal of Petrology*, 5(2), 310-357.

Caldeira, R., Ribeiro, M. L., & Moreira, M. E. (2007). Geoquímica das sequências máficas e félsicas entre Alvito, Torrão e Alcáçovas (SW da ZOM). *Comun. Geológicas*, 94, 5-28.

Casquet, C., Galindo, C., Tornos, F., Velasco, F. T., & Canales, A. (2001). The Aguablanca Cu–Ni ore deposit (Extremadura, Spain), a case of synorogenic orthomagmatic mineralization: age and isotope composition of magmas (Sr, Nd) and ore (S). *Ore Geology Reviews*, *18*(3-4), 237-250.

Castro, A., Fernández, C., El-Hmidi, H., El-Biad, M., Díaz, M., De la Rosa, J., & Stuart, F. (1999). Age constraints to the relationships between magmatism, metamorphism and tectonism in the Aracena metamorphic belt, southern Spain. *International Journal of Earth Sciences*, 88, 26-37.

Chiaradia, M., Müntener, O., & Beate, B. (2011). Enriched basaltic andesites from mid-crustal fractional crystallization, recharge, and assimilation (Pilavo Volcano, Western Cordillera of Ecuador). *Journal of Petrology*, 52(6), 1107-1141.

Chichorro, M. A. F. D. S. (2006). A evolução tectónica da zona de cisalhamento de Montemor-o-Novo (sudoeste da zona de Ossa Morena-área de Santiago do Escoural-Cabrela). Universidade de Évora (PhD Thesis).

Cox, K. G. (Ed.). (1979). The interpretation of igneous rocks. *Springer Science & Business Media*.

da Silva, J. E. C. (2011). Estudo Petrológico e Geoquímico dos metavulcanitos devónicos da região de Odivelas (Alentejo): Implicações Geodinâmicas e Metalogenéticas. Universidade de Lisboa (MSc Thesis).

Dallmeyer, R. D., Fonseca, P. E., Quesada, C., & Ribeiro, A. (1993). 40Ar/39Ar mineral age constraints for the tectonothermal evolution of a Variscan suture in southwest Iberia. *Tectonophysics*, 222(2), 177-194.

Deer, W. A., Howie, R. A., & Zussman, J. (2013). An introduction to the rock-forming minerals. *Mineralogical Society of Great Britain and Ireland*.

DePaolo, D. J. (1981). Trace element and isotopic effects of combined wallrock assimilation and fractional crystallization. *Earth and planetary science letters*, 53(2), 189-202.

Eggler, D. H. (1972). Amphibole stability in H2O-undersaturated calc-alkaline melts. *Earth and Planetary Science Letters*, *15*(1), 28-34.

Ersoy, Y., & Helvacı, C. (2010). FC–AFC–FCA and mixing modeler: a Microsoft® Excel© spreadsheet program for modeling geochemical differentiation of magma by crystal fractionation, crustal assimilation and mixing. *Computers & Geosciences*, *36*(3), 383-390.

Feig, S. T., Koepke, J., & Snow, J. E. (2010). Effect of oxygen fugacity and water on phase equilibria of a hydrous tholeiitic basalt. *Contributions to Mineralogy and Petrology*, *160*, 551-568.

Ferreira, P., Caldeira, R., & Calvo, R. (2014). Geoquímica das rochas ígneas aflorantes na região de S. Matias, Cuba (Alentejo). *Comun. Geológicas*, 101, 93-97.

Fonseca, P. (1995). Estudo da sutura Varisca no SW Ibérico nas regiões de Serpa-Beja-Torrão e Alvito-Viana do Alentejo. Universidade de Lisboa (PhD Thesis).

Fonseca, P., Munhá, J., Pedro, J., Rosas, F., Moita, P., Araújo, A., & Leal, N. (1999). Variscan ophiolites and high-pressure metamorphism in southern Iberia. *Ofioliti*, 24(2), 259-268.

Frost, B. R., & Lindsley, D. H. (1991). Occurrence of iron-titanium oxides in igneous rocks. In *Oxide Minerals* (pp. 433-468).

Frost, B. R., Lindsley, D. H., & Andersen, D. J. (1988). Fe-Ti oxide-silicate equilibria; assemblages with fayalitic olivine. *American Mineralogist*, *73*(7-8), 727-740.

Fujimaki, H. (1986). Partition coefficients of Hf, Zr, and REE between zircon, apatite, and liquid. *Contributions to Mineralogy and Petrology, 94*(1), 42-45.

Giese, U., Hoegen, R. V., Hoymann, K. H., Kramm, U., & Walter, R. (1994). The Palaeozoic evolution of the Ossa Morena Zone and its boundary to the South Portuguese Zone in SW Spain. Geological constraints and geodynamic interpretation of a suture in the Iberian Variscan orogen. Neues Jahrbuch für Geologie und Paläontologie. *Abhandlungen*, 192(3), 383-412.

Gomes E. (2000). Metamorfismo de rochas carbonatadas siliciosas da região de Alvito (Alentejo, Sul de Portugal). Universidade de Coimbra (PhD Thesis).

Green, T. H. (1995). Significance of Nb/Ta as an indicator of geochemical processes in the crust-mantle system. *Chemical geology, 120*(3-4), 347-359.

Grove, T., Parman, S., Bowring, S., Price, R., & Baker, M. (2002). The role of an H 2 O-rich fluid component in the generation of primitive basaltic andesites and andesites from the Mt. Shasta region, N California. *Contributions to Mineralogy and Petrology*, *142*, 375-396.

Gualda, G. A., Ghiorso, M. S., Lemons, R. V., & Carley, T. L. (2012). Rhyolite-MELTS: a modified calibration of MELTS optimized for silica-rich, fluid-bearing magmatic systems. *Journal of Petrology*, 53(5), 875-890.

Gündüz, M., & Asan, K. (2023). MagMin_PT: An Excel-based mineral classification and geothermobarometry program for magmatic rocks. *Mineralogical Magazine*, 87(1), 1-9.

Haggerty, S. E. (1991). Oxide textures; a mini-atlas. *Reviews in Mineralogy and Geochemistry*, 25(1), 129-219.

Harrison, T. M., & Watson, E. B. (1984). The behavior of apatite during crustal anatexis: equilibrium and kinetic considerations. *Geochimica et cosmochimica acta*, 48(7), 1467-1477.

Henry, D. J., Guidotti, C. V., & Thomson, J. A. (2005). The Ti-saturation surface for low-to-medium pressure metapelitic biotites: Implications for geothermometry and Ti-substitution mechanisms. *American mineralogist*, 90(2-3), 316-328.

Holland, T., & Blundy, J. (1994). Non-ideal interactions in calcic amphiboles and their bearing on amphibole-plagioclase thermometry. *Contributions to mineralogy and petrology*, 116, 433-447.

Hürlimann, N., Müntener, O., Ulmer, P., Nandedkar, R., Chiaradia, M., & Ovtcharova, M. (2016). Primary magmas in continental arcs and their differentiated products: petrology of a post-plutonic dyke suite in the Tertiary Adamello batholith (Alps). *Journal of Petrology*, 57(3), 495-534.

Irvine, T. N., & Baragar, W. R. A. F. (1971). A guide to the chemical classification of the common volcanic rocks. *Canadian journal of earth sciences, 8*(5), 523-548.

Jackson, M. D., Blundy, J., & Sparks, R. S. J. (2018). Chemical differentiation, cold storage and remobilization of magma in the Earth’s crust. *Nature*, 564(7736), 405-409.

Jesus, A. P., Mateus, A., Munhá, J. M., & Tassinari, C. (2014). Internal architecture and Fe–Ti–V oxide ore genesis in a Variscan synorogenic layered mafic intrusion, the Beja Layered Gabbroic Sequence (Portugal). *Lithos*, 190, 111-136.

Jesus, A. P., Mateus, A., Munhá, J. M., Tassinari, C. C., dos Santos, T. M. B., & Benoit, M. (2016). Evidence for underplating in the genesis of the Variscan synorogenic Beja Layered Gabbroic Sequence (Portugal) and related mesocratic rocks. *Tectonophysics*, 683, 148-171.

Jesus, A. P., Mateus, A., Oliveira, V., & Munhá, J. (2003a). Ore-forming systems in the layered gabbroic sequence of the Beja Igneous Complex (Ossa-Morena Zone, Portugal); state of the art and future perspectives. In *Mineral Exploration and Sustainable Development*. Proceedings of the 7th Biennial SGA Meeting, Athens, Greece (pp. 24-28).

Jesus, A. P., Mateus, A., Waerenborgh, J. C., Figueiras, J., Alves, L. C., & Oliveira, V. (2003b). Hypogene titanian, vanadian maghemite in reworked oxide cumulates in the Beja Layered Gabbro Complex, Odivelas, Southeastern Portugal. *The Canadian Mineralogist*, 41(5), 1105-1124.

Jesus, A. P., Munhá, J., Mateus, A., Tassinari, C., & Nutman, A. P. (2007). The Beja layered gabbroic sequence (Ossa-Morena Zone, Southern Portugal): geochronology and geodynamic implications. *Geodinamica Acta*, 20(3), 139-157.

Jesus, A.P. (2011). Ore forming systems in the western compartment of the Beja Layered Gabbroic Sequence (Ossa Morena Zone Portugal). Universidade de Lisboa (PhD Thesis).

Kelemen, P. B., Hanghøj, K., & Greene, A. R. (2003). One view of the geochemistry of subduction-related magmatic arcs, with an emphasis on primitive andesite and lower crust. *Treatise on geochemistry*, *3*, 659.

Koepke, J., Schoenborn, S., Oelze, M., Wittmann, H., Feig, S., Hellebrand, E., Boudier, F. & Schoenberg, R. (2009). Petrogenesis of crustal wehrlites in the Oman ophiolite: experiments and natural rocks. *Geochemistry Geophysics Geosystems, 10*.

Kovalenko, V. I., Naumov, V. B., Girnis, A. V., Dorofeeva, V. A., & Yarmolyuk, V. V. (2007). Average compositions of magmas and mantle sources of mid-ocean ridges and intraplate oceanic and continental settings estimated from the data on melt inclusions and quenched glasses of basalts. *Petrology*, *15*, 335-368.

Kushiro, I., Syono, Y., & Akimoto, S. I. (1968). Melting of a peridotite nodule at high pressures and high water pressures. *Journal of Geophysical Research*, *73*(18), 6023-6029.

Le Maitre, R.W. (1989). A classification of igneous rocks and glossary of terms. Recommendations of the international union of geological sciences subcommission on the systematics of igneous rocks, 193.

Lee, J. K., Williams, I. S., & Ellis, D. J. (1997). Pb, U and Th diffusion in natural zircon. *Nature*, 390(6656), 159-162.

Lepage, L. D. (2003). ILMAT: an Excel worksheet for ilmenite–magnetite geothermometry and geobarometry. *Computers & Geosciences*, *29*(5), 673-678.

Li, X., Zhang, C., Behrens, H., & Holtz, F. (2020). Calculating biotite formula from electron microprobe analysis data using a machine learning method based on principal components regression. *Lithos*, 356, 105371.

Lindsley, D. H., & Frost, B. R. (1992). Equilibria among Fe-Ti oxides, pyroxenes, olivine, and quartz: Part I. Theory. *American Mineralogist*, 77(9-10), 987-1003.

Linnen, R. L., & Keppler, H. (2002). Melt composition control of Zr/Hf fractionation in magmatic processes. *Geochimica et Cosmochimica Acta*, *66*(18), 3293-3301.

Liu, J., Xia, Q. K., Kuritani, T., Hanski, E., & Yu, H. R. (2017). Mantle hydration and the role of water in the generation of large igneous provinces. *Nature Communications*, *8*(1), 1824.

Ludington, S. (1978). The biotite-apatite geothermometer revisited. *American Mineralogist*, 63(5-6), 551-553.

Marxer, F., Ulmer, P., & Müntener, O. (2022). Polybaric fractional crystallization of arc magmas: an experimental study simulating trans-crustal magmatic systems. *Contributions to Mineralogy and Petrology*, 177(1), 3.

Mason, D. R. (1978). Compositional variations in ferromagnesian minerals from porphyry copper-generating and barren intrusions of the Western Highlands, Papua New Guinea. *Economic Geology*, *73*(5), 878-890.

Mateus, A., Figueiras, J., Gonçalves, M., & Fonseca, P. (1999). Evolving fluid circulation within the Variscan Beja-Acebuches Ophiolite Complex (SE, Portugal). *Ofioliti*, 24(2), 269-282.

Miyashiro, A. (1974). Volcanic rock series in island arcs and active continental margins. *American journal of science*, 274(4), 321-355.

Moita, P., Munhá, J., Fonseca, P., Pedro, J., Araújo, A., Tassinari, C., & Palacios, T. (2005a). Phase equilibria and geochronology of Ossa-Morena eclogites.

Moita, P., Munhá, J., Fonseca, P., Tassinari, C., Araújo, A., & Palácios, T. (2005b). Dating orogenic events in Ossa-Morena Zone. In XIV Semana de Geoquímica/VIII Congresso de Geoquímica dos Países de Língua Portuguesa, Univ. Aveiro, Aveiro, Portugal (pp. 459-461).

Molina, J. F., Cambeses, A., Moreno, J. A., Morales, I., Montero, P., & Bea, F. (2021). A reassessment of the amphibole-plagioclase NaSi-CaAl exchange thermometer with applications to igneous and high-grade metamorphic rocks. *American Mineralogist*, 106(5), 782-800.

Molina, J. F., Moreno, J. A., Castro, A., Rodríguez, C., & Fershtater, G. B. (2015). Calcic amphibole thermobarometry in metamorphic and igneous rocks: New calibrations based on plagioclase/amphibole Al-Si partitioning and amphibole/liquid Mg partitioning. *Lithos*, 232, 286-305.

Muñoz, G., Mateus, A., Pous, J., Heise, W., Monteiro Santos, F., & Almeida, E. (2008). Unraveling middle-crust conductive layers in Paleozoic Orogens through 3D modeling of magnetotelluric data: The Ossa-Morena Zone case study (SW Iberian Variscides). *Journal of Geophysical Research: Solid Earth*, *113*(B6).

Müntener, O., Kelemen, P. B., & Grove, T. L. (2001). The role of H2O during crystallization of primitive arc magmas under uppermost mantle conditions and genesis of igneous pyroxenites: an experimental study. *Contributions to Mineralogy and Petrology*, *141*, 643-658.

Mutch, E. J. F., Blundy, J. D., Tattitch, B. C., Cooper, F. J., & Brooker, R. A. (2016). An experimental study of amphibole stability in low-pressure granitic magmas and a revised Al-in-hornblende geobarometer. *Contributions to Mineralogy and Petrology*, 171, 1-27.

Nachit, H., Ibhi, A., & Ohoud, M. B. (2005). Discrimination between primary magmatic biotites, reequilibrated biotites and neoformed biotites. Comptes rendus. *Géoscience*, 337(16), 1415-1420.

Nandedkar, R. H., Ulmer, P., & Müntener, O. (2014). Fractional crystallization of primitive, hydrous arc magmas: an experimental study at 0.7 GPa. *Contributions to Mineralogy and Petrology*, 167(6), 1015.

Oliveira J. T., Oliveira V.E. & Piçarra J.M. (1991). Traços gerais da evolução tectonoestratigráfica da Zona de Ossa-Morena em Portugal. Cuad. Lab. Xeol. Laxe, 16, 221-250.

Otamendi, J. E., Ducea, M. N., Tibaldi, A. M., Bergantz, G. W., de la Rosa, J. D., & Vujovich, G. I. (2009). Generation of tonalitic and dioritic magmas by coupled partial melting of gabbroic and metasedimentary rocks within the deep crust of the Famatinian magmatic arc, Argentina. *Journal of Petrology*, 50(5), 841-873.

Palme, H. & O'Neill, H.St.C. (2003). Cosmochemical Estimates of Mantle Composition. *Treatise on Geochemistry*.

Parsons, I. (Ed.). (2013). Origins of igneous layering (Vol. 196). *Springer Science & Business Media*.

Pichavant, M., Montel, J. M., & Richard, L. R. (1992). Apatite solubility in peraluminous liquids: Experimental data and an extension of the Harrison-Watson model. *Geochimica et Cosmochimica Acta*, 56(10), 3855-3861.

Pin C., Paquette J.-L. & Fonseca P. (1999). 350 Ma (U-Pb zircon) igneous emplacement age and Sr-Nd isotopic study of the Beja gabbroic complex (S. Portugal). In: Gámez J.A., Eguiluz L. & Palacios T. (Eds.). XV Reunión de Geología del Oeste Peninsular. Diputación de Badajoz, Badajoz, Spain, pp. 190-194.

Pin, C., Fonseca, P. E., Paquette, J. L., Castro, P., & Matte, P. (2008). The *ca.* 350 Ma Beja Igneous Complex: A record of transcurrent slab break-off in the Southern Iberia Variscan Belt? *Tectonophysics*, 461(1-4), 356-377.

Priem, H. N. A., Boelrijke, N. A. I. M., Hebeda, E. H., Verdurmen, E. A., Verschure, R. H., & Schermerhorn, L. J. G. (1976). Isotopic dating in southern Portugal. E.C.O.G. IV Meeting.

Putirka, K. (2016). Amphibole thermometers and barometers for igneous systems and some implications for eruption mechanisms of felsic magmas at arc volcanoes. *American Mineralogist*, 101(4), 841-858.

Qian, Q., & Hermann, J. (2010). Formation of high-Mg diorites through assimilation of peridotite by monzodiorite magma at crustal depths. *Journal of Petrology*, *51*(7), 1381-1416.

Quesada, C., Fonseca, P. E., Munhá, J., Oliveira, J. T., & Ribeiro, A. (1994). The Beja-Acebuches Ophiolite (Southern Iberia Variscan fold belt): geological characterisation and geodynamic significance. *Boletín Geológico y Minero*, 105.

Ribeiro, A., Munhá, J., Dias, R., Mateus, A., Pereira, E., Ribeiro, L., Fonseca, P., Araújo, A., Oliveira, T., Romão, J., Chaminé, H., Coke, C. & Pedro, J. (2007). Geodynamic evolution of the SW Europe Variscides. *Tectonics*, 26(6).

Ribeiro, A., Munhá, J., Fonseca, P. E., Araújo, A., Pedro, J. C., Mateus, A., Tassinari, C., Machado, G. & Jesus, A. (2010). Variscan ophiolite belts in the Ossa-Morena Zone (Southwest Iberia): Geological characterisation and geodynamic significance. *Gondwana Research*, 17(2-3), 408-421.

Ridolfi, F. (2021). Amp-TB2: an updated model for calcic amphibole thermobarometry. *Minerals*, 11(3), 324.

Ridolfi, F., Renzulli, A., & Puerini, M. (2010). Stability and chemical equilibrium of amphibole in calc-alkaline magmas: an overview, new thermobarometric formulations and application to subduction-related volcanoes. *Contributions to mineralogy and petrology*, 160, 45-66.

Romeo, I., Lunar, R., Capote, R., Quesada, C., Dunning, G. R., Piña, R., & Ortega, L. (2006). U–Pb age constraints on Variscan magmatism and Ni–Cu–PGE metallogeny in the Ossa–Morena Zone (SW Iberia). *Journal of the Geological Society*, 163(5), 837-846.

Rosas F. (2003). Estudo tectónico do sector de Viana do Alentejo – Alvito; evolução geodinâmica e modelação analógica de estruturas em afloramentos chave (Ramo Sul ds Cadeia Varisca Ibérica – SW da Zona de Ossa-Morena). Universidade de Lisboa, p. 264 (PhD Thesis).

Rosas, F. M., Marques, F. O., Ballevre, M., & Tassinari, C. (2008). Geodynamic evolution of the SW Variscides: Orogenic collapse shown by new tectonometamorphic and isotopic data from western Ossa-Morena Zone, SW Iberia. *Tectonics*, 27(6).

Ruffet, G. (1990). 40Ar– 39Ar dating of the Beja Gabbro: Timing of the accretion of southern Portugal. *Geophysical Research Letters*, 17(12), 2121-2124.

Santos, J. F., Andrade, A. S., & Munhã, J. M. (1990). Magmatismo básico-intermédio do Devónico superior no bordo sudoeste da Zona de Ossa-Morena. Resumo). VIII Semana de Geoquímica, Univ. Lisboa.

Scaillet, B., & Evans, B. W. (1999). The 15 June 1991 eruption of Mount Pinatubo. I. Phase equilibria and pre-eruption P–T–f O2–f H2O conditions of the dacite magma. *Journal of Petrology*, *40*(3), 381-411.

Schäfer, H. J. (1900). Geochronological Investigations in the Ossa-Morena Zone, SW Spain. ETH Zurich (PhD Thesis).

Simancas, J. F., Carbonell, R., González Lodeiro, F., Pérez Estaún, A., Juhlin, C., Ayarza, P., Kashubin, A., Azor. A., Martínez Poyatos, D., Almodóvar, G. R., Pascual, E., Sáez, R. & Expósito, I. (2003). Crustal structure of the transpressional Variscan orogen of SW Iberia: SW Iberia deep seismic reflection profile (IBERSEIS). *Tectonics*, *22*(6).

Solano, J. M. S., Jackson, M. D., Sparks, R. S. J., Blundy, J. D., & Annen, C. (2012). Melt segregation in deep crustal hot zones: a mechanism for chemical differentiation, crustal assimilation and the formation of evolved magmas. *Journal of Petrology*, 53(10), 1999-2026.

Spear, F. S. (1981). An experimental study of hornblende stability and compositional variability in amphibolite. *American Journal of science*, 281(6), 697-734.

Spiering, E. D., Rodriguez Pevida, L., Castelo, J. M., Garcia Nieto, J., & Martinez, C. (2005). Aguablanca: a new nickel mine in a potential new Ni/Cu and IOCG belt of southern Spain and Portugal. In *Proceedings Geological Society Nevada*. Symposium.

Stanley, C. R. (2020). Molar element ratio analysis of lithogeochemical data: a toolbox for use in mineral exploration and mining. *Geochemistry: Exploration, Environment, Analysis*, *20*(2), 233-256.

Tornos, F., Galindo, C., Casquet, C., Rodríguez Pevida, L., Martínez, C., Martínez, E., Velasco. F. & Iriondo, A. (2006). The Aguablanca Ni–(Cu) sulphide deposit, SW Spain: geologic and geochemical controls and the relationship with a midcrustal layered mafic complex. *Mineralium Deposita*, 41, 737-769.

Uchida, E., Endo, S., & Makino, M. (2007). Relationship between solidification depth of granitic rocks and formation of hydrothermal ore deposits. *Resource Geology*, *57*(1), 47-56.

Weyer, S., Münker, C., & Mezger, K. (2003). Nb/Ta, Zr/Hf and REE in the depleted mantle: implications for the differentiation history of the crust–mantle system. *Earth and Planetary Science Letters*, *205*(3-4), 309-324.

Weyer, S., Münker, C., Rehkämper, M., & Mezger, K. (2002). Determination of ultra-low Nb, Ta, Zr and Hf concentrations and the chondritic Zr/Hf and Nb/Ta ratios by isotope dilution analyses with multiple collector ICP-MS. *Chemical Geology*, *187*(3-4), 295-313.

Whitaker, M. L., Nekvasil, H., Lindsley, D. H., & Difrancesco, N. J. (2007). The role of pressure in producing compositional diversity in intraplate basaltic magmas. *Journal of Petrology*, 48(2), 365-393.

Wilson, M. (Ed.). (1989). Igneous petrogenesis. Dordrecht: Springer Netherlands.

Winter, J. D. (2014). *Principles of igneous and metamorphic petrology* (Vol. 2). Harlow, UK: Pearson education.

Zhu, C., & Sverjensky, D. A. (1992). F-Cl-OH partitioning between biotite and apatite. *Geochimica et Cosmochimica Acta*, 56(9), 3435-3467.

XIII. Supplementary Data 1

Mineral chemistry

Standards

Table XIII-1. Analytical standards used in electron probe micro-analysis of amphibole.

Amphibole	
Element	**Standard**
TiO_2	Benitoite
F	Apatite
Cl	Tugtupite
SiO_2	Kaersutite
MnO	Johannsenite
Na_2O	Jadeite
Cr_2O_3	Chromium Oxide
FeO	Biotite
MgO	Kaersutite
ZnO	Rhodonite
K_2O	Sanidine
Al_2O_3	Kaersutite
CaO	Kaersutite

Table XIII-2. Analytical standards used in electron probe micro-analysis of plagioclase.

Plagioclase	
Element	**Name**
CaO	Diopside
Na_2O	Albite
SrO	Celestite
SiO_2	Sanidine
BaO	Benitoite
MgO	Olivine
TiO_2	Rutile
K_2O	Sanidine
MnO	Johannsenite
Al_2O_3	Sanidine
FeO	Almandine Garnet

Table XIII-3. Analytical standards used in electron probe micro-analysis of phyllosilicates.

Phyllosilicates	
Element	**Name**
CaO	Kaersutite
F	Fluorite
SiO_2	Biotite
Rb_2O	Cal-STD
TiO_2	Rutile
Na_2O	Jadeite
Cl	Tugtupite
K_2O	Biotite
Cr_2O_3	Chromium Oxide
MgO	Biotite
Cs_2O	Pollucite
BaO	Benitoite
MnO	Rhodonite
Al_2O_3	Biotite
NiO	Nickel Silicide
FeO	Almandine Garnet

Table XIII-4. Analytical standards used in electron probe micro-analysis of zircon.

Zircon	
Element	**Name**
CaO	Diopside
F	Apatite
P_2O_5	Monazite
SiO_2	Tugtupite
TiO_2	Rutile
MgO	Periclase
Ce_2O_3	Cerium Fluoride
Nd_2O_3	Neodymium Fluoride
La_2O_3	Lanthanum Fluoride
Al_2O_3	Sanidine
ThO_2	Thorium
FeO	Hematite
MnO	Rhodonite
ZrO_2	Cubic Zirconia
HfO_2	Hafnium
UO_2	Uranium

Table XIII-5. Analytical standards used in electron microanalysis of pyroxene.

Pyroxene	
Element	**Name**
NiO	Nickel Silicide
F	Fluorite
CaO	Diopside
SiO_2	Diopside
Cr_2O_3	Chromium Oxide
Na_2O	Jadeite
TiO_2	Rutile
V_2O_3	Vanadium
MnO	Johannsenite
MgO	Diopside
ZnO	Willemite
FeO	Almandine Garnet
Al_2O_3	Spodumene
K_2O	Sanidine

Table XIII-6. Analytical standards used in electron microanalysis of apatite.

Apatite	
Element	**Name**
La_2O_3	Monazite
F	Apatite
SrO	Celestite
P_2O_5	Apatite
Nd_2O_3	Monazite
Na_2O	Jadeite
Ce_2O_3	Monazite
CaO	Apatite
MnO	Johannsenite
MgO	Periclase
Cl	Tugtupite
FeO	Almandine Garnet

Table XIII-7. Analytical standards used in electron microanalysis of oxide minerals.

Oxides	
Element	**Name**
P_2O_5	Monazite
Na_2O	Tugtupite
SO_3	Barite
BaO	Benitoite
Bi_2O_3	Bismute Selenide
MgO	Periclase
PbO	Diopside
V_2O_3	Vanadium
Ag_2O	Silver
As_2O_5	Galium Arsenide
K_2O	Sanidine
FeO	Hematite
CaO	Diopside
Al_2O_3	Jadeite
TiO_2	Rutile
NiO	Nickel Silicide
ZnO	Willemite
SiO_2	Quartz
Cr_2O_3	Chromium Oxide
CuO	Cuprite
CoO	Cobalt
ZrO_2	Cubic Zirconia
MnO	Rhodonite
Au_2O	Gold

Detection limits

Table XIII-8. Detection limits for electron micro-analysis of amphibole.

Amphibole	
Element	**Detection limit (ppm)**
Ti	190
F	980
Cl	95
Si	108
Mn	215
Na	152
Cr	177
Fe	188
Mg	107
Zn	619
K	54
Al	113
Ca	63

Table XIII-9. Detection limits for electron micro-analysis of plagioclase

Plagioclase	
Element	**Detection limit (ppm)**
Ca	210
Na	206
Sr	803
Si	162
Ba	519
Mg	152
Ti	295
K	85
Mn	347
Al	161
Fe	251

Table XIII-10. Detection limits for electron micro-analysis of phyllosilicates.

Phyllosilicates	
Element	**Detection limit (ppm)**
CaO	148
F	833
SiO_2	235
Rb_2O	345
TiO_2	216
Na_2O	108
Cl	81
K_2O	60
Cr_2O_3	199
MgO	105
Cs_2O	334
BaO	369
MnO	238
Al_2O_3	111
NiO	372
FeO	189

Table XIII-11. Detection limits for electron micro-analysis of zircon

Zircon	
Element	**Detection limit (ppm)**
Ca	170
F	1188
P	400
Si	193
Ti	255
Mg	99
Ce	915
Nd	383
La	432
Al	129
Th	353
Fe	218
Mn	297
Zr	369
Hf	594
U	437

Table XIII-12. Detection limits for electron micro-analysis of pyroxene.

Pyroxene	
Element	**Detection limit (ppm)**
Ni	298
F	522
Ca	134
Si	107
Cr	175
Na	119
Ti	195
V	150

Mn	247
Mg	103
Zn	595
Fe	183
Al	95
K	58

Table XIII-13. Detection limits for electron micro-analysis of apatite.

Apatite	
Element	**Detection limit (ppm)**
La	348
F	1025
Sr	575
P	109
Nd	226
Na	121
Ce	980
Ca	73
Mn	238
Mg	90
Cl	93
Fe	188

Table XIII-14. Detection limits for electron micro-analysis of oxide minerals.

Oxides	
Element	**Detection limit (ppm)**
P	275
Na	121
S	197
Ba	444
Bi	572
Mg	79
Pb	446
V	182
Ag	255
As	336
K	150
Fe	196
Ca	153
Al	107
Ti	251
Ni	259
Zn	636
Si	119
Cr	230
Cu	310
Co	319
Zr	261
Mn	293
Au	246

Amphibole Electronic Probe Micro-Analyses

Table XIII-15. Micro-analyses of amphibole crystals.

Lithology	Sample	SiO_2	TiO_2	Al_2O_3	Cr_2O_3	MgO	CaO	MnO	FeO	Na_2O	K_2O	Total
Amphibolite	SEM-TOR-15A	46.15	2.23	8.65	0.09	11.99	10.41	0.33	15.37	1.86	0.21	**97.29**
Amphibolite	SEM-TOR-15A	45.18	2.34	9.74	0.08	11.31	10.60	0.30	15.49	2.15	0.21	**97.39**
Amphibolite	SEM-TOR-15A	44.59	2.48	10.19	0.08	11.00	10.61	0.31	15.65	2.22	0.23	**97.36**
Amphibolite	SEM-TOR-15A	44.62	2.41	10.18	0.10	10.91	10.68	0.31	15.63	2.11	0.24	**97.17**
Amphibolite	SEM-TOR-15A	46.75	2.10	8.54	0.12	11.90	10.68	0.32	14.99	1.93	0.21	**97.52**
Amphibolite	SEM-TOR-15A	44.48	2.49	10.34	0.10	10.90	10.65	0.31	15.90	2.22	0.21	**97.59**
Amphibolite	SEM-TOR-15A	45.03	2.46	9.52	0.11	11.63	10.44	0.28	15.46	2.27	0.21	**97.42**
Amphibolite	SEM-TOR-15A	45.06	2.24	9.78	0.10	11.58	10.48	0.35	15.35	2.18	0.22	**97.33**
Amphibolite	SEM-TOR-15A	45.44	2.28	9.20	0.15	11.65	10.38	0.30	15.44	2.23	0.19	**97.25**
Amphibolite	SEM-TOR-15A	44.82	2.36	9.80	0.09	11.17	10.39	0.32	15.40	2.13	0.23	**96.69**
Amphibolite	SEM-TOR-15B	44.22	2.43	9.92	0.16	10.42	10.16	0.36	16.23	2.04	0.20	**96.15**
Amphibolite	SEM-TOR-15B	43.97	2.41	10.24	0.13	10.17	10.16	0.32	16.43	2.13	0.21	**96.16**
Amphibolite	SEM-TOR-15B	44.84	2.20	9.60	0.10	10.65	10.22	0.30	16.08	1.85	0.27	**96.12**
Amphibolite	SEM-TOR-15B	44.57	1.94	10.03	0.11	10.35	10.49	0.38	15.97	1.73	0.34	**95.91**
Amphibolite	SEM-TOR-15B	44.29	2.36	9.78	0.12	10.61	10.15	0.37	16.34	2.00	0.22	**96.24**
Amphibolite	SEM-TOR-15B	44.33	2.05	10.05	0.10	10.45	10.41	0.35	16.04	1.79	0.32	**95.89**

Amphibolite	SEM-TOR-15B	43.51	2.54	10.44	0.15	10.03	10.17	0.33	16.49	2.20	0.27	**96.14**
Amphibolite	SEM-TOR-15B	43.77	2.09	10.17	0.12	10.41	10.30	0.34	16.35	2.02	0.32	**95.87**
Amphibolite	SEM-TOR-3A	46.56	2.02	8.25	0.18	11.65	10.78	0.31	15.48	1.75	0.38	**97.36**
Amphibolite	SEM-TOR-3A	47.24	1.64	7.49	0.15	12.04	10.61	0.34	15.42	1.50	0.31	**96.74**
Amphibolite	SEM-TOR-3A	46.07	2.05	8.32	0.15	11.65	11.15	0.30	14.87	1.74	0.42	**96.72**
Amphibolite	SEM-TOR-3A	46.73	1.91	7.77	0.20	11.81	10.64	0.34	15.12	1.64	0.39	**96.53**
Amphibolite	SEM-TOR-3A	47.74	1.79	7.30	0.11	12.34	10.84	0.36	14.45	1.50	0.29	**96.72**
Amphibolite	SEM-TOR-3A	47.27	1.83	7.96	0.13	12.17	10.74	0.35	14.73	1.59	0.31	**97.08**
Amphibolite	SEM-TOR-3A	47.16	1.77	7.54	0.17	12.04	10.88	0.41	14.46	1.60	0.32	**96.33**
Amphibolite	SEM-TOR-3A	47.59	1.65	7.12	0.13	12.46	10.82	0.40	14.26	1.56	0.27	**96.26**
Amphibolite	SEM-TOR-3A	45.88	1.54	7.96	0.41	11.34	11.28	0.37	15.65	1.54	0.40	**96.38**
Amphibolite	SEM-TOR-3A	46.74	1.43	7.81	0.35	11.69	11.39	0.34	15.02	1.46	0.43	**96.64**
Amphibolite	SEM-TOR-3A	47.04	1.36	7.66	0.08	11.97	11.13	0.39	15.17	1.54	0.32	**96.65**
Amphibolite	SEM-TOR-3A	47.52	1.46	7.24	0.15	12.24	11.11	0.37	14.74	1.48	0.31	**96.62**
Amphibolite	SEM-TOR-3B	47.27	2.07	7.74	0.10	12.42	11.37	0.31	14.39	1.66	0.35	**97.69**
Amphibolite	SEM-TOR-3B	47.02	2.00	7.98	0.10	12.25	11.41	0.36	14.48	1.57	0.36	**97.52**
Amphibolite	SEM-TOR-3B	48.72	1.57	6.67	0.16	13.31	11.31	0.30	13.96	1.45	0.32	**97.76**
Amphibolite	SEM-TOR-3B	45.67	2.33	8.79	0.11	11.59	11.49	0.31	14.96	1.87	0.38	**97.50**

Amphibolite	SEM-TOR-3B	49.74	1.38	5.90	0.14	13.51	11.67	0.31	13.27	1.19	0.28	**97.38**
Amphibolite	SEM-TOR-3B	46.26	2.07	8.46	0.07	11.87	11.49	0.35	14.71	1.79	0.39	**97.46**
Amphibolite	SEM-TOR-3B	47.79	1.79	7.28	0.09	12.38	11.99	0.24	14.01	1.34	0.44	**97.33**
Amphibolite	SEM-TOR-3B	46.13	2.20	8.68	0.09	11.31	11.79	0.31	14.79	1.64	0.49	**97.43**
Amphibolite	SEM-TOR-6	47.92	0.99	6.43	0.02	12.79	10.42	0.35	15.82	1.18	0.41	**96.34**
Amphibolite	SEM-TOR-6	50.60	0.22	4.91	0.07	13.65	10.87	0.37	14.96	0.97	0.24	**96.86**
Amphibolite	SEM-TOR-6	49.55	0.56	5.13	0.10	13.43	10.86	0.41	15.20	0.92	0.29	**96.45**
Amphibolite	SEM-TOR-6	49.63	0.51	5.25	0.03	13.25	10.99	0.36	15.46	1.01	0.31	**96.79**
Amphibolite	SEM-TOR-6	46.69	1.79	7.11	0.07	11.66	11.27	0.29	15.76	1.47	0.44	**96.55**
Amphibolite	SEM-TOR-6	49.03	1.12	5.57	0.10	12.84	10.83	0.29	15.53	1.19	0.36	**96.85**
Amphibolite	SEM-TOR-6	46.95	1.36	6.90	0.12	11.80	11.19	0.32	15.84	1.43	0.46	**96.37**
Amphibolite	SEM-TOR-6	46.07	1.77	7.51	0.11	11.21	11.40	0.31	16.16	1.45	0.56	**96.55**
Amphibolite	SEM-TOR-6	46.64	1.75	7.35	0.07	11.27	11.39	0.34	15.67	1.33	0.60	**96.41**
Amphibolite	SEM-TOR-6	44.78	2.20	8.69	0.13	10.36	11.44	0.27	16.40	1.70	0.74	**96.72**
Amphibolite	SEM-TOR-6	45.51	1.83	7.85	0.05	10.98	11.26	0.36	16.06	1.49	0.59	**95.97**
Amphibolite	SEM-TOR-6	46.28	1.72	7.86	0.11	10.75	11.47	0.28	15.98	1.45	0.68	**96.57**
Amphibolite	SEM-TOR-6	47.11	1.67	6.93	0.12	11.48	11.00	0.34	15.85	1.44	0.45	**96.37**
Amphibolite	SEM-TOR-6	45.49	1.88	8.05	0.08	10.72	11.27	0.34	16.13	1.59	0.65	**96.21**

Amphibolite	SEM-TOR-6	45.74	2.09	7.83	0.08	11.08	11.01	0.39	16.31	1.66	0.51	**96.70**
Amphibolite	SEM-TOR-6	45.04	2.10	8.52	0.10	10.49	11.26	0.31	16.29	1.59	0.66	**96.36**
Amphibolite	SEM-TOR-7A	51.15	0.81	5.16	0.09	14.98	11.28	0.18	12.24	1.00	0.29	**97.16**
Amphibolite	SEM-TOR-7A	50.73	0.89	5.48	0.11	15.03	11.33	0.21	12.21	1.04	0.31	**97.33**
Amphibolite	SEM-TOR-7A	51.77	0.64	4.96	0.11	15.36	11.29	0.20	11.88	0.81	0.23	**97.25**
Amphibolite	SEM-TOR-7B	45.19	2.74	8.38	0.13	11.16	10.86	0.28	14.88	2.03	0.53	**96.18**
Amphibolite	SEM-TOR-7B	51.86	0.38	3.95	0.12	14.19	10.99	0.36	13.43	0.82	0.20	**96.30**
Amphibolite	SEM-TOR-7B	44.60	2.76	9.05	0.15	10.84	10.87	0.27	15.21	2.04	0.57	**96.35**
Amphibolite	SEM-TOR-7B	51.73	0.29	3.98	0.09	14.09	10.91	0.34	13.82	0.82	0.19	**96.25**
Amphibolite	SEM-TOR-7B	44.17	2.89	9.09	0.11	10.60	10.82	0.28	15.61	2.15	0.57	**96.28**
Amphibolite	SEM-TOR-7B	51.84	0.38	4.03	0.09	13.89	11.35	0.41	13.56	0.82	0.20	**96.58**
Amphibolite	SEM-TOR-7B	49.02	1.43	5.88	0.15	13.13	10.91	0.37	14.07	1.22	0.32	**96.49**
Amphibolite	SEM-TOR-7B	49.43	1.35	5.51	0.15	13.19	10.79	0.34	14.06	1.19	0.31	**96.32**
Amphibolite	SEM-TOR-7B	50.01	1.31	4.96	0.05	13.53	10.83	0.33	13.72	1.13	0.26	**96.13**
Amphibolite	SEM-TOR-7B	49.89	1.33	5.23	0.12	13.21	10.88	0.37	13.64	1.16	0.28	**96.10**
Digested enclave	SEM-TOR-8A	44.16	2.46	9.39	0.04	10.07	10.44	0.39	16.77	1.90	0.57	**96.18**
Digested enclave	SEM-TOR-8A	44.75	2.04	8.92	0.07	10.68	10.54	0.42	16.35	1.68	0.49	**95.94**
Digested enclave	SEM-TOR-8A	44.00	2.38	9.41	0.12	10.12	10.58	0.46	16.67	1.83	0.56	**96.11**

Digested enclave	SEM-TOR-8A	44.44	2.04	8.92	0.06	10.34	10.88	0.37	16.42	1.66	0.52	**95.65**
Digested enclave	SEM-TOR-8A	44.57	2.01	9.11	0.07	10.27	10.59	0.39	16.62	1.79	0.54	**95.96**
Digested enclave	SEM-TOR-8A	44.46	2.19	9.27	0.08	9.93	10.73	0.37	16.49	1.63	0.57	**95.70**
Digested enclave	SEM-TOR-8A	43.83	2.47	9.79	0.03	9.89	10.60	0.46	17.41	2.17	0.63	**97.29**
Digested enclave	SEM-TOR-8A	43.42	2.62	9.95	0.11	9.75	10.78	0.41	17.47	2.09	0.66	**97.24**
Digested enclave	SEM-TOR-8A	44.59	2.48	9.50	0.07	10.15	10.58	0.45	17.18	2.00	0.59	**97.56**
Digested enclave	SEM-TOR-8A	46.37	1.84	8.28	0.03	11.16	11.25	0.38	16.03	1.35	0.51	**97.19**
Digested enclave	SEM-TOR-8A	44.47	2.29	9.68	0.08	10.31	11.02	0.38	16.63	1.84	0.64	**97.33**
Digested enclave	SEM-TOR-8A	44.30	2.58	9.56	0.09	10.26	10.59	0.47	16.64	1.94	0.62	**97.06**
Digested enclave	SEM-TOR-8B	43.38	2.38	10.01	0.09	9.88	10.78	0.43	17.46	2.08	0.64	**97.13**
Digested enclave	SEM-TOR-8B	44.49	2.18	9.80	0.06	10.19	10.81	0.41	16.97	1.85	0.59	**97.34**
Digested enclave	SEM-TOR-8B	43.61	2.66	9.77	0.08	10.00	10.53	0.50	17.13	2.16	0.65	**97.10**
Digested enclave	SEM-TOR-8B	44.29	2.27	9.79	0.10	10.08	10.96	0.35	16.91	1.82	0.63	**97.19**
Digested enclave	SEM-TOR-8B	55.25	0.12	1.10	0.12	16.95	1.27	0.99	21.97	0.19	0.01	**97.95**
Digested enclave	SEM-TOR-8B	54.39	0.30	1.76	0.06	16.36	2.21	0.92	21.66	0.24	0.05	**97.96**
Digested enclave	SEM-TOR-8B	45.73	1.66	7.90	0.12	11.78	10.46	0.45	16.17	1.39	0.40	**96.05**
Digested enclave	SEM-TOR-8B	44.03	2.53	9.81	0.09	10.57	10.77	0.46	16.31	1.99	0.59	**97.14**
Digested enclave	SEM-TOR-8B	44.01	2.40	9.42	0.07	10.61	10.72	0.48	16.51	1.78	0.57	**96.56**

Digested enclave	SEM-TOR-8B	44.10	2.45	9.58	0.04	10.37	10.50	0.48	16.79	2.08	0.58	**96.96**
Diorite	SEM-TOR-13	43.85	2.64	10.43	0.08	10.07	10.50	0.33	16.93	2.00	0.17	**97.01**
Diorite	SEM-TOR-13	46.43	1.65	8.35	0.10	10.90	9.86	0.47	17.98	1.68	0.23	**97.63**
Diorite	SEM-TOR-13	43.11	2.59	10.78	0.06	9.42	10.28	0.39	18.39	2.13	0.19	**97.35**
Diorite	SEM-TOR-13	43.63	2.57	10.65	0.11	9.40	10.36	0.35	18.11	2.10	0.18	**97.44**
Diorite	SEM-TOR-13	43.47	2.84	10.95	0.08	10.67	10.37	0.28	16.29	2.55	0.14	**97.62**
Diorite	SEM-TOR-13	43.79	2.32	10.40	0.06	9.58	10.56	0.37	17.94	1.95	0.24	**97.21**
Diorite	SEM-TOR-13	44.27	2.43	10.48	0.05	9.89	10.27	0.39	17.63	2.30	0.15	**97.86**
Diorite	SEM-TOR-13	43.25	3.03	10.74	0.08	10.36	10.44	0.32	16.63	2.56	0.17	**97.56**
Diorite	SEM-TOR-13	43.62	2.94	10.57	0.07	10.52	10.59	0.28	15.97	2.45	0.17	**97.16**
Diorite	SEM-TOR-13	44.65	2.51	9.79	0.05	10.03	10.38	0.40	17.39	1.97	0.26	**97.42**
Diorite	SEM-TOR-13	43.47	2.94	10.34	0.07	9.78	10.59	0.34	17.07	2.54	0.15	**97.29**
Diorite	SEM-TOR-13	46.82	1.58	7.46	0.07	10.92	10.56	0.37	17.48	1.38	0.27	**96.89**
Diorite	SEM-TOR-13	44.01	2.42	9.73	0.07	9.81	10.38	0.36	17.61	2.32	0.20	**96.92**
Diorite	SEM-TOR-13	46.02	1.70	8.44	0.08	10.39	9.97	0.47	18.06	1.72	0.22	**97.07**
Diorite	SEM-TOR-18A	42.69	2.73	11.51	0.03	11.31	10.90	0.24	14.30	2.45	0.20	**96.35**
Diorite	SEM-TOR-18A	44.86	2.00	9.29	0.02	11.58	10.17	0.31	15.41	1.87	0.27	**95.77**
Diorite	SEM-TOR-18A	42.83	2.87	11.44	0.10	12.09	11.10	0.23	12.97	2.42	0.21	**96.24**

Diorite	SEM-TOR-18A	44.97	2.04	9.40	0.08	11.61	10.47	0.25	15.23	1.99	0.29	**96.32**
Diorite	SEM-TOR-18A	42.68	2.75	11.88	0.08	11.38	11.15	0.21	14.16	2.47	0.19	**96.94**
Diorite	SEM-TOR-18A	43.10	2.86	11.45	0.06	11.56	11.18	0.23	13.97	2.50	0.16	**97.06**
Diorite	SEM-TOR-18A	42.72	2.65	11.62	0.06	12.02	11.25	0.19	13.28	2.44	0.18	**96.40**
Diorite	SEM-TOR-18A	43.06	2.38	10.97	0.07	11.25	10.53	0.29	15.34	2.16	0.30	**96.33**
Diorite	SEM-TOR-18A	45.90	1.64	9.00	0.05	12.09	10.63	0.27	14.94	1.62	0.37	**96.51**
Diorite	SEM-TOR-18A	45.76	1.93	8.71	0.04	12.01	10.59	0.26	15.11	1.60	0.36	**96.38**
Diorite	SEM-TOR-18A	47.54	1.33	7.68	0.06	12.93	10.60	0.30	14.79	1.31	0.28	**96.81**
Diorite	SEM-TOR-18B	42.92	2.76	11.69	0.09	11.68	11.32	0.15	13.37	2.20	0.18	**96.36**
Diorite	SEM-TOR-18B	42.88	2.91	11.51	0.08	12.15	11.19	0.19	12.77	2.47	0.16	**96.31**
Diorite	SEM-TOR-18B	43.63	2.64	11.26	0.12	12.50	11.03	0.17	12.41	2.42	0.15	**96.32**
Diorite	SEM-TOR-18B	44.46	2.35	10.33	0.07	11.61	10.63	0.24	14.38	2.14	0.27	**96.48**
Diorite	SEM-TOR-18B	43.66	2.61	10.96	0.11	11.85	10.45	0.23	13.99	2.29	0.29	**96.43**
Diorite	SEM-TOR-18B	44.95	2.24	9.76	0.05	11.98	10.50	0.27	14.20	2.09	0.22	**96.25**
Diorite	SEM-TOR-18B	42.83	2.96	11.59	0.07	12.06	11.32	0.21	12.32	2.34	0.17	**95.86**
Diorite	SEM-TOR-18B	44.80	2.00	9.30	0.11	11.67	10.40	0.26	15.18	1.91	0.28	**95.91**
Diorite	SEM-TOR-18B	45.21	2.07	9.26	0.13	11.84	10.42	0.28	14.79	1.87	0.30	**96.16**
Diorite	SEM-TOR-18B	44.82	2.05	9.53	0.07	11.83	10.45	0.33	14.85	1.84	0.28	**96.05**

Diorite	SEM-TOR-20	43.42	2.85	11.05	0.09	11.73	10.91	0.24	14.36	2.32	0.16	**97.12**
Diorite	SEM-TOR-20	47.16	1.54	8.24	0.07	12.91	10.35	0.33	14.80	1.66	0.20	**97.26**
Diorite	SEM-TOR-20	43.92	2.41	10.64	0.07	11.84	10.54	0.24	14.64	2.35	0.22	**96.88**
Diorite	SEM-TOR-20	43.79	2.39	10.32	0.13	11.23	10.59	0.34	15.63	2.23	0.23	**96.89**
Diorite	SEM-TOR-20	43.83	2.65	10.93	0.09	11.97	10.68	0.25	14.16	2.40	0.16	**97.12**
Diorite	SEM-TOR-20	42.93	3.05	11.23	0.07	11.24	10.87	0.31	14.94	2.59	0.16	**97.39**
Diorite	SEM-TOR-20	43.35	2.96	11.20	0.05	11.42	10.93	0.28	14.22	2.44	0.16	**97.02**
Diorite	SEM-TOR-20	43.21	2.99	11.13	0.08	10.93	10.84	0.25	15.36	2.33	0.18	**97.29**
Diorite	SEM-TOR-20	43.44	2.93	11.00	0.08	11.74	10.91	0.28	14.14	2.39	0.17	**97.07**
Diorite	SEM-TOR-20	45.68	2.01	9.23	0.08	11.43	10.34	0.31	16.17	1.94	0.23	**97.42**
Diorite	SEM-TOR-4	49.19	0.92	5.28	0.08	10.97	10.64	0.39	17.53	0.86	0.31	**96.16**
Diorite	SEM-TOR-4	43.99	2.10	9.58	0.10	8.66	10.49	0.46	19.14	1.69	0.29	**96.50**
Diorite	SEM-TOR-4	43.61	2.15	9.17	0.08	9.64	9.86	0.44	18.80	1.95	0.28	**95.98**
Diorite	SEM-TOR-4	46.76	1.29	7.52	0.10	9.96	10.18	0.49	18.52	1.27	0.28	**96.35**
Diorite	SEM-TOR-4	51.34	0.54	1.97	0.09	14.27	2.34	0.78	23.53	0.28	0.06	**95.19**
Diorite	SEM-TOR-4	52.85	0.28	1.95	0.09	13.64	2.68	0.95	23.98	0.26	0.05	**96.72**
Diorite	SEM-TOR-4	52.98	0.29	1.98	0.05	14.25	1.81	0.91	24.33	0.25	0.01	**96.86**
Diorite	SEM-TOR-4	52.80	0.26	2.00	0.05	14.31	1.84	0.88	24.26	0.29	0.03	**96.70**

Diorite	SEM-TOR-9B	43.97	3.06	9.85	0.12	11.18	10.68	0.27	15.48	2.32	0.39	**97.30**
Diorite	SEM-TOR-9B	43.82	3.08	9.91	0.08	10.77	10.56	0.32	16.14	2.27	0.37	**97.32**
Diorite	SEM-TOR-9B	43.78	3.49	9.73	0.10	11.07	10.76	0.26	15.58	2.35	0.42	**97.54**
Diorite	SEM-TOR-9B	45.32	2.03	8.95	0.04	10.96	10.31	0.34	16.97	1.79	0.30	**96.99**
Diorite	SEM-TOR-9B	47.58	1.27	7.37	0.08	11.89	10.25	0.38	16.90	1.55	0.29	**97.54**
Diorite	SEM-TOR-9B	49.98	0.82	5.28	0.09	12.57	10.93	0.35	16.33	0.93	0.28	**97.57**
Fine-grained amphibolite	SEM-TOR-1	44.96	1.62	9.01	0.08	10.95	10.66	0.27	15.24	1.94	0.39	**95.12**
Fine-grained amphibolite	SEM-TOR-1	45.35	1.61	8.97	0.09	10.92	10.67	0.34	15.01	1.90	0.40	**95.24**
Fine-grained amphibolite	SEM-TOR-1	44.97	1.54	9.37	0.10	10.86	10.82	0.34	15.07	1.90	0.44	**95.39**
Fine-grained amphibolite	SEM-TOR-2	45.28	2.20	8.79	0.06	11.35	10.81	0.32	15.94	2.01	0.38	**97.14**
Fine-grained amphibolite	SEM-TOR-2	45.73	2.23	8.76	0.05	11.33	10.80	0.28	15.93	2.09	0.37	**97.55**
Fine-grained amphibolite	SEM-TOR-2	45.77	2.13	8.55	0.10	11.57	10.74	0.31	15.89	1.81	0.38	**97.27**
Fine-grained amphibolite	SEM-TOR-2	45.06	1.93	9.13	0.05	11.17	10.95	0.27	15.92	1.89	0.44	**96.81**
Fine-grained amphibolite	SEM-TOR-2	45.74	1.98	8.61	0.08	11.56	10.92	0.30	15.73	1.85	0.41	**97.18**

Fine-grained amphibolite	SEM-TOR-2	45.04	2.13	9.15	0.12	11.15	10.83	0.31	16.04	2.07	0.41	**97.24**
Gabbro	SEM-TOR-9A	53.31	0.34	2.78	0.06	15.36	2.83	0.70	22.36	0.45	0.03	**98.22**
Gabbro	SEM-TOR-9A	52.33	0.40	3.58	0.08	14.31	4.80	0.63	21.50	0.55	0.11	**98.28**
Gabbro	SEM-TOR-9A	53.77	0.34	2.28	0.07	16.09	1.95	0.65	22.95	0.36	0.03	**98.48**
Gabbro	SEM-TOR-9A	53.67	0.22	2.02	0.06	16.27	1.53	0.69	23.02	0.21	0.01	**97.69**
Gabbro	SEM-TOR-9C	44.84	2.05	9.45	0.10	11.28	10.16	0.31	16.29	2.06	0.26	**96.79**
Gabbro	SEM-TOR-9C	45.84	1.81	9.07	0.07	11.04	10.20	0.32	16.59	1.66	0.29	
Gabbro	SEM-TOR-9C	44.71	1.95	9.26	0.08	10.89	10.16	0.37	16.18	2.01	0.28	**95.89**
Gabbro	SEM-TOR-9C	47.32	1.23	7.58	0.10	10.88	10.69	0.39	17.23	1.12	0.42	**96.95**
Gabbro	SEM-TOR-9C	48.98	0.89	6.24	0.06	12.69	9.88	0.44	16.56	0.99	0.23	**96.95**
Gabbro	SEM-TOR-9C	54.34	0.08	1.40	0.02	15.40	3.17	0.77	22.00	0.15	0.02	**97.35**
Leucocratic inj.	SEM-TOR-1	44.89	2.64	9.00	0.08	11.30	10.84	0.33	15.28	2.13	0.37	**96.85**
Leucocratic inj.	SEM-TOR-1	45.08	2.23	8.98	0.12	10.74	10.68	0.29	16.32	1.88	0.40	**96.71**
Leucocratic inj.	SEM-TOR-1	49.95	0.92	5.33	0.09	11.97	11.17	0.33	15.45	0.88	0.39	**96.47**
Leucocratic inj.	SEM-TOR-1	45.16	2.46	8.79	0.08	11.20	10.74	0.33	15.44	2.14	0.34	**96.68**
Leucocratic inj.	SEM-TOR-1	44.73	2.30	9.04	0.09	10.44	10.68	0.34	16.67	2.02	0.40	**96.70**
Leucocratic inj.	SEM-TOR-1	44.82	2.11	9.11	0.08	10.30	10.63	0.38	16.81	1.92	0.41	**96.58**
Leucocratic inj.	SEM-TOR-2	44.95	2.48	8.98	0.11	11.23	10.70	0.29	15.80	2.00	0.35	**96.89**

Leucocratic inj.	SEM-TOR-2	44.98	2.45	9.01	0.05	11.17	10.74	0.30	15.97	2.13	0.34	**97.13**
Leucocratic inj.	SEM-TOR-2	44.83	2.49	8.99	0.06	11.02	10.74	0.32	15.76	2.12	0.38	**96.70**
Leucocratic inj.	SEM-TOR-2	44.71	2.33	9.13	0.04	10.83	10.67	0.35	16.25	2.04	0.36	**96.71**
Pegmatoid	SEM-TOR-16A	43.23	4.01	11.39	0.16	13.82	11.39	0.11	9.71	2.31	0.29	**96.41**
Pegmatoid	SEM-TOR-16A	43.13	4.01	11.39	0.12	12.56	11.28	0.13	11.22	2.40	0.30	**96.52**
Pegmatoid	SEM-TOR-16A	43.30	3.92	11.47	0.24	13.76	11.40	0.09	9.40	2.46	0.30	**96.34**
Pegmatoid	SEM-TOR-16A	43.05	4.06	11.57	0.21	13.46	11.34	0.15	10.00	2.51	0.29	**96.64**
Pegmatoid	SEM-TOR-16A	47.96	1.37	7.54	0.10	12.42	10.62	0.24	14.82	1.46	0.28	**96.80**
Pegmatoid	SEM-TOR-16A	50.10	0.91	5.85	0.10	13.74	10.57	0.23	13.79	1.14	0.23	**96.66**
Pegmatoid	SEM-TOR-16A	50.97	0.85	4.93	0.11	13.63	11.00	0.26	14.07	0.84	0.23	**96.90**
Pegmatoid	SEM-TOR-16A	49.82	1.06	6.25	0.11	13.16	10.71	0.27	14.24	1.07	0.26	**96.94**
Pegmatoid	SEM-TOR-16A	43.69	2.98	12.34	0.17	14.31	11.11	0.11	9.83	2.82	0.18	**97.54**
Pegmatoid	SEM-TOR-16A	45.06	2.28	10.25	0.12	13.02	10.54	0.23	13.30	2.30	0.21	**97.29**
Pegmatoid	SEM-TOR-16A	45.92	1.89	9.02	0.07	12.52	10.54	0.29	14.25	2.02	0.24	**96.76**
Pegmatoid	SEM-TOR-16A	45.79	1.95	9.20	0.11	12.35	10.50	0.25	15.04	1.94	0.28	**97.42**
Pegmatoid	SEM-TOR-16A	43.63	2.80	10.05	0.07	11.11	10.62	0.20	15.25	2.20	0.26	**96.19**
Pegmatoid	SEM-TOR-16A	45.88	1.97	8.95	0.08	11.79	10.04	0.29	15.19	1.83	0.27	**96.27**
Pegmatoid	SEM-TOR-16A	49.81	1.00	5.73	0.09	13.74	10.82	0.27	13.87	1.09	0.24	**96.65**

Pegmatoid	SEM-TOR-16A	50.93	0.80	5.00	0.07	13.97	10.34	0.30	13.88	0.94	0.21	**96.43**
Pegmatoid	SEM-TOR-16B	43.02	2.95	12.18	0.07	12.66	11.36	0.17	12.28	2.71	0.19	**97.59**
Pegmatoid	SEM-TOR-16B	46.44	1.75	9.17	0.11	12.32	10.35	0.29	15.10	1.85	0.23	**97.61**
Pegmatoid	SEM-TOR-16B	46.66	1.72	8.91	0.09	12.76	10.02	0.34	14.85	1.89	0.21	**97.44**
Pegmatoid	SEM-TOR-16B	49.45	1.15	6.57	0.07	13.71	10.44	0.28	14.30	1.16	0.25	**97.38**
Pegmatoid	SEM-TOR-16B	50.36	0.90	5.63	0.04	13.54	10.99	0.26	14.53	0.99	0.22	**97.46**
Pegmatoid	SEM-TOR-16B	46.32	1.71	9.13	0.05	11.86	10.46	0.30	15.65	1.75	0.32	**97.54**
Pegmatoid	SEM-TOR-16B	45.61	1.96	9.58	0.10	13.26	10.34	0.26	13.62	2.04	0.24	**97.00**
Pegmatoid	SEM-TOR-16B	49.77	0.95	5.95	0.08	13.92	11.04	0.25	13.82	1.06	0.22	**97.05**
Pegmatoid	SEM-TOR-16B	46.16	1.85	9.10	0.05	12.70	10.46	0.24	14.71	2.03	0.25	**97.54**
Pegmatoid	SEM-TOR-16B	50.50	0.92	5.66	0.08	14.12	10.94	0.28	13.69	1.13	0.22	**97.53**
Pegmatoid	SEM-TOR-16B	43.09	2.72	12.04	0.08	12.44	11.19	0.21	12.53	2.48	0.16	**96.95**
Pegmatoid	SEM-TOR-16B	45.25	2.36	9.60	0.10	12.17	10.23	0.29	14.89	2.14	0.19	**97.23**
Pegmatoid	SEM-TOR-16B	46.58	1.73	8.82	0.08	12.81	10.35	0.27	14.74	1.73	0.22	**97.34**
Pegmatoid	SEM-TOR-16B	45.54	2.18	9.46	0.06	12.39	10.48	0.27	14.46	1.98	0.20	**97.01**
Quartz-diorite	SEM-TOR-10	50.23	0.74	5.43	0.07	13.49	10.65	0.40	15.01	0.79	0.22	**97.03**
Quartz-diorite	SEM-TOR-10	47.27	1.18	7.63	0.06	11.48	11.14	0.41	16.02	1.09	0.28	**96.56**
Quartz-diorite	SEM-TOR-10	50.45	0.63	5.01	0.14	13.60	10.93	0.30	14.39	0.90	0.20	**96.54**

Quartz-diorite	SEM-TOR-10	49.86	0.68	5.64	0.12	13.51	10.49	0.32	14.73	0.95	0.21	**96.51**
Quartz-diorite	SEM-TOR-10	45.70	1.59	8.70	0.07	12.17	10.31	0.38	15.77	1.54	0.28	**96.51**
Quartz-diorite	SEM-TOR-10	49.43	0.74	5.04	0.09	13.72	10.80	0.39	15.04	0.83	0.22	**96.30**
Quartz-diorite	SEM-TOR-10	46.04	1.39	8.46	0.10	13.14	9.90	0.36	15.26	1.53	0.24	**96.41**
Quartz-diorite	SEM-TOR-10	48.40	0.75	5.95	0.08	13.22	10.82	0.33	15.17	1.08	0.26	**96.05**
Quartz-diorite	SEM-TOR-11	50.84	0.57	5.31	0.09	14.12	10.74	0.45	13.69	0.75	0.17	**96.73**
Quartz-diorite	SEM-TOR-11	51.37	0.33	4.96	0.07	14.18	11.18	0.42	13.42	0.59	0.13	**96.64**
Quartz-diorite	SEM-TOR-11	50.34	0.77	5.38	0.09	14.34	10.49	0.48	13.76	0.84	0.20	**96.69**
Quartz-diorite	SEM-TOR-11	47.41	1.18	7.54	0.06	12.70	10.32	0.45	15.08	1.24	0.30	**96.28**
Quartz-diorite	SEM-TOR-11	54.41	0.29	1.65	0.05	17.39	2.96	0.92	19.47	0.23	0.03	**97.40**
Quartz-diorite	SEM-TOR-11	50.29	0.58	5.78	0.09	13.92	11.11	0.48	13.91	0.82	0.16	**97.13**
Quartz-diorite	SEM-TOR-12	50.17	0.77	5.36	0.08	14.32	10.48	0.42	14.56	1.04	0.20	**97.40**
Quartz-diorite	SEM-TOR-12	49.05	1.35	5.88	0.07	13.81	10.82	0.31	14.20	1.26	0.25	**97.01**
Quartz-diorite	SEM-TOR-12	54.79	0.29	1.91	0.09	17.86	2.50	0.74	19.44	0.27	0.03	**97.92**
Quartz-diorite	SEM-TOR-12	52.73	0.22	3.46	0.08	14.97	8.09	0.73	16.54	0.45	0.06	**97.32**
Quartz-diorite	SEM-TOR-14	44.79	2.32	9.83	0.12	11.92	10.50	0.30	14.97	2.08	0.21	**97.05**
Quartz-diorite	SEM-TOR-14	46.28	1.72	8.86	0.08	11.82	10.45	0.36	15.72	1.66	0.25	**97.20**
Quartz-diorite	SEM-TOR-14	45.53	1.80	9.24	0.09	11.34	10.65	0.33	15.91	1.93	0.34	**97.15**

Quartz-diorite	SEM-TOR-14	45.82	1.65	8.94	0.06	11.01	10.72	0.32	16.65	1.75	0.35	**97.25**
Quartz-diorite	SEM-TOR-14	47.69	1.23	7.51	0.11	12.38	10.14	0.33	16.02	1.35	0.29	**97.04**
Quartz-diorite	SEM-TOR-14	49.18	0.97	6.29	0.09	12.98	10.63	0.36	15.01	1.07	0.24	**96.81**
Quartz-diorite	SEM-TOR-14	47.18	1.77	7.93	0.09	12.25	10.42	0.22	15.18	1.64	0.33	**97.00**
Quartz-diorite	SEM-TOR-14	45.41	1.99	9.22	0.12	11.70	10.31	0.32	15.80	2.07	0.26	**97.20**
Quartz-diorite	SEM-TOR-14	46.76	1.78	8.53	0.06	12.06	10.02	0.33	15.70	1.75	0.30	**97.28**
Quartz-diorite	SEM-TOR-14	47.90	1.15	7.47	0.07	12.48	9.71	0.40	16.46	1.50	0.29	**97.42**
Quartz-diorite	SEM-TOR-17A	52.14	0.17	1.52	0.02	13.23	0.62	1.06	26.42	0.30	0.00	**95.47**
Quartz-diorite	SEM-TOR-17A	52.35	0.14	1.48	0.06	13.47	0.72	1.18	25.81	0.26	0.00	**95.45**
Quartz-diorite	SEM-TOR-17A	52.34	0.23	1.69	0.09	13.35	0.65	1.11	26.11	0.29	0.00	**95.85**
Quartz-diorite	SEM-TOR-17A	52.78	0.19	1.60	0.12	13.20	1.30	1.15	25.62	0.23	0.02	**96.19**
Quartz-diorite	SEM-TOR-17A	52.41	0.25	1.50	0.08	13.12	0.80	1.36	26.13	0.22	0.00	**95.86**
Quartz-diorite	SEM-TOR-17A	52.76	0.18	1.35	0.09	13.28	0.91	1.36	25.57	0.19	0.01	**95.70**
Quartz-diorite	SEM-TOR-17A	53.27	0.15	1.33	0.08	13.79	0.92	1.46	25.83	0.21	0.00	**97.03**
Quartz-diorite	SEM-TOR-17A	53.33	0.19	1.36	0.08	13.49	1.12	1.36	26.01	0.23	0.01	**97.17**
Quartz-diorite	SEM-TOR-17A	52.07	0.14	1.50	0.08	13.02	1.20	1.24	24.29	0.28	0.03	**93.85**
Quartz-diorite	SEM-TOR-17A	52.78	0.21	1.47	0.05	13.17	1.38	1.46	25.62	0.25	0.01	**96.38**
Quartz-diorite	SEM-TOR-17A	52.62	0.26	1.82	0.04	12.97	1.61	1.30	25.71	0.32	0.02	**96.67**

Quartz-diorite	SEM-TOR-17A	53.49	0.10	0.93	0.06	13.35	1.12	1.51	26.09	0.14	0.00	**96.78**
Quartz-diorite	SEM-TOR-17B	51.37	0.29	6.92	0.07	9.96	2.40	0.87	23.12	0.38	1.00	**96.38**
Quartz-diorite	SEM-TOR-17B	53.14	0.23	1.62	0.08	12.86	2.02	1.46	26.12	0.23	0.04	**97.79**
Quartz-diorite	SEM-TOR-17B	50.99	0.27	2.03	0.09	12.70	1.76	1.36	25.31	0.42	0.04	**94.97**
Quartz-diorite	SEM-TOR-17B	55.18	0.13	0.91	0.05	12.85	1.18	1.32	23.47	0.19	0.01	**95.29**
Quartz-diorite	SEM-TOR-17B	52.45	0.33	2.41	0.08	12.95	1.70	1.34	25.97	0.57	0.02	**97.83**
Quartz-diorite	SEM-TOR-17B	52.87	0.30	2.08	0.07	13.33	1.12	1.23	26.11	0.50	0.00	**97.62**
Quartz-diorite	SEM-TOR-17B	52.71	0.32	2.08	0.05	12.73	1.10	1.52	27.23	0.58	0.02	**98.33**
Quartz-diorite	SEM-TOR-17B	52.95	0.23	1.58	0.05	13.28	1.11	1.39	26.63	0.21	0.02	**97.45**
Quartz-diorite	SEM-TOR-3B	47.82	1.21	7.08	0.09	11.55	10.03	0.50	17.28	1.28	0.30	**97.13**
Quartz-diorite	SEM-TOR-3B	53.61	0.29	1.86	0.10	15.90	1.98	0.96	22.34	0.27	0.05	**97.36**
Quartz-diorite	SEM-TOR-5	42.89	3.33	11.91	0.08	13.34	11.21	0.13	10.95	2.24	0.17	**96.25**
Quartz-diorite	SEM-TOR-5	42.50	3.78	11.55	0.06	13.31	11.24	0.15	10.83	2.77	0.13	**96.32**
Quartz-diorite	SEM-TOR-5	45.50	1.96	9.20	0.06	11.76	10.46	0.28	14.95	1.91	0.25	**96.32**
Quartz-diorite	SEM-TOR-5	46.11	1.65	8.63	0.09	11.46	10.30	0.28	15.55	1.70	0.21	**95.99**
Quartz-diorite	SEM-TOR-5	46.69	1.34	7.95	0.11	11.93	10.79	0.30	15.31	1.46	0.27	**96.15**
Quartz-diorite	SEM-TOR-5	43.56	2.83	11.18	0.05	13.43	11.44	0.15	11.61	2.58	0.17	**97.00**
Quartz-diorite	SEM-TOR-5	43.50	2.89	11.64	0.09	13.46	11.53	0.13	11.10	2.74	0.17	**97.25**

Quartz-diorite	SEM-TOR-5	43.35	2.68	10.54	0.10	11.33	10.33	0.21	14.56	2.23	0.20	**95.54**
Reaction rim	SEM-TOR-15A	43.41	2.97	10.85	0.03	10.75	10.56	0.30	15.62	2.45	0.16	**97.09**
Reaction rim	SEM-TOR-15A	43.24	2.81	10.49	0.07	10.10	10.47	0.29	16.96	2.39	0.18	**97.00**
Reaction rim	SEM-TOR-15A	43.11	3.07	10.64	0.09	10.64	10.62	0.28	16.35	2.38	0.15	**97.33**
Reaction rim	SEM-TOR-15A	43.13	2.76	10.48	0.08	9.72	10.51	0.36	17.67	2.24	0.18	**97.13**
Reaction rim	SEM-TOR-15B	44.00	2.42	9.80	0.05	9.78	10.24	0.37	17.80	2.17	0.25	**96.87**
Reaction rim	SEM-TOR-15B	43.81	2.30	9.79	0.07	9.61	10.34	0.36	17.75	2.02	0.36	**96.41**
Reaction rim	SEM-TOR-15B	49.50	0.92	5.34	0.08	11.53	10.59	0.50	17.00	0.94	0.27	**96.66**
Reaction rim	SEM-TOR-15B	49.58	0.84	5.30	0.12	11.49	10.24	0.51	17.70	0.95	0.28	**97.00**
Reaction rim	SEM-TOR-15B	53.09	0.04	2.61	0.03	12.51	11.96	0.36	15.99	0.27	0.06	**96.91**
Reaction rim	SEM-TOR-15B	53.46	0.06	2.58	0.04	12.35	11.95	0.39	15.94	0.26	0.05	**97.08**
Reaction rim	SEM-TOR-15B	44.46	0.72	12.07	0.08	7.20	14.67	0.24	14.95	0.81	0.18	**95.38**
Reaction rim	SEM-TOR-15B	49.15	0.25	5.85	0.10	10.73	11.66	0.33	17.38	0.82	0.18	**96.45**
Reaction rim	SEM-TOR-15B	49.56	0.37	5.29	0.05	11.12	11.35	0.40	17.34	0.92	0.18	**96.58**
Reaction rim	SEM-TOR-15B	50.92	0.61	4.58	0.09	12.27	10.84	0.42	16.61	0.72	0.20	**97.26**
Reaction rim	SEM-TOR-15B	47.41	1.25	7.17	0.07	10.62	10.29	0.38	18.39	1.23	0.25	**97.07**
Reaction rim	SEM-TOR-15B	46.61	1.37	7.58	0.12	10.15	10.36	0.42	18.75	1.47	0.28	**97.11**
Reaction rim	SEM-TOR-15B	42.95	2.25	10.38	0.04	8.59	10.38	0.38	19.36	2.13	0.25	**96.71**

Reaction rim	SEM-TOR-2	45.86	1.91	7.94	0.09	10.60	10.73	0.42	16.91	1.64	0.36	**96.46**
Reaction rim	SEM-TOR-2	45.41	1.62	8.29	0.07	10.07	10.50	0.39	17.60	1.79	0.39	**96.13**
Reaction rim	SEM-TOR-2	46.14	1.75	8.13	0.08	10.92	10.75	0.40	16.24	1.55	0.42	**96.38**
Reaction rim	SEM-TOR-2	44.50	2.04	9.08	0.10	10.22	10.70	0.38	16.78	1.95	0.44	**96.17**
Reaction rim	SEM-TOR-2	44.97	2.13	8.97	0.07	10.56	10.34	0.34	16.19	1.99	0.40	**95.95**
Reaction rim	SEM-TOR-3A	46.76	1.57	7.73	0.09	11.59	10.38	0.39	16.30	1.60	0.31	**96.72**
Reaction rim	SEM-TOR-3A	45.85	1.86	8.08	0.11	10.99	10.42	0.42	17.11	1.84	0.36	**97.03**
Reaction rim	SEM-TOR-3A	45.08	2.34	8.69	0.14	10.60	10.74	0.30	16.64	1.99	0.40	**96.92**
Reaction rim	SEM-TOR-3A	45.97	1.82	8.06	0.10	10.88	10.49	0.41	17.13	1.67	0.37	**96.89**
Reaction rim	SEM-TOR-3A	45.24	2.35	8.80	0.07	10.67	10.60	0.40	16.51	1.98	0.36	**96.97**
Reaction rim	SEM-TOR-3A	45.35	2.12	8.72	0.10	10.55	10.57	0.38	16.79	1.86	0.39	**96.82**
Reaction rim	SEM-TOR-3A	46.47	1.62	7.59	0.06	10.48	10.67	0.37	17.56	1.54	0.40	**96.76**
Reaction rim	SEM-TOR-3A	44.87	1.87	8.73	0.05	10.04	10.57	0.46	17.88	1.78	0.44	**96.70**
Reaction rim	SEM-TOR-3A	46.02	1.93	8.57	0.04	10.73	10.36	0.40	16.48	1.83	0.39	**96.74**
Reaction rim	SEM-TOR-3A	44.86	2.64	8.94	0.10	11.07	10.71	0.34	15.55	2.01	0.36	**96.59**
Reaction rim	SEM-TOR-3B	48.42	1.45	6.84	0.02	12.61	10.59	0.37	15.26	1.35	0.31	**97.22**
Reaction rim	SEM-TOR-3B	45.77	1.88	8.59	0.13	11.38	10.86	0.30	16.16	1.59	0.42	**97.07**
Reaction rim	SEM-TOR-3B	48.23	1.37	6.91	0.08	12.39	10.67	0.35	15.34	1.45	0.34	**97.12**

Reaction rim	SEM-TOR-3B	46.20	1.89	8.14	0.11	11.42	10.67	0.42	15.85	1.64	0.39	**96.73**
Reaction rim	SEM-TOR-3B	45.71	2.10	8.84	0.11	10.89	10.85	0.38	16.43	1.74	0.42	**97.47**
Reaction rim	SEM-TOR-3B	45.17	2.23	9.04	0.16	10.76	10.71	0.35	16.72	1.76	0.41	**97.30**
Reaction rim	SEM-TOR-9A	49.43	0.92	5.97	0.11	11.85	10.84	0.46	17.10	1.17	0.33	**98.18**
Reaction rim	SEM-TOR-9A	49.46	0.84	5.81	0.06	12.55	10.46	0.38	16.63	1.18	0.27	**97.64**
Reaction rim	SEM-TOR-9A	44.70	2.03	9.40	0.07	10.62	10.46	0.39	17.19	1.88	0.30	**97.04**
Reaction rim	SEM-TOR-9A	47.42	1.45	6.88	0.09	11.06	10.95	0.42	17.38	1.42	0.54	**97.60**
Reaction rim	SEM-TOR-9B	44.45	3.08	9.63	0.13	11.25	10.60	0.25	15.15	2.33	0.37	**97.22**
Reaction rim	SEM-TOR-9B	48.71	1.06	6.25	0.08	12.33	10.47	0.34	16.22	1.37	0.29	**97.11**
Reaction rim	SEM-TOR-9B	44.11	3.33	9.71	0.12	11.17	10.79	0.26	15.11	2.27	0.43	**97.29**
Reaction rim	SEM-TOR-9B	47.45	1.45	8.04	0.07	11.45	10.69	0.32	16.10	1.21	0.34	**97.13**
Reaction rim	SEM-TOR-9B	43.48	2.95	10.34	0.10	10.12	10.73	0.27	16.46	2.14	0.44	**97.02**
Reaction rim	SEM-TOR-9B	44.06	2.26	9.82	0.08	10.10	10.35	0.39	17.46	2.16	0.36	**97.04**
Reaction rim	SEM-TOR-9C	43.98	2.77	9.38	0.07	10.52	10.62	0.31	16.36	1.53	0.33	**95.87**
Reaction rim	SEM-TOR-9C	49.46	0.86	5.26	0.09	11.96	11.09	0.43	16.35	0.71	0.35	**96.55**
Reaction rim	SEM-TOR-9C	44.87	2.10	9.59	0.07	11.28	10.09	0.31	15.95	2.20	0.27	**96.71**
Reaction rim	SEM-TOR-9C	48.92	0.71	5.55	0.06	12.12	11.08	0.44	16.13	0.68	0.35	**96.05**
Reaction rim	SEM-TOR-9C	43.89	0.79	14.42	0.00	12.37	9.14	0.29	14.87	2.10	0.12	**97.99**

Sulph. Inj.	SEM-TOR-7A	45.42	2.70	8.65	0.15	11.64	11.02	0.21	15.15	2.13	0.53	**97.58**
Sulph. Inj.	SEM-TOR-7A	46.22	2.37	8.22	0.11	11.97	11.01	0.19	14.97	2.15	0.48	**97.69**
Sulph. Inj.	SEM-TOR-7A	52.16	0.30	4.25	0.10	13.74	11.06	0.28	14.86	0.96	0.20	**97.92**
Sulph. Inj.	SEM-TOR-7A	51.39	0.47	3.06	0.08	12.53	9.12	0.40	13.99	0.88	0.15	**92.07**
Sulph. Inj.	SEM-TOR-7A	51.09	0.35	3.21	0.10	12.27	9.08	0.37	14.05	0.97	0.17	**91.65**
Sulph. Inj.	SEM-TOR-7A	44.88	2.96	9.22	0.12	11.71	10.95	0.30	14.87	2.18	0.59	**97.76**
Sulph. Inj.	SEM-TOR-7A	44.98	3.11	8.71	0.11	11.66	10.20	0.28	14.86	2.19	0.56	**96.65**
Sulph. Inj.	SEM-TOR-7A	45.58	2.85	8.68	0.12	11.65	10.83	0.25	14.67	2.28	0.52	**97.43**
Sulph. Inj.	SEM-TOR-7A	48.47	1.72	6.43	0.13	12.69	10.80	0.26	14.04	1.72	0.37	**96.63**
Sulph. Inj.	SEM-TOR-7A	44.26	2.87	8.85	0.13	11.72	10.53	0.22	14.87	2.19	0.61	**96.25**
Sulph. Inj.	SEM-TOR-7A	45.01	2.91	8.96	0.12	11.80	10.75	0.25	14.84	2.12	0.59	**97.34**
Sulph. Inj.	SEM-TOR-7B	50.34	0.83	5.08	0.17	13.08	11.35	0.34	13.94	0.99	0.29	**96.40**
Sulph. Inj.	SEM-TOR-7B	50.26	0.66	4.90	0.14	13.12	11.40	0.30	14.14	1.02	0.28	**96.23**
Sulph. Inj.	SEM-TOR-7B	45.61	2.30	8.37	0.18	12.00	10.94	0.30	14.60	1.97	0.49	**96.75**
Sulph. Inj.	SEM-TOR-7B	50.35	0.94	5.09	0.06	13.60	11.12	0.31	14.04	1.15	0.27	**96.91**
Sulph. Inj.	SEM-TOR-7B	44.59	3.04	9.16	0.14	11.49	10.73	0.24	15.00	2.23	0.55	**97.18**
Sulph. Inj.	SEM-TOR-7B	44.76	2.89	9.14	0.15	11.60	10.80	0.20	14.73	2.26	0.60	**97.13**
Sulph. Inj.	SEM-TOR-7B	51.15	0.82	4.73	0.10	13.65	11.23	0.34	14.14	1.07	0.26	**97.48**

Sulph. Inj.	SEM-TOR-7B	51.01	0.66	4.62	0.11	13.58	11.28	0.27	14.28	1.04	0.28	**97.12**
Sulph. Inj.	SEM-TOR-7B	50.81	0.38	4.73	0.10	12.88	11.70	0.34	15.13	0.85	0.37	**97.28**
Vein	SEM-TOR-15B	44.63	2.43	9.56	0.07	10.75	10.07	0.37	16.51	1.89	0.23	**96.50**
Vein	SEM-TOR-15B	44.28	2.12	10.04	0.10	10.38	10.32	0.38	16.44	1.91	0.35	**96.31**
Vein	SEM-TOR-15B	43.90	2.31	10.35	0.10	10.12	10.27	0.38	16.56	2.06	0.32	**96.37**
Vein	SEM-TOR-15B	44.50	1.93	10.03	0.10	10.41	10.29	0.38	16.52	1.94	0.35	**96.44**
Vein	SEM-TOR-15B	43.71	2.39	10.35	0.06	10.09	10.15	0.31	16.82	2.11	0.26	**96.26**
Vein	SEM-TOR-15B	44.23	1.93	9.92	0.09	10.45	10.15	0.34	16.74	1.99	0.30	**96.13**

Plagioclase Electronic Probe Micro-Analyses

Table XIII-16. Micro-analyses of plagioclase crystals.

Lithology	Sample	SiO_2	Na_2O	BaO	K_2O	CaO	MgO	TiO_2	SrO	Al_2O_3	MnO	FeO	Total
Amphibolite	SEM-TOR-15A	57.83	6.07	0.07	0.03	9.38	0.01	0.00	0.15	27.28	0.02	0.20	**101.02**
Amphibolite	SEM-TOR-15A	56.15	5.71	0.02	0.03	10.21	0.00	0.00	0.11	27.93	0.01	0.26	**100.42**
Amphibolite	SEM-TOR-15A	56.95	6.14	0.01	0.04	9.67	0.00	0.00	0.19	27.76	0.00	0.16	**100.92**
Amphibolite	SEM-TOR-15A	56.95	5.94	0.02	0.06	9.63	0.00	0.00	0.07	27.53	0.04	0.13	**100.36**
Amphibolite	SEM-TOR-15A	58.29	6.59	0.00	0.07	8.65	0.00	0.00	0.11	26.47	0.00	0.11	**100.29**
Amphibolite	SEM-TOR-15A	58.39	6.39	0.00	0.06	9.13	0.00	0.01	0.11	27.16	0.02	0.21	**101.49**
Amphibolite	SEM-TOR-15A	57.09	5.90	0.00	0.06	9.63	0.00	0.00	0.00	27.75	0.00	0.22	**100.65**
Amphibolite	SEM-TOR-15A	56.02	5.37	0.00	0.04	10.20	0.00	0.08	0.15	27.98	0.00	0.36	**100.19**
Amphibolite	SEM-TOR-15A	56.88	5.93	0.03	0.07	9.54	0.01	0.00	0.11	27.53	0.02	0.18	**100.30**
Amphibolite	SEM-TOR-15A	56.35	5.94	0.00	0.06	9.94	0.00	0.00	0.00	27.80	0.02	0.27	**100.37**
Amphibolite	SEM-TOR-15B	55.53	5.17	0.00	0.03	9.85	0.00	0.00	0.14	27.75	0.01	0.09	**98.57**
Amphibolite	SEM-TOR-15B	53.72	4.64	0.00	0.02	11.11	0.00	0.03	0.00	28.43	0.05	0.24	**98.24**
Amphibolite	SEM-TOR-15B	54.76	4.97	0.00	0.03	10.72	0.02	0.00	0.00	28.31	0.00	0.24	**99.05**
Amphibolite	SEM-TOR-15B	54.60	4.78	0.03	0.03	10.70	0.00	0.03	0.06	28.19	0.07	0.16	**98.64**
Amphibolite	SEM-TOR-15B	56.84	5.65	0.00	0.05	9.09	0.00	0.03	0.12	26.80	0.02	0.15	**98.76**
Amphibolite	SEM-TOR-15B	56.83	5.70	0.00	0.06	9.12	0.02	0.00	0.10	26.67	0.00	0.16	**98.65**

Amphibolite	SEM-TOR-15B	55.01	4.95	0.00	0.04	10.26	0.01	0.03	0.16	27.86	0.00	0.15	**98.46**
Amphibolite	SEM-TOR-15B	54.92	5.03	0.03	0.04	10.70	0.00	0.02	0.01	28.25	0.00	0.26	**99.25**
Amphibolite	SEM-TOR-3A	56.07	6.73	0.03	0.08	8.19	0.01	0.01	0.06	25.94	0.02	0.20	**97.34**
Amphibolite	SEM-TOR-3A	56.07	6.33	0.00	0.11	8.49	0.00	0.00	0.05	26.17	0.02	0.26	**97.50**
Amphibolite	SEM-TOR-3A	56.83	6.56	0.05	0.11	8.44	0.00	0.03	0.08	26.27	0.07	0.32	**98.77**
Amphibolite	SEM-TOR-3A	56.92	6.34	0.00	0.10	8.69	0.00	0.06	0.00	26.29	0.00	0.23	**98.62**
Amphibolite	SEM-TOR-3A	56.96	6.12	0.03	0.11	9.08	0.01	0.01	0.03	26.67	0.00	0.10	**99.12**
Amphibolite	SEM-TOR-3A	58.94	6.91	0.05	0.08	7.87	0.02	0.00	0.08	25.59	0.00	0.16	**99.69**
Amphibolite	SEM-TOR-3A	57.30	6.52	0.00	0.16	8.58	0.02	0.00	0.00	25.89	0.00	0.17	**98.65**
Amphibolite	SEM-TOR-3A	57.55	6.42	0.00	0.14	8.35	0.00	0.06	0.08	25.98	0.00	0.22	**98.80**
Amphibolite	SEM-TOR-3A	58.20	6.78	0.00	0.08	7.93	0.00	0.00	0.09	24.52	0.00	0.19	**97.78**
Amphibolite	SEM-TOR-3A	57.85	6.69	0.05	0.11	8.10	0.01	0.00	0.15	24.88	0.02	0.20	**98.05**
Amphibolite	SEM-TOR-3B	58.23	6.78	0.00	0.18	8.17	0.00	0.00	0.00	26.33	0.00	0.22	**99.90**
Amphibolite	SEM-TOR-3B	57.93	6.78	0.06	0.16	8.48	0.00	0.02	0.15	26.65	0.00	0.26	**100.49**
Amphibolite	SEM-TOR-3B	59.27	7.31	0.09	0.26	7.19	0.00	0.01	0.06	25.65	0.01	0.14	**99.98**
Amphibolite	SEM-TOR-3B	58.19	6.96	0.09	0.15	7.97	0.00	0.02	0.03	26.26	0.01	0.13	**99.79**
Amphibolite	SEM-TOR-6	59.22	7.14	0.00	0.29	7.65	0.00	0.00	0.23	26.01	0.00	0.15	**100.69**
Amphibolite	SEM-TOR-6	57.06	6.21	0.00	0.24	9.39	0.01	0.01	0.05	26.91	0.03	0.19	**100.09**

Amphibolite	SEM-TOR-6	59.58	7.32	0.05	0.33	7.43	0.01	0.00	0.03	25.28	0.01	0.20	**100.24**
Amphibolite	SEM-TOR-6	58.82	6.66	0.01	0.23	7.79	0.00	0.00	0.01	25.50	0.05	0.15	**99.22**
Amphibolite	SEM-TOR-6	58.38	6.55	0.09	0.24	8.24	0.00	0.00	0.00	26.37	0.00	0.20	**100.08**
Amphibolite	SEM-TOR-6	60.41	7.78	0.01	0.33	6.44	0.01	0.00	0.00	24.88	0.00	0.30	**100.15**
Amphibolite	SEM-TOR-6	59.87	7.12	0.06	0.35	7.10	0.02	0.02	0.05	25.26	0.07	0.41	**100.33**
Amphibolite	SEM-TOR-6	59.20	7.16	0.06	0.33	7.63	0.00	0.04	0.00	25.41	0.00	0.31	**100.13**
Amphibolite	SEM-TOR-6	59.06	6.73	0.01	0.18	8.24	0.01	0.00	0.03	25.59	0.04	0.40	**100.29**
Amphibolite	SEM-TOR-6	58.26	6.61	0.09	0.23	7.77	0.00	0.00	0.00	25.36	0.00	0.22	**98.54**
Amphibolite	SEM-TOR-6	56.06	5.66	0.04	0.23	9.50	0.00	0.09	0.10	26.86	0.00	0.59	**99.12**
Amphibolite	SEM-TOR-6	58.32	6.56	0.01	0.22	8.11	0.00	0.02	0.00	26.09	0.03	0.32	**99.70**
Amphibolite	SEM-TOR-6	57.66	6.28	0.00	0.19	8.60	0.01	0.03	0.00	26.29	0.00	0.30	**99.35**
Amphibolite	SEM-TOR-7A	58.62	6.79	0.01	0.10	8.19	0.01	0.02	0.00	26.63	0.00	0.26	**100.61**
Amphibolite	SEM-TOR-7A	58.75	6.91	0.01	0.31	7.85	0.02	0.00	0.03	26.28	0.06	0.23	**100.45**
Amphibolite	SEM-TOR-7A	59.30	7.04	0.00	0.19	8.03	0.00	0.00	0.26	26.28	0.00	0.20	**101.29**
Amphibolite	SEM-TOR-7A	58.84	6.98	0.06	0.18	8.19	0.02	0.00	0.14	26.59	0.00	0.21	**101.20**
Amphibolite	SEM-TOR-7B	58.06	6.49	0.12	0.15	8.31	0.00	0.01	0.02	26.69	0.08	0.20	**100.13**
Amphibolite	SEM-TOR-7B	59.88	7.41	0.03	0.14	6.82	0.00	0.02	0.00	25.30	0.01	0.31	**99.91**
Amphibolite	SEM-TOR-7B	59.30	7.33	0.15	0.13	6.88	0.01	0.03	0.21	25.25	0.01	0.17	**99.46**

Amphibolite	SEM-TOR-7B	58.94	6.97	0.00	0.14	7.39	0.02	0.02	0.22	25.78	0.02	0.23	**99.73**
Amphibolite	SEM-TOR-7B	59.31	6.97	0.00	0.14	7.28	0.00	0.00	0.00	25.49	0.00	0.16	**99.36**
Amphibolite	SEM-TOR-7B	59.87	7.20	0.15	0.12	7.05	0.00	0.01	0.09	25.29	0.00	0.20	**99.97**
Digested enclave	SEM-TOR-8A	59.79	7.55	0.00	0.35	6.88	0.00	0.02	0.17	25.01	0.01	0.07	**99.86**
Digested enclave	SEM-TOR-8A	59.72	7.54	0.01	0.09	6.56	0.00	0.09	0.00	24.76	0.00	0.25	**99.04**
Digested enclave	SEM-TOR-8A	59.33	7.19	0.04	0.11	6.81	0.01	0.00	0.20	25.08	0.03	0.11	**98.93**
Digested enclave	SEM-TOR-8A	58.90	6.94	0.00	0.16	7.31	0.00	0.03	0.12	25.48	0.00	0.14	**99.08**
Digested enclave	SEM-TOR-8A	58.59	7.07	0.07	0.16	7.56	0.00	0.03	0.08	25.69	0.06	0.11	**99.40**
Digested enclave	SEM-TOR-8A	58.98	7.23	0.03	0.14	7.23	0.00	0.01	0.08	25.62	0.00	0.23	**99.54**
Digested enclave	SEM-TOR-8A	59.54	7.17	0.00	0.17	7.69	0.01	0.01	0.23	25.84	0.05	0.14	**100.85**
Digested enclave	SEM-TOR-8A	60.10	7.21	0.00	0.10	7.47	0.00	0.00	0.11	25.67	0.00	0.06	**100.72**
Digested enclave	SEM-TOR-8B	58.29	6.65	0.01	0.24	7.99	0.00	0.02	0.19	25.95	0.02	0.15	**99.51**
Digested enclave	SEM-TOR-8B	58.40	6.53	0.11	0.18	8.24	0.00	0.00	0.16	26.09	0.07	0.15	**99.92**
Digested enclave	SEM-TOR-8B	59.73	6.99	0.05	0.21	7.42	0.01	0.00	0.25	25.33	0.02	0.13	**100.14**
Digested enclave	SEM-TOR-8B	59.02	6.96	0.00	0.22	7.15	0.01	0.04	0.06	25.22	0.02	0.14	**98.84**
Digested enclave	SEM-TOR-8B	59.08	6.54	0.00	0.14	7.84	0.01	0.03	0.02	25.59	0.00	0.16	**99.41**
Digested enclave	SEM-TOR-8B	59.23	7.08	0.02	0.12	7.48	0.00	0.00	0.12	25.49	0.00	0.13	**99.66**
Digested enclave	SEM-TOR-8B	59.27	7.34	0.00	0.09	7.61	0.00	0.00	0.15	25.25	0.00	0.11	**99.83**

Digested enclave	SEM-TOR-8B	58.89	6.96	0.12	0.48	7.91	0.00	0.06	0.08	25.84	0.02	0.21	**100.56**
Digested enclave	SEM-TOR-8B	59.95	7.30	0.00	0.11	7.32	0.01	0.00	0.19	25.45	0.04	0.14	**100.50**
Digested enclave	SEM-TOR-8B	61.24	7.76	0.00	0.07	6.50	0.00	0.01	0.10	24.89	0.03	0.21	**100.82**
Diorite	SEM-TOR-13	55.37	5.47	0.00	0.14	10.35	0.02	0.00	0.16	28.36	0.05	0.17	**100.08**
Diorite	SEM-TOR-13	55.48	5.31	0.00	0.15	10.59	0.01	0.01	0.01	28.56	0.00	0.16	**100.27**
Diorite	SEM-TOR-13	56.23	5.79	0.00	0.16	10.07	0.01	0.00	0.03	27.82	0.00	0.13	**100.25**
Diorite	SEM-TOR-13	58.32	6.73	0.00	0.13	8.19	0.00	0.01	0.04	26.34	0.00	0.21	**99.97**
Diorite	SEM-TOR-13	56.02	5.72	0.04	0.16	10.31	0.04	0.00	0.17	28.37	0.07	0.25	**101.16**
Diorite	SEM-TOR-13	55.99	5.76	0.04	0.15	10.36	0.00	0.00	0.00	28.26	0.01	0.20	**100.77**
Diorite	SEM-TOR-13	54.42	5.05	0.00	0.13	11.42	0.00	0.00	0.00	28.94	0.03	0.14	**100.12**
Diorite	SEM-TOR-13	55.53	5.68	0.06	0.14	10.35	0.00	0.00	0.00	27.92	0.00	0.19	**99.87**
Diorite	SEM-TOR-18A	60.53	7.64	0.03	0.18	6.72	0.00	0.02	0.13	24.84	0.00	0.14	**100.23**
Diorite	SEM-TOR-18A	61.60	8.00	0.00	0.16	6.07	0.00	0.00	0.14	24.28	0.00	0.26	**100.51**
Diorite	SEM-TOR-18A	57.22	6.23	0.03	0.12	9.18	0.00	0.00	0.10	27.01	0.01	0.12	**100.03**
Diorite	SEM-TOR-18A	59.89	7.28	0.03	0.11	7.48	0.01	0.00	0.00	25.47	0.06	0.18	**100.51**
Diorite	SEM-TOR-18A	56.58	5.83	0.09	0.11	9.40	0.01	0.02	0.00	27.13	0.00	0.15	**99.32**
Diorite	SEM-TOR-18A	60.09	7.75	0.00	0.21	6.53	0.00	0.02	0.00	24.79	0.00	0.26	**99.65**
Diorite	SEM-TOR-18A	56.50	6.03	0.00	0.16	9.43	0.00	0.00	0.09	27.26	0.00	0.17	**99.63**

Diorite	SEM-TOR-18A	59.40	7.34	0.03	0.13	7.24	0.01	0.00	0.13	25.31	0.01	0.17	**99.77**
Diorite	SEM-TOR-18B	58.53	6.69	0.00	0.15	8.12	0.00	0.06	0.01	25.83	0.05	0.12	**99.56**
Diorite	SEM-TOR-18B	59.95	7.60	0.00	0.14	6.46	0.01	0.00	0.20	24.06	0.04	0.13	**98.58**
Diorite	SEM-TOR-18B	55.97	6.34	0.06	0.11	8.97	0.00	0.03	0.00	26.96	0.02	0.21	**98.68**
Diorite	SEM-TOR-18B	56.08	6.17	0.01	0.11	9.43	0.01	0.00	0.09	26.99	0.03	0.24	**99.14**
Diorite	SEM-TOR-20	54.28	5.22	0.00	0.11	10.91	0.02	0.00	0.18	28.85	0.00	0.17	**99.74**
Diorite	SEM-TOR-20	58.12	6.74	0.00	0.11	8.47	0.01	0.00	0.20	26.50	0.00	0.14	**100.29**
Diorite	SEM-TOR-20	53.91	5.24	0.07	0.10	10.96	0.00	0.00	0.13	28.76	0.00	0.22	**99.38**
Diorite	SEM-TOR-20	55.26	5.96	0.01	0.14	10.29	0.03	0.00	0.11	28.00	0.00	0.11	**99.90**
Diorite	SEM-TOR-20	54.34	5.13	0.00	0.10	11.31	0.00	0.05	0.04	29.19	0.01	0.15	**100.32**
Diorite	SEM-TOR-20	54.96	5.76	0.00	0.08	10.50	0.00	0.11	0.03	28.27	0.00	0.42	**100.13**
Diorite	SEM-TOR-20	55.29	5.32	0.00	0.10	10.14	0.00	0.06	0.08	27.88	0.06	0.20	**99.13**
Diorite	SEM-TOR-20	55.88	5.76	0.01	0.08	9.68	0.00	0.03	0.02	27.49	0.00	0.12	**99.08**
Diorite	SEM-TOR-20	51.76	3.63	0.00	0.05	13.36	0.00	0.05	0.14	30.62	0.00	0.19	**99.79**
Diorite	SEM-TOR-20	53.97	5.06	0.00	0.07	11.51	0.00	0.01	0.11	29.07	0.11	0.25	**100.16**
Diorite	SEM-TOR-4	56.87	6.21	0.00	0.11	8.32	0.01	0.00	0.07	26.26	0.02	0.14	**97.99**
Diorite	SEM-TOR-4	54.76	5.08	0.03	0.15	10.56	0.02	0.03	0.10	27.80	0.02	0.22	**98.78**
Diorite	SEM-TOR-4	56.47	5.92	0.00	0.16	9.30	0.00	0.00	0.13	26.76	0.00	0.19	**98.94**

Diorite	SEM-TOR-4	56.36	5.91	0.01	0.12	9.24	0.00	0.04	0.00	26.79	0.03	0.28	**98.78**
Diorite	SEM-TOR-4	55.17	5.26	0.00	0.16	10.02	0.02	0.01	0.03	27.49	0.00	0.16	**98.33**
Diorite	SEM-TOR-4	55.08	5.32	0.06	0.16	9.86	0.00	0.00	0.19	27.42	0.00	0.27	**98.37**
Diorite	SEM-TOR-4	55.77	5.58	0.00	0.16	9.44	0.00	0.00	0.12	27.05	0.04	0.12	**98.29**
Diorite	SEM-TOR-4	55.29	5.65	0.05	0.15	9.74	0.01	0.02	0.07	26.99	0.00	0.15	**98.11**
Diorite	SEM-TOR-9B	57.52	6.56	0.02	0.20	8.90	0.00	0.00	0.15	27.10	0.00	0.18	**100.63**
Diorite	SEM-TOR-9B	56.10	5.79	0.03	0.16	9.98	0.00	0.04	0.09	27.70	0.00	0.16	**100.05**
Diorite	SEM-TOR-9B	56.41	6.17	0.01	0.16	9.40	0.00	0.03	0.08	27.52	0.01	0.15	**99.93**
Diorite	SEM-TOR-9B	55.39	5.81	0.00	0.11	10.44	0.00	0.00	0.00	28.11	0.02	0.11	**99.99**
Fine-grained amphibolite	SEM-TOR-1	56.85	6.39	0.09	0.07	7.73	0.01	0.02	0.00	26.40	0.00	0.24	**97.78**
Fine-grained amphibolite	SEM-TOR-1	59.17	7.25	0.00	0.10	6.28	0.02	0.04	0.00	24.13	0.05	0.25	**97.29**
Fine-grained amphibolite	SEM-TOR-1	58.45	7.14	0.06	0.08	6.88	0.00	0.05	0.01	25.32	0.01	0.39	**98.39**
Fine-grained amphibolite	SEM-TOR-1	56.75	6.18	0.00	0.06	8.01	0.02	0.13	0.04	26.75	0.01	0.46	**98.40**
Fine-grained amphibolite	SEM-TOR-3B	58.12	6.62	0.00	0.16	8.40	0.01	0.00	0.07	26.41	0.09	0.15	**100.03**
Fine-grained amphibolite	SEM-TOR-3B	58.15	6.62	0.00	0.19	8.42	0.01	0.02	0.00	26.42	0.02	0.16	**100.01**

Fine-grained amphibolite	SEM-TOR-3B	57.54	6.51	0.05	0.16	8.42	0.00	0.00	0.00	26.50	0.04	0.13	**99.35**
Fine-grained amphibolite	SEM-TOR-3B	58.88	6.99	0.00	0.14	8.04	0.00	0.00	0.11	26.33	0.03	0.10	**100.61**
Gabbro	SEM-TOR-9A	55.81	6.15	0.00	0.13	9.48	0.00	0.00	0.07	27.79	0.07	0.09	**99.58**
Gabbro	SEM-TOR-9A	57.77	6.69	0.02	0.14	8.27	0.00	0.00	0.17	26.89	0.07	0.08	**100.10**
Gabbro	SEM-TOR-9A	55.41	5.72	0.00	0.09	9.96	0.00	0.01	0.08	28.12	0.03	0.25	**99.67**
Gabbro	SEM-TOR-9A	56.37	6.00	0.03	0.09	9.35	0.14	0.00	0.03	27.17	0.04	0.26	**99.47**
Gabbro	SEM-TOR-9B	56.18	6.10	0.00	0.14	9.35	0.00	0.00	0.22	27.20	0.00	0.11	**99.30**
Gabbro	SEM-TOR-9B	56.55	6.05	0.00	0.13	9.33	0.00	0.00	0.00	27.30	0.04	0.15	**99.55**
Gabbro	SEM-TOR-9B	56.93	6.23	0.00	0.15	9.05	0.02	0.00	0.07	27.32	0.00	0.17	**99.94**
Gabbro	SEM-TOR-9B	56.63	6.03	0.02	0.11	9.39	0.00	0.01	0.17	27.36	0.01	0.21	**99.94**
Gabbro	SEM-TOR-9B	57.05	6.01	0.00	0.14	9.23	0.00	0.03	0.11	27.52	0.00	0.11	**100.20**
Gabbro	SEM-TOR-9B	56.46	6.04	0.01	0.13	9.48	0.00	0.00	0.14	27.33	0.07	0.21	**99.86**
Gabbro(Pl)	SEM-TOR-9C	58.23	6.80	0.12	0.22	7.97	0.00	0.06	0.12	26.31	0.01	0.22	**100.06**
Gabbro(Pl)	SEM-TOR-9C	58.63	7.12	0.00	0.17	7.39	0.00	0.01	0.07	25.66	0.00	0.08	**99.13**
Gabbro(Pl)	SEM-TOR-9C	58.60	6.66	0.00	0.20	8.08	0.02	0.06	0.14	26.17	0.06	0.19	**100.16**
Gabbro(Pl)	SEM-TOR-9C	57.10	6.16	0.02	0.26	8.95	0.03	0.00	0.02	27.37	0.03	0.15	**100.08**
Gabbro(Pl)	SEM-TOR-9C	57.09	6.11	0.02	0.10	9.17	0.03	0.00	0.05	27.36	0.02	0.11	**100.05**

Gabbro(Pl)	SEM-TOR-9C	60.69	8.17	0.00	0.14	6.02	0.01	0.00	0.14	24.15	0.00	0.11	**99.42**
Gabbro(Pl)	SEM-TOR-9C	55.77	5.55	0.02	0.14	10.22	0.00	0.00	0.15	27.99	0.00	0.12	**99.96**
Gabbro(Pl)	SEM-TOR-9C	60.99	8.20	0.04	0.10	6.36	0.00	0.00	0.27	25.39	0.03	0.14	**101.51**
Gabbro(Pl)	SEM-TOR-9C	56.72	6.01	0.01	0.07	9.55	0.01	0.01	0.11	27.54	0.00	0.13	**100.15**
Gabbro(Pl)	SEM-TOR-9C	57.10	6.02	0.04	0.18	9.27	0.00	0.02	0.07	27.07	0.00	0.20	**99.97**
Leucocratic inj.	SEM-TOR-1	58.54	6.73	0.03	0.24	8.00	0.01	0.00	0.05	25.71	0.00	0.26	**99.56**
Leucocratic inj.	SEM-TOR-1	57.98	6.50	0.05	0.22	8.20	0.02	0.03	0.09	26.02	0.00	0.23	**99.35**
Leucocratic inj.	SEM-TOR-2	58.37	6.56	0.06	0.23	7.99	0.00	0.00	0.05	25.27	0.00	0.17	**98.70**
Leucocratic inj.	SEM-TOR-2	58.37	6.90	0.03	0.25	7.70	0.00	0.03	0.13	24.95	0.00	0.20	**98.56**
Leucocratic inj.	SEM-TOR-2	58.36	6.82	0.00	0.24	7.59	0.02	0.00	0.08	25.26	0.04	0.22	**98.63**
Leucocratic inj.	SEM-TOR-2	56.98	6.31	0.02	0.12	9.01	0.00	0.01	0.05	26.22	0.02	0.15	**98.90**
Leucocratic inj.	SEM-TOR-2	57.79	6.62	0.05	0.21	8.17	0.00	0.00	0.11	25.75	0.00	0.16	**98.87**
Leucocratic inj.	SEM-TOR-2	57.28	6.36	0.01	0.12	8.78	0.00	0.00	0.00	26.25	0.00	0.11	**98.90**
Pegmatoid	SEM-TOR-16A	66.25	10.69	0.00	0.43	0.81	0.16	0.00	0.24	20.81	0.01	0.13	**99.56**
Pegmatoid	SEM-TOR-16A	67.38	10.79	0.03	0.27	1.18	0.02	0.00	0.17	20.75	0.01	0.12	**100.71**
Pegmatoid	SEM-TOR-16A	67.74	11.08	0.03	0.05	1.21	0.00	0.00	0.09	20.47	0.00	0.09	**100.76**
Pegmatoid	SEM-TOR-16A	64.60	9.71	0.00	1.55	0.89	0.12	0.00	0.07	22.20	0.00	0.31	**99.45**
Pegmatoid	SEM-TOR-16A	67.35	11.03	0.03	0.05	1.56	0.01	0.01	0.26	20.94	0.03	0.10	**101.37**

Pegmatoid	SEM-TOR-16A	67.08	10.84	0.00	0.06	1.43	0.00	0.00	0.00	20.54	0.05	0.08	**100.07**
Pegmatoid	SEM-TOR-16A	67.67	11.39	0.09	0.46	0.34	0.05	0.00	0.01	20.23	0.00	0.18	**100.41**
Quartz-diorite	SEM-TOR-10	59.21	7.18	0.04	0.26	7.20	0.00	0.02	0.12	25.49	0.00	0.22	**99.73**
Quartz-diorite	SEM-TOR-10	54.66	4.90	0.00	0.13	10.96	0.00	0.02	0.00	28.87	0.04	0.17	**99.76**
Quartz-diorite	SEM-TOR-10	59.65	7.64	0.01	0.09	6.63	0.00	0.00	0.00	24.82	0.00	0.11	**98.94**
Quartz-diorite	SEM-TOR-10	57.03	5.98	0.00	0.14	8.97	0.00	0.01	0.04	26.86	0.00	0.12	**99.14**
Quartz-diorite	SEM-TOR-10	59.35	7.34	0.04	0.15	7.26	0.00	0.00	0.04	25.63	0.04	0.09	**99.92**
Quartz-diorite	SEM-TOR-10	56.80	5.95	0.00	0.14	9.43	0.00	0.05	0.02	27.40	0.00	0.14	**99.94**
Quartz-diorite	SEM-TOR-10	55.91	5.52	0.05	0.09	10.22	0.02	0.00	0.28	28.05	0.00	0.11	**100.25**
Quartz-diorite	SEM-TOR-10	57.30	6.15	0.04	0.14	9.15	0.02	0.01	0.14	27.14	0.04	0.15	**100.29**
Quartz-diorite	SEM-TOR-11	61.30	7.98	0.05	0.23	5.94	0.00	0.00	0.00	23.81	0.04	0.20	**99.53**
Quartz-diorite	SEM-TOR-11	62.66	8.33	0.00	0.30	4.63	0.00	0.05	0.14	22.65	0.00	0.13	**98.89**
Quartz-diorite	SEM-TOR-11	62.51	8.37	0.00	0.24	4.75	0.00	0.03	0.22	22.46	0.00	0.10	**98.68**
Quartz-diorite	SEM-TOR-11	62.19	8.39	0.00	0.10	4.91	0.01	0.00	0.00	22.83	0.03	0.11	**98.57**
Quartz-diorite	SEM-TOR-11	62.34	8.46	0.02	0.21	5.17	0.00	0.00	0.11	23.24	0.00	0.14	**99.67**
Quartz-diorite	SEM-TOR-11	60.73	7.85	0.00	0.11	6.05	0.00	0.01	0.09	24.27	0.04	0.09	**99.24**
Quartz-diorite	SEM-TOR-11	61.45	8.20	0.04	0.08	5.80	0.00	0.01	0.20	23.85	0.00	0.07	**99.70**
Quartz-diorite	SEM-TOR-11	60.32	7.59	0.09	0.14	6.59	0.01	0.00	0.12	24.62	0.00	0.15	**99.63**

Quartz-diorite	SEM-TOR-12	61.49	8.10	0.03	0.11	6.16	0.00	0.01	0.05	24.61	0.02	0.19	**100.75**
Quartz-diorite	SEM-TOR-12	61.10	8.05	0.03	0.13	6.84	0.00	0.02	0.13	25.53	0.00	0.28	**102.11**
Quartz-diorite	SEM-TOR-12	61.69	8.01	0.00	0.16	6.14	0.01	0.00	0.16	24.86	0.05	0.20	**101.28**
Quartz-diorite	SEM-TOR-12	62.45	8.75	0.00	0.10	5.65	0.01	0.00	0.11	24.60	0.08	0.14	**101.88**
Quartz-diorite	SEM-TOR-12	61.94	8.23	0.00	0.15	6.13	0.00	0.04	0.03	24.93	0.00	0.10	**101.54**
Quartz-diorite	SEM-TOR-12	62.07	8.73	0.04	0.10	5.85	0.01	0.04	0.11	24.60	0.00	0.15	**101.68**
Quartz-diorite	SEM-TOR-12	62.62	8.47	0.00	0.22	5.42	0.01	0.02	0.22	23.97	0.02	0.13	**101.10**
Quartz-diorite	SEM-TOR-12	62.58	8.52	0.05	0.20	5.35	0.00	0.06	0.05	23.91	0.00	0.14	**100.86**
Quartz-diorite	SEM-TOR-14	57.70	6.66	0.03	0.10	8.09	0.00	0.00	0.12	26.03	0.04	0.17	**98.94**
Quartz-diorite	SEM-TOR-14	56.69	6.22	0.00	0.10	9.25	0.00	0.04	0.22	27.17	0.01	0.16	**99.85**
Quartz-diorite	SEM-TOR-14	56.69	6.18	0.01	0.14	9.11	0.00	0.06	0.04	26.96	0.00	0.22	**99.40**
Quartz-diorite	SEM-TOR-14	56.94	6.02	0.00	0.15	8.98	0.01	0.01	0.25	26.50	0.00	0.15	**99.01**
Quartz-diorite	SEM-TOR-14	56.69	5.95	0.05	0.09	9.47	0.01	0.00	0.00	27.30	0.00	0.12	**99.68**
Quartz-diorite	SEM-TOR-14	60.49	7.71	0.00	0.16	6.57	0.00	0.01	0.02	24.68	0.01	0.09	**99.75**
Quartz-diorite	SEM-TOR-14	57.48	6.18	0.06	0.11	9.12	0.00	0.00	0.22	26.88	0.03	0.17	**100.24**
Quartz-diorite	SEM-TOR-14	57.14	6.22	0.06	0.13	8.74	0.00	0.02	0.00	26.73	0.00	0.11	**99.13**
Quartz-diorite	SEM-TOR-17A	59.07	7.20	0.01	0.20	7.12	0.00	0.00	0.09	24.50	0.00	0.09	**98.28**
Quartz-diorite	SEM-TOR-17A	61.72	8.16	0.00	0.24	5.21	0.02	0.02	0.05	23.04	0.00	0.14	**98.60**

Quartz-diorite	SEM-TOR-17A	58.61	6.71	0.00	0.21	7.37	0.00	0.02	0.00	25.22	0.05	0.15	**98.33**
Quartz-diorite	SEM-TOR-17A	62.03	8.26	0.00	0.19	4.83	0.01	0.00	0.00	22.89	0.00	0.09	**98.32**
Quartz-diorite	SEM-TOR-17A	59.61	7.41	0.00	0.50	5.98	0.00	0.01	0.10	24.43	0.00	0.13	**98.18**
Quartz-diorite	SEM-TOR-17A	60.06	7.55	0.04	0.15	6.38	0.00	0.00	0.08	24.05	0.02	0.09	**98.42**
Quartz-diorite	SEM-TOR-17A	61.24	7.73	0.03	0.30	5.48	0.01	0.00	0.00	23.78	0.02	0.08	**98.66**
Quartz-diorite	SEM-TOR-17A	60.74	7.85	0.00	0.27	5.95	0.00	0.00	0.01	23.73	0.05	0.16	**98.77**
Quartz-diorite	SEM-TOR-17A	63.98	9.06	0.05	0.18	3.84	0.00	0.00	0.08	22.01	0.00	0.13	**99.33**
Quartz-diorite	SEM-TOR-17A	61.83	8.20	0.00	0.22	5.52	0.01	0.00	0.12	23.69	0.00	0.09	**99.68**
Quartz-diorite	SEM-TOR-17A	62.50	8.11	0.06	0.38	4.76	0.01	0.01	0.03	22.64	0.01	0.11	**98.61**
Quartz-diorite	SEM-TOR-17A	63.56	8.94	0.00	0.24	4.04	0.00	0.00	0.10	21.51	0.00	0.08	**98.46**
Quartz-diorite	SEM-TOR-17A	60.22	7.05	0.03	0.29	6.88	0.00	0.00	0.14	24.47	0.05	0.14	**99.27**
Quartz-diorite	SEM-TOR-17A	60.77	7.66	0.08	0.23	5.93	0.00	0.00	0.04	23.37	0.02	0.07	**98.17**
Quartz-diorite	SEM-TOR-17B	60.94	7.66	0.00	0.16	6.64	0.00	0.00	0.02	24.73	0.00	0.05	**100.19**
Quartz-diorite	SEM-TOR-17B	61.71	8.22	0.02	0.20	6.00	0.00	0.00	0.12	24.24	0.01	0.16	**100.68**
Quartz-diorite	SEM-TOR-17B	62.09	8.18	0.00	0.24	5.99	0.00	0.00	0.04	24.57	0.00	0.11	**101.20**
Quartz-diorite	SEM-TOR-17B	61.33	8.07	0.00	0.24	5.90	0.01	0.00	0.01	23.43	0.03	0.11	**99.14**
Quartz-diorite	SEM-TOR-17B	60.17	7.41	0.01	0.17	6.46	0.00	0.00	0.05	23.18	0.00	0.10	**97.54**
Quartz-diorite	SEM-TOR-17B	61.00	7.77	0.00	0.19	5.68	0.00	0.00	0.03	23.01	0.02	0.14	**97.84**

Quartz-diorite	SEM-TOR-17B	59.88	7.49	0.02	0.22	7.35	0.00	0.02	0.08	25.42	0.09	0.14	**100.71**
Quartz-diorite	SEM-TOR-17B	62.29	8.36	0.06	0.17	5.21	0.01	0.00	0.02	23.91	0.00	0.11	**100.14**
Quartz-diorite	SEM-TOR-17B	60.29	7.79	0.04	0.13	6.87	0.00	0.00	0.09	25.02	0.06	0.06	**100.35**
Quartz-diorite	SEM-TOR-17B	95.48	1.17	0.00	0.03	0.60	0.00	0.00	0.04	3.39	0.00	0.11	**100.83**
Quartz-diorite	SEM-TOR-3B	58.18	6.47	0.00	0.12	8.33	0.00	0.01	0.05	25.94	0.00	0.23	**99.32**
Quartz-diorite	SEM-TOR-3B	58.34	6.64	0.00	0.15	8.12	0.00	0.00	0.00	25.59	0.00	0.15	**98.98**
Quartz-diorite	SEM-TOR-3B	56.88	6.40	0.00	0.07	8.90	0.01	0.00	0.20	26.90	0.02	0.14	**99.50**
Quartz-diorite	SEM-TOR-3B	58.33	7.00	0.03	0.15	7.83	0.00	0.02	0.03	26.03	0.00	0.16	**99.57**
Quartz-diorite	SEM-TOR-3B	54.32	4.74	0.01	0.12	11.26	0.01	0.01	0.00	28.66	0.01	0.28	**99.42**
Quartz-diorite	SEM-TOR-3B	57.53	6.47	0.00	0.15	8.35	0.00	0.03	0.15	26.33	0.01	0.19	**99.22**
Quartz-diorite	SEM-TOR-5	56.32	5.89	0.00	0.07	9.49	0.00	0.00	0.07	27.09	0.00	0.13	**99.05**
Quartz-diorite	SEM-TOR-5	56.12	5.91	0.04	0.08	9.52	0.00	0.03	0.13	27.18	0.00	0.14	**99.17**
Quartz-diorite	SEM-TOR-5	53.80	4.57	0.00	0.12	11.64	0.00	0.00	0.15	29.00	0.04	0.29	**99.60**
Quartz-diorite	SEM-TOR-5	54.53	5.20	0.05	0.12	10.57	0.01	0.00	0.07	28.03	0.09	0.23	**98.90**
Quartz-diorite	SEM-TOR-5	56.50	6.14	0.08	0.08	9.29	0.00	0.00	0.02	27.21	0.00	0.09	**99.41**
Quartz-diorite	SEM-TOR-5	57.01	5.98	0.00	0.11	8.80	0.00	0.00	0.04	26.78	0.02	0.16	**98.90**
Quartz-diorite	SEM-TOR-5	62.84	8.71	0.00	0.17	4.99	0.00	0.00	0.02	23.31	0.12	0.14	**100.31**
Quartz-diorite	SEM-TOR-5	57.08	6.21	0.00	0.07	8.88	0.00	0.00	0.02	27.08	0.03	0.08	**99.46**

Quartz-diorite	SEM-TOR-5	57.95	6.27	0.06	0.09	8.57	0.02	0.00	0.09	26.35	0.00	0.11	**99.51**
Reaction rim	SEM-TOR-15A	59.89	7.37	0.00	0.25	6.87	0.02	0.00	0.25	24.84	0.05	0.09	**99.62**
Reaction rim	SEM-TOR-15A	60.70	7.40	0.05	0.23	6.76	0.01	0.00	0.09	24.72	0.00	0.05	**100.00**
Reaction rim	SEM-TOR-15A	56.37	5.60	0.02	0.15	9.86	0.00	0.00	0.07	27.48	0.01	0.16	**99.72**
Reaction rim	SEM-TOR-15A	59.82	7.13	0.00	0.20	7.16	0.00	0.03	0.00	25.07	0.01	0.15	**99.57**
Reaction rim	SEM-TOR-15B	55.73	5.48	0.01	0.15	9.91	0.00	0.02	0.00	27.44	0.01	0.16	**98.89**
Reaction rim	SEM-TOR-15B	59.08	7.20	0.02	0.20	7.36	0.00	0.00	0.04	25.46	0.00	0.16	**99.53**
Reaction rim	SEM-TOR-15B	55.55	5.66	0.01	0.10	10.23	0.00	0.02	0.02	27.68	0.04	0.28	**99.58**
Reaction rim	SEM-TOR-15B	55.88	5.61	0.08	0.09	10.26	0.00	0.02	0.02	27.96	0.05	0.30	**100.27**
Reaction rim	SEM-TOR-15B	56.09	5.40	0.05	0.06	10.19	0.01	0.00	0.10	27.87	0.00	0.20	**99.95**
Reaction rim	SEM-TOR-15B	55.95	5.56	0.13	0.09	10.18	0.00	0.00	0.18	27.81	0.00	0.28	**100.18**
Reaction rim	SEM-TOR-15B	54.99	5.30	0.07	0.05	10.56	0.00	0.05	0.15	28.06	0.00	0.30	**99.53**
Reaction rim	SEM-TOR-15B	56.24	5.83	0.01	0.06	9.71	0.01	0.00	0.00	27.52	0.00	0.33	**99.69**
Reaction rim	SEM-TOR-2	57.94	6.50	0.00	0.15	8.02	0.00	0.00	0.07	25.63	0.02	0.13	**98.46**
Reaction rim	SEM-TOR-2	56.89	6.17	0.02	0.16	8.64	0.01	0.00	0.21	26.35	0.02	0.36	**98.81**
Reaction rim	SEM-TOR-3A	59.21	7.18	0.00	0.25	7.33	0.00	0.01	0.07	25.30	0.00	0.20	**99.54**
Reaction rim	SEM-TOR-3A	59.19	6.92	0.01	0.22	7.70	0.00	0.00	0.00	25.70	0.00	0.19	**99.93**
Reaction rim	SEM-TOR-3A	56.96	6.01	0.00	0.13	9.22	0.00	0.00	0.14	26.82	0.02	0.13	**99.44**

Reaction rim	SEM-TOR-3A	57.89	6.29	0.00	0.13	8.54	0.01	0.02	0.13	26.26	0.00	0.12	**99.39**
Reaction rim	SEM-TOR-3A	57.40	6.58	0.01	0.22	8.67	0.00	0.00	0.03	26.30	0.00	0.19	**99.39**
Reaction rim	SEM-TOR-3A	57.05	6.61	0.00	0.12	8.64	0.00	0.00	0.08	26.22	0.00	0.17	**98.89**
Reaction rim	SEM-TOR-3B	59.63	7.39	0.00	0.10	7.16	0.00	0.02	0.00	25.11	0.01	0.23	**99.64**
Reaction rim	SEM-TOR-3B	57.66	6.53	0.08	0.08	8.77	0.01	0.00	0.00	26.68	0.01	0.36	**100.17**
Reaction rim	SEM-TOR-3B	58.13	6.49	0.00	0.11	8.79	0.00	0.00	0.03	26.39	0.01	0.13	**100.07**
Reaction rim	SEM-TOR-3B	57.73	6.54	0.01	0.11	8.90	0.00	0.00	0.08	26.82	0.05	0.27	**100.49**
Reaction rim	SEM-TOR-3B	57.97	6.70	0.00	0.10	8.74	0.01	0.01	0.00	26.79	0.06	0.19	**100.56**
Reaction rim	SEM-TOR-3B	57.72	6.45	0.03	0.07	8.96	0.00	0.00	0.05	26.55	0.00	0.30	**100.13**
Reaction rim	SEM-TOR-9B	57.73	6.51	0.06	0.07	8.97	0.00	0.00	0.09	26.72	0.06	0.09	**100.30**
Reaction rim	SEM-TOR-9B	57.66	6.48	0.02	0.15	8.87	0.00	0.00	0.05	26.95	0.00	0.15	**100.32**
Reaction rim	SEM-TOR-9C	60.69	8.20	0.04	0.29	5.32	0.01	0.02	0.02	23.89	0.00	0.09	**98.56**
Reaction rim	SEM-TOR-9C	61.76	8.59	0.00	0.48	4.53	0.03	0.00	0.13	22.86	0.00	0.17	**98.54**
Reaction rim	SEM-TOR-9C	61.41	8.49	0.07	0.40	4.86	0.01	0.02	0.01	23.25	0.00	0.15	**98.66**
Reaction rim	SEM-TOR-9C	61.89	9.20	0.02	0.12	4.63	0.00	0.01	0.00	23.15	0.02	0.15	**99.18**
Sulph. Inj.	SEM-TOR-7A	61.81	8.06	0.00	0.15	6.26	0.01	0.00	0.04	24.59	0.07	0.16	**101.14**
Sulph. Inj.	SEM-TOR-7A	61.95	8.19	0.09	0.24	5.88	0.02	0.00	0.13	24.40	0.00	0.17	**101.06**
Sulph. Inj.	SEM-TOR-7A	61.08	7.83	0.14	0.38	6.35	0.01	0.00	0.12	24.55	0.01	0.18	**100.65**

Sulph. Inj.	SEM-TOR-7A	61.86	8.09	0.00	0.28	6.09	0.00	0.00	0.00	24.15	0.00	0.16	**100.63**
Sulph. Inj.	SEM-TOR-7A	59.51	6.90	0.08	0.25	7.94	0.00	0.01	0.10	26.00	0.05	0.20	**101.03**
Sulph. Inj.	SEM-TOR-7A	59.92	7.26	0.01	0.28	7.56	0.02	0.03	0.03	25.97	0.00	0.22	**101.28**
Sulph. Inj.	SEM-TOR-7A	59.29	7.24	0.00	0.24	7.62	0.03	0.03	0.11	26.36	0.02	0.21	**101.15**
Sulph. Inj.	SEM-TOR-7A	59.50	7.31	0.00	0.22	7.80	0.00	0.04	0.00	25.74	0.00	0.18	**100.80**
Vein	SEM-TOR-15B	54.89	5.16	0.00	0.07	10.82	0.01	0.00	0.10	28.09	0.00	0.19	**99.34**
Vein	SEM-TOR-15B	55.16	5.21	0.06	0.05	10.49	0.00	0.02	0.04	28.07	0.00	0.36	**99.46**
Vein	SEM-TOR-15B	55.55	5.54	0.00	0.07	9.86	0.01	0.00	0.19	27.51	0.00	0.16	**98.87**
Vein	SEM-TOR-15B	56.80	6.03	0.02	0.07	9.20	0.00	0.06	0.11	27.12	0.00	0.13	**99.53**
Vein	SEM-TOR-15B	56.19	5.68	0.01	0.04	9.57	0.00	0.03	0.08	27.54	0.00	0.16	**99.30**
Vein	SEM-TOR-15B	56.33	5.99	0.06	0.06	9.33	0.00	0.00	0.16	27.31	0.00	0.18	**99.42**

Biotite Electronic Probe Micro-Analyses

Table XIII-17. Micro-analyses of biotite crystals.

Lithology	Sample	SiO_2	Al_2O_3	TiO_2	FeO	MgO	MnO	CaO	Cr_2O_3	BaO	Na_2O	K_2O	Cl	F	Total
Digested enclave	SEM-TOR-8A	35.99	14.30	4.16	18.10	12.49	0.15	0.04	0.08	0.43	0.33	8.72	0.10	0.16	**94.78**
Digested enclave	SEM-TOR-8A	36.40	14.12	4.21	17.67	12.35	0.14	0.04	0.07	0.49	0.29	8.78	0.10	0.08	**94.56**
Digested enclave	SEM-TOR-8A	35.68	14.59	4.02	18.61	12.38	0.10	0.06	0.08	0.52	0.32	8.26	0.09	0.05	**94.62**
Digested enclave	SEM-TOR-8A	36.26	14.39	3.95	18.11	12.48	0.12	0.08	0.07	0.50	0.27	8.80	0.10	0.00	**95.02**
Digested enclave	SEM-TOR-8A	36.45	14.42	4.25	18.18	12.17	0.11	0.03	0.03	0.54	0.31	8.75	0.10	0.14	**95.23**
Digested enclave	SEM-TOR-8A	36.11	14.32	3.99	18.58	12.25	0.11	0.03	0.05	0.48	0.24	8.55	0.09	0.00	**94.71**
Digested enclave	SEM-TOR-8B	36.38	14.22	4.30	19.34	11.64	0.10	0.05	0.06	0.46	0.32	8.78	0.10	0.20	**95.64**
Digested enclave	SEM-TOR-8B	36.56	14.36	4.06	19.19	11.56	0.09	0.02	0.03	0.50	0.31	9.11	0.12	0.11	**95.78**
Digested enclave	SEM-TOR-8B	36.70	13.85	4.19	19.39	11.42	0.14	0.06	0.05	0.40	0.33	9.07	0.13	0.00	**95.61**
Digested enclave	SEM-TOR-8B	36.21	14.06	4.16	18.95	11.77	0.12	0.08	0.07	0.42	0.24	8.78	0.12	0.12	**94.86**
Digested enclave	SEM-TOR-8B	35.65	14.95	3.66	20.48	12.26	0.12	0.10	0.05	0.43	0.26	6.99	0.09	0.05	**94.94**
Digested enclave	SEM-TOR-8B	36.77	14.41	4.40	19.50	11.51	0.16	0.02	0.04	0.44	0.28	8.98	0.12	0.00	**96.51**
Digested enclave	SEM-TOR-8B	36.80	14.31	3.88	17.93	13.05	0.11	0.03	0.06	0.39	0.24	8.62	0.09	0.00	**95.42**
Digested enclave	SEM-TOR-8B	36.40	14.61	3.94	18.13	13.05	0.08	0.04	0.06	0.42	0.31	8.22	0.06	0.01	**95.26**
Digested enclave	SEM-TOR-8B	36.42	14.40	4.15	17.53	13.08	0.13	0.09	0.07	0.56	0.38	8.26	0.09	0.16	**95.06**
Digested enclave	SEM-TOR-8B	36.62	14.50	4.09	17.34	12.82	0.12	0.06	0.04	0.55	0.37	8.81	0.09	0.06	**95.31**

Quartz-diorite	SEM-TOR-10	36.23	14.88	3.31	18.42	13.76	0.16	0.03	0.06	0.12	0.23	7.11	0.05	0.18	**94.31**
Quartz-diorite	SEM-TOR-12	34.39	15.42	3.29	19.82	14.85	0.16	0.07	0.07	0.19	0.14	5.15	0.08	0.01	**93.56**
Quartz-diorite	SEM-TOR-17A	35.34	14.11	3.81	22.85	9.53	0.25	0.02	0.06	0.33	0.25	8.02	0.08	0.00	**94.57**
Quartz-diorite	SEM-TOR-17A	35.68	13.88	3.86	22.11	9.52	0.18	0.04	0.06	0.23	0.20	8.57	0.07	0.00	**94.32**
Quartz-diorite	SEM-TOR-17A	34.64	14.07	3.89	22.70	9.88	0.24	0.03	0.04	0.15	0.13	7.72	0.06	0.12	**93.49**
Quartz-diorite	SEM-TOR-17A	35.11	13.81	4.06	22.43	9.40	0.26	0.11	0.10	0.20	0.21	8.05	0.06	0.00	**93.74**
Quartz-diorite	SEM-TOR-17A	35.84	13.45	4.34	22.09	8.85	0.27	0.09	0.06	0.12	0.18	8.29	0.07	0.09	**93.56**
Quartz-diorite	SEM-TOR-17A	35.55	14.32	3.59	22.59	10.18	0.24	0.16	0.11	0.41	0.15	7.83	0.08	0.00	**95.11**
Quartz-diorite	SEM-TOR-17A	36.65	13.92	4.01	22.08	9.82	0.19	0.00	0.03	0.32	0.21	9.04	0.10	0.00	**96.27**
Quartz-diorite	SEM-TOR-17A	36.22	13.83	3.87	22.34	9.67	0.27	0.00	0.08	0.22	0.20	8.46	0.07	0.00	**95.16**
Quartz-diorite	SEM-TOR-17A	35.92	13.65	3.81	22.96	9.80	0.23	0.03	0.08	0.22	0.20	8.13	0.06	0.00	**95.00**
Quartz-diorite	SEM-TOR-17A	36.43	13.87	3.93	22.40	9.54	0.27	0.01	0.10	0.26	0.22	8.66	0.08	0.00	**95.70**
Quartz-diorite	SEM-TOR-17A	36.15	14.13	3.74	22.61	9.81	0.26	0.02	0.08	0.28	0.18	8.11	0.08	0.00	**95.35**

Quartz-diorite	SEM-TOR-17B	34.96	14.45	3.84	23.48	10.69	0.25	0.19	0.04	0.32	0.15	6.28	0.07	0.00	**94.65**
Quartz-diorite	SEM-TOR-17B	35.87	14.27	3.83	22.67	9.93	0.28	0.06	0.01	0.44	0.21	8.49	0.09	0.00	**96.04**
Quartz-diorite	SEM-TOR-17B	35.77	13.90	3.48	22.60	10.22	0.26	0.10	0.09	0.14	0.15	7.65	0.09	0.05	**94.37**
Quartz-diorite	SEM-TOR-17B	37.00	13.82	3.75	22.04	9.83	0.24	0.05	0.09	0.15	0.21	8.87	0.09	0.04	**96.06**
Quartz-diorite	SEM-TOR-17B	36.18	14.17	3.91	22.35	9.72	0.25	0.05	0.09	0.30	0.27	8.93	0.07	0.00	**96.22**
Quartz-diorite	SEM-TOR-17B	36.47	13.80	4.12	22.30	9.36	0.30	0.02	0.06	0.29	0.24	9.06	0.09	0.09	**96.01**
Quartz-diorite	SEM-TOR-17B	35.82	14.75	3.90	23.38	10.19	0.32	0.09	0.07	0.24	0.17	7.26	0.09	0.04	**96.18**
Quartz-diorite	SEM-TOR-17B	35.43	14.01	4.54	22.16	10.14	0.26	0.08	0.09	0.15	0.26	8.05	0.08	0.08	**95.15**
Quartz-diorite	SEM-TOR-17B	34.39	14.84	3.31	24.32	10.81	0.26	0.09	0.12	0.17	0.11	6.25	0.06	0.04	**94.66**
Quartz-diorite	SEM-TOR-17B	36.96	14.12	5.18	21.73	9.02	0.24	0.04	0.06	0.30	0.15	9.57	0.10	0.02	**97.36**

Chlorite Electronic Probe Micro-Analyses

Table XIII-18. Micro-analyses of chlorite grains.

Lithology	Sample	SiO_2	TiO_2	Al_2O_3	Cr_2O_3	FeO^T	MnO	MgO	CaO	Na_2O	K_2O	Total
Digested enclave	SEM-TOR-8A	26.37	0.00	19.41	0.08	30.67	0.24	12.35	0.10	0.04	0.00	**89.26**
Digested enclave	SEM-TOR-8A	26.85	0.10	19.22	0.10	30.11	0.25	12.62	0.04	0.02	0.01	**89.31**
Digested enclave	SEM-TOR-8A	26.67	0.14	19.11	0.09	29.83	0.24	12.98	0.05	0.00	0.02	**89.11**
Digested enclave	SEM-TOR-8A	26.34	0.07	19.31	0.07	31.30	0.20	11.83	0.05	0.03	0.01	**89.21**
Diorite	SEM-TOR-13	26.35	0.05	19.80	0.08	29.73	0.30	12.70	0.03	0.00	0.00	**89.03**
Diorite	SEM-TOR-13	26.39	0.02	19.90	0.08	30.03	0.25	12.28	0.06	0.03	0.00	**89.04**
Diorite	SEM-TOR-13	25.98	0.03	19.96	0.09	29.63	0.31	12.86	0.05	0.00	0.00	**88.92**
Diorite	SEM-TOR-13	27.06	0.09	19.56	0.04	29.01	0.29	13.43	0.05	0.00	0.01	**89.54**
Diorite	SEM-TOR-13	26.69	0.00	19.47	0.06	28.59	0.29	13.98	0.01	0.02	0.01	**89.12**
Diorite	SEM-TOR-13	27.05	0.02	19.70	0.07	29.29	0.29	13.40	0.06	0.01	0.00	**89.88**
Diorite	SEM-TOR-13	27.17	0.05	19.57	0.06	28.59	0.29	13.83	0.05	0.01	0.01	**89.64**
Diorite	SEM-TOR-18A	26.48	0.02	19.84	0.08	28.53	0.25	13.74	0.01	0.00	0.00	**88.95**
Diorite	SEM-TOR-18A	26.78	0.06	19.86	0.08	27.51	0.20	14.30	0.01	0.00	0.01	**88.81**
Diorite	SEM-TOR-18A	27.90	0.05	19.10	0.08	22.99	0.18	17.83	0.07	0.03	0.00	**88.23**
Diorite	SEM-TOR-18A	27.89	0.00	19.38	0.06	23.28	0.20	17.97	0.04	0.02	0.00	**88.83**
Diorite	SEM-TOR-18A	28.10	0.00	19.18	0.11	23.49	0.22	17.71	0.05	0.02	0.00	**88.88**

Diorite	SEM-TOR-18A	27.97	0.02	18.93	0.09	23.75	0.23	17.63	0.03	0.00	0.01	**88.66**
Diorite	SEM-TOR-18B	26.61	0.03	20.18	0.03	24.15	0.20	16.92	0.00	0.01	0.01	**88.12**
Diorite	SEM-TOR-18B	44.75	1.76	10.55	0.05	14.43	0.27	12.03	9.51	1.53	0.29	**95.15**
Diorite	SEM-TOR-18B	26.71	0.07	20.17	0.06	24.00	0.22	16.84	0.05	0.01	0.00	**88.13**
Diorite	SEM-TOR-18B	26.80	0.02	20.07	0.06	23.91	0.19	16.93	0.04	0.02	0.01	**88.04**
Diorite	SEM-TOR-20	26.00	0.01	20.53	0.07	29.35	0.23	13.41	0.03	0.04	0.01	**89.68**
Diorite	SEM-TOR-20	25.32	0.00	21.33	0.07	28.56	0.23	14.27	0.07	0.01	0.00	**89.85**
Diorite	SEM-TOR-20	25.82	0.02	20.68	0.06	28.88	0.23	13.62	0.02	0.00	0.00	**89.33**
Diorite	SEM-TOR-20	26.46	0.02	20.32	0.04	28.15	0.25	13.75	0.03	0.00	0.00	**89.01**
Diorite	SEM-TOR-20	26.41	0.07	20.53	0.05	29.11	0.27	13.13	0.03	0.00	0.01	**89.60**
Diorite	SEM-TOR-20	25.98	0.01	20.42	0.08	29.23	0.28	12.84	0.05	0.02	0.00	**88.91**
Diorite	SEM-TOR-20	25.99	0.03	20.37	0.08	28.29	0.25	13.84	0.05	0.00	0.01	**88.91**
Diorite	SEM-TOR-4	26.68	0.04	19.16	0.06	29.11	0.33	13.07	0.05	0.02	0.00	**88.52**
Diorite	SEM-TOR-4	26.87	0.03	19.45	0.02	28.76	0.32	13.51	0.05	0.02	0.00	**89.03**
Diorite	SEM-TOR-9B	27.25	0.02	19.09	0.09	27.45	0.15	14.76	0.13	0.03	0.00	**88.97**
Diorite	SEM-TOR-9B	27.41	0.10	19.32	0.04	27.36	0.17	15.01	0.05	0.02	0.01	**89.48**
Diorite	SEM-TOR-9B	26.74	0.00	19.46	0.07	29.01	0.19	13.48	0.05	0.01	0.00	**89.00**
Leucocratic inj.	SEM-TOR-1	26.29	0.04	19.43	0.05	33.09	0.31	9.87	0.03	0.02	0.00	**89.13**

Leucocratic inj.	SEM-TOR-1	26.36	0.01	19.41	0.08	33.41	0.30	9.53	0.06	0.02	0.01	**89.17**
Leucocratic inj.	SEM-TOR-2	25.11	0.00	19.48	0.09	36.23	0.33	7.79	0.00	0.01	0.01	**89.05**
Leucocratic inj.	SEM-TOR-2	25.76	0.03	19.15	0.07	35.51	0.27	8.16	0.04	0.03	0.00	**89.02**
Pegmatoid	SEM-TOR-16A	27.43	0.07	19.90	0.06	22.32	0.18	19.19	0.02	0.00	0.02	**89.19**
Pegmatoid	SEM-TOR-16A	27.40	0.00	19.83	0.07	22.58	0.18	18.80	0.05	0.02	0.00	**88.93**
Pegmatoid	SEM-TOR-16A	28.00	0.01	19.90	0.07	22.48	0.24	18.81	0.00	0.00	0.02	**89.52**
Pegmatoid	SEM-TOR-16A	28.17	0.00	19.70	0.06	22.27	0.18	18.58	0.06	0.02	0.01	**89.07**
Pegmatoid	SEM-TOR-16B	27.35	0.02	20.27	0.11	23.25	0.15	17.84	0.07	0.07	0.01	**89.14**
Pegmatoid	SEM-TOR-16B	27.48	0.03	20.40	0.10	23.16	0.19	17.73	0.09	0.03	0.02	**89.22**
Pegmatoid	SEM-TOR-16B	28.06	0.04	19.17	0.08	23.45	0.12	18.01	0.04	0.00	0.02	**88.97**
Pegmatoid	SEM-TOR-16B	27.46	0.00	19.96	0.08	24.65	0.19	16.90	0.05	0.00	0.01	**89.29**
Pegmatoid	SEM-TOR-16B	27.35	0.00	19.89	0.06	24.38	0.21	17.13	0.01	0.01	0.00	**89.04**
Pegmatoid	SEM-TOR-16B	27.58	0.03	19.71	0.05	24.11	0.16	17.20	0.10	0.04	0.01	**88.99**
Quartz-diorite	SEM-TOR-10	47.73	0.77	6.24	0.08	15.69	0.39	13.53	10.40	0.87	0.21	**95.90**
Quartz-diorite	SEM-TOR-10	50.25	0.59	4.56	0.10	14.78	0.43	14.44	10.20	0.61	0.17	**96.13**
Quartz-diorite	SEM-TOR-11	28.08	0.01	19.24	0.06	22.83	0.23	18.64	0.08	0.00	0.01	**89.17**
Quartz-diorite	SEM-TOR-11	28.01	0.00	19.20	0.08	22.85	0.27	18.06	0.06	0.00	0.01	**88.54**
Quartz-diorite	SEM-TOR-14	26.35	0.02	19.97	0.08	24.95	0.19	16.92	0.01	0.01	0.01	**88.51**

Quartz-diorite	SEM-TOR-14	27.40	0.02	19.43	0.09	24.87	0.25	16.65	0.00	0.01	0.01	**88.71**
Quartz-diorite	SEM-TOR-17B	27.14	0.50	18.65	0.06	29.15	0.41	12.75	0.57	0.00	0.02	**89.26**
Quartz-diorite	SEM-TOR-17B	27.01	0.52	17.75	0.07	30.15	0.45	13.17	0.55	0.01	0.04	**89.72**
Quartz-diorite	SEM-TOR-17B	27.11	0.05	19.09	0.06	29.63	0.47	12.56	0.07	0.00	0.02	**89.06**
Quartz-diorite	SEM-TOR-5	27.12	0.03	19.94	0.07	23.89	0.22	17.37	0.00	0.01	0.01	**88.66**
Quartz-diorite	SEM-TOR-5	27.28	0.12	19.18	0.07	24.02	0.17	16.87	0.08	0.01	0.00	**87.80**
Quartz-diorite	SEM-TOR-5	27.88	0.04	19.72	0.06	24.66	0.22	16.83	0.05	0.00	0.02	**89.47**
Quartz-diorite	SEM-TOR-5	27.14	0.05	19.89	0.09	24.71	0.19	16.98	0.04	0.01	0.02	**89.10**
Reaction rim	SEM-TOR-15B	26.60	0.00	19.93	0.05	29.76	0.33	12.46	0.04	0.03	0.00	**89.19**
Reaction rim	SEM-TOR-15B	26.64	0.02	20.04	0.11	29.06	0.31	13.20	0.03	0.00	0.00	**89.41**
Reaction rim	SEM-TOR-15B	25.97	0.02	20.12	0.09	29.72	0.32	12.65	0.06	0.02	0.01	**88.96**
Reaction rim	SEM-TOR-3A	27.07	0.10	18.85	0.08	29.90	0.31	12.94	0.09	0.00	0.01	**89.34**
Reaction rim	SEM-TOR-3A	26.75	0.06	18.68	0.02	30.68	0.34	12.19	0.03	0.02	0.01	**88.78**
Reaction rim	SEM-TOR-9A	26.54	0.02	19.77	0.05	27.56	0.18	15.30	0.04	0.00	0.00	**89.47**
Reaction rim	SEM-TOR-9A	27.08	0.07	19.39	0.05	27.44	0.19	15.71	0.01	0.01	0.01	**89.95**
Reaction rim	SEM-TOR-9A	27.25	0.00	19.36	0.01	27.68	0.20	15.00	0.03	0.02	0.01	**89.56**
Reaction rim	SEM-TOR-9B	26.95	0.00	19.58	0.07	26.62	0.20	15.28	0.02	0.01	0.00	**88.73**
Reaction rim	SEM-TOR-9B	27.24	0.04	19.45	0.10	27.45	0.24	14.89	0.05	0.00	0.00	**89.45**

Reaction rim	SEM-TOR-9B	27.35	0.07	19.11	0.06	27.37	0.15	14.75	0.06	0.00	0.01	**88.93**
Reaction rim	SEM-TOR-9C	26.13	0.03	20.11	0.06	25.81	0.22	15.49	0.08	0.03	0.00	**87.96**
Reaction rim	SEM-TOR-9C	26.94	0.09	19.58	0.06	25.84	0.19	14.92	0.05	0.03	0.01	**87.72**
Reaction rim	SEM-TOR-9C	26.52	0.00	19.52	0.09	26.69	0.20	14.87	0.02	0.04	0.00	**87.95**

Apatite Electronic Probe Micro-Analyses

Table XIII-19. Micro-analyses of apatite crystals.

Lithology	Sample	P_2O_5	Nd_2O_3	Ce_2O_3	La_2O_3	FeO	MnO	CaO	MgO	Na_2O	Cl	F	Total#	O=F	O=Cl	Total
Amphibolite	SEM-TOR-15A	43.26	0.02	0.16	0.04	0.21	0.10	55.71	0.05	0.04	0.43	3.04	103.05	-1.28	-0.10	**101.68**
Amphibolite	SEM-TOR-15A	42.45	0.07	0.26	0.11	0.40	0.10	54.99	0.05	0.03	0.39	2.47	101.31	-1.04	-0.09	**100.18**
Amphibolite	SEM-TOR-15A	42.98	0.03	0.00	0.07	0.46	0.09	55.57	0.05	0.02	0.46	2.64	102.36	-1.11	-0.10	**101.15**
Amphibolite	SEM-TOR-15B	41.94	0.05	0.31	0.07	0.25	0.13	54.36	0.04	0.05	0.53	2.81	100.52	-1.18	-0.12	**99.22**
Amphibolite	SEM-TOR-15B	41.98	0.05	0.39	0.09	0.55	0.11	54.14	0.05	0.00	0.51	2.50	100.38	-1.05	-0.11	**99.21**
Amphibolite	SEM-TOR-15B	42.02	0.07	0.21	0.10	0.38	0.06	54.47	0.04	0.01	0.49	2.49	100.32	-1.05	-0.11	**99.16**
Digested enclave	SEM-TOR-8A	42.01	0.03	0.22	0.12	0.27	0.14	54.24	0.04	0.10	0.90	2.22	100.27	-0.93	-0.20	**99.14**
Digested enclave	SEM-TOR-8A	41.96	0.07	0.20	0.10	0.16	0.08	54.28	0.01	0.13	0.97	2.46	100.40	-1.04	-0.22	**99.14**
Digested enclave	SEM-TOR-8A	42.17	0.07	0.28	0.17	0.11	0.10	54.15	0.03	0.08	1.05	2.62	100.83	-1.10	-0.24	**99.49**
Digested enclave	SEM-TOR-8A	42.69	0.14	0.30	0.12	0.08	0.12	54.96	0.04	0.09	0.84	2.37	101.74	-1.00	-0.19	**100.56**

Digested enclave	SEM-TOR-8A	42.90	0.08	0.27	0.10	0.09	0.12	54.80	0.01	0.13	0.65	2.36	101.51	-0.99	-0.15	**100.37**
Digested enclave	SEM-TOR-8B	42.34	0.11	0.34	0.23	0.34	0.10	54.38	0.03	0.11	0.81	2.49	101.27	-1.05	-0.18	**100.04**
Digested enclave	SEM-TOR-8B	42.73	0.12	0.36	0.29	0.33	0.18	54.42	0.04	0.09	0.74	2.20	101.48	-0.93	-0.17	**100.39**
Digested enclave	SEM-TOR-8B	42.79	0.13	0.50	0.15	0.25	0.12	54.23	0.02	0.09	0.80	2.02	101.10	-0.85	-0.18	**100.07**
Diorite	SEM-TOR-13	42.31	0.06	0.17	0.08	0.19	0.12	54.92	0.00	0.00	0.66	2.66	101.17	-1.12	-0.15	**99.90**
Diorite	SEM-TOR-13	42.17	0.05	0.11	0.06	0.28	0.10	54.82	0.03	0.04	0.62	2.43	100.70	-1.02	-0.14	**99.53**
Diorite	SEM-TOR-13	39.99	0.03	0.08	0.00	2.62	0.14	51.74	0.88	0.04	0.52	2.40	98.43	-1.01	-0.12	**97.31**
Diorite	SEM-TOR-13	42.80	0.02	0.08	0.00	0.18	0.11	55.06	0.02	0.01	0.61	2.66	101.55	-1.12	-0.14	**100.29**
Diorite	SEM-TOR-13	42.73	0.00	0.02	0.00	0.28	0.13	54.89	0.03	0.06	0.55	2.78	101.46	-1.17	-0.12	**100.16**
Diorite	SEM-TOR-13	42.68	0.03	0.12	0.05	0.27	0.11	55.03	0.02	0.03	0.67	3.01	102.01	-1.27	-0.15	**100.59**
Diorite	SEM-TOR-13	42.94	0.03	0.31	0.07	0.22	0.07	55.01	0.00	0.05	0.51	2.82	102.03	-1.19	-0.11	**100.72**
Diorite	SEM-TOR-18A	42.51	0.00	0.25	0.11	0.26	0.08	54.53	0.00	0.07	0.62	2.40	100.83	-1.01	-0.14	**99.68**

Diorite	SEM-TOR-18A	42.74	0.03	0.16	0.00	0.17	0.02	55.13	0.01	0.00	0.27	2.73	101.24	-1.15	-0.06	**100.03**
Diorite	SEM-TOR-18A	42.72	0.04	0.29	0.15	0.20	0.07	54.43	0.02	0.04	0.76	2.02	100.75	-0.85	-0.17	**99.72**
Diorite	SEM-TOR-4	42.04	0.07	0.12	0.06	0.12	0.10	54.74	0.04	0.04	0.52	1.96	99.80	-0.82	-0.12	**98.86**
Diorite	SEM-TOR-4	42.17	0.03	0.16	0.04	0.13	0.07	54.55	0.02	0.06	0.75	2.00	99.98	-0.84	-0.17	**98.97**
Diorite	SEM-TOR-4	41.34	0.04	0.00	0.02	0.18	0.07	53.70	0.03	0.04	0.52	2.04	97.96	-0.86	-0.12	**96.99**
Diorite	SEM-TOR-4	42.59	0.06	0.06	0.00	0.10	0.10	54.59	0.01	0.05	0.63	2.21	100.38	-0.93	-0.14	**99.31**
Diorite	SEM-TOR-4	42.43	0.02	0.17	0.09	0.18	0.06	54.59	0.03	0.07	0.64	2.36	100.63	-0.99	-0.14	**99.49**
Fine-grained amphibolite	SEM-TOR-2	42.57	0.00	0.12	0.10	0.43	0.05	54.52	0.03	0.07	0.80	2.54	101.22	-1.07	-0.18	**99.97**
Gabbro	SEM-TOR-9A	43.33	0.05	0.34	0.08	0.16	0.12	55.52	0.03	0.06	0.80	2.41	102.90	-1.02	-0.18	**101.70**
Gabbro	SEM-TOR-9A	43.29	0.01	0.26	0.06	0.14	0.13	55.72	0.02	0.04	0.67	2.43	102.75	-1.02	-0.15	**101.58**
Gabbro	SEM-TOR-9A	43.49	0.01	0.34	0.06	0.16	0.12	55.44	0.03	0.05	0.85	2.60	103.15	-1.10	-0.19	**101.86**
Gabbro	SEM-TOR-9B	43.09	0.00	0.19	0.08	0.35	0.13	55.18	0.06	0.03	0.74	2.01	101.86	-0.85	-0.17	**100.85**
Gabbro	SEM-TOR-9B	43.33	0.08	0.00	0.00	0.49	0.11	55.24	0.04	0.04	0.81	2.31	102.46	-0.97	-0.18	**101.30**
Gabbro	SEM-TOR-9B	42.94	0.05	0.39	0.07	0.17	0.12	55.15	0.02	0.04	0.87	2.09	101.91	-0.88	-0.20	**100.83**

Gabbro	SEM-TOR-9B	42.76	0.07	0.31	0.09	0.90	0.12	54.60	0.26	0.03	0.58	2.29	101.99	-0.96	-0.13	**100.90**
Gabbro	SEM-TOR-9C	42.53	0.11	0.30	0.06	0.08	0.12	54.41	0.00	0.05	0.81	1.97	100.45	-0.83	-0.18	**99.44**
Gabbro	SEM-TOR-9C	39.08	0.10	0.30	0.07	0.23	0.14	54.83	0.06	0.05	0.99	1.74	97.58	-0.73	-0.22	**96.63**
Gabbro	SEM-TOR-9C	42.41	0.08	0.43	0.09	0.05	0.11	54.42	0.00	0.06	0.82	2.00	100.47	-0.84	-0.19	**99.44**
Leucocratric inj.	SEM-TOR-1	42.94	0.00	0.41	0.12	0.54	0.06	55.13	0.00	0.05	0.42	2.78	102.45	-1.17	-0.09	**101.18**
Leucocratric inj.	SEM-TOR-1	42.89	0.06	0.10	0.11	0.29	0.14	54.78	0.01	0.09	0.45	2.24	101.15	-0.94	-0.10	**100.11**
Leucocratric inj.	SEM-TOR-1	42.66	0.08	0.17	0.04	0.15	0.11	54.68	0.04	0.06	0.92	2.10	101.02	-0.89	-0.21	**99.92**
Leucocratric inj.	SEM-TOR-15B	42.41	0.01	0.25	0.11	0.12	0.17	54.42	0.02	0.06	0.60	2.02	100.17	-0.85	-0.14	**99.19**
Leucocratric inj.	SEM-TOR-15B	42.99	0.01	0.09	0.00	0.01	0.02	55.37	0.00	0.01	0.09	2.83	101.42	-1.19	-0.02	**100.21**
Leucocratric inj.	SEM-TOR-15B	42.57	0.01	0.22	0.11	0.12	0.20	54.60	0.00	0.03	0.53	2.52	100.91	-1.06	-0.12	**99.73**
Leucocratric inj.	SEM-TOR-2	42.50	0.09	0.29	0.14	0.13	0.19	54.42	0.04	0.07	0.84	2.16	100.86	-0.91	-0.19	**99.76**
Leucocratric inj.	SEM-TOR-2	42.65	0.07	0.28	0.08	0.08	0.14	54.51	0.01	0.06	0.76	2.33	100.97	-0.98	-0.17	**99.82**
Leucocratric inj.	SEM-TOR-2	43.10	0.00	0.16	0.03	0.07	0.11	55.32	0.01	0.00	0.22	2.43	101.44	-1.02	-0.05	**100.36**
Leucocratric inj.	SEM-TOR-2	43.07	0.03	0.00	0.11	0.02	0.04	55.27	0.00	0.03	0.22	2.24	101.03	-0.94	-0.05	**100.03**

Pegmatoid	SEM-TOR-16A	42.98	0.07	0.20	0.11	0.13	0.08	55.08	0.03	0.09	0.81	2.41	101.99	-1.01	-0.18	**100.80**
Pegmatoid	SEM-TOR-16A	42.81	0.12	0.43	0.16	0.15	0.09	55.30	0.02	0.09	0.70	2.39	102.24	-1.00	-0.16	**101.08**
Pegmatoid	SEM-TOR-16A	42.59	0.12	0.40	0.22	0.17	0.14	54.93	0.02	0.08	1.19	1.54	101.40	-0.65	-0.27	**100.48**
Pegmatoid	SEM-TOR-16A	42.97	0.07	0.25	0.12	0.13	0.09	55.14	0.03	0.12	1.06	2.23	102.21	-0.94	-0.24	**101.03**
Pegmatoid	SEM-TOR-16A	42.90	0.04	0.40	0.08	0.14	0.09	55.12	0.03	0.07	0.82	2.30	102.01	-0.97	-0.18	**100.85**
Pegmatoid	SEM-TOR-16B	42.97	0.04	0.05	0.01	0.08	0.01	55.44	0.01	0.03	0.21	2.51	101.36	-1.06	-0.05	**100.26**
Pegmatoid	SEM-TOR-16B	43.04	0.00	0.00	0.05	0.09	0.02	55.53	0.00	0.00	0.11	2.84	101.68	-1.20	-0.03	**100.46**
Pegmatoid	SEM-TOR-16B	42.68	0.09	0.25	0.17	0.15	0.06	54.68	0.03	0.10	0.83	1.90	100.95	-0.80	-0.19	**99.96**
Pegmatoid	SEM-TOR-16B	42.70	0.06	0.26	0.12	0.18	0.08	54.74	0.03	0.06	0.82	2.07	101.10	-0.87	-0.18	**100.05**
Pegmatoid	SEM-TOR-16B	42.91	0.03	0.31	0.16	0.19	0.10	54.90	0.04	0.10	0.96	2.41	102.10	-1.01	-0.22	**100.87**
Pegmatoid	SEM-TOR-16B	42.83	0.10	0.28	0.15	0.19	0.09	54.68	0.05	0.09	1.05	1.64	101.15	-0.69	-0.24	**100.22**
Pegmatoid	SEM-TOR-16B	42.97	0.05	0.24	0.14	0.13	0.09	54.54	0.04	0.09	1.05	1.75	101.08	-0.74	-0.24	**100.11**

Pegmatoid	SEM-TOR-16B	42.88	0.12	0.52	0.18	0.17	0.07	54.86	0.03	0.08	1.00	2.17	102.08	-0.91	-0.23	**100.95**
Quartz-diorite	SEM-TOR-10	42.51	0.05	0.21	0.12	0.09	0.11	54.52	0.01	0.09	0.83	2.55	101.08	-1.07	-0.19	**99.82**
Quartz-diorite	SEM-TOR-10	42.41	0.09	0.38	0.14	0.09	0.13	54.68	0.00	0.07	0.30	2.69	100.96	-1.13	-0.07	**99.76**
Quartz-diorite	SEM-TOR-11	42.28	0.11	0.40	0.17	0.14	0.09	54.32	0.02	0.15	0.70	2.65	101.02	-1.11	-0.16	**99.75**
Quartz-diorite	SEM-TOR-11	41.96	0.06	0.43	0.10	0.41	0.10	54.34	0.03	0.09	0.53	2.49	100.54	-1.05	-0.12	**99.38**
Quartz-diorite	SEM-TOR-11	42.51	0.08	0.39	0.10	0.10	0.10	54.57	0.01	0.13	0.56	2.26	100.80	-0.95	-0.13	**99.72**
Quartz-diorite	SEM-TOR-11	42.82	0.07	0.38	0.04	1.46	0.11	50.48	0.72	0.08	0.25	3.41	99.80	-1.43	-0.06	**98.31**
Quartz-diorite	SEM-TOR-12	42.52	0.10	0.45	0.17	0.23	0.14	54.31	0.03	0.13	0.91	2.49	101.47	-1.05	-0.21	**100.22**
Quartz-diorite	SEM-TOR-12	42.66	0.07	0.48	0.18	0.22	0.15	54.35	0.03	0.15	0.95	2.57	101.81	-1.08	-0.21	**100.51**
Quartz-diorite	SEM-TOR-12	42.44	0.15	0.48	0.17	0.10	0.13	54.12	0.04	0.15	0.89	2.25	100.92	-0.95	-0.20	**99.77**
Quartz-diorite	SEM-TOR-12	42.32	0.07	0.54	0.19	0.14	0.16	54.15	0.02	0.16	0.87	2.30	100.94	-0.97	-0.20	**99.77**
Quartz-diorite	SEM-TOR-14	42.79	0.09	0.09	0.07	0.21	0.08	55.02	0.02	0.08	0.76	2.81	102.02	-1.18	-0.17	**100.66**

Quartz-diorite	SEM-TOR-14	41.38	0.09	0.38	0.06	0.12	0.07	55.05	0.01	0.07	0.55	3.15	100.94	-1.33	-0.12	**99.49**
Quartz-diorite	SEM-TOR-17A	42.17	0.03	0.03	0.09	0.50	0.10	54.31	0.02	0.08	0.38	2.94	100.64	-1.24	-0.09	**99.31**
Quartz-diorite	SEM-TOR-17A	36.39	0.00	0.24	0.06	4.61	0.15	45.90	1.82	0.11	0.31	1.88	91.45	-0.79	-0.07	**90.59**
Quartz-diorite	SEM-TOR-17B	42.26	0.06	0.51	0.10	0.35	0.09	54.79	0.01	0.12	0.50	2.52	101.28	-1.06	-0.11	**100.11**
Quartz-diorite	SEM-TOR-17B	41.89	0.00	0.30	0.07	0.56	0.10	54.52	0.01	0.13	0.50	2.17	100.25	-0.91	-0.11	**99.22**
Quartz-diorite	SEM-TOR-17B	40.87	0.05	0.23	0.12	0.59	0.16	52.97	0.58	0.19	0.54	2.26	98.56	-0.95	-0.12	**97.49**
Reaction rim	SEM-TOR-15A	42.78	0.08	0.22	0.07	0.35	0.13	54.96	0.05	0.02	0.75	2.22	101.62	-0.93	-0.17	**100.51**
Reaction rim	SEM-TOR-15A	42.76	0.04	0.20	0.00	0.30	0.11	54.60	0.03	0.05	0.61	2.41	101.11	-1.01	-0.14	**99.95**
Reaction rim	SEM-TOR-15A	42.28	0.02	0.17	0.04	0.27	0.06	54.55	0.03	0.07	0.79	2.38	100.66	-1.00	-0.18	**99.48**
Reaction rim	SEM-TOR-15A	42.64	0.05	0.30	0.11	0.19	0.12	54.58	0.01	0.07	0.64	2.27	100.98	-0.95	-0.14	**99.88**
Reaction rim	SEM-TOR-15B	42.64	0.09	0.28	0.09	0.18	0.14	54.72	0.03	0.06	0.71	2.00	100.93	-0.84	-0.16	**99.93**
Reaction rim	SEM-TOR-15B	42.58	0.06	0.00	0.09	0.12	0.14	54.85	0.03	0.04	0.66	2.35	100.92	-0.99	-0.15	**99.79**

Reaction rim	SEM-TOR-3A	42.48	0.07	0.27	0.18	0.42	0.12	54.62	0.01	0.08	0.62	2.27	101.14	-0.95	-0.14	**100.05**
Reaction rim	SEM-TOR-3A	42.64	0.10	0.41	0.11	0.32	0.16	54.75	0.00	0.08	0.82	2.17	101.56	-0.91	-0.18	**100.46**
Reaction rim	SEM-TOR-3A	42.63	0.08	0.40	0.12	0.23	0.14	54.84	0.03	0.06	0.62	2.40	101.55	-1.01	-0.14	**100.40**
Reaction rim	SEM-TOR-9A	43.62	0.10	0.25	0.01	0.10	0.15	55.46	0.04	0.10	0.63	2.75	103.22	-1.16	-0.14	**101.92**
Reaction rim	SEM-TOR-9A	43.26	0.06	0.14	0.07	0.16	0.07	55.65	0.03	0.05	0.63	2.43	102.56	-1.02	-0.14	**101.40**
Reaction rim	SEM-TOR-9A	43.53	0.10	0.32	0.06	0.08	0.11	55.46	0.00	0.08	0.53	2.19	102.46	-0.92	-0.12	**101.42**
Reaction rim	SEM-TOR-9B	42.86	0.05	0.16	0.04	0.26	0.13	55.55	0.05	0.15	0.66	2.58	102.50	-1.09	-0.15	**101.26**
Reaction rim	SEM-TOR-9C	42.58	0.07	0.27	0.11	0.09	0.12	54.56	0.00	0.04	0.65	2.39	100.87	-1.00	-0.15	**99.72**
Reaction rim	SEM-TOR-9C	42.76	0.05	0.20	0.06	0.10	0.05	54.65	0.00	0.04	0.51	2.24	100.64	-0.94	-0.11	**99.58**
Reaction rim	SEM-TOR-9C	42.39	0.05	0.19	0.06	0.11	0.08	54.48	0.01	0.03	0.60	2.64	100.64	-1.11	-0.13	**99.39**
Sulph inj.	SEM-TOR-7A	43.19	0.09	0.25	0.06	0.35	0.13	55.27	0.06	0.05	0.97	1.50	101.92	-0.63	-0.22	**101.07**
Sulph inj.	SEM-TOR-7A	43.31	0.04	0.17	0.11	0.41	0.14	55.10	0.04	0.02	0.98	1.75	102.06	-0.73	-0.22	**101.10**

Sulph inj.	SEM-TOR-7B	42.47	0.04	0.14	0.13	0.16	0.11	54.24	0.05	0.08	0.93	1.70	100.06	-0.72	-0.21	**99.13**
Sulph inj.	SEM-TOR-7B	42.48	0.10	0.35	0.00	0.15	0.12	54.30	0.01	0.07	0.86	1.79	100.21	-0.75	-0.20	**99.27**
Sulph inj.	SEM-TOR-7B	42.54	0.01	0.22	0.07	0.08	0.04	54.46	0.00	0.05	0.68	1.74	99.90	-0.73	-0.15	**99.02**
Sulph inj.	SEM-TOR-7B	42.43	0.07	0.16	0.09	0.06	0.10	54.21	0.01	0.03	0.75	1.51	99.41	-0.64	-0.17	**98.60**

Pyroxene Electronic Probe Micro-Analyses

Table XIII-20. Micro-analyses of pyroxene crystals.

Lithology	Sample	SiO_2	TiO_2	Al_2O_3	V_2O_3	Cr_2O_3	MgO	CaO	MnO	FeO	NiO	ZnO	Na_2O	K_2O	Total
Amphibolite	SEM-TOR-7B	52.43	0.08	0.75	0.01	0.16	13.49	21.59	0.41	9.54	0.00	0.00	0.32	0.00	**98.78**
Amphibolite	SEM-TOR-7B	52.53	0.06	0.73	0.01	0.07	12.87	21.51	0.49	10.38	0.04	0.03	0.30	0.00	**99.02**
Digested gabbro	SEM-TOR-8B	52.76	0.20	1.68	0.00	0.06	17.34	1.70	0.98	21.34	0.05	0.00	0.22	0.01	**96.32**
Digested gabbro	SEM-TOR-8B	49.41	0.72	4.39	0.02	0.04	14.08	7.11	0.62	18.02	0.00	0.03	0.90	0.14	**95.48**
Digested gabbro	SEM-TOR-8B	52.09	0.25	2.65	0.03	0.03	16.90	2.77	0.80	20.46	0.00	0.04	0.32	0.07	**96.41**
Digested gabbro	SEM-TOR-8B	52.06	0.32	2.53	0.00	0.06	16.36	3.34	0.77	20.79	0.01	0.00	0.30	0.06	**96.60**
Digested gabbro	SEM-TOR-8B	54.17	0.11	1.16	0.01	0.05	16.99	2.53	0.87	20.82	0.00	0.02	0.21	0.03	**96.96**
Digested gabbro	SEM-TOR-8B	51.70	0.35	3.05	0.02	0.06	16.14	4.00	0.77	19.91	0.00	0.00	0.35	0.09	**96.43**
Gabbro	SEM-TOR-9B	52.38	0.13	0.80	0.00	0.01	19.17	1.13	0.84	26.35	0.00	0.00	0.00	0.00	**100.83**
Gabbro	SEM-TOR-9B	52.31	0.16	0.84	0.00	0.08	19.06	1.34	0.74	26.15	0.00	0.00	0.03	0.01	**100.71**
Gabbro	SEM-TOR-9B	52.28	0.13	0.83	0.00	0.03	19.02	0.96	0.83	26.83	0.00	0.02	0.01	0.00	**100.94**
Gabbro	SEM-TOR-9B	52.05	0.12	0.86	0.00	0.10	18.70	1.28	0.80	26.57	0.00	0.04	0.02	0.01	**100.56**
Gabbro	SEM-TOR-9B	52.75	0.10	0.70	0.00	0.05	20.56	1.30	0.76	24.87	0.00	0.10	0.05	0.00	**101.24**
Gabbro	SEM-TOR-9B	52.31	0.13	0.86	0.02	0.03	19.54	1.29	0.79	25.70	0.04	0.00	0.05	0.00	**100.75**
Gabbro	SEM-TOR-9B	52.18	0.12	1.24	0.01	0.10	19.22	0.90	0.72	26.29	0.00	0.05	0.03	0.01	**100.88**
Gabbro	SEM-TOR-9B	52.07	0.15	0.96	0.00	0.08	19.12	1.02	0.84	26.51	0.02	0.04	0.01	0.00	**100.82**

Quartz-diorite	SEM-TOR-12	53.95	0.34	1.55	0.00	0.04	18.92	1.66	0.87	20.25	0.00	0.03	0.20	0.03	**97.84**
Quartz-diorite	SEM-TOR-12	53.24	0.21	2.05	0.00	0.04	17.94	2.69	0.97	20.01	0.04	0.01	0.21	0.06	**97.46**
Quartz-diorite	SEM-TOR-12	53.45	0.18	1.99	0.02	0.07	17.81	3.33	0.95	19.68	0.01	0.05	0.21	0.04	**97.77**
Quartz-diorite	SEM-TOR-12	52.77	0.25	2.89	0.00	0.06	17.08	5.36	0.83	18.15	0.00	0.06	0.27	0.08	**97.79**
Quartz-diorite	SEM-TOR-12	54.32	0.10	0.95	0.00	0.07	18.24	1.60	1.02	21.09	0.00	0.03	0.12	0.01	**97.55**
Quartz-diorite	SEM-TOR-12	53.64	0.17	1.55	0.01	0.07	17.88	2.22	1.01	20.72	0.00	0.05	0.16	0.03	**97.50**
Quartz-diorite	SEM-TOR-12	53.34	0.23	1.66	0.01	0.07	18.37	1.91	0.76	19.88	0.01	0.00	0.19	0.02	**96.46**
Quartz-diorite	SEM-TOR-12	53.74	0.14	1.26	0.02	0.06	18.69	1.33	0.81	20.10	0.00	0.08	0.11	0.01	**96.33**
Quartz-diorite	SEM-TOR-12	52.78	0.29	2.38	0.02	0.06	17.47	3.15	0.76	19.29	0.02	0.08	0.27	0.08	**96.66**
Quartz-diorite	SEM-TOR-12	53.75	0.10	1.16	0.00	0.07	18.67	1.53	0.88	20.22	0.07	0.01	0.10	0.02	**96.57**
Quartz-diorite	SEM-TOR-3B	52.46	0.26	2.27	0.03	0.08	15.74	3.90	1.07	21.38	0.03	0.00	0.26	0.06	**97.52**
Quartz-diorite	SEM-TOR-3B	52.43	0.30	2.16	0.00	0.03	16.75	2.19	0.95	21.65	0.00	0.11	0.28	0.04	**96.88**
Quartz-diorite	SEM-TOR-3B	52.43	0.30	1.98	0.01	0.04	16.19	1.98	1.08	22.72	0.04	0.00	0.29	0.04	**97.11**
Quartz-diorite	SEM-TOR-3B	53.05	0.15	1.29	0.01	0.08	16.57	1.24	1.17	22.96	0.03	0.01	0.18	0.00	**96.74**
Quartz-diorite	SEM-TOR-3B	51.72	0.35	2.59	0.02	0.05	15.81	2.70	0.93	21.83	0.01	0.05	0.37	0.05	**96.45**
Quartz-diorite	SEM-TOR-3B	52.00	0.27	2.21	0.03	0.06	15.93	2.06	0.99	22.35	0.06	0.12	0.31	0.04	**96.43**
Sulph. Inj.	SEM-TOR-7B	52.07	0.06	0.62	0.05	0.08	12.88	22.20	0.41	9.78	0.00	0.04	0.29	0.00	**98.47**
Sulph. Inj.	SEM-TOR-7B	52.50	0.01	0.50	0.00	0.09	13.04	22.55	0.44	9.34	0.00	0.03	0.29	0.01	**98.79**

Sulph. Inj.	SEM-TOR-7B	52.26	0.03	0.59	0.01	0.11	13.31	21.87	0.42	9.72	0.00	0.01	0.33	0.00	**98.64**
Sulph. Inj.	SEM-TOR-7B	52.22	0.02	0.60	0.05	0.03	13.47	21.91	0.49	9.77	0.00	0.01	0.29	0.00	**98.84**
Sulph. Inj.	SEM-TOR-7B	52.83	0.00	0.54	0.04	0.06	12.99	22.95	0.44	9.86	0.01	0.00	0.31	0.00	**100.04**
Sulph. Inj.	SEM-TOR-7B	52.95	0.00	0.46	0.05	0.07	13.05	22.81	0.49	9.82	0.00	0.07	0.27	0.00	**100.04**
Sulph. Inj.	SEM-TOR-7B	52.70	0.03	0.56	0.03	0.08	12.77	22.88	0.43	10.07	0.00	0.02	0.34	0.00	**99.91**
Sulph. Inj.	SEM-TOR-7B	52.48	0.04	0.73	0.01	0.10	13.47	21.61	0.42	10.13	0.01	0.04	0.33	0.00	**99.36**

Magnetite Electronic Probe Micro-Analyses

Table XIII-21. Micro-analyses of magnetite crystals.

Lithology	Sample	Al_2O_3	MgO	MnO	V_2O_3	TiO_2	ZnO	NiO	FeO	Cr_2O_3	TOTAL
Diorite	SEM-TOR-13	0.28	0.00	0.00	0.57	0.46	0.06	0.00	90.16	0.18	**91.71**
Diorite	SEM-TOR-13	0.06	0.00	0.00	0.36	0.10	0.00	0.00	90.73	0.17	**91.41**
Diorite	SEM-TOR-13	0.13	0.02	0.00	0.53	0.04	0.04	0.00	91.31	0.11	**92.18**
Diorite	SEM-TOR-13	0.06	0.01	0.05	0.55	0.24	0.00	0.00	90.83	0.16	**91.89**
Diorite	SEM-TOR-13	0.04	0.02	0.02	0.55	0.33	0.00	0.00	90.72	0.16	**91.83**
Diorite	SEM-TOR-13	0.06	0.01	0.00	0.65	0.14	0.00	0.01	90.57	0.17	**91.61**
Diorite	SEM-TOR-13	0.03	0.01	0.05	0.44	0.41	0.04	0.00	91.36	0.14	**92.48**
Diorite	SEM-TOR-13	0.04	0.02	0.01	0.45	0.25	0.00	0.00	90.82	0.16	**91.74**
Diorite	SEM-TOR-13	0.01	0.00	0.02	0.46	0.11	0.05	0.00	91.59	0.09	**92.32**
Diorite	SEM-TOR-13	0.08	0.00	0.04	0.52	0.56	0.00	0.00	90.82	0.15	**92.17**
Diorite	SEM-TOR-13	0.13	0.00	0.01	0.55	0.67	0.02	0.00	90.87	0.16	**92.41**
Diorite	SEM-TOR-13	0.02	0.01	0.00	0.44	0.00	0.08	0.00	91.53	0.16	**92.24**
Diorite	SEM-TOR-13	0.14	0.00	0.03	0.48	0.10	0.04	0.00	91.79	0.16	**92.74**
Diorite	SEM-TOR-13	0.11	0.00	0.03	0.48	0.20	0.00	0.00	91.45	0.11	**92.37**
Diorite	SEM-TOR-18A	0.21	0.00	0.00	0.84	0.05	0.03	0.00	91.02	0.20	**92.36**
Diorite	SEM-TOR-18A	0.15	0.00	0.03	0.91	0.22	0.13	0.01	90.78	0.22	**92.45**

Diorite	SEM-TOR-18A	0.36	0.01	0.01	0.86	0.12	0.07	0.00	90.36	0.23	**92.01**
Diorite	SEM-TOR-18A	0.34	0.02	0.00	0.86	0.19	0.00	0.00	90.39	0.21	**92.00**
Diorite	SEM-TOR-18A	0.08	0.00	0.00	0.76	0.02	0.00	0.00	92.12	0.20	**93.18**
Diorite	SEM-TOR-18A	0.83	0.00	0.00	0.77	0.22	0.04	0.01	90.82	0.17	**92.85**
Diorite	SEM-TOR-18A	0.01	0.00	0.00	0.69	0.08	0.03	0.00	92.06	0.23	**93.10**
Diorite	SEM-TOR-18A	0.02	0.00	0.01	0.79	0.01	0.06	0.00	92.24	0.21	**93.34**
Diorite	SEM-TOR-18B	1.80	0.00	0.01	1.17	0.55	0.45	0.00	87.86	0.33	**92.16**
Diorite	SEM-TOR-18B	1.34	0.00	0.03	1.19	0.17	0.22	0.01	89.52	0.29	**92.76**
Diorite	SEM-TOR-20	1.00	0.00	0.00	0.66	0.51	0.00	0.02	90.10	0.18	**92.46**
Diorite	SEM-TOR-20	0.80	0.00	0.00	0.59	0.54	0.03	0.00	90.27	0.16	**92.40**
Diorite	SEM-TOR-20	0.69	0.01	0.01	0.60	0.54	0.07	0.00	90.23	0.17	**92.32**
Diorite	SEM-TOR-20	0.35	0.00	0.00	0.56	0.38	0.02	0.00	90.92	0.18	**92.41**
Diorite	SEM-TOR-20	0.59	0.02	0.00	0.74	0.52	0.05	0.00	90.31	0.20	**92.42**
Diorite	SEM-TOR-20	0.13	0.00	0.00	0.65	0.55	0.09	0.04	90.60	0.23	**92.29**
Diorite	SEM-TOR-20	0.28	0.07	5.31	0.26	29.61	0.07	0.00	58.79	0.10	**94.49**
Diorite	SEM-TOR-20	0.30	0.00	0.00	0.70	0.56	0.02	0.00	90.24	0.19	**92.00**
Diorite	SEM-TOR-20	0.32	0.00	0.00	0.69	0.44	0.01	0.02	90.00	0.20	**91.68**
Diorite	SEM-TOR-20	1.12	0.02	0.02	0.59	0.53	0.07	0.00	89.41	0.14	**91.89**

Diorite	SEM-TOR-20	0.11	0.00	0.00	0.56	0.24	0.06	0.00	90.42	0.18	**91.56**
Diorite	SEM-TOR-4	0.99	0.02	0.21	0.23	3.21	0.32	0.00	86.48	0.12	**91.58**
Diorite	SEM-TOR-4	0.58	0.02	0.03	0.23	0.86	0.07	0.00	89.61	0.10	**91.51**
Diorite	SEM-TOR-4	0.11	0.02	0.00	0.20	0.50	0.00	0.00	90.27	0.14	**91.23**
Diorite	SEM-TOR-4	0.60	0.01	0.01	0.24	0.77	0.07	0.00	89.72	0.11	**91.52**
Diorite	SEM-TOR-4	0.62	0.00	0.01	0.25	0.83	0.12	0.01	89.27	0.09	**91.19**
Diorite	SEM-TOR-4	0.49	0.00	0.21	0.30	0.98	0.13	0.01	89.50	0.16	**91.78**
Diorite	SEM-TOR-4	0.14	0.01	0.00	0.19	0.14	0.05	0.00	90.65	0.09	**91.26**
Diorite	SEM-TOR-4	0.17	0.03	0.07	0.23	0.88	0.03	0.00	90.52	0.10	**92.04**

Ilmenite Electronic Probe Micro-Analyses

Table XIII-22. Micro-analyses of ilmenite crystals.

Lithology	Sample	SiO_2	TiO_2	Al_2O_3	V_2O_3	Cr_2O_3	MgO	CaO	MnO	FeO	NiO	ZnO	Na_2O	BaO	Total
Amphibolite	SEM-TOR-15A	0.01	49.33	0.03	0.13	0.15	0.18	0.28	0.92	47.51	0.00	0.08	0.00	0.12	**98.74**
Amphibolite	SEM-TOR-15A	0.02	50.62	0.01	0.07	0.10	0.03	0.20	6.95	40.48	0.00	0.00	0.01	0.14	**98.65**
Amphibolite	SEM-TOR-15A	0.02	50.76	0.00	0.10	0.09	1.01	0.11	0.84	46.28	0.00	0.09	0.00	0.13	**99.42**
Amphibolite	SEM-TOR-15A	0.03	50.10	0.00	0.14	0.15	0.68	0.22	0.69	46.51	0.00	0.00	0.00	0.22	**98.74**
Amphibolite	SEM-TOR-15A	0.05	50.30	0.01	0.04	0.15	0.98	0.26	0.72	46.08	0.03	0.00	0.02	0.18	**98.81**
Amphibolite	SEM-TOR-15B	1.78	45.19	1.15	0.14	0.16	0.11	1.31	8.28	37.05	0.00	0.05	0.10	0.19	**95.51**
Amphibolite	SEM-TOR-15B	0.02	51.20	0.00	0.07	0.13	0.01	0.25	4.03	41.23	0.00	0.00	0.00	0.21	**97.15**
Amphibolite	SEM-TOR-15B	0.06	50.40	0.01	0.08	0.12	0.00	0.23	4.42	41.66	0.00	0.00	0.03	0.14	**97.16**
Amphibolite	SEM-TOR-15B	0.03	49.50	0.02	0.11	0.18	0.01	0.18	3.50	43.45	0.00	0.08	0.00	0.10	**97.14**
Amphibolite	SEM-TOR-15B	0.00	49.02	0.00	0.09	0.14	0.03	0.16	4.50	43.23	0.00	0.05	0.00	0.12	**97.34**
Amphibolite	SEM-TOR-3B	0.00	50.89	0.00	0.19	0.10	0.07	0.04	1.35	46.27	0.01	0.05	0.00	0.21	**99.18**

Amphibolite	SEM-TOR-3B	0.01	50.50	0.01	0.15	0.13	0.04	0.09	1.61	46.48	0.00	0.05	0.00	0.18	**99.25**
Amphibolite	SEM-TOR-3B	0.01	51.45	0.01	0.14	0.10	0.19	0.11	1.51	45.50	0.00	0.00	0.00	0.16	**99.18**
Amphibolite	SEM-TOR-3B	0.04	51.33	0.01	0.10	0.13	0.09	0.18	1.73	45.30	0.00	0.10	0.01	0.25	**99.26**
Amphibolite	SEM-TOR-3B	0.04	51.54	0.00	0.14	0.08	0.16	0.12	1.57	45.46	0.00	0.06	0.02	0.21	**99.38**
Amphibolite	SEM-TOR-3B	0.02	51.39	0.00	0.09	0.10	0.10	0.10	1.71	45.66	0.00	0.12	0.01	0.15	**99.43**
Amphibolite	SEM-TOR-6	0.02	48.54	0.00	0.24	0.15	0.20	0.04	2.40	46.39	0.00	0.06	0.03	0.15	**98.22**
Amphibolite	SEM-TOR-6	9.92	48.67	0.11	0.00	0.12	1.45	0.61	4.46	39.28	0.02	0.00	0.00	0.13	**104.78**
Amphibolite	SEM-TOR-6	0.01	49.01	0.05	0.15	0.09	0.33	0.07	2.74	45.53	0.00	0.02	0.00	0.13	**98.13**
Amphibolite	SEM-TOR-6	0.00	49.56	0.02	0.19	0.14	0.04	0.14	5.91	42.06	0.05	0.05	0.00	0.16	**98.31**
Amphibolite	SEM-TOR-6	0.00	48.05	0.01	0.14	0.16	0.24	0.03	3.35	45.68	0.00	0.11	0.00	0.14	**97.92**
Amphibolite	SEM-TOR-6	0.01	47.72	0.03	0.19	0.12	0.07	0.15	4.83	44.51	0.00	0.01	0.00	0.13	**97.77**
Amphibolite	SEM-TOR-6	0.02	48.10	0.04	0.15	0.12	0.15	0.16	5.15	43.54	0.01	0.10	0.00	0.13	**97.66**
Amphibolite	SEM-TOR-6	0.03	45.94	0.01	0.12	0.10	0.00	0.30	6.24	44.17	0.01	0.00	0.02	0.13	**97.06**
Amphibolite	SEM-TOR-6	0.02	47.56	0.03	0.14	0.14	0.01	0.20	5.66	43.30	0.02	0.00	0.02	0.11	**97.20**
Amphibolite	SEM-TOR-7A	0.01	50.55	0.00	0.59	0.31	0.02	0.14	3.22	44.63	0.01	0.00	0.00	0.19	**99.66**
Amphibolite	SEM-TOR-7A	0.02	51.00	0.00	0.78	0.37	0.03	0.09	4.08	43.86	0.00	0.00	0.03	0.16	**100.42**
Amphibolite	SEM-TOR-7A	0.06	50.28	0.01	0.30	0.25	0.03	0.23	3.08	44.82	0.02	0.00	0.01	0.19	**99.26**
Amphibolite	SEM-TOR-7B	0.02	49.49	0.00	0.13	0.14	0.05	0.13	2.01	45.90	0.00	0.10	0.01	0.23	**98.21**

Amphibolite	SEM-TOR-7B	0.07	49.80	0.00	0.02	0.15	0.02	0.27	3.92	43.25	0.03	0.15	0.00	0.09	**97.76**
Amphibolite	SEM-TOR-7B	0.04	50.11	0.00	0.03	0.11	0.03	0.21	4.25	42.56	0.01	0.00	0.00	0.14	**97.48**
Digested enclave	SEM-TOR-8A	0.00	48.27	0.00	0.03	0.10	0.08	0.00	1.45	47.08	0.00	0.07	0.00	0.18	**97.27**
Digested enclave	SEM-TOR-8A	0.00	48.78	0.02	0.07	0.09	0.03	0.03	1.70	46.43	0.00	0.03	0.03	0.11	**97.31**
Digested enclave	SEM-TOR-8A	0.00	48.72	0.01	0.06	0.08	0.02	0.00	1.60	46.69	0.00	0.00	0.04	0.14	**97.37**
Digested enclave	SEM-TOR-8A	0.01	48.64	0.00	0.04	0.15	0.03	0.03	1.57	46.64	0.00	0.01	0.00	0.12	**97.23**
Digested enclave	SEM-TOR-8A	0.00	48.15	0.00	0.05	0.11	0.07	0.00	1.29	47.25	0.00	0.05	0.00	0.15	**97.12**
Digested enclave	SEM-TOR-8A	0.00	48.43	0.00	0.09	0.18	0.06	0.00	1.39	46.86	0.03	0.03	0.00	0.14	**97.21**
Digested enclave	SEM-TOR-8A	0.01	48.62	0.01	0.05	0.11	0.01	0.00	2.30	47.15	0.00	0.00	0.00	0.17	**98.41**
Digested enclave	SEM-TOR-8A	0.00	48.89	0.02	0.08	0.08	0.01	0.03	2.10	47.03	0.00	0.06	0.00	0.18	**98.47**
Digested enclave	SEM-TOR-8A	0.01	48.60	0.00	0.11	0.12	0.03	0.01	2.84	46.51	0.00	0.00	0.03	0.19	**98.44**
Digested enclave	SEM-TOR-8A	0.02	49.77	0.02	0.06	0.11	0.02	0.02	2.36	45.90	0.00	0.03	0.02	0.17	**98.48**
Digested enclave	SEM-TOR-8B	0.00	48.24	0.00	0.13	0.12	0.08	0.00	1.10	48.58	0.00	0.00	0.00	0.14	**98.39**
Digested enclave	SEM-TOR-8B	0.00	48.08	0.00	0.15	0.12	0.06	0.01	1.18	48.50	0.00	0.04	0.00	0.18	**98.32**
Digested enclave	SEM-TOR-8B	0.01	48.69	0.01	0.13	0.06	0.11	0.03	1.07	48.24	0.04	0.00	0.00	0.25	**98.63**
Digested enclave	SEM-TOR-8B	0.01	48.87	0.00	0.07	0.13	0.06	0.01	1.20	48.00	0.00	0.02	0.00	0.11	**98.47**
Digested enclave	SEM-TOR-8B	0.00	49.24	0.00	0.06	0.07	0.04	0.01	2.00	47.09	0.02	0.02	0.00	0.15	**98.70**
Digested enclave	SEM-TOR-8B	0.02	50.19	0.01	0.04	0.10	0.07	0.04	2.21	46.03	0.00	0.09	0.00	0.10	**98.91**

Digested enclave	SEM-TOR-8B	0.00	49.21	0.00	0.07	0.10	0.03	0.02	2.37	46.51	0.00	0.08	0.00	0.15	**98.54**
Digested enclave	SEM-TOR-8B	0.02	49.50	0.02	0.07	0.11	0.01	0.01	2.10	46.70	0.00	0.03	0.00	0.21	**98.77**
Diorite	SEM-TOR-13	0.00	49.12	0.01	0.05	0.12	0.06	0.00	2.37	46.63	0.00	0.00	0.00	0.19	**98.55**
Diorite	SEM-TOR-13	0.04	49.94	0.03	0.09	0.10	0.07	0.05	2.89	45.52	0.00	0.00	0.00	0.11	**98.84**
Diorite	SEM-TOR-13	0.01	49.24	0.01	0.05	0.11	0.03	0.00	2.34	46.58	0.01	0.01	0.00	0.20	**98.58**
Diorite	SEM-TOR-13	0.01	49.85	0.01	0.07	0.12	0.06	0.02	2.00	46.52	0.00	0.00	0.02	0.15	**98.83**
Diorite	SEM-TOR-13	0.02	51.49	0.00	0.07	0.11	0.08	0.09	3.08	43.72	0.00	0.00	0.00	0.09	**98.73**
Diorite	SEM-TOR-13	0.00	49.72	0.00	0.08	0.13	0.08	0.02	2.23	46.12	0.00	0.07	0.02	0.13	**98.60**
Diorite	SEM-TOR-13	0.02	50.53	0.01	0.09	0.11	0.07	0.07	3.69	44.23	0.02	0.09	0.03	0.16	**99.13**
Diorite	SEM-TOR-13	0.00	49.08	0.02	0.05	0.12	0.09	0.00	1.98	47.09	0.00	0.00	0.00	0.08	**98.52**
Diorite	SEM-TOR-13	0.01	51.02	0.00	0.06	0.11	0.08	0.05	2.15	45.31	0.00	0.00	0.00	0.11	**98.91**
Diorite	SEM-TOR-13	0.02	49.34	0.00	0.09	0.12	0.05	0.01	2.32	46.68	0.00	0.00	0.04	0.12	**98.78**
Diorite	SEM-TOR-13	0.00	52.10	0.00	0.04	0.11	0.05	0.07	2.66	43.92	0.00	0.00	0.05	0.09	**99.09**
Diorite	SEM-TOR-18A	0.00	49.33	0.00	0.15	0.08	0.05	0.17	2.79	45.64	0.00	0.08	0.00	0.19	**98.49**
Diorite	SEM-TOR-18A	0.01	49.98	0.00	0.16	0.16	0.03	0.03	3.61	43.98	0.00	0.06	0.03	0.17	**98.22**
Diorite	SEM-TOR-18A	0.00	48.17	0.14	0.16	0.16	0.09	0.00	2.05	48.01	0.04	0.14	0.00	0.12	**99.09**

Diorite	SEM-TOR-18A	0.00	48.98	0.02	0.22	0.14	0.12	0.02	2.05	47.50	0.00	0.03	0.01	0.18	**99.28**
Diorite	SEM-TOR-18A	0.02	49.01	0.08	0.16	0.09	0.06	0.03	2.17	46.86	0.00	0.16	0.00	0.16	**98.79**
Diorite	SEM-TOR-18A	0.00	50.11	0.00	0.21	0.10	0.08	0.01	2.23	46.10	0.00	0.03	0.00	0.11	**98.97**
Diorite	SEM-TOR-18A	0.00	49.49	0.00	0.10	0.09	0.01	0.08	2.63	46.20	0.04	0.13	0.00	0.08	**98.86**
Diorite	SEM-TOR-18B	0.02	49.53	0.00	0.26	0.12	0.10	0.06	2.34	46.17	0.00	0.02	0.00	0.11	**98.74**
Diorite	SEM-TOR-18B	0.00	48.97	0.01	0.34	0.15	0.10	0.01	2.05	46.65	0.00	0.08	0.01	0.16	**98.51**
Diorite	SEM-TOR-18B	0.01	48.95	0.00	0.21	0.13	0.03	0.04	2.31	46.96	0.00	0.07	0.00	0.18	**98.89**
Diorite	SEM-TOR-18B	0.03	50.07	0.00	0.16	0.12	0.03	0.02	2.54	45.80	0.03	0.02	0.01	0.21	**99.04**
Diorite	SEM-TOR-20	0.06	50.44	0.00	0.14	0.09	0.06	0.15	3.72	44.39	0.00	0.07	0.00	0.07	**99.18**
Diorite	SEM-TOR-20	0.02	48.83	0.00	0.15	0.09	0.06	0.09	1.85	47.39	0.04	0.09	0.00	0.14	**98.77**
Diorite	SEM-TOR-20	0.01	51.02	0.01	0.10	0.16	0.07	0.04	2.09	45.40	0.00	0.04	0.00	0.18	**99.13**
Diorite	SEM-TOR-20	0.01	48.08	0.00	0.17	0.13	0.09	0.00	1.81	48.22	0.00	0.00	0.01	0.15	**98.67**
Diorite	SEM-TOR-20	0.05	49.64	0.01	0.11	0.10	0.08	0.11	2.06	46.73	0.00	0.09	0.02	0.12	**99.10**
Diorite	SEM-TOR-20	0.01	48.58	0.00	0.11	0.11	0.10	0.00	1.99	47.84	0.00	0.00	0.00	0.09	**98.83**

Diorite	SEM-TOR-20	0.02	49.64	0.02	0.08	0.08	0.08	0.06	2.11	46.73	0.00	0.10	0.01	0.13	**99.06**
Diorite	SEM-TOR-20	7.14	27.69	2.47	0.23	0.12	0.84	4.84	2.74	45.65	0.01	0.00	0.05	0.15	**91.91**
Diorite	SEM-TOR-20	0.01	46.28	0.01	0.18	0.08	0.02	0.00	1.50	47.86	0.00	0.01	0.00	0.09	**96.03**
Diorite	SEM-TOR-20	0.09	48.08	0.00	0.13	0.10	0.00	0.04	1.72	46.30	0.00	0.00	0.01	0.16	**96.64**
Diorite	SEM-TOR-20	0.01	46.74	0.00	0.24	0.13	0.01	0.01	1.55	47.84	0.00	0.04	0.00	0.17	**96.73**
Diorite	SEM-TOR-4	0.00	48.97	0.01	0.02	0.07	0.08	0.00	2.11	45.76	0.00	0.09	0.00	0.11	**97.23**
Diorite	SEM-TOR-4	0.00	49.78	0.01	0.04	0.10	0.06	0.00	2.22	44.99	0.00	0.03	0.04	0.21	**97.47**
Diorite	SEM-TOR-4	0.00	48.70	0.01	0.05	0.12	0.06	0.00	2.26	45.50	0.04	0.08	0.00	0.14	**96.97**
Diorite	SEM-TOR-4	0.00	47.99	0.00	0.02	0.10	0.08	0.01	2.13	44.74	0.00	0.00	0.01	0.20	**95.28**
Diorite	SEM-TOR-4	0.00	49.49	0.00	0.04	0.12	0.05	0.01	2.38	46.17	0.00	0.09	0.00	0.18	**98.54**
Diorite	SEM-TOR-4	0.00	47.67	0.03	0.02	0.09	0.05	0.01	2.19	46.18	0.00	0.01	0.04	0.15	**96.44**
Diorite	SEM-TOR-4	0.00	48.19	0.00	0.00	0.09	0.08	0.01	1.97	46.38	0.02	0.04	0.02	0.13	**96.94**
Diorite	SEM-TOR-4	0.00	48.87	0.00	0.02	0.13	0.09	0.02	2.01	45.89	0.00	0.00	0.01	0.11	**97.15**
Diorite	SEM-TOR-9B	0.02	49.28	0.01	0.11	0.11	0.08	0.02	1.55	47.82	0.00	0.07	0.01	0.15	**99.22**
Diorite	SEM-TOR-9B	0.02	50.14	0.00	0.09	0.12	0.07	0.02	1.63	47.19	0.00	0.05	0.01	0.13	**99.45**
Diorite	SEM-TOR-9B	0.00	49.03	0.00	0.13	0.09	0.09	0.00	1.48	47.90	0.00	0.04	0.00	0.18	**98.94**
Diorite	SEM-TOR-9B	0.00	50.20	0.03	0.13	0.13	0.06	0.01	1.57	46.80	0.00	0.10	0.00	0.18	**99.20**
Fine-grained amphibolite	SEM-TOR-1	0.02	48.74	0.00	0.21	0.08	0.02	0.05	2.64	45.39	0.00	0.04	0.00	0.11	**97.30**

Fine-grained amphibolite	SEM-TOR-1	0.04	48.79	0.01	0.15	0.11	0.01	0.15	1.85	45.88	0.00	0.00	0.00	0.16	**97.13**
Fine-grained amphibolite	SEM-TOR-1	0.01	48.52	0.01	0.17	0.09	0.00	0.10	1.61	46.16	0.03	0.07	0.04	0.10	**96.90**
Fine-grained amphibolite	SEM-TOR-2	0.01	48.87	0.01	0.13	0.13	0.02	0.14	1.66	46.98	0.00	0.00	0.00	0.11	**98.05**
Fine-grained amphibolite	SEM-TOR-2	0.02	49.65	0.00	0.06	0.10	0.03	0.14	1.75	46.34	0.00	0.02	0.01	0.11	**98.22**
Fine-grained amphibolite	SEM-TOR-2	0.02	48.46	0.00	0.12	0.14	0.04	0.26	1.63	46.94	0.00	0.03	0.02	0.18	**97.83**
Fine-grained amphibolite	SEM-TOR-2	0.01	48.89	0.01	0.12	0.15	0.03	0.16	1.65	47.03	0.02	0.04	0.00	0.20	**98.32**
Fine-grained amphibolite	SEM-TOR-2	0.02	49.21	0.00	0.11	0.09	0.03	0.13	1.65	46.43	0.00	0.06	0.02	0.18	**97.91**
Gabbro	SEM-TOR-9A	0.00	48.17	0.03	0.13	0.13	0.03	0.01	1.97	48.69	0.00	0.00	0.00	0.16	**99.32**
Gabbro	SEM-TOR-9A	0.01	48.27	0.00	0.12	0.09	0.04	0.02	2.20	48.69	0.00	0.03	0.00	0.17	**99.64**
Gabbro	SEM-TOR-9A	0.01	48.06	0.00	0.14	0.11	0.06	0.00	2.11	48.91	0.01	0.00	0.00	0.14	**99.55**
Gabbro	SEM-TOR-9A	0.00	49.25	0.00	0.10	0.09	0.03	0.02	1.33	48.33	0.00	0.00	0.00	0.10	**99.25**
Gabbro	SEM-TOR-9A	0.08	49.92	0.00	0.07	0.10	0.00	0.10	1.48	47.37	0.00	0.10	0.00	0.18	**99.40**
Gabbro	SEM-TOR-9B	0.02	49.88	0.00	0.13	0.14	0.02	0.10	1.82	47.09	0.00	0.00	0.00	0.13	**99.32**
Gabbro	SEM-TOR-9B	0.01	49.85	0.00	0.11	0.12	0.00	0.04	1.77	47.29	0.00	0.00	0.01	0.19	**99.39**
Gabbro	SEM-TOR-9B	0.00	49.17	0.01	0.14	0.13	0.02	0.01	1.72	47.85	0.01	0.07	0.03	0.18	**99.33**

Gabbro	SEM-TOR-9B	0.28	48.66	0.07	0.12	0.09	0.05	0.21	2.86	46.49	0.01	0.00	0.02	0.19	**99.05**
Gabbro	SEM-TOR-9B	0.00	50.00	0.00	0.13	0.09	0.03	0.02	1.79	47.19	0.01	0.04	0.00	0.15	**99.46**
Gabbro	SEM-TOR-9B	0.02	49.23	0.02	0.19	0.11	0.04	0.13	1.56	47.76	0.02	0.00	0.00	0.22	**99.28**
Gabbro	SEM-TOR-9C	0.02	47.96	0.00	0.12	0.12	0.01	0.04	1.39	48.43	0.00	0.01	0.00	0.13	**98.22**
Gabbro	SEM-TOR-9C	0.01	47.63	0.00	0.20	0.14	0.03	0.00	1.35	48.63	0.00	0.02	0.00	0.15	**98.16**
Gabbro	SEM-TOR-9C	0.04	48.33	0.03	0.12	0.08	0.07	0.01	1.31	47.68	0.02	0.00	0.01	0.16	**97.84**
Gabbro	SEM-TOR-9C	0.00	48.33	0.00	0.13	0.07	0.06	0.03	1.27	47.83	0.02	0.07	0.00	0.19	**98.00**
Leucocratic inj.	SEM-TOR-1	0.10	0.00	0.01	0.01	0.11	0.00	0.03	0.00	0.01	109.98	0.00	0.01	0.05	**110.30**
Leucocratic inj.	SEM-TOR-15A	0.00	51.11	0.02	0.07	0.12	0.03	0.04	4.04	43.16	0.00	0.00	0.00	0.13	**98.72**
Leucocratic inj.	SEM-TOR-15A	0.01	51.12	0.02	0.12	0.08	0.03	0.06	3.23	43.66	0.00	0.03	0.00	0.08	**98.44**
Leucocratic inj.	SEM-TOR-15A	0.03	51.46	0.00	0.04	0.10	0.05	0.15	2.52	43.78	0.00	0.06	0.00	0.17	**98.36**
Leucocratic inj.	SEM-TOR-15A	0.02	51.24	0.00	0.02	0.09	0.06	0.23	3.08	43.13	0.01	0.05	0.00	0.18	**98.10**
Leucocratic inj.	SEM-TOR-2	0.00	51.12	0.02	0.11	0.15	0.02	0.10	1.70	45.08	0.00	0.05	0.00	0.17	**98.51**
Leucocratic inj.	SEM-TOR-2	0.01	50.63	0.00	0.14	0.10	0.01	0.10	1.59	45.47	0.00	0.04	0.00	0.13	**98.23**
Pegmatoid	SEM-TOR-16A	0.05	51.40	0.01	0.26	0.15	0.05	0.20	1.15	43.50	0.00	0.00	0.06	0.19	**97.02**

Pegmatoid	SEM-TOR-16A	0.00	51.48	0.02	0.30	0.16	0.07	0.05	1.28	43.00	0.00	0.06	0.04	0.09	**96.53**
Pegmatoid	SEM-TOR-16A	0.01	49.31	0.00	0.23	0.17	0.09	0.03	2.17	47.31	0.00	0.15	0.02	0.14	**99.63**
Pegmatoid	SEM-TOR-16A	0.00	48.63	0.03	0.30	0.18	0.13	0.00	1.93	48.22	0.00	0.02	0.00	0.21	**99.65**
Pegmatoid	SEM-TOR-16A	0.00	48.78	0.00	0.21	0.16	0.08	0.03	1.75	47.83	0.00	0.00	0.00	0.15	**98.98**
Pegmatoid	SEM-TOR-16A	0.00	49.30	0.02	0.17	0.13	0.09	0.02	1.67	47.55	0.00	0.00	0.00	0.19	**99.13**
Pegmatoid	SEM-TOR-16A	0.02	48.70	0.01	0.25	0.16	0.13	0.01	1.67	48.13	0.00	0.06	0.00	0.15	**99.28**
Pegmatoid	SEM-TOR-16A	0.01	49.70	0.01	0.17	0.09	0.10	0.05	1.80	46.75	0.02	0.04	0.00	0.17	**98.89**
Pegmatoid	SEM-TOR-16B	0.01	49.03	0.00	0.16	0.14	0.08	0.01	1.81	47.56	0.00	0.02	0.02	0.14	**98.98**
Pegmatoid	SEM-TOR-16B	0.00	49.43	0.00	0.16	0.12	0.05	0.01	1.72	47.11	0.00	0.10	0.03	0.17	**98.90**
Pegmatoid	SEM-TOR-16B	0.00	49.43	0.01	0.23	0.19	0.06	0.01	1.35	47.81	0.00	0.01	0.00	0.14	**99.21**
Pegmatoid	SEM-TOR-16B	0.02	51.50	0.02	0.11	0.12	0.02	0.02	5.15	42.20	0.00	0.00	0.01	0.13	**99.31**
Quartz-diorite	SEM-TOR-10	0.02	48.41	0.01	0.21	0.16	0.09	0.02	2.91	45.95	0.00	0.00	0.04	0.14	**97.96**
Quartz-diorite	SEM-TOR-10	0.00	48.83	0.00	0.19	0.14	0.11	0.03	3.14	45.45	0.00	0.00	0.02	0.19	**98.09**

Quartz-diorite	SEM-TOR-10	0.01	49.05	0.00	0.21	0.16	0.11	0.00	2.69	46.41	0.00	0.14	0.01	0.16	**98.96**
Quartz-diorite	SEM-TOR-10	0.04	49.12	0.00	0.19	0.10	0.12	0.01	2.74	44.75	0.03	0.06	0.01	0.14	**97.29**
Quartz-diorite	SEM-TOR-11	0.12	0.00	0.29	0.00	0.15	0.02	0.04	0.00	0.07	108.39	0.00	0.12	0.02	**109.22**
Quartz-diorite	SEM-TOR-11	0.03	36.53	0.00	0.11	0.10	0.06	0.00	2.69	45.01	0.00	0.11	0.00	0.20	**84.83**
Quartz-diorite	SEM-TOR-11	0.01	35.83	0.00	0.16	0.06	0.11	0.03	2.41	46.46	0.00	0.05	0.01	0.12	**85.24**
Quartz-diorite	SEM-TOR-11	0.00	37.98	0.01	0.14	0.09	0.13	0.06	2.48	43.52	0.00	0.04	0.06	0.18	**84.69**
Quartz-diorite	SEM-TOR-11	0.02	48.62	0.00	0.10	0.11	0.02	0.14	3.75	44.62	0.00	0.04	0.00	0.13	**97.55**
Quartz-diorite	SEM-TOR-11	6.63	48.20	0.00	0.00	0.09	0.05	0.12	4.84	43.15	0.03	0.00	0.05	0.14	**103.30**
Quartz-diorite	SEM-TOR-11	0.03	48.63	0.02	0.02	0.10	0.05	0.20	5.45	42.93	0.00	0.00	0.03	0.17	**97.61**
Quartz-diorite	SEM-TOR-12	0.01	48.34	0.00	0.12	0.10	0.02	0.07	3.28	46.71	0.00	0.04	0.03	0.17	**98.88**
Quartz-diorite	SEM-TOR-12	0.03	49.13	0.00	0.12	0.12	0.02	0.12	3.57	45.33	0.01	0.03	0.00	0.13	**98.61**
Quartz-diorite	SEM-TOR-12	0.00	49.95	0.00	0.04	0.12	0.03	0.05	2.12	46.34	0.00	0.12	0.01	0.21	**98.99**
Quartz-diorite	SEM-TOR-12	0.03	51.20	0.02	0.02	0.12	0.02	0.10	2.14	45.52	0.04	0.07	0.00	0.16	**99.42**
Quartz-diorite	SEM-TOR-12	0.04	49.64	0.01	0.08	0.10	0.05	0.15	4.89	43.72	0.00	0.03	0.00	0.12	**98.83**
Quartz-diorite	SEM-TOR-12	0.02	49.60	0.01	0.04	0.09	0.05	0.04	2.94	45.59	0.00	0.00	0.04	0.16	**98.57**
Quartz-diorite	SEM-TOR-14	0.00	47.70	0.00	0.19	0.17	0.07	0.01	1.85	48.07	0.02	0.04	0.00	0.18	**98.30**
Quartz-diorite	SEM-TOR-14	0.00	49.46	0.00	0.14	0.10	0.08	0.06	2.15	46.61	0.00	0.00	0.02	0.16	**98.78**
Quartz-diorite	SEM-TOR-14	0.00	48.65	0.01	0.13	0.12	0.07	0.00	1.31	48.00	0.01	0.06	0.00	0.24	**98.60**

Quartz-diorite	SEM-TOR-14	0.03	49.87	0.00	0.09	0.10	0.07	0.03	1.42	46.91	0.00	0.16	0.00	0.19	**98.87**
Quartz-diorite	SEM-TOR-14	0.00	48.78	0.00	0.14	0.13	0.04	0.01	1.49	47.53	0.00	0.04	0.03	0.13	**98.33**
Quartz-diorite	SEM-TOR-14	0.02	50.11	0.00	0.10	0.12	0.03	0.08	1.48	46.27	0.00	0.04	0.00	0.16	**98.41**
Quartz-diorite	SEM-TOR-14	0.01	48.81	0.02	0.12	0.13	0.05	0.08	1.65	47.48	0.00	0.06	0.00	0.11	**98.50**
Quartz-diorite	SEM-TOR-17A	0.00	49.72	0.01	0.02	0.10	0.03	0.02	2.26	45.06	0.00	0.00	0.03	0.17	**97.41**
Quartz-diorite	SEM-TOR-17A	0.02	50.15	0.02	0.04	0.08	0.03	0.06	2.36	44.42	0.00	0.11	0.02	0.19	**97.50**
Quartz-diorite	SEM-TOR-17A	0.02	49.22	0.03	0.00	0.13	0.04	0.01	3.54	44.42	0.00	0.03	0.02	0.19	**97.65**
Quartz-diorite	SEM-TOR-17A	0.02	49.02	0.00	0.03	0.13	0.04	0.04	3.64	44.05	0.00	0.08	0.00	0.18	**97.22**
Quartz-diorite	SEM-TOR-17A	0.00	50.44	0.01	0.09	0.11	0.05	0.00	2.74	44.04	0.00	0.05	0.00	0.18	**97.72**
Quartz-diorite	SEM-TOR-17A	0.01	49.35	0.00	0.04	0.10	0.04	0.01	3.14	44.28	0.00	0.03	0.00	0.17	**97.18**
Quartz-diorite	SEM-TOR-17A	0.00	50.67	0.01	0.12	0.15	0.00	0.03	5.44	42.72	0.02	0.00	0.00	0.07	**99.24**
Quartz-diorite	SEM-TOR-17A	0.03	51.33	0.01	0.09	0.06	0.02	0.09	4.80	42.29	0.00	0.08	0.00	0.15	**98.95**
Quartz-diorite	SEM-TOR-17A	0.03	51.08	0.00	0.10	0.11	0.01	0.00	3.56	43.86	0.00	0.08	0.01	0.14	**98.96**

Quartz-diorite	SEM-TOR-17A	0.02	51.05	0.02	0.12	0.08	0.00	0.04	4.38	42.83	0.00	0.06	0.00	0.22	**98.83**
Quartz-diorite	SEM-TOR-17B	0.02	50.23	0.02	0.08	0.09	0.08	0.01	3.10	45.07	0.03	0.08	0.01	0.09	**98.91**
Quartz-diorite	SEM-TOR-17B	0.01	50.13	0.01	0.03	0.13	0.03	0.01	3.26	44.76	0.00	0.00	0.00	0.23	**98.59**
Quartz-diorite	SEM-TOR-17B	0.00	50.32	0.00	0.02	0.11	0.04	0.00	3.07	45.49	0.00	0.08	0.03	0.16	**99.32**
Quartz-diorite	SEM-TOR-17B	0.02	50.57	0.01	0.03	0.04	0.00	0.04	3.04	45.15	0.00	0.00	0.02	0.16	**99.07**
Quartz-diorite	SEM-TOR-17B	0.02	50.95	0.00	0.03	0.11	0.03	0.02	3.11	45.21	0.02	0.00	0.00	0.18	**99.68**
Quartz-diorite	SEM-TOR-17B	0.87	51.09	0.00	0.00	0.05	0.02	0.14	3.25	43.25	0.00	0.00	0.00	0.15	**98.82**
Quartz-diorite	SEM-TOR-3B	0.00	48.49	0.00	0.11	0.10	0.05	0.03	2.07	47.53	0.00	0.09	0.02	0.14	**98.63**
Quartz-diorite	SEM-TOR-3B	0.01	49.82	0.00	0.07	0.09	0.03	0.05	2.09	46.11	0.01	0.06	0.01	0.20	**98.55**
Quartz-diorite	SEM-TOR-3B	0.01	48.83	0.00	0.05	0.12	0.08	0.00	2.16	47.47	0.04	0.08	0.00	0.15	**98.99**
Quartz-diorite	SEM-TOR-3B	0.03	50.43	0.01	0.05	0.07	0.08	0.06	2.15	45.71	0.00	0.02	0.04	0.11	**98.76**
Quartz-diorite	SEM-TOR-5	0.00	49.29	0.00	0.26	0.15	0.10	0.02	3.58	44.52	0.00	0.08	0.00	0.16	**98.14**
Quartz-diorite	SEM-TOR-5	0.02	49.56	0.02	0.23	0.12	0.09	0.15	4.59	43.29	0.00	0.00	0.02	0.23	**98.32**
Quartz-diorite	SEM-TOR-5	0.02	50.57	0.03	0.27	0.18	0.08	0.24	3.39	43.47	0.05	0.05	0.01	0.15	**98.53**
Quartz-diorite	SEM-TOR-5	0.00	48.22	0.00	0.20	0.13	0.06	0.01	2.08	47.57	0.00	0.00	0.00	0.15	**98.42**

Quartz-diorite	SEM-TOR-5	0.00	49.37	0.01	0.20	0.13	0.01	0.06	4.74	44.10	0.01	0.00	0.02	0.19	**98.83**
Quartz-diorite	SEM-TOR-5	0.00	48.92	0.02	0.17	0.10	0.07	0.06	2.25	46.19	0.01	0.00	0.00	0.19	**97.99**
Quartz-diorite	SEM-TOR-5	0.00	47.39	0.00	0.25	0.14	0.07	0.02	1.92	47.97	0.01	0.01	0.00	0.19	**97.96**
Quartz-diorite	SEM-TOR-5	0.00	47.01	0.00	0.19	0.15	0.08	0.00	1.86	48.45	0.00	0.02	0.01	0.13	**97.90**
Reaction rim	SEM-TOR-15B	0.02	48.99	0.00	0.03	0.06	0.06	0.01	2.34	46.06	0.00	0.05	0.00	0.14	**97.76**
Reaction rim	SEM-TOR-15B	0.00	49.26	0.00	0.04	0.08	0.05	0.03	2.18	45.76	0.01	0.12	0.00	0.12	**97.64**
Reaction rim	SEM-TOR-15B	0.02	49.11	0.01	0.05	0.14	0.08	0.02	3.34	44.58	0.00	0.12	0.03	0.17	**97.65**
Reaction rim	SEM-TOR-15B	0.00	49.10	0.00	0.06	0.16	0.07	0.02	2.13	45.46	0.01	0.17	0.00	0.24	**97.41**
Reaction rim	SEM-TOR-15B	0.00	49.78	0.01	0.06	0.12	0.07	0.03	2.33	44.78	0.00	0.00	0.00	0.11	**97.28**
Reaction rim	SEM-TOR-15B	0.02	49.79	0.00	0.08	0.14	0.02	0.04	2.74	44.20	0.00	0.00	0.02	0.13	**97.16**
Reaction rim	SEM-TOR-15B	0.00	48.97	0.00	0.08	0.11	0.04	0.00	2.08	47.08	0.02	0.05	0.00	0.13	**98.56**
Reaction rim	SEM-TOR-15B	0.01	49.98	0.01	0.03	0.10	0.04	0.00	2.05	46.06	0.00	0.00	0.01	0.20	**98.48**
Reaction rim	SEM-TOR-15B	0.02	48.94	0.02	0.04	0.08	0.07	0.02	2.37	46.64	0.00	0.00	0.01	0.16	**98.35**

Reaction rim	SEM-TOR-15B	0.00	49.23	0.01	0.03	0.09	0.08	0.01	1.92	46.98	0.01	0.00	0.00	0.13	**98.49**
Reaction rim	SEM-TOR-15B	0.00	49.17	0.02	0.06	0.09	0.07	0.00	2.03	47.02	0.00	0.00	0.00	0.12	**98.59**
Reaction rim	SEM-TOR-2	0.03	49.33	0.03	0.06	0.13	0.06	0.04	1.73	46.26	0.00	0.04	0.03	0.15	**97.89**
Reaction rim	SEM-TOR-2	0.05	49.25	0.00	0.03	0.09	0.04	0.12	1.71	45.69	0.00	0.08	0.00	0.18	**97.24**
Reaction rim	SEM-TOR-2	0.02	49.64	0.00	0.04	0.09	0.06	0.12	1.64	45.42	0.00	0.07	0.02	0.16	**97.29**
Reaction rim	SEM-TOR-3A	0.02	51.50	0.01	0.02	0.12	0.05	0.08	2.87	44.29	0.00	0.10	0.02	0.26	**99.35**
Reaction rim	SEM-TOR-3A	0.00	48.30	0.00	0.01	0.10	0.06	0.00	2.19	47.01	0.00	0.11	0.02	0.21	**98.01**
Reaction rim	SEM-TOR-3A	0.01	48.28	0.01	0.05	0.12	0.05	0.01	2.32	46.23	0.00	0.02	0.05	0.24	**97.39**
Reaction rim	SEM-TOR-3A	0.00	48.59	0.01	0.05	0.12	0.07	0.00	2.22	47.16	0.00	0.01	0.00	0.20	**98.42**
Reaction rim	SEM-TOR-3A	0.00	49.38	0.00	0.09	0.12	0.06	0.00	2.35	46.68	0.00	0.01	0.02	0.15	**98.87**
Reaction rim	SEM-TOR-9A	0.00	49.24	0.01	0.13	0.12	0.08	0.01	1.65	48.51	0.01	0.09	0.00	0.23	**100.09**
Reaction rim	SEM-TOR-9A	0.01	49.20	0.00	0.12	0.14	0.06	0.00	1.51	48.36	0.01	0.00	0.02	0.17	**99.58**
Reaction rim	SEM-TOR-9A	0.00	49.51	0.00	0.14	0.11	0.10	0.04	1.73	47.90	0.00	0.00	0.00	0.17	**99.68**
Reaction rim	SEM-TOR-9A	0.00	50.87	0.00	0.10	0.14	0.07	0.03	1.62	46.98	0.00	0.02	0.00	0.17	**100.00**
Reaction rim	SEM-TOR-9B	0.00	48.67	0.00	0.19	0.12	0.08	0.00	1.54	47.63	0.00	0.00	0.04	0.15	**98.42**
Reaction rim	SEM-TOR-9B	0.02	48.89	0.02	0.14	0.13	0.11	0.03	1.55	47.26	0.00	0.03	0.00	0.17	**98.35**
Reaction rim	SEM-TOR-9B	0.02	48.72	0.00	0.08	0.09	0.07	0.02	1.37	47.72	0.00	0.00	0.00	0.18	**98.28**

Reaction rim	SEM-TOR-9B	0.02	49.80	0.01	0.13	0.13	0.05	0.06	1.28	46.55	0.00	0.03	0.05	0.17	**98.28**
Reaction rim	SEM-TOR-9C	0.00	48.64	0.01	0.14	0.14	0.11	0.00	1.88	47.13	0.01	0.02	0.00	0.16	**98.22**
Reaction rim	SEM-TOR-9C	0.02	48.60	0.00	0.13	0.09	0.08	0.00	1.86	46.85	0.00	0.03	0.00	0.18	**97.83**
Reaction rim	SEM-TOR-9C	0.00	48.92	0.00	0.06	0.08	0.11	0.02	1.98	46.71	0.03	0.01	0.00	0.17	**98.10**

XIV. Supplementary Data 2

Torrão and Beja airport whole-rock geochemical data

Major elements

Table XIV-1. Major element contents of the several rock types cropping out at Torrão. Values are given in wt%.

Sample	SiO_2	Al_2O_3	$Fe_2O_3^T$	MnO	MgO	CaO	Na_2O	K_2O	TiO_2	P_2O_5	LOI	Total
SEM-TOR-1	44.24	14.14	17.28	0.26	5.89	8.99	3.32	0.34	3.729	0.49	0.6	**99.28**
SEM-TOR-6	48.81	16.19	9.76	0.191	7.31	6.5	4.16	0.79	1.65	0.23	3.08	**98.67**
SEM-TOR-3E	51.79	16.97	8.37	0.157	6.65	10.5	3.8	0.35	1.228	0.14	0.71	**100.67**
SEM-TOR-15E	49.13	16.42	11.13	0.199	7.83	9.99	3.39	0.29	1.483	0.13	0.95	**100.94**
SEM-TOR-2E	44.99	14.69	17.16	0.235	5.67	9.06	3.4	0.34	3.749	0.5	1.09	**100.88**
SEM-II1-R2	49.11	16.49	9.71	0.165	6.53	10.82	3.53	0.45	0.583	0.07	0.94	**98.40**
SEM-II2-R4-GR	55.19	17.56	8.83	0.107	2.22	9.02	4.67	0.28	1.044	0.14	0.63	**99.69**
SEM-II2-R4-BL	53.56	17.27	9.48	0.138	3.66	8.09	4.58	0.55	1.29	0.17	0.4	**99.19**
SEM-II2-R3	55.48	17.28	6.46	0.119	4.84	9	4.29	0.45	1.108	0.23	0.82	**100.08**
SEM-TOR-17	60.05	19.46	6.09	0.142	1.62	4.85	5.46	1.01	0.72	0.32	0.97	**100.69**
SEM-TOR-10	55.24	19.21	6.83	0.145	4.4	6.53	3.9	1.33	0.867	0.17	1.83	**100.45**
SEM-TOR-3D	55.92	20.17	7.82	0.158	2.53	6.85	4.95	0.37	0.861	0.51	0.65	**100.79**
SEM-TOR-12	56.47	18.26	7.42	0.148	3.4	5.23	5.31	0.95	1.327	0.42	1.5	**100.44**
SEM-TOR-14	50.44	17.49	9.34	0.183	4.62	7.53	4.16	0.72	2.576	0.87	1.31	**99.24**

SEM-TOR-16	50.63	18.63	7.45	0.167	6.93	5.71	4.34	1.35	1.034	0.14	3.34	**99.72**
SEM-TOR-5	53.64	19.94	7.12	0.166	5.07	5.71	4.08	1.77	0.829	0.16	2.4	**100.89**
SEM-TOR-4	51.09	20.28	9.42	0.198	3.22	7.79	4.56	0.71	1.463	0.71	1.2	**100.64**
SEM-TOR-13	49.12	20.26	9.35	0.184	3.8	8.12	4.21	1.32	1.567	0.75	1.8	**100.48**
SEM-TOR-20	46.86	19.57	11.32	0.164	5.29	9.45	3.53	0.44	1.871	0.15	1.98	**100.63**
SEM-TOR-8	50.19	18.37	11.41	0.228	4.32	6.88	4.44	0.67	2.247	0.86	0.87	**100.49**
SEM-TOR-15D	50.6	20.04	8.07	0.138	2.79	8.82	4.6	0.95	1.292	0.71	2.87	**100.88**
SEM-TOR-9	52.96	18.88	8.08	0.154	4.2	8.08	4.09	0.85	1.403	0.23	1.51	**100.44**
SEM-TOR-2D	51.47	20.25	7.11	0.064	1.33	9	5.22	0.63	0.873	0.34	2.39	**98.68**
SEM-TOR-18	48.71	20.94	8.38	0.127	4.59	8.9	3.77	0.97	1.312	0.08	2.6	**100.38**
SEM-TOR-7	52.45	8.35	13.88	0.263	8.75	10.74	1.87	0.27	0.903	0.22	2.53	**100.23**
SEM-I10-R12												

Rare-Earth elements

Table XIV-2. Rare-Earth element contents of the several rock types cropping out at Torrão and near the Beja airport. Values are given in ppm.

Sample	La	Ce	Pr	Nd	Sm	Eu	Gd	Tb	Dy	Ho	Er	Tm	Yb	Lu
SEM-TOR-1	17.2	45.4	7.4	34.6	9.8	2.5	10.8	1.9	11.6	2.4	6.7	0.9	5.7	0.9
SEM-TOR-6	13.0	29.7	4.0	20.4	5.3	1.6	5.9	1.0	6.4	1.2	3.5	0.5	3.2	0.5
SEM-TOR-3E	9.7	21.8	3.1	15.3	4.2	1.2	4.7	0.8	5.4	1.0	3.1	0.5	2.8	0.5
SEM-TOR-15E	7.4	23.0	3.7	21.5	6.1	1.7	6.4	1.2	7.3	1.5	4.3	0.6	3.9	0.6
SEM-TOR-2E	16.8	44.1	7.1	34.8	9.9	2.4	10.2	1.7	11.5	2.2	6.7	0.9	5.9	0.9
SEM-II1-R2	4.4	10.2	1.4	6.9	1.8	0.6	2.0	0.3	2.2	0.5	1.4	0.2	1.4	0.2
SEM-II2-R4-GR	7.5	17.3	2.5	12.5	3.5	1.3	4.0	0.7	5.1	1.0	3.0	0.4	3.0	0.5
SEM-II2-R4-BL	6.2	14.4	2.1	11.8	3.4	1.0	4.6	0.8	5.3	1.0	3.2	0.5	3.3	0.5
SEM-II2-R3	20.9	42.6	5.6	23.2	5.2	1.4	5.1	0.9	5.4	1.0	3.1	0.5	3.0	0.5
SEM-TOR-17	20.6	35.7	3.8	15.2	2.8	1.3	2.3	0.3	2.0	0.4	1.4	0.2	1.8	0.3
SEM-TOR-10	12.9	27.3	3.6	15.7	3.6	1.1	3.3	0.6	3.7	0.8	2.2	0.3	2.2	0.4
SEM-TOR-3D	18.5	35.3	3.9	16.7	3.0	1.3	2.6	0.4	2.2	0.4	1.3	0.2	1.3	0.2
SEM-TOR-12	40.1	78.9	8.7	30.5	5.8	1.5	5.2	0.6	3.4	0.7	1.8	0.3	1.7	0.3
SEM-TOR-14	30.0	69.6	9.3	36.8	8.5	2.0	7.8	1.2	6.7	1.2	3.3	0.5	2.9	0.5
SEM-TOR-16	10.9	23.5	3.0	13.5	3.1	0.9	3.1	0.5	3.2	0.7	2.0	0.3	2.0	0.3
SEM-TOR-5	11.6	24.8	3.5	16.7	3.9	1.1	3.8	0.7	3.9	0.8	2.4	0.4	2.4	0.4

SEM-TOR-4	11.9	30.8	4.7	21.9	5.6	1.9	5.8	1.0	5.6	1.0	2.9	0.4	2.6	0.4
SEM-TOR-13	13.0	32.1	5.2	24.2	6.7	2.3	7.1	1.1	6.7	1.3	3.4	0.5	3.0	0.4
SEM-TOR-20	7.0	17.5	2.7	15.6	4.4	1.6	5.5	0.9	5.7	1.1	3.0	0.4	2.7	0.4
SEM-TOR-8	45.4	95.3	11.4	43.0	8.5	2.4	7.3	1.1	6.5	1.1	3.2	0.5	3.1	0.5
SEM-TOR-15D	13.5	30.2	4.0	21.3	5.0	1.7	5.4	0.8	4.9	0.9	2.5	0.4	2.3	0.3
SEM-TOR-9	13.9	30.7	4.9	22.7	6.1	1.7	6.4	1.0	6.5	1.2	3.5	0.5	3.1	0.5
SEM-TOR-2D	12.5	25.2	3.3	14.6	3.0	1.3	3.0	0.5	3.0	0.6	1.6	0.2	1.5	0.2
SEM-TOR-18	6.7	15.1	2.0	10.8	2.9	1.1	3.2	0.6	3.4	0.7	1.9	0.3	1.9	0.3
SEM-TOR-7	10.9	24.1	3.4	17.0	4.2	0.9	4.8	0.9	5.6	1.1	3.1	0.5	3.1	0.5
SEM-I10-R12	0.7	1.6	0.2	0.8	0.2	0.0	0.1	0.0	0.1	0.0	0.1		0.1	0.0

Other minor and trace elements

Table XIV-3. Minor and trace element contents of the several rock types cropping out at Torrão and near the Beja airport. Values are given in ppm except for S, which is given in wt%.

Sample	S	Be	Sc	V	Co	Cr	Ni	Cu	Zn	Ga	Ge	As	Rb	Sr	Y	Zr	Nb	Mo	Ag	In	Sn	Sb	Cs	Ba	Hf	Ta	W	Tl	Pb	Bi	Th	U
SEM-TOR-1	0.2	1.0	44.0	535.0	45.0	30.0	15.0	70.0	119.0	24.0	1.4	5.0	5.0	321.0	63.9	154.0	8.3	< 2	< 0.3	0.1	1.0	< 0.2	0.2	119.0	4.2	0.5	< 0.5	< 0.05	12.0	< 0.1	0.8	0.5
SEM-TOR-6	0.1	1.0	37.0	275.0	34.0	50.0	23.0	35.0	76.0	19.0	1.2	< 5	20.0	290.0	35.1	142.0	3.1	< 2	< 0.3	0.1	1.0	0.3	0.8	144.0	3.3	0.3	< 0.5	0.1	< 5	< 0.1	1.5	0.7
SEM-TOR-3E	0.2	1.0	37.0	220.0	36.0	110.0	35.0	81.0	85.0	17.0	1.3	< 5	5.0	357.0	31.0	90.0	2.4	< 2	< 0.3	0.1	1.0	0.2	0.2	145.0	2.4	0.3	< 0.5	< 0.05	13.0	< 0.1	1.4	0.7
SEM-TOR-15E	0.0	< 1	44.0	268.0	41.0	130.0	30.0	24.0	79.0	19.0	1.6	< 5	5.0	412.0	38.3	74.0	3.7	< 2	< 0.3	0.1	1.0	< 0.2	0.4	98.0	2.7	0.3	< 0.5	< 0.05	< 5	< 0.1	0.4	0.2
SEM-TOR-2E	0.3	1.0	44.0	543.0	45.0	30.0	14.0	60.0	105.0	24.0	1.4	< 5	6.0	324.0	64.7	151.0	7.3	< 2	< 0.3	0.1	1.0	0.3	0.2	97.0	4.2	0.5	< 0.5	< 0.05	5.0	< 0.1	1.0	0.5
SEM-II1-R2	0.0	< 1	40.0	245.0	40.0	200.0	60.0	54.0	79.0	14.0	1.2	< 5	6.0	261.0	14.8	32.0	1.0	2.0	< 0.3	0.1	1.0	< 0.2	0.1	152.0	0.9	0.1	5.8	0.1	< 5	< 0.1	1.0	0.3
SEM-II2-R4-GR	0.0	< 1	32.0	203.0	17.0	< 20	9.0	41.0	42.0	20.0	1.6	< 5	3.0	376.0	29.8	67.0	1.3	< 2	< 0.3	< 0.1	3.0	< 0.2	0.3	233.0	1.9	0.1	< 0.5	< 0.05	< 5	< 0.1	2.4	1.1
SEM-II2-R4-BL	0.0	< 1	36.0	161.0	28.0	< 20	7.0	22.0	65.0	20.0	1.5	< 5	5.0	345.0	31.9	66.0	1.3	< 2	< 0.3	< 0.1	1.0	< 0.2	0.2	244.0	1.8	0.1	< 0.5	< 0.05	< 5	< 0.1	0.7	0.4
SEM-II2-R3	0.0	2.0	27.0	184.0	21.0	70.0	25.0	6.0	45.0	20.0	1.5	< 5	5.0	366.0	31.5	157.0	5.1	< 2	< 0.3	0.1	2.0	< 0.2	0.3	230.0	4.1	0.4	< 0.5	< 0.05	< 5	< 0.1	6.8	2.4
SEM-TOR-17	0.0	1.0	4.0	17.0	7.0	< 20	2.0	< 1	65.0	21.0	1.2	< 5	26.0	507.0	14.0	445.0	8.8	< 2	< 0.3	< 0.1	1.0	< 0.2	0.8	272.0	8.5	0.7	< 0.5	0.1	< 5	< 0.1	3.9	2.1
SEM-TOR-10	0.0	1.0	19.0	141.0	20.0	50.0	23.0	3.0	68.0	19.0	1.3	< 5	36.0	369.0	23.8	94.0	4.7	< 2	< 0.3	0.1	1.0	< 0.2	1.4	252.0	2.3	0.4	< 0.5	0.1	< 5	< 0.1	1.9	0.7
SEM-TOR-3D	0.1	1.0	5.0	72.0	15.0	< 20	8.0	20.0	68.0	23.0	1.1	< 5	9.0	575.0	13.9	78.0	6.4	< 2	< 0.3	< 0.1	1.0	< 0.2	0.4	180.0	1.8	0.4	< 0.5	< 0.05	< 5	< 0.1	1.4	0.6
SEM-TOR-12	0.0	2.0	11.0	115.0	18.0	< 20	25.0	16.0	69.0	23.0	1.2	< 5	23.0	723.0	20.0	191.0	26.3	< 2	< 0.3	< 0.1	1.0	0.2	0.5	348.0	4.1	1.9	< 0.5	0.1	< 5	< 0.1	3.4	0.9
SEM-TOR-14	0.0	1.0	21.0	212.0	25.0	30.0	29.0	39.0	78.0	19.0	1.2	< 5	16.0	501.0	35.5	86.0	23.9	< 2	< 0.3	0.1	1.0	< 0.2	1.0	154.0	2.3	1.9	< 0.5	< 0.05	5.0	< 0.1	2.1	0.8
SEM-TOR-16	0.0	1.0	27.0	205.0	28.0	50.0	34.0	10.0	95.0	18.0	1.4	< 5	39.0	362.0	21.3	74.0	5.4	< 2	< 0.3	< 0.1	1.0	0.3	1.8	280.0	1.9	0.4	< 0.5	0.1	10.0	< 0.1	1.3	0.4
SEM-TOR-5	0.0	1.0	19.0	137.0	23.0	30.0	27.0	15.0	73.0	20.0	1.3	< 5	48.0	376.0	25.8	70.0	4.8	< 2	< 0.3	< 0.1	1.0	0.3	1.9	417.0	2.0	0.4	< 0.5	0.2	< 5	< 0.1	1.7	0.7
SEM-TOR-4	0.0	< 1	12.0	64.0	14.0	< 20	1.0	9.0	93.0	21.0	1.1	< 5	19.0	608.0	30.5	52.0	4.4	< 2	< 0.3	0.1	< 1	< 0.2	0.5	190.0	1.6	0.3	< 0.5	0.1	6.0	< 0.1	0.8	0.3
SEM-TOR-13	0.0	< 1	18.0	144.0	17.0	< 20	1.0	4.0	70.0	23.0	1.3	< 5	34.0	542.0	36.2	49.0	4.4	< 2	< 0.3	0.1	1.0	0.2	1.6	189.0	1.6	0.3	11.1	0.1	< 5	< 0.1	1.0	0.4
SEM-TOR-20	0.4	< 1	32.0	307.0	29.0	< 20	3.0	32.0	82.0	22.0	1.2	< 5	10.0	461.0	30.7	54.0	3.3	< 2	< 0.3	0.1	1.0	< 0.2	0.5	111.0	1.9	0.2	< 0.5	< 0.05	22.0	< 0.1	0.6	0.2
SEM-TOR-8	0.0	2.0	13.0	97.0	25.0	< 20	21.0	31.0	71.0	18.0	1.0	< 5	15.0	822.0	36.2	303.0	39.1	2.0	< 0.3	0.1	1.0	< 0.2	0.5	308.0	5.6	3.1	< 0.5	0.1	< 5	< 0.1	2.1	0.8

SEM-TOR-15D	0.0	1.0	13.0	109.0	11.0	< 20	5.0	53.0	56.0	20.0	1.4	< 5	31.0	510.0	27.5	48.0	4.0	< 2	< 0.3	0.1	1.0	0.4	0.7	180.0	1.5	0.3	< 0.5	0.2	< 5	< 0.1	1.7	0.4
SEM-TOR-9	0.0	1.0	26.0	157.0	19.0	< 20	6.0	3.0	60.0	20.0	1.2	< 5	22.0	493.0	35.1	72.0	13.7	< 2	< 0.3	0.1	1.0	< 0.2	1.1	209.0	2.3	0.8	< 0.5	0.1	< 5	< 0.1	2.0	0.7
SEM-TOR-2D	0.0	1.0	10.0	62.0	8.0	< 20	3.0	18.0	40.0	24.0	1.0	< 5	23.0	354.0	18.2	59.0	2.7	< 2	< 0.3	< 0.1	1.0	< 0.2	0.3	141.0	1.5	0.2	< 0.5	0.1	< 5	< 0.1	1.7	0.7
SEM-TOR-18	0.1	< 1	22.0	243.0	23.0	< 20	10.0	54.0	64.0	19.0	1.0	6.0	27.0	480.0	19.9	57.0	3.3	< 2	< 0.3	0.1	1.0	0.3	1.1	196.0	1.5	0.2	< 0.5	0.1	22.0	< 0.1	0.9	0.3
SEM-TOR-7	2.4	< 1	53.0	226.0	109.0	140.0	46.0	1150.0	106.0	11.0	1.5	9.0	5.0	159.0	31.1	100.0	3.4	2.0	< 0.3	0.1	1.0	0.4	0.3	116.0	2.5	0.3	< 0.5	< 0.05	< 5	0.1	4.4	2.0
SEM-I10-R12		0.1	0.0	7.0	0.0	3.0	8.0	1.0	3.0	0.0			0.4	299.0	0.9	3.0	0.3	5.9				0.0	0.0	2.0	0.1	0.0	0.1		0.1		0.1	1.6

Layered Gabbroic Sequence whole-rock geochemical data

Major elements

Table XIV-4. Major element contents of the LGS. Data is as reported in Jesus (2011) and Jesus *et al.* (2016). Values are given in wt%.

Sample	**SiO_2**	**Al_2O_3**	**$Fe_2O_3^T$**	**MnO**	**MgO**	**CaO**	**Na_2O**	**K_2O**	**TiO_2**	**P_2O_5**	**LOI**	**Total**
RS-6	42.66	23.92	3.63	0.05	11.42	12.16	1.04	0.06	0.04	0.02	4.24	**99.24**
RS-7	42.71	24.05	3.47	0.05	11.47	12.29	1.18	0.03	0.04	0.02	5.17	**100.48**
RS-15	46.40	24.53	3.25	0.05	7.95	14.63	1.44	0.10	0.13	0.02	2.18	**100.68**
RS-17	47.40	23.70	5.21	0.08	7.15	11.91	2.53	0.10	0.11	0.01	1.11	**99.31**
RS-3	47.82	19.13	7.48	0.12	11.02	10.90	1.83	0.13	0.26	0.05	1.31	**100.06**
RS-11	49.82	17.38	9.56	0.16	6.99	12.06	2.63	0.17	1.39	0.15	0.28	**100.59**
ODV-4-A1												**0.00**
ODV-G-36	39.40	13.71	23.50	0.28	10.11	5.97	2.81	0.14	3.97	0.25	<0.86	**100.14**
ODV-G-34	47.60	17.03	12.31	0.17	4.96	11.46	3.51	0.16	2.12	0.03	0.09	**99.44**
ODV-G-26	49.51	20.28	6.91	0.11	7.18	11.52	3.21	0.18	0.32	0.06	1.09	**100.37**
ODV-G-25	50.16	19.9	5.59	0.11	7.19	12.11	3.11	0.25	0.59	0.03	0.47	**99.52**
ODV-G-23	45.99	15.43	15.25	0.22	5.68	11.63	2.95	0.14	2.78	0.03	0.31	**100.41**
ODV-G-22	46.65	19.82	11.24	0.15	4.07	9.4	3.84	0.13	1.37	0.04	3.43	**100.13**
ODV-G-21	46.43	17.85	10.18	0.19	5.7	9.54	3.54	0.26	3.48	0.03	1.72	**98.92**
ODV-G-24	49.72	16.01	8.49	0.17	7.16	12.47	3.2	0.41	0.99	0.02	1.37	**100.01**
ODV-D1	46.75	15.13	15.92	0.23	5.26	8.38	3.21	0.61	3.63	0.34	0.79	**100.25**
ODV-G-38	46.74	17.01	11.51	0.13	6.81	13.06	2.65	0.15	1.63	0.05	0.31	**100.05**
ODV-G-37	50.95	21.91	5.52	0.09	5.92	11.87	3.51	0.12	0.22	0.04	0.32	**100.47**
ODV-A-20	54.44	27.68	0.69	0.01	0.13	9.97	5.93	0.30	0.10	0.04	1.10	**100.39**
ODV-A-27	53.82	27.72	1.09	0.02	0.56	10.98	5.26	0.26	0.11	0.04	0.66	**100.51**
ODV-A-39	52.51	29.04	0.87	0.01	0.18	11.69	4.79	0.11	0.12	0.03	1.07	**100.42**
ODV-G-35	47.09	18.55	13.85	0.15	5.30	9.27	3.69	0.21	2.30	0.03	<0.32	**100.44**
ODV-G-41	42.55	15.50	16.32	0.14	6.92	12.88	2.18	0.06	2.66	0.02	<0.06	**99.23**
ODV-G-28	48.30	18.64	7.60	0.12	10.07	12.27	2.65	0.04	0.42	0.02	0.16	**100.29**
ODV-G-32	49.45	20.23	4.78	0.11	9.12	12.15	2.77	0.14	0.29	0.01	0.39	**99.44**
ODV-G-33	48.47	19.24	6.75	0.11	9.19	11.92	2.56	0.14	0.31	0.03	1.67	**100.39**
ODV-G-31	52.02	28.91	0.85	0.02	0.35	12.04	4.49	0.27	0.24	0.06	0.98	**100.23**
ODV-G-29	48.52	18.39	5.48	0.13	11.45	11.58	2.60	0.11	0.36	0.02	0.15	**98.80**

ODV-G-40	49.31	20.29	5.99	0.10	8.24	12.57	2.84	0.10	0.34	0.03	0.38	**100.19**
ODV-D3	49.20	18.26	7.15	0.12	10.14	12.25	2.44	0.09	0.26	0.02	0.35	**100.28**
ODV-D4	51.37	20.45	4.96	0.09	6.92	13.14	3.00	0.06	0.30	0.02	0.34	**100.66**
CVD-19A	50.01	19.22	6.38	0.10	8.11	13.15	2.63	0.07	0.34	0.02	0.48	**100.51**
CDV-17	50.42	20.68	6.48	0.10	7.93	11.16	3.20	0.17	0.36	0.03	0.26	**100.79**
CVD-16A	49.58	16.67	6.12	0.11	9.58	15.36	1.87	0.07	0.45	0.02	0.62	**100.45**
CV-31	48.93	15.80	6.57	0.13	9.75	14.49	2.16	0.19	0.44	0.02	1.84	**100.32**
CV-28	45.59	17.14	10.19	0.12	9.00	11.67	2.31	0.16	0.29	0.02	3.06	**99.56**
CVD-6A	50.49	20.27	4.41	0.08	6.56	14.13	2.83	0.13	0.32	0.02	0.97	**100.21**
CVD-2D	46.31	13.42	10.63	0.16	16.31	10.40	1.68	< 0.01	0.24	0.02	1.07	**100.25**
CVD-20	49.40	23.59	6.58	0.08	6.21	10.16	3.49	0.15	0.22	0.02	0.41	**100.31**
PEROG 5	47.81	17.21	7.67	0.12	10.72	13.17	1.77	0.17	0.55	0.04	1.35	**100.58**
CNT-23A	47.63	20.84	7.90	0.11	9.97	10.68	2.57	0.10	0.16	0.02	0.23	**100.21**
CNT-25	47.63	17.04	5.57	0.10	10.77	15.56	1.40	0.07	0.33	0.02	1.80	**100.28**
CNT-24	49.90	17.17	7.83	0.13	8.84	13.80	2.41	0.06	0.61	0.02	0.19	**100.96**
CNT-26	49.24	23.05	5.69	0.07	6.61	10.51	3.31	0.12	0.13	0.02	0.46	**99.21**
CNT-19	48.29	18.34	5.72	0.10	9.66	15.43	1.57	0.08	0.30	0.02	0.79	**100.30**
SB-W3	48.49	19.21	8.65	0.12	10.54	10.71	2.63	0.07	0.19	0.02	0.13	**100.76**
CNT-15A	48.48	23.98	3.24	0.06	5.49	16.05	1.89	0.10	0.20	0.02	0.89	**100.40**
CNT-15	49.37	28.18	2.58	0.01	0.38	13.00	3.04	1.56	0.08	0.02	2.58	**100.80**
CNT-20	47.12	19.11	8.03	0.12	10.85	12.49	1.90	0.07	0.20	0.01	0.34	**100.24**
CNT-18	47.53	18.59	6.89	0.11	10.44	13.90	1.62	0.03	0.31	0.02	0.80	**100.24**
SB-6	46.43	19.02	6.98	0.10	10.67	13.49	1.46	0.04	0.22	0.02	2.34	**100.77**
CNT-27	50.35	20.96	6.08	0.10	8.02	12.13	2.82	0.14	0.19	0.02	0.18	**100.99**
SB-13	48.26	17.97	5.92	0.10	10.71	15.08	1.42	0.10	0.30	0.02	1.08	**100.96**
CNT-22	47.79	20.88	9.34	0.09	6.24	10.91	3.18	0.16	0.93	0.01	0.25	**99.79**
CNT-28	50.38	19.18	5.31	0.10	7.77	13.70	2.51	0.11	0.27	0.02	0.55	**99.90**
SB-11	43.16	16.01	15.60	0.12	6.88	13.37	2.03	0.04	1.89	0.02	0.16	**99.28**
CNT-21	50.23	11.20	6.97	0.15	12.81	17.08	1.19	0.04	0.46	0.02	0.21	**100.36**
SB-S3	50.19	20.98	6.28	0.09	7.38	11.55	2.99	0.16	0.29	0.05	0.44	**100.41**
CNT-8	49.50	19.13	6.86	0.10	9.37	11.65	2.39	0.08	0.30	0.02	0.80	**100.20**
CNT-2	50.40	17.22	7.08	0.11	10.08	12.72	2.27	0.07	0.41	0.02	1.00	**101.38**
CNT-29	49.40	19.55	7.47	0.11	10.69	11.38	2.55	0.07	0.23	0.03	0.60	**102.08**
CNT-9	51.80	19.50	6.13	0.09	8.29	12.23	2.81	0.10	0.34	0.03	0.80	**102.12**
CNT-1	48.50	24.24	3.09	0.05	4.82	13.73	2.48	0.09	0.19	0.02	0.80	**98.01**
CNT-30	49.20	20.12	7.86	0.11	7.09	11.66	3.13	0.13	1.15	0.05	0.80	**101.30**

FG-8											**0.00**
FG-7	55.00	20.88	6.67	0.16	4.51	7.01	4.60	0.31	0.10	<0.01	2.70	**101.94**
CNT-10	49.70	18.81	7.79	0.11	10.06	11.90	2.60	0.09	0.29	<0.01	0.60	**101.95**
FG-5	45.40	19.25	12.84	0.10	6.61	10.70	2.66	0.10	2.21	<0.01	0.60	**100.47**
CNT-11	50.20	21.68	7.15	0.08	6.23	12.68	3.07	0.10	0.71	0.01	0.60	**102.51**
CNT-7	49.30	26.37	3.88	0.05	5.74	11.21	3.14	0.10	0.10	0.03	1.50	**101.42**
FG-3	44.80	11.47	12.68	0.15	10.40	14.18	1.50	0.08	1.91	0.04	1.10	**98.31**
CNT-12	50.40	20.81	5.73	0.08	8.16	12.16	2.57	0.07	0.24	<0.01	0.60	**100.82**
CNT-14A	49.50	19.82	5.76	0.09	8.85	13.51	2.27	0.08	0.34	<0.01	1.00	**101.22**
CNT-32	48.80	18.31	7.30	0.11	10.79	12.39	2.29	0.07	0.31	0.04	0.70	**101.11**
CNT-6A	50.80	19.22	6.95	0.11	10.65	11.84	2.44	0.09	0.24	0.05	0.90	**103.29**
MB-16	44.00	27.99	2.80	0.04	4.57	13.75	2.04	0.06	0.09	0.03	2.20	**97.57**
CNT-13	49.50	20.20	6.87	0.10	9.98	12.24	2.44	0.09	0.29	0.03	0.60	**102.34**
CNT-31	50.40	19.81	5.39	0.09	8.16	13.27	2.81	0.08	0.33	0.03	0.80	**101.17**
CNT-33	48.40	18.74	6.77	0.10	10.44	12.36	1.95	0.07	0.23	0.06	0.90	**100.02**
CNT-36	49.40	19.32	7.00	0.11	10.75	11.94	2.41	0.07	0.25	0.06	0.90	**102.21**
CNT-34	48.60	20.01	4.80	0.08	9.17	14.01	1.99	0.05	0.30	0.06	1.40	**100.47**
CNT-35	48.30	19.37	7.07	0.10	10.13	12.28	2.14	0.08	0.24	0.05	1.00	**100.76**
CNT-4	49.40	27.13	2.50	0.03	3.38	14.05	2.48	0.12	0.24	0.02	1.40	**100.75**
MB-11	49.80	21.11	5.43	0.08	8.00	12.83	2.49	0.08	0.30	0.03	0.80	**100.95**
MB-13	50.00	19.98	7.07	0.11	10.75	11.72	2.57	0.09	0.26	<0.01	1.10	**103.65**
CNT-5B	48.20	20.16	6.67	0.10	11.62	13.29	1.60	0.04	0.21	<0.01	2.20	**104.09**
CNT-3A	48.90	18.86	7.47	0.11	10.28	12.21	2.43	0.05	0.33	0.05	0.70	**101.39**
FA-4	41.10	21.91	3.99	0.06	12.47	11.44	1.60	0.22	0.10	0.03	7.30	**100.22**
FA-5	44.30	27.12	2.73	0.04	8.90	12.91	1.30	0.14	0.04	0.02	3.90	**101.40**
Beja 2a	46.90	17.80	11.00	0.17	6.20	11.60	2.50	0.17	2.63		0.05	**99.02**
Beja 2b	47.70	17.50	12.00	0.18	7.01	11.50	2.29	0.18	2.59		0.05	**101.00**
Beja 2c	45.50	30.50	14.70	0.24	4.20	0.62	1.27	1.01	1.47		0.43	**99.94**
CVD-19B	54.51	16.27	8.01	0.13	5.22	8.68	3.85	1.33	1.05	0.17	1.46	**100.70**
CVD-19	64.43	14.00	5.31	0.10	4.51	6.88	3.18	0.68	0.57	0.07	1.25	**101.00**
CVD-19C	56.70	17.11	7.42	0.13	4.13	5.82	4.73	1.36	1.17	0.26	1.75	**100.60**
CVD-5	55.25	10.96	8.07	0.17	9.53	9.60	3.90	0.30	0.42	0.03	2.02	**100.20**
ODV-G-43	61.95	18.73	2.98	0.05	0.63	7.66	5.76	0.40	0.64	0.10	1.40	**100.29**
MB-3	57.22	21.63	1.73	0.02	2.55	9.49	5.84	0.09	0.32	0.10	0.99	**99.99**

Rare-Earth elements

Table XIV-5. Rare-Earth element contents of the LGS. Data is as reported in Jesus (2011) and Jesus *et al.* (2016). Values are given in ppm.

Sample	**La**	**Ce**	**Pr**	**Nd**	**Sm**	**Eu**	**Gd**	**Tb**	**Dy**	**Ho**	**Er**	**Tm**	**Yb**	**Lu**
RS-6	0.5	1.0	0.1	0.5	0.1	0.2	0.1	0.0	0.1	0.0	0.1		0.1	0.0
RS-7	0.5	1.1	0.1	0.6	0.1	0.2	0.1	0.0	0.1	0.0	0.1		0.1	0.0
RS-15	0.8	1.7	0.2	1.3	0.4	0.3	0.5	0.1	0.5	0.1	0.3		0.3	0.0
RS-17	0.9	2.0	0.3	1.3	0.4	0.5	0.4	0.1	0.4	0.1	0.2		0.2	0.0
RS-3	2.1	4.6	0.6	2.9	0.8	0.6	1.0	0.2	1.1	0.2	0.7		0.6	0.1
RS-11	4.7	12.3	1.9	10.1	3.2	1.2	4.1	0.7	4.5	1.0	2.7		2.6	0.4
ODV-4-A1	0.8	<3		<5	1.3	0.5		<0.5					1.3	0.2
ODV-G-36	1.6	3.4	0.5	2.5	0.7	0.7	0.7	0.1	0.6	0.1	0.3	0.0	0.2	0.0
ODV-G-34	1.4	3.6	0.6	3.6	1.2	1.0	1.5	0.3	1.7	0.3	0.9	0.1	0.7	0.1
ODV-G-26	1.9	4.3	0.6	3.3	0.9	0.7	1.1	0.2	1.1	0.2	0.6	0.1	0.5	0.1
ODV-G-25	1.6	3.8	0.5	3.1	1.0	0.6	1.1	0.2	1.2	0.2	0.6	0.1	0.5	0.1
ODV-G-23	1.4	3.5	0.6	3.7	1.3	1.1	1.6	0.3	1.8	0.3	0.9	0.1	0.7	0.1
ODV-G-22	1.4	2.7	0.4	1.9	0.5	1.0	0.5	0.1	0.6	0.1	0.3	0.0	0.3	0.0
ODV-G-21	1.5	3.1	0.5	2.8	0.9	0.9	1.1	0.2	1.2	0.2	0.6	0.1	0.5	0.1
ODV-G-24	2.4	6.4	1.0	6.1	1.9	0.9	2.3	0.4	2.6	0.5	1.4	0.2	1.2	0.2
ODV-D1	8.0	18.1	2.5	11.6	3.3	1.6	4.0	0.7	3.8	0.8	2.2	0.3	2.0	0.3
ODV-G-38	1.3	3.4	0.6	3.6	1.2	0.6	1.4	0.3	1.6	0.3	0.8	0.1	0.7	0.1
ODV-G-37	1.5	3.3	0.5	2.7	0.8	0.7	0.9	0.2	0.9	0.2	0.5	0.1	0.4	0.1
ODV-A-20	1.9	3.4	0.4	1.6	0.3	1.0	0.3	0.0	0.2	0.0	0.1	<0.005	0.1	0.0

ODV-A-27	2.0	3.7	0.4	2.0	0.4	0.9	0.4	0.1	0.3	0.1	0.1	0.0	0.1	0.0
ODV-A-39	1.6	2.9	0.3	1.4	0.3	0.5	0.2	0.0	0.2	0.0	0.1	0.0	0.1	0.0
ODV-G-35	1.3	2.8	0.4	2.3	0.7	0.8	0.8	0.1	0.8	0.2	0.4	0.1	0.4	0.1
ODV-G-41	1.2	3.1	0.5	3.4	1.2	0.6	1.5	0.3	1.7	0.3	0.9	0.1	0.8	0.1
ODV-G-28	1.0	2.7	0.4	2.5	0.8	0.6	1.0	0.2	1.2	0.2	0.7	0.1	0.6	0.1
ODV-G-32	1.3	3.0	0.4	2.5	0.8	0.5	0.9	0.2	1.0	0.2	0.6	0.1	0.5	0.1
ODV-G-33	1.2	3.0	0.5	2.9	0.8	0.5	1.1	0.2	1.1	0.2	0.6	0.1	0.5	0.1
ODV-G-31	2.6	5.2	0.6	2.7	0.5	0.6	0.5	0.1	0.4	0.1	0.2	0.0	0.2	0.0
ODV-G-29	0.9	2.3	0.3	2.0	0.6	0.5	0.8	0.2	0.9	0.2	0.5	0.1	0.4	0.1
ODV-G-40	1.3	3.1	0.5	2.8	0.9	0.5	1.1	0.2	1.1	0.2	0.7	0.1	0.5	0.1
ODV-D3	1.1	2.4	0.4	2.2	0.7	0.6	1.0	0.2	1.2	0.2	0.6	0.1	0.5	0.1
ODV-D4	1.5	3.4	0.5	3.0	1.0	0.7	1.3	0.2	1.5	0.3	0.8	0.1	0.7	0.1
CVD-19A	1.3	2.9	0.5	2.8	0.9	0.6	1.3	0.2	1.4	0.3	0.7	0.1	0.6	0.1
CDV-17	1.9	3.7	0.5	2.4	0.7	0.7	0.9	0.2	1.0	0.2	0.5	0.1	0.5	0.1
CVD-16A	1.3	3.4	0.6	3.6	1.3	0.7	1.8	0.3	1.9	0.4	1.1	0.2	0.9	0.1
CV-31	1.1	3.2	0.5	3.3	1.2	0.6	1.5	0.3	1.9	0.4	1.0	0.1	0.8	0.1
CV-28	0.9	2.3	0.4	2.3	0.7	0.4	0.9	0.2	1.1	0.2	0.6	0.1	0.5	0.1
CVD-6A	1.1	2.4	0.4	2.3	0.8	0.6	1.1	0.2	1.3	0.2	0.7	0.1	0.6	0.1
CVD-2D	0.8	2.0	0.3	2.1	0.7	0.5	1.0	0.2	1.1	0.2	0.6	0.1	0.5	0.1
CVD-20	0.9	1.5	0.2	0.7	0.2	0.3	0.1	0.0	0.1	0.0	0.1	< 0.005	0.1	0.0
PEROG 5	3.7	8.9	1.4	6.5	1.9	0.8	2.3	0.4	2.5	0.5	1.4	0.2	1.3	0.2
CNT-23A	0.8	1.4	0.2	0.9	0.3	0.4	0.3	0.1	0.3	0.1	0.2	0.0	0.2	0.0
CNT-25	1.2	2.9	0.5	2.9	1.0	0.6	1.3	0.2	1.4	0.3	0.8	0.1	0.7	0.1
CNT-24	1.4	3.4	0.6	3.4	1.2	0.7	1.7	0.3	1.8	0.4	1.0	0.1	0.9	0.1

CNT-26	1.3	1.7	0.2	0.9	0.2	0.4	0.2	0.0	0.2	0.0	0.1	0.0	0.1	0.0
CNT-19	1.2	2.8	0.5	2.7	0.9	0.5	1.3	0.2	1.4	0.3	0.8	0.1	0.7	0.1
SB-W3	0.7	1.5	0.2	1.3	0.4	0.5	0.5	0.1	0.7	0.1	0.4	0.0	0.3	0.0
CNT-15A	1.3	2.7	0.4	2.0	0.6	0.5	0.8	0.1	0.8	0.2	0.4	0.1	0.4	0.1
CNT-15	1.9	3.1	0.3	1.3	0.2	0.5	0.2	0.0	0.1	0.0	0.1	< 0.005	0.0	0.0
CNT-20	0.7	1.4	0.3	1.5	0.5	0.4	0.6	0.1	0.7	0.2	0.4	0.1	0.3	0.0
CNT-18	1.1	2.5	0.4	2.4	0.8	0.6	1.1	0.2	1.2	0.2	0.7	0.1	0.6	0.1
SB-6	1.1	2.2	0.4	2.0	0.6	0.5	0.8	0.1	0.9	0.2	0.5	0.1	0.4	0.1
CNT-27	1.2	2.6	0.4	1.9	0.6	0.5	0.7	0.1	0.8	0.2	0.4	0.1	0.4	0.1
SB-13	1.1	2.9	0.5	2.8	1.0	0.5	1.3	0.2	1.4	0.3	0.8	0.1	0.6	0.1
CNT-22	1.2	2.0	0.3	1.6	0.5	0.4	0.5	0.1	0.6	0.1	0.4	0.1	0.3	0.0
CNT-28	1.3	2.9	0.5	2.6	0.9	0.6	1.1	0.2	1.3	0.3	0.7	0.1	0.6	0.1
SB-11	0.7	2.1	0.4	2.4	0.9	0.5	1.3	0.2	1.4	0.3	0.8	0.1	0.7	0.1
CNT-21	1.0	3.3	0.7	4.1	1.6	0.6	2.1	0.4	2.4	0.5	1.3	0.2	1.1	0.2
SB-S3	1.2	2.7	0.4	1.8	0.6	0.5	0.7	0.1	0.7	0.1	0.4	0.1	0.4	0.1
CNT-8	<2	<2												
CNT-2	<2	<2												
CNT-29	<2	<2												
CNT-9	<2	<2												
CNT-1	<2	<2												
CNT-30	<2	<2												
FG-8	<2	<2												
FG-7	<2	<2												
CNT-10	<2	<2												
FG-5	<2	<2												
CNT-11	<2	<2												
CNT-7	<2	<2												
FG-3	<2	<2												
CNT-12	<2	<2												
CNT-14A	<2	<2												
CNT-32	<2	<2												
CNT-6A	<2	<2												
MB-16	<2	<2												
CNT-13	<2	<2												
CNT-31	<2	<2												
CNT-33	<2	<2												

CNT-36	<2	<2
CNT-34	<2	<2
CNT-35	<2	<2
CNT-4	<2	<2
MB-11	<2	<2
MB-13	<2	<2
CNT-5B	<2	<2
CNT-3A	<2	<2
FA-4	<2	<2
FA-5	<2	<2

Other minor and trace elements

Table XIV-6. Minor and trace element contents of the LGS. Data is as reported in Jesus (2011) and Jesus *et al.* (2016). Values are given in ppm except for S, which is given in wt%.

Sample	S	Be	Sc	V	Co	Cr	Ni	Cu	Zn	Ga	Ge	As	Rb	Sr	Y	Zr	Nb	Mo	Ag	In	Sn	Sb	Cs	Ba	Hf	Ta	W	Tl	Pb	Bi	Th	U
RS-6	0.0	0.1		13.0	45.0	828.0	250.0	30.0	40.0	11.0	0.5	0.1	0.8	274.0	0.6	2.0	0.1		0.0	< 0.1	0.1	0.0	0.4	26.0	0.1	0.0	14.0	6.4	0.6	0.0	0.0	0.0
RS-7	0.0	0.1		9.0	52.0	251.0	410.0	< 10	40.0	11.0	0.4	0.2	0.7	339.0	0.8	3.0	0.1	0.1	0.0	< 0.1		0.0	0.4	25.0	0.1	0.0	37.0	1.7	0.5	0.0	0.1	0.0
RS-15	0.0	0.1	14.0	43.0	34.0	726.0	150.0	110.0	30.0	13.0	0.4	0.1	1.7	318.0	2.9	6.0	0.1	0.1	0.0	< 0.1	0.1	0.0	0.7	36.0	0.2	0.0	11.0	2.1	0.7	0.0	0.1	0.0
RS-17	0.0	0.2	6.0	27.0	49.0	110.0	130.0	70.0	50.0	14.0	0.6	0.0	0.4	270.0	2.1	3.0	0.1	0.1	0.0	< 0.1	0.0	0.0	0.1	43.0	0.1	0.0	62.0	1.6	0.7	0.0	0.0	0.0
RS-3	0.1	0.4	19.0	69.0	61.0	219.0	260.0	110.0	60.0	13.0	1.0	0.1	0.7	238.0	6.9	11.0	0.2	0.1	0.0	< 0.1	0.2	0.0	0.3	77.0	0.3	0.0	50.0	2.3	1.2	0.0	0.1	0.1
RS-11	0.1	0.5	42.0	231.0	53.0	261.0	90.0	80.0	110.0	16.0	1.1	0.2	0.8	204.0	27.6	52.0	1.6	0.3	0.0	< 0.1	0.6	0.0	0.0	93.0	1.6	0.1	22.0	1.1	1.5	0.0	0.3	0.1
ODV-4-A1	0.0	<1	79.0	438.0	110.0	63.0	58.0	85.0	114.0		0.7	<0.5	<15	16.0	11.0			<1	<0.3	<0.2	<0.1	<0.2	<1	<50	<1	<0.5	53.0	<0.1	5.0	0.7	<0.2	<0.5
ODV-G-36		<1	20.0	634.0	77.0	<20	<20	32.0	103.0	14.0	<0.5	<5	<1	337.0	3.3	13.0	<0.2	5.0	<0.5	<0.1	<1	<0.2	0.2	83.0	0.3	0.1	72.0	<0.05	<5	0.2	<0.05	0.0
ODV-G-34		<1	58.0	672.0	34.0	<20	<20	46.0	58.0	16.0	<0.5	<5	1.0	435.0	9.0	16.0	<0.2	<2	<0.5	<0.1	<1	<0.2	0.1	106.0	0.4	0.0	75.0	0.1	<5	0.2	0.1	0.0
ODV-G-26		<1	26.0	85.0	41.0	43.0	32.0	41.0	40.0	13.0	<0.5	<5	1.0	370.0	5.8	12.0	<0.2	<2	<0.5	<0.1	<1	<0.2	0.2	96.0	0.3	0.0	94.0	<0.05	<5	0.1	0.1	0.0
ODV-G-25		<1	33.0	155.0	22.0	<20	<20	19.0	<30	11.0	<0.5	<5	2.0	398.0	6.5	12.0	<0.2	<2	0.7	<0.1	0.0	0.4	0.2	86.0	0.3	0.0	54.0	<0.05	<5	0.2	0.1	0.0
ODV-G-23		<1	59.0	554.0	55.0	65.0	50.0	79.0	92.0	14.0	<0.5	<5	1.0	322.0	9.1	17.0	<0.2	<2	<0.5	<0.1	<1	<0.2	0.2	89.0	0.4	0.0	146.0	<0.05	<5	0.3	<0.05	0.0
ODV-G-22		<1	21.0	274.0	33.0	<20	<20	67.0	51.0	15.0	<0.5	<5	1.0	415.0	3.1	9.0	<0.2	<2	<0.5	<0.1	<1	<0.2	0.4	223.0	0.2	0.0	87.0	<0.05	<5	0.3	<0.05	0.0
ODV-G-21		<1	35.0	466.0	29.0	<20	<20	64.0	<30	12.0	<0.5	<5	4.0	403.0	6.2	20.0	0.7	<2	<0.5	<0.1	<1	0.6	0.5	130.0	0.4	0.2	51.0	<0.05	<5	0.1	0.1	0.0
ODV-G-24		<1	52.0	291.0	33.0	57.0	29.0	32.0	42.0	12.0	<0.5	<5	5.0	367.0	13.7	23.0	0.2	<2	0.8	<0.1	<1	<0.2	0.5	157.0	0.6	0.1	65.0	<0.05	<5	0.2	0.2	0.0
ODV-D1	0.0	2.0	45.0	557.0	55.0	< 20	50.0	60.0	130.0	22.0	1.7	< 5	12.0	321.0	22.0	50.0	6.6	< 2	< 0.3	< 0.1	< 1	1.0	0.5	209.0	1.5	0.5	85.0	0.1	< 5	0.6	0.6	0.3
ODV-G-38		<1	51.0	532.0	50.0	237.0	28.0	92.0	56.0	15.0	<0.5	<5	2.0	352.0	8.5	16.0	<0.2	<2	<0.5	<0.1	<1	<0.2	0.2	73.0	0.4	0.0	68.0	<0.05	<5	0.2	<0.05	0.0
ODV-G-37		<1	24.0	58.0	37.0	32.0	24.0	54.0	34.0	15.0	<0.5	<5	<1	416.0	4.9	8.0	<0.2	<2	<0.5	<0.1	1.0	0.4	0.1	105.0	0.2	<0.01	96.0	<0.05	<5	0.2	0.1	0.0
ODV-A-20		<1	2.0	10.0	10.0	<20	<20	<10	<30	19.0	<0.5	<5	3.0	644.0	1.1	7.0	<0.2	<2	<0.5	<0.1	<1	0.2	0.3	178.0	<0.1	<0.01	154.0	<0.05	<5	0.2	0.1	0.0
ODV-A-27		<1	5.0	15.0	11.0	<20	<20	151.0	<30	17.0	<0.5	<5	2.0	582.0	1.8	7.0	<0.2	<2	<0.5	<0.1	<1	<0.2	<0.1	159.0	0.1	<0.01	138.0	<0.05	<5	0.2	0.1	0.0
ODV-A-39		<1	<1	9.0	14.0	<20	<20	55.0	<30	16.0	<0.5	<5	2.0	660.0	1.2	4.0	<0.2	<2	<0.5	<0.1	<1	0.6	0.1	127.0	<0.1	<0.01	146.0	0.1	<5	0.3	0.1	0.0
ODV-G-35		<1	28.0	506.0	25.0	<20	<20	16.0	65.0	12.0	<0.5	<5	1.0	434.0	4.5	10.0	<0.2	<0.2	<0.5	<0.1	<1	<0.2	0.2	126.0	0.3	0.0	54.0	<0.05	<5	0.2	0.1	0.0
ODV-G-41		<1	54.0	1120.0	73.0	55.0	127.0	1560.0	100.0	17.0	1.0	<5	<1	314.0	9.3	19.0	<0.2	<2	<0.5	<0.1	<1	<0.2	<0.1	48.0	0.5	0.0	83.0	<0.05	<5	0.3	<0.05	0.0
ODV-G-28		<1	35.0	110.0	47.0	283.0	114.0	74.0	44.0	11.0	<0.5	<5	<1	323.0	6.2	13.0	<0.2	<2	<0.5	<0.1	<1	<0.2	0.2	39.0	0.3	<0.01	116.0	<0.05	<5	0.3	<0.05	<0.01
ODV-G-32		<1	26.0	74.0	27.0	109.0	33.0	29.0	<30	10.0	<0.5	<5	2.0	392.0	5.7	13.0	<0.2	<2	<0.5	<0.1	3.0	0.6	0.2	60.0	0.3	<0.01	75.0	<0.05	<5	0.2	0.1	0.0
ODV-G-33		<1	30.0	88.0	42.0	107.0	50.0	32.0	44.0	13.0	<0.5	<5	<1	373.0	6.4	14.0	<0.2	<2	<0.5	<0.1	<1	<0.2	0.2	55.0	0.3	<0.01	85.0	<0.05	<5	0.3	0.1	0.0

ODV-G-31		<1	2.0	13.0	11.0	<20	<20	<10	<30	18.0	<0.5	<5	4.0	625.0	2.8	30.0	<0.2	<2	<0.5	<0.1	<1	<0.2	0.3	124.0	0.4	0.1	141.0	<0.05	<5	0.2	0.5	0.2
ODV-G-29		<1	29.0	71.0	26.0	323.0	163.0	35.0	50.0	6.0	<0.5	<5	1.0	305.0	4.7	9.0	<0.2	<2	1.2	<0.1	<1	0.3	0.4	41.0	0.3	<0.01	68.0	<0.05	9.0	0.9	<0.05	0.1
ODV-G-40		<1	30.0	92.0	37.0	110.0	37.0	31.0	53.0	13.0	<0.5	<5	<1	413.0	6.6	17.0	<0.2	<2	<0.5	<0.1	<1	<0.2	0.1	62.0	0.3	<0.01	70.0	<0.05	<5	0.2	0.1	0.0
ODV-D3	0.1	< 1	31.0	95.0	60.0	390.0	160.0	60.0	50.0	15.0	1.4	< 5	< 1	244.0	6.5	< 4	< 0.2	< 2	0.4	< 0.1	< 1	1.1	0.2	58.0	0.3	< 0.01	88.0	< 0.05	< 5	< 0.1	< 0.05	0.1
ODV-D4	0.0	< 1	34.0	102.0	44.0	70.0	30.0	< 10	50.0	18.0	1.2	< 5	< 1	417.0	8.3	8.0	< 0.2	< 2	< 0.3	< 0.1	< 1	0.5	< 0.1	64.0	0.3	< 0.01	114.0	< 0.05	< 5	0.2	0.1	0.1
CVD-19A	0.1	< 1	36.0	116.0	50.0	270.0	130.0	110.0	60.0	17.0	1.4	< 5	< 1	334.0	7.8	6.0	< 0.2	< 2	< 0.3	< 0.1	< 1	0.8	< 0.1	63.0	0.3	< 0.01	93.0	< 0.05	< 5	0.4	0.1	0.1
CDV-17	0.0	< 1	20.0	71.0	53.0	30.0	40.0	< 10	50.0	18.0	1.1	< 5	2.0	405.0	5.4	5.0	< 0.2	< 2	< 0.3	< 0.1	< 1	0.2	< 0.1	83.0	0.3	< 0.01	96.0	< 0.05	< 5	0.1	0.1	0.1
CVD-16A	0.1	< 1	52.0	170.0	46.0	470.0	140.0	210.0	50.0	14.0	1.4	< 5	< 1	279.0	10.8	10.0	< 0.2	< 2	< 0.3	< 0.1	< 1	1.1	< 0.1	48.0	0.5	< 0.01	78.0	< 0.05	< 5	0.7	< 0.05	0.0
CV-31		<1	59.0	166.0	32.0	511.0	22.0	84.0	45.0	11.0	<0.5	<5	3.0	259.0	9.8	19.0	<0.2	<2	0.7	<0.1	<1	0.5	0.6	50.0	0.5	<0.01	47.0	<0.05	<5	0.3	0.1	0.0
CV-28		<1		112.0	75.0	211.0	44.0	310.0	79.0	11.0	<0.5	<5	4.0	279.0	5.9	12.0	<0.2	<2	<0.5	<0.1	<1	0.2	0.7	54.0	0.3	<0.01	67.0	0.1	<5	0.7	0.1	0.0
CVD-6A	0.0	< 1	38.0	119.0	26.0	270.0	60.0	30.0	< 30	14.0	1.0	< 5	< 1	339.0	6.8	8.0	< 0.2	< 2	< 0.3	< 0.1	< 1	< 0.2	< 0.1	56.0	0.3	< 0.01	55.0	< 0.05	< 5	0.1	< 0.05	< 0.01
CVD-2D	0.1	< 1	35.0	98.0	77.0	320.0	130.0	60.0	60.0	10.0	1.1	< 5	< 1	222.0	6.1	6.0	< 0.2	< 2	< 0.3	< 0.1	< 1	0.9	0.5	37.0	0.3	< 0.01	33.0	< 0.05	< 5	< 0.1	< 0.05	0.0
CVD-20	0.0	< 1	3.0	88.0	47.0	80.0	40.0	30.0	40.0	18.0	0.9	< 5	< 1	449.0	0.7	< 4	< 0.2	< 2	< 0.3	< 0.1	< 1	1.2	0.3	69.0	< 0.1	< 0.01	77.0	< 0.05	< 5	< 0.1	< 0.05	0.0
PEROG 5	0.1	< 1	35.0	131.0	54.0	540.0	130.0	390.0	100.0	14.0	1.2	< 5	2.0	290.0	14.5	24.0	0.6	< 2	< 0.3	0.2	60.0	0.4	0.2	82.0	1.0	< 0.01	96.0	< 0.05	51.0	0.1	0.3	0.1
CNT-23A	0.0	< 1	12.0	45.0	55.0	120.0	150.0	30.0	60.0	15.0	0.9	< 5	< 1	330.0	1.8	< 4	< 0.2	< 2	< 0.3	< 0.1	< 1	0.8	< 0.1	57.0	< 0.1	< 0.01	75.0	< 0.05	< 5	0.3	< 0.05	0.0
CNT-25	0.0	< 1	48.0	124.0	39.0	940.0	170.0	50.0	30.0	13.0	1.3	< 5	< 1	256.0	8.1	10.0	< 0.2	< 2	< 0.3	< 0.1	< 1	1.1	0.3	38.0	0.4	< 0.01	76.0	< 0.05	< 5	0.6	0.1	0.0
CNT-24	0.1	< 1	47.0	228.0	48.0	320.0	40.0	90.0	50.0	15.0	1.4	< 5	< 1	386.0	10.5	6.0	< 0.2	< 2	< 0.3	< 0.1	2.0	1.4	< 0.1	72.0	0.4	< 0.01	73.0	< 0.05	< 5	< 0.1	< 0.05	0.1
CNT-26	0.0	< 1	6.0	39.0	42.0	170.0	20.0	20.0	40.0	19.0	1.0	< 5	< 1	425.0	1.0	< 4	< 0.2	< 2	0.3	< 0.1	< 1	0.5	< 0.1	70.0	< 0.1	< 0.01	88.0	< 0.05	< 5	0.2	< 0.05	< 0.01
CNT-19	0.1	< 1	45.0	123.0	43.0	120.0	130.0	210.0	40.0	14.0	1.4	< 5	< 1	278.0	7.8	5.0	< 0.2	< 2	< 0.3	< 0.1	< 1	1.3	< 0.1	36.0	0.3	< 0.01	70.0	< 0.05	< 5	0.7	0.1	0.0
SB-W3	0.3	< 1	18.0	53.0	65.0	200.0	340.0	370.0	50.0	15.0	1.0	< 5	< 1	230.0	3.7	< 4	< 0.2	< 2	< 0.3	< 0.1	< 1	1.5	< 0.1	44.0	0.1	< 0.01	68.0	< 0.05	< 5	2.0	< 0.05	< 0.01
CNT-15A	0.0	< 1	28.0	75.0	28.0	340.0	60.0	90.0	30.0	17.0	1.1	< 5	< 1	345.0	5.0	4.0	< 0.2	< 2	< 0.3	< 0.1	< 1	1.1	< 0.1	58.0	0.2	< 0.01	82.0	< 0.05	< 5	0.1	< 0.05	0.0
CNT-15	0.7	< 1	2.0	6.0	59.0	< 20	180.0	370.0	< 30	22.0	0.6	< 5	52.0	463.0	0.9	< 4	< 0.2	< 2	< 0.3	< 0.1	< 1	1.0	0.8	113.0	< 0.1	< 0.01	86.0	0.1	< 5	< 0.1	0.1	0.1
CNT-20	0.1	< 1	27.0	78.0	51.0	320.0	170.0	100.0	50.0	13.0	1.0	< 5	< 1	256.0	4.0	< 4	< 0.2	< 2	< 0.3	< 0.1	< 1	0.8	< 0.1	37.0	0.2	< 0.01	72.0	< 0.05	< 5	0.3	< 0.05	0.0
CNT-18	0.0	< 1	35.0	101.0	44.0	460.0	140.0	70.0	40.0	13.0	1.0	< 5	< 1	292.0	7.1	5.0	< 0.2	< 2	< 0.3	< 0.1	< 1	0.6	< 0.1	40.0	0.3	< 0.01	72.0	< 0.05	< 5	0.4	< 0.05	0.0
SB-6	0.0	< 1	28.0	73.0	45.0	360.0	180.0	40.0	50.0	13.0	1.7	< 5	< 1	295.0	4.7	5.0	< 0.2	< 2	< 0.3	< 0.1	< 1	1.0	0.5	155.0	0.2	< 0.01	41.0	< 0.05	< 5	< 0.1	< 0.05	0.0
CNT-27	0.1	< 1	24.0	69.0	48.0	50.0	80.0	190.0	40.0	17.0	1.0	< 5	< 1	405.0	4.9	< 4	< 0.2	< 2	0.3	< 0.1	< 1	0.4	< 0.1	66.0	0.2	< 0.01	63.0	< 0.05	< 5	0.2	< 0.05	0.0
SB-13	0.0	< 1	45.0	120.0	46.0	370.0	120.0	70.0	40.0	13.0	1.2	< 5	1.0	264.0	7.9	7.0	< 0.2	< 2	< 0.3	< 0.1	< 1	0.5	0.3	36.0	0.3	< 0.01	64.0	0.1	< 5	0.6	< 0.05	< 0.01
CNT-22	0.1	1.0	21.0	428.0	44.0	50.0	20.0	80.0	50.0	19.0	1.0	< 5	1.0	414.0	3.2	< 4	< 0.2	< 2	< 0.3	< 0.1	< 1	0.6	0.2	73.0	0.1	0.1	72.0	< 0.05	< 5	0.2	< 0.05	0.0
CNT-28	0.0	< 1	39.0	118.0	42.0	100.0	50.0	40.0	40.0	16.0	1.3	< 5	1.0	362.0	7.7	< 4	< 0.2	< 2	< 0.3	< 0.1	< 1	0.5	< 0.1	73.0	0.3	< 0.01	111.0	< 0.05	< 5	0.2	< 0.05	0.0

SB-11	0.2	2.0	*51.2*	1206.0	71.0	*< 5*	60.0	270.0	70.0	17.0	1.3	*< 0.5*	< 1	251.0	7.7	11.0	< 0.2	< 2	5.0	< 0.1	< 1	0.7	< 0.1	35.0	0.4	< 0.01	69.0	< 0.05	< 5	1.5	< 0.05	0.0
CNT-21	0.0	< 1	80.0	227.0	47.0	170.0	70.0	30.0	40.0	10.0	2.0	< 5	< 1	185.0	14.1	10.0	< 0.2	< 2	< 0.3	< 0.1	< 1	0.5	< 0.1	23.0	0.5	< 0.01	79.0	< 0.05	< 5	0.3	< 0.05	0.0
SB-S3	0.0	< 1	23.0	81.0	42.0	50.0	70.0	90.0	40.0	16.0	1.0	< 5	1.0	393.0	4.2	6.0	< 0.2	< 2	< 0.3	< 0.1	< 1	0.4	< 0.1	72.0	0.2	< 0.01	78.0	0.1	< 5	0.6	0.1	0.0
CNT-8	0.1	<1	3.0	29.0	37.0	167.0	110.0	82.0	28.0	10.0	<2	<5	<50	233.0	<1	<1	<5	<1	<0.5		<5	<5		30.0		<2	<5	<5	6.0	<5	<5	<5
CNT-2	0.1	<1	5.0	35.0	32.0	228.0	130.0	106.0	25.0	9.0	<2	<5	<50	174.0	<1	<1	<5	<1	<0.5		<5	<5		26.0		<2	<5	<5	5.0	<5	<5	<5
CNT-29	0.1	<1	3.0	12.0	45.0	102.0	169.0	71.0	36.0	10.0	<2	<5	<50	223.0	<1	<1	<5	<1	<0.5		<5	<5		30.0		<2	<5	<5	7.0	<5	<5	<5
CNT-9	0.0	<1	3.0	24.0	25.0	63.0	62.0	46.0	20.0	8.0	<2	6.0	<50	172.0	<1	<1	<5	<1	<0.5		<5	<5		23.0		<2	<5	<5	4.0	<5	<5	<5
CNT-1	<0.01	<1	3.0	11.0	11.0	52.0	26.0	25.0	9.0	17.0	<2	<5	<50	421.0	<1	<1	<5	<1	<0.5		<5	<5		45.0		<2	<5	<5	9.0	<5	<5	<5
CNT-30	0.1	<1	6.0	144.0	27.0	94.0	38.0	76.0	20.0	9.0	<2	<5	<50	198.0	<1	2.0	<5	<1	<0.5		<5	<5		34.0		<2	<5	<5	4.0	<5	<5	<5
FG-8	0.8	<1	2.0	13.0	48.0	71.0	46.0	888.0	26.0	<5	<2	<5	<50	37.0	<1	<1	<5	<1	<0.5		<5	<5		106.0		<2	<5	<5	5.0	<5	<5	<5
FG-7	1.2	<1	3.0	12.0	57.0	117.0	41.0	947.0	37.0	<5	<2	<5	<50	44.0	<1	<1	<5	<1	<0.5		<5	<5		31.0		<2	<5	<5	3.0	<5	<5	<5
CNT-10	0.1	<1	3.0	26.0	39.0	163.0	128.0	95.0	30.0	7.0	<2	<5	<50	157.0	<1	<1	<5	<1	<0.5		<5	<5		23.0		<2	<5	<5	4.0	<5	<5	<5
FG-5	0.2	<1	7.0	425.0	47.0	139.0	23.0	147.0	32.0	13.0	<2	<5	<50	272.0	<1	2.0	<5	<1	<0.5		<5	<5		46.0		<2	<5	<5	6.0	<5	<5	<5
CNT-11	<0.01	<1	4.0	202.0	22.0	60.0	76.0	49.0	14.0	11.0	<2	<5	<50	217.0	<1	<1	<5	<1	<0.5		<5	<5		31.0		<2	<5	<5	5.0	<5	<5	<5
CNT-7	0.0	<1	<1	5.0	28.0	44.0	90.0	31.0	24.0	18.0	<2	11.0	<50	375.0	<1	<1	<5	<1	<0.5		<5	<5		54.0		<2	<5	<5	9.0	<5	<5	<5
FG-3	0.2	<1	13.0	328.0	32.0	545.0	53.0	152.0	29.0	9.0	<2	<5	<50	164.0	2.0	2.0	<5	<1	<0.5		<5	<5		24.0		<2	<5	<5	5.0	<5	<5	<5
CNT-12	0.1	<1	2.0	19.0	29.0	126.0	97.0	70.0	23.0	10.0	<2	<5	<50	191.0	<1	<1	<5	<1	<0.5		<5	<5		23.0		<2	<5	<5	6.0	<5	<5	<5
CNT-14A	0.1	<1	3.0	20.0	25.0	168.0	81.0	105.0	18.0	11.0	<2	<5	<50	237.0	<1	<1	<5	<1	<0.5		<5	<5		30.0		<2	<5	<5	6.0	<5	<5	<5
CNT-32	0.1	<1	3.0	16.0	46.0	126.0	101.0	62.0	27.0	9.0	<2	<5	<50	212.0	<1	<1	<5	<1	<0.5		<5	<5		26.0		<2	<5	<5	5.0	<5	<5	<5
CNT-6A	0.0	<1	3.0	13.0	35.0	121.0	172.0	80.0	30.0	10.0	<2	<5	<50	214.0	<1	<1	<5	<1	<0.5		<5	<5		35.0		<2	<5	<5	6.0	<5	<5	<5
MB-16	<0.01	<1	1.0	3.0	19.0	69.0	72.0	8.0	15.0	19.0	<2	<5	<50	425.0	<1	<1	<5	<1	<0.5		<5	<5		38.0		<2	<5	<5	12.0	<5	<5	<5
CNT-13	0.1	<1	3.0	14.0	39.0	50.0	112.0	64.0	28.0	11.0	<2	<5	<50	269.0	<1	<1	<5	<1	<0.5		<5	<5		30.0		<2	<5	<5	7.0	<5	<5	<5
CNT-31	0.1	<1	4.0	22.0	24.0	99.0	53.0	147.0	14.0	8.0	<2	<5	<50	203.0	<1	<1	<5	<1	<0.5		<5	<5		25.0		<2	<5	<5	4.0	<5	<5	<5
CNT-33	0.0	<1	3.0	10.0	39.0	85.0	135.0	75.0	29.0	12.0	<2	<5	<50	249.0	<1	<1	<5	<1	<0.5		<5	<5		33.0		<2	<5	<5	8.0	<5	<5	<5
CNT-36	0.1	<1	3.0	12.0	38.0	113.0	153.0	89.0	30.0	10.0	<2	<5	<50	210.0	<1	<1	<5	<1	<0.5		<5	<5		31.0		<2	<5	<5	6.0	<5	<5	<5
CNT-34	0.1	<1	4.0	12.0	24.0	125.0	89.0	112.0	15.0	13.0	<2	<5	<50	294.0	<1	<1	<5	<1	<0.5		<5	<5		32.0		<2	<5	<5	8.0	<5	<5	<5
CNT-35	0.1	<1	4.0	17.0	36.0	122.0	141.0	91.0	28.0	11.0	<2	<5	<50	300.0	<1	<1	<5	<1	<0.5		<5	<5		38.0		<2	<5	<5	7.0	<5	<5	<5
CNT-4	0.1	<1	4.0	17.0	8.0	91.0	58.0	98.0	6.0	19.0	<2	<5	<50	454.0	1.0	3.0	<5	<1	<0.5		<5	<5		42.0		<2	<5	<5	10.0	<5	<5	<5
MB-11	0.1	<1	5.0	28.0	29.0	157.0	63.0	235.0	17.0	12.0	<2	<5	<50	281.0	<1	<1	<5	<1	<0.5		<5	<5		38.0		<2	<5	<5	8.0	<5	<5	<5
MB-13	0.1	<1	5.0	23.0	39.0	135.0	137.0	74.0	32.0	11.0	<2	<5	<50	243.0	<1	<1	<5	<1	<0.5		<5	<5		36.0		<2	<5	<5	6.0	<5	<5	<5
CNT-5B	0.0	<1	4.0	13.0	38.0	173.0	175.0	74.0	27.0	13.0	<2	<5	<50	319.0	<1	<1	<5	<1	<0.5		<5	<5		23.0		<2	<5	<5	8.0	<5	<5	<5
CNT-3A	0.1	<1	4.0	23.0	39.0	132.0	152.0	114.0	33.0	9.0	<2	<5	<50	179.0	<1	<1	<5	<1	<0.5		<5	<5		21.0		<2	<5	<5	5.0	<5	<5	<5
FA-4	0.0	<1	3.0	7.0	42.0	109.0	508.0	61.0	22.0	9.0	<2	<5	<50	173.0	<1	<1	<5	<1	<0.5		<5	<5		11.0		<2	<5	<5	8.0	<5	<5	<5
FA-5	0.0	<1	<1	2.0	31.0	39.0	259.0	57.0	10.0	12.0	<2	<5	<50	254.0	<1	<1	<5	<1	<0.5		<5	<5		18.0		<2	<5	<5	11.0	<5	<5	<5

Low-Ti diorites, high-Ti diorites and ATT suite whole-rock geochemical data

Major elements

Table XIV-7. Major element contents of the low-Ti diorites, high-Ti diorites and rocks belonging to the ATT suite. Values are given in wt%. References: 1 – Pin *et al.* (2008); 2 – Jesus *et al.* (2016); 3 – Caldeira *et al.* (2007).

Reference	**Sample**	**SiO_2**	**Al_2O_3**	**$Fe_2O_3^T$**	**MnO**	**MgO**	**CaO**	**Na_2O**	**K_2O**	**TiO_2**	**P_2O_5**	**LOI**	**Total**
1	Beja 2a	46.90	17.80	11.00	0.17	6.20	11.60	2.50	0.17	2.63		0.05	**99.02**
1	Beja 2b	47.70	17.50	12.00	0.18	7.01	11.50	2.29	0.18	2.59		0.05	**101.00**
1	Beja 2c	45.50	30.50	14.70	0.24	4.20	0.62	1.27	1.01	1.47		0.43	**99.94**
2	CVD-19B	54.51	16.27	8.01	0.13	5.22	8.68	3.85	1.33	1.05	0.17	1.46	**100.70**
2	CVD-19	64.43	14.00	5.31	0.10	4.51	6.88	3.18	0.68	0.57	0.07	1.25	**101.00**
2	CVD-19C	56.70	17.11	7.42	0.13	4.13	5.82	4.73	1.36	1.17	0.26	1.75	**100.60**
2	CVD-5	55.25	10.96	8.07	0.17	9.53	9.60	3.90	0.30	0.42	0.03	2.02	**100.20**
2	ODV-G-43	61.95	18.73	2.98	0.05	0.63	7.66	5.76	0.40	0.64	0.10	1.40	**100.29**
2	MB-3	57.22	21.63	1.73	0.02	2.55	9.49	5.84	0.09	0.32	0.10	0.99	**99.99**
1	Torrão 2	49.6	18.60	13.30	0.23	3.77	7.55	4.05	0.57	1.48		0.03	**99.18**
1	Torrão 6	49.3	19.60	9.99	0.18	4.00	9.18	3.89	0.82	1.48		1.53	**99.97**
1	Torrão 94z	48.1	18.80	10.60	0.17	4.21	9.45	4.21	0.86	1.57		1.14	**99.11**
1	Torrão 4	48.2	18.10	11.50	0.19	5.27	9.51	3.67	0.26	1.74		0.95	**99.39**
1	Torrão 1	50.9	15.90	10.80	0.16	6.00	9.10	4.13	0.50	1.46		0.76	**99.71**
1	Torrão 3	52.2	18.20	8.67	0.16	6.12	8.18	3.54	0.81	0.91		1.41	**100.20**
1	Torrão 5	51.6	16.50	6.95	0.15	7.79	11.80	3.57	0.14	0.70		0.99	**100.19**
3	39D-1	47.16	15.92	11.6	0.24	8.96	9.69	2.74	0.36	1	0.15	2	**99.82**
3	39D-2	47.09	18.39	11.91	0.18	5.54	8.53	3.64	0.58	1.9	0.16	1.92	**99.84**
3	39D-8	48.9	19.5	11.47	0.22	3.53	8.34	4.1	0.77	1.51	0.54	0.87	**99.75**
3	40C-4	57.45	17.26	7.84	0.14	2.74	5.07	4.29	1.87	1.12	0.21	1.75	**99.74**
3	40C-10	52.24	18.58	6.81	0.23	6.15	6.87	3.32	2.32	0.54	0.07	2.6	**99.73**
3	40C-20	55.54	17.64	7.3	0.09	4.49	6.53	3.26	1.8	0.86	0.16	2.06	**99.73**

Rare-Earth elements

Table XIV-8. Rare-Earth Element contents of the low-Ti diorites, high-Ti diorites and rocks belonging to the ATT suite. Values are given in ppm. References: 1 – Pin *et al.* (2008); 2 – Jesus *et al.* (2016); 3 – Caldeira *et al.* (2007).

Reference	**Sample**	**La**	**Ce**	**Pr**	**Nd**	**Sm**	**Eu**	**Gd**	**Tb**	**Dy**	**Ho**	**Er**	**Tm**	**Yb**	**Lu**
1	Beja 2a	3.2	6.6		4.5	1.4	0.9	1.6		1.7		1.0		0.9	0.2
1	Beja 2b														
1	Beja 2c	42.9	70.6		21.6	2.6	2.0	1.5		0.7		0.4		0.3	0.1
2	CVD-19B	15.5	34.0	4.5	19.1	4.6	1.3	4.9	0.9	5.0	1.0	3.0	0.4	2.8	0.4
2	CVD-19	8.4	18.8	2.3	9.6	2.5	0.8	2.7	0.5	3.1	0.6	1.8	0.3	1.8	0.3
2	CVD-19C	20.7	45.1	5.6	22.9	5.5	1.6	5.9	1.1	6.1	1.2	3.8	0.6	3.9	0.6
2	CVD-5	18.3	44.3	5.9	25.5	6.2	0.8	6.7	1.2	7.4	1.5	4.4	0.7	4.2	0.6
2	ODV-G-43	16.9	29.7	3.0	10.8	2.0	1.3	1.9	0.3	1.8	0.4	1.4		1.8	0.3
2	MB-3	8.5	17.8	2.2	9.1	2.1	0.8	2.2	0.4	2.3	0.5	1.4		1.3	0.2
1	Torrão 2	11.4	29.7		19.8	4.6	2.0	4.7		4.1		2.2		1.9	0.3
1	Torrão 6	9.4	25.7		19.6	5.2	2.1	6.0		5.7		3.2		2.9	0.4
1	Torrão 94z	8.7	23.1		16.5	4.6	1.7	5.5		5.4		3.1		2.7	0.4
1	Torrão 4														
1	Torrão 1														
1	Torrão 3														
1	Torrão 5														
3	39D-1	10.3	23.5	4.1	17.9	4.6	1.3	4.2	0.8	4.6	0.8	2.3	0.3	2.0	0.3
3	39D-2	5.0	9.0		17.0	< 3									
3	39D-8	16.7	36.8	6.7	31.7	8.4	2.6	7.9	1.5	9.6	1.9	5.2	0.7	4.5	0.7
3	40C-4	18.0	54.0		24.0	9.0									
3	40C-10	15.8	31.1	4.8	18.8	4.4	0.9	4.2	0.9	5.4	1.1	3.2	0.5	3.1	0.5

Other minor and trace elements

Table XIV-9. Minor and trace element contents of the low-Ti diorites, high-Ti diorites and rocks belonging to the ATT suite. Values are given in ppm except for S, which is given in wt%. References: 1 – Pin *et al.* (2008); 2 – Jesus *et al.* (2016); 3 – Caldeira *et al.* (2007).

Reference	Sample	S	Be	Sc	V	Co	Cr	Ni	Cu	Zn	Ga	Ge	As	Rb	Sr	Y	Zr	Nb	Mo	Ag	In	Sn	Sb	Cs	Ba	Hf	Ta	W	Tl	Pb	Bi	Th	U
1	Beja 2a							22.0						2.0	360.0	9.2	18.0	4.3														0.1	
1	Beja 2b													2.0	353.0	10.0	24.0	4.0															
1	Beja 2c							116.0						42.0	92.0	5.0	104.0	16.0															
2	CVD-19B		2.0	32.0	199.0	34.0	60.0	30.0	40.0	60.0	17.0	1.8	< 5	33.0	323.0	31.0	128.0	6.0	< 2		< 0.1	1.0	0.7	0.8	403.0	3.3	0.5	74.0	0.1	6.0	0.8	5.6	1.6
2	CVD-19		1.0	29.0	139.0	54.0	110.0	40.0	30.0	40.0	13.0	1.3	< 5	19.0	224.0	18.0	77.0	1.7	< 2		< 0.1	< 1	0.6	1.1	151.0	2.1	0.2	446.0	0.1	< 5	0.3	7.8	1.4
2	CVD-19C		2.0	20.0	153.0	36.0	110.0	50.0	40.0	60.0	20.0	1.1	< 5	23.0	286.0	39.0	405.0	5.5	< 2		< 0.1	1.0	0.5	1.9	758.0	9.0	0.4	182.0	0.1	6.0	0.4	9.0	2.8
2	CVD-5		1.0	43.0	126.0	52.0	420.0	110.0	< 10	70.0	12.0	1.6	< 5	3.0	125.0	48.0	125.0	6.5	< 2		< 0.1	2.0	0.5	< 0.1	33.0	3.7	0.7	113.0	< 0.05	< 5	0.3	13.9	5.3
2	ODV-G-43		1.9		178.0	27.0	1.0	2.0	<10	<30	20.8	0.5	0.5	8.0	706.0	14.0	405.0	7.9	0.3	0.2	<0.1	1.0	0.4	0.8	122.0	8.0	0.6	50.0	2.5	3.5	0.0	14.5	4.1
2	MB-3		1.3	9.0	38.0	22.0	5.0	18.0	< 10	< 30	17.6	0.3	0.2	0.9	593.0	14.0	49.0	1.9	0.1	0.0	< 0.1	< 1	0.0	0.1	145.0	1.2	0.2	26.0	0.3	1.6	0.0	1.1	0.6
1	Torrão 2							12.0						14.0	625.0	21.0	33.0	4.0															
1	Torrão 6							4.0						24.0	543.0	28.0	45.0	4.0														24.0	
1	Torrão 94z							2.0						21.0	510.0	29.0	56.0	6.0														21.0	
1	Torrão 4							6.0						5.0	479.0	32.0	52.0	5.0														5.0	
1	Torrão 1																																
1	Torrão 3																																
1	Torrão 5																																
3	39D-1				193.0	25.0	570.0	220.0	5.0	180.0	20.0	1.0	< 5	9.0	265.0	24.0	69.0	4.0				2.0		1.0	67.0	2.2	0.3	4.0		< 5		1.1	0.6
3	39D-2				302.0	27.0	6.0	3.0	52.0		20.0			13.0	385.0	28.0	54.0								139.0			7.0		< 6			
3	39D-8				82.0	16.0			7.0	120.0	28.0	2.0	< 5	19.0	489.0	55.0	69.0	10.0				< 1		1.5	155.0	2.6	0.5	5.0		< 5		0.7	0.3
3	40C-4				152.0	19.0	25.0	10.0	20.0		20.0			55.0	292.0	29.0	62.0	9.0							566.0			8.0		< 6			
3	40C-10				219.0	31.0	80.0	40.0	40.0	150.0	28.0	2.0	< 5	116.0	290.0	32.0	73.0	5.0				2.0		2.8	783.0	2.4	0.4	9.0		38.0		4.0	2.0

Escoural siliciclastic, felsic and mafic metaigneous rocks and Odivelas metabasalts

Major elements

Table XIV-10. Major element contents of the Escoural siliciclastic, felsic and mafic metaigneous rocks and Odivelas metabasalts rocks. Values are given in wt%. References: 1 – da Silva (2011); 2 –Chichorro (2006).

Reference	Sample	SiO_2	Al_2O_3	$Fe_2O_3^T$	MnO	MgO	CaO	Na_2O	K_2O	TiO_2	P_2O_5	LOI	Total
1	BODI-1	52.61	18.88	10.91	0.17	3.33	5.03	2.91	3.5	0.959	0.15	2.46	**100.91**
1	BODI-2	53.05	18.11	10.55	0.168	3.12	4.39	2.59	4	0.911	0.16	2.16	**99.21**
1	BODI-3	54.99	14.36	10.81	0.101	3.55	4.29	2.88	1.79	0.672	0.27	5.67	**99.38**
1	BODI-4	52.69	17.44	9.8	0.137	2.81	3.95	3.35	2.55	0.874	0.18	5.7	**99.48**
1	BODI-5	53.32	16.27	10.74	0.227	3.84	8.81	2.95	0.24	0.749	0.16	2.04	**99.35**
1	BODI-6	52.48	17.07	9.99	0.124	4.5	7.33	2.26	0.82	0.738	0.16	3.56	**99.03**
1	BODI-7	55.24	14.54	13.97	0.276	3.34	6.65	2.39	0.09	1.083	0.18	2.92	**100.68**
1	BODI-9	57.74	14.93	11.79	0.118	3.33	3.39	4.29	0.29	0.76	0.09	3.76	**100.49**
1	BODI-11	54.96	16.94	8.16	0.17	4.14	2.3	2.65	3.79	0.937	0.12	4.77	**98.94**
1	BODI-12	42.81	14.87	8.96	0.237	2.99	11.66	1.8	3.61	0.725	0.12	11.6	**99.38**
1	BODI-13	56.36	14.89	11.71	0.217	3.36	6.2	3.133	0.7	1.038	0.19	2.51	**100.31**
1	BODI-15	67.39	13.31	4.93	0.059	0.5	2.2	3.6	3.15	0.455	0.11	2.77	**98.47**
1	BODI-16	61.42	15.16	6.44	0.105	2.07	3.05	3.33	2.98	0.99	0.21	3.23	**98.99**
1	BODI-18	68.74	13.03	5.68	0.056	0.51	1.67	3.66	3.37	0.456	0.09	2.42	**99.68**
2	BSC-2	51.93	13.58	15.41	0.26	5.13	6.98	3.02	0.11	2.45	0.23		**99.10**
2	BSC-3	51.74	12.73	17.02	0.34	3.34	6.37	3.59	0.55	3.13	0.95		**99.76**
2	BSC-10	49.33	14.58	10.88	0.18	6.83	9.87	2.9	0.73	1.62	0.2		**97.12**
2	CSN-A24	51.81	13.58	15.41	0.26	5.13	6.98	3.02	0.11	2.45	0.23		**98.98**
2	CSN-B24	49.05	13.7	14.02	0.23	6.44	8.06	2.33	1.91	2.19	0.22		**98.15**
2	BSC-6	48.52	14.62	12.55	0.21	7.21	9.33	3.3	0.37	2.02	0.18		**98.31**
2	BSC-1	58.6	18.1	8.01	0.1	3.5	1.31	3.27	4.18	0.88	0.19	1.87	**100.01**
2	SEC-1	67.5	16.3	2.28	0.01	0.81	1.31	5.71	0.42	0.69	0.1	3.65	**98.78**
2	ATA-2	82.6	8.2	1.13	0	0.38	0.26	0.96	1.17	0.35	0.03	5.22	**100.30**
2	CSN-1	62.1	17.8	6.39	0.06	2.79	0.9	3.03	3.64	0.82	0.17	2.49	**100.19**
2	CSN-2	61.7	16.5	6.19	0.06	2.53	1.06	2.8	4.24	0.72	0.3	4.04	**100.14**
2	CSN-3	64	16.8	5.57	0.03	2.73	1.38	5.09	1.98	0.75	0.18	1.92	**100.43**
2	MTN-1	74.2	13.5	3.9	0.03	0.71	0.03	1.32	3.26	0.72	0.04	2.35	**100.06**
2	XC-20	72.3	14.2	4.44	0.04	0.97	0.22	1.03	3.59	0.64	0.09	2.03	**99.55**
2	ESC-100	76.28	12.35	1.48	0.011	0.41	0.02	0.12	7.53	0.104	0.02	1.62	**99.95**

2	ESC-101	75.42	13.22	1.34	0.002	0.18	0.37	3.71	4.23	0.2	0.05	1.24	**99.96**
2	ESC-102	72.31	14.65	0.83	0.018	0.88	1.34	7.91	0.26	0.815	0.07	0.61	**99.69**

Rare-Earth elements

Table XIV-11. Rare-Earth element contents of the Escoural siliciclastic, felsic and mafic metaigneous rocks and Odivelas metabasalts rocks. Values are given in ppm. References: 1 – da Silva (2011); 2 –Chichorro (2006).

Reference	**Sample**	**La**	**Ce**	**Pr**	**Nd**	**Sm**	**Eu**	**Gd**	**Tb**	**Dy**	**Ho**	**Er**	**Tm**	**Yb**	**Lu**
1	BODI-1	9.1	20.6		13.3	3.9	1.2							2.9	0.5
1	BODI-2	10.2	20.6		13.4	3.8	1.2							2.9	0.5
1	BODI-3	8.4	18.2		11.7	3.5	1.1							3.2	0.5
1	BODI-4	10.0	19.7		12.2	3.5	1.1							3.1	0.5
1	BODI-5	6.9	15.4		9.9	2.9	0.9							2.5	0.4
1	BODI-6	8.1	16.8		10.1	2.9	1.0							2.4	0.4
1	BODI-7	6.8	15.4		10.5	3.3	0.9							3.0	0.5
1	BODI-9	7.1	16.3		10.5	3.0	1.1							3.0	0.5
1	BODI-11	9.2	19.4		13.1	4.0	1.1							3.2	0.5
1	BODI-12	4.2	9.0		5.9	1.9	0.7							1.8	0.3
1	BODI-13	7.7	17.2		11.5	3.6	1.1							3.3	0.5
1	BODI-15	52.5	104.0		46.5	10.2	1.6							5.5	0.9
1	BODI-16	37.4	72.2		33.3	7.4	1.3							4.1	0.6
1	BODI-18	43.7	86.9		39.9	8.9	1.3							5.3	0.9
2	BSC-2	9.8	45.1	6.5	32.8	9.8	3.0	11.3	2.1	12.8	2.6	7.8	1.2	7.2	1.0
2	BSC-3	29.0	66.7	9.6	47.5	13.0	3.9	14.5	2.6	15.4	3.1	9.0	1.3	8.2	1.1
2	BSC-10	8.0	19.2	2.9	14.8	4.4	1.5	5.5	1.0	6.0	1.2	3.7	0.5	3.3	0.5
2	CSN-A24	8.1	19.6	3.2	17.7	5.9	2.1	6.9	1.3	8.6	1.8	5.5	0.8	5.1	0.8
2	CSN-B24	8.5	18.9	2.9	15.9	5.1	1.9	5.9	1.1	6.9	1.4	4.3	0.6	4.0	0.6
2	BSC-6	6.8	17.5	2.7	14.6	4.7	1.7	6.0	1.1	7.0	1.4	4.3	0.6	4.0	0.6
2	BSC-1	38.4	74.7	8.3	32.1	6.4	1.6	5.2	0.9	4.8	0.9	2.9	0.5	2.8	0.4
2	SEC-1	26.8	51.3	5.6	21.5	4.1	1.0	3.2	0.5	2.8	0.6	1.8	0.3	1.8	0.3
2	ATA-2	30.5	60.0	7.2	30.0	6.6	1.3	6.7	1.1	7.1	1.5	4.4	0.7	4.5	0.7

2	CSN-1	51.4	94.8	10.7	40.4	8.1	1.6	6.5	1.1	5.9	1.2	3.4	0.5	3.2	0.5
2	CSN-2	39.2	69.2	8.2	31.2	6.4	1.5	5.7	0.9	5.4	1.1	3.3	0.5	3.1	0.5
2	CSN-3	38.4	73.4	8.3	31.9	6.4	1.2	5.3	0.9	4.7	1.0	2.7	0.4	2.7	0.4
2	MTN-1	39.2	80.8	8.7	31.4	5.6	1.2	4.8	0.9	4.9	1.0	3.3	0.5	3.3	0.5
2	XC-20	33.7	71.1	7.5	28.2	5.1	1.2	4.5	0.8	4.6	0.9	2.8	0.4	2.7	0.4
2	ESC-100	11.2	135.0	2.8	11.7	2.7	0.2	3.0	0.7	5.7	1.4	4.7	0.8	5.3	0.8
2	ESC-101	18.3	36.6	4.6	18.3	4.5	0.6	5.0	1.0	6.6	1.4	4.3	0.7	4.4	0.6
2	ESC-102	8.2	19.8	3.5	17.3	5.2	0.9	6.3	1.3	8.6	1.8	6.0	1.0	6.9	1.0

Other minor and trace elements

Table XIV-12. Minor and trace element contents of the Escoural siliciclastic, felsic and mafic metaigneous rocks and Odivelas metabasalts rocks. Values are given in ppm except for S, which is given in wt%. References: 1 – da Silva (2011); 2 –Chichorro (2006).

Reference	Sample	S	Be	Sc	V	Co	Cr	Ni	Cu	Zn	Ga	Ge	As	Rb	Sr	Y	Zr	Nb	Mo	Ag	In	Sn	Sb	Cs	Ba	Hf	Ta	W	Tl	Pb	Bi	Th	U
1	BODI-1	0.0			211.0			9.0	58.0	71.0				41.0	213.0	28.0	97.0	1.9						0.5	360.0	2.9	0.1					2.6	0.5
1	BODI-2				195.0			8.0	1.0	66.0				49.0	201.0	27.1	98.0	1.9						0.4	434.0	2.9	0.1					2.6	0.6
1	BODI-3				166.0			4.0	8.0	60.0				40.0	120.0	32.7	58.0	1.2						1.1	89.0	1.8	0.1					1.6	0.7
1	BODI-4				194.0			5.0	8.0	25.0				68.0	141.0	28.8	89.0	1.6						1.0	163.0	2.6	0.1					2.4	1.1
1	BODI-5				181.0			6.0	36.0	74.0				5.0	263.0	22.9	6.0	1.4						0.4	67.0	1.9	0.1					1.7	0.8
1	BODI-6				228.0			5.0	44.0	76.0				14.0	260.0	24.5	57.0	1.2						0.8	198.0	1.8	0.1					1.5	0.7
1	BODI-7				250.0			5.0	70.0	96.0				2.0	198.0	27.4	68.0	1.4						0.1	62.0	2.2	0.1					1.5	0.7
1	BODI-9				162.0			5.0	10.0	78.0				7.0	298.0	27.3	64.0	1.2						0.3	81.0	1.9	0.1					1.8	0.4
1	BODI-11				262.0			7.0	362.0	74.0				52.0	135.0	31.8	79.0	1.2						2.3	378.0	2.4	0.1					1.7	0.5
1	BODI-12				259.0			7.0	53.0	41.0				66.0	165.0	17.4	42.0	0.6						2.0	250.0	1.3	0.0					0.8	1.0
1	BODI-13				178.0			6.0	62.0	78.0				18.0	249.0	31.0	76.0	1.6						2.1	201.0	2.4	0.1					1.7	0.8
1	BODI-15				10.0			3.0	25.0	28.0				68.0	138.0	53.5	324.0	15.5						0.8	1024.0	9.1	1.3					19.2	5.5
1	BODI-16				135.0			14.0	6.0	37.0				76.0	256.0	43.3	263.0	11.5						2.3	1029.0	7.2	1.0					14.6	5.3
1	BODI-18				7.0			6.0	13.0	26.0				74.0	99.0	52.0	330.0	15.4						0.3	948.0	9.1	1.3					19.5	4.4
2	BSC-2		1.0	46.0	405.0	37.0	39.0	< 20			22.0			3.0	74.0	67.0	311.0	11.0						0.5	186.0	4.6	0.8					0.8	0.3
2	BSC-3		2.0	41.0	311.0	27.0	< 20	< 20			24.0			14.0	100.0	81.0	366.0	13.0						0.6	122.0	9.0	0.8					3.2	1.2
2	BSC-10		1.0	43.0	264.0	32.0	301.0	30.0			17.0			22.0	194.0	32.0	134.0	4.0						< 0.5	643.0	3.5	0.2					0.8	0.4
2	CSN-A24		1.0	46.0	405.0	37.0	39.0	13.0			22.0			3.0	74.0	46.8	150.0	3.4						0.5	186.0	4.6	0.2					0.8	0.3
2	CSN-B24			55.0	260.0	44.0	1430.0	118.0			16.0			5.0	147.0	20.7	51.0	4.6						0.5	25.0	1.9	0.1					0.1	0.1
2	BSC-6		1.0	50.0	307.0	45.0	259.0	31.0			2.0			9.0	160.0	38.0	126.0	4.0						< 0.5	89.0	3.6	0.2					0.2	0.2
2	BSC-1			21.0	144.0	22.0	94.0	55.0			24.0			133.0	167.0	27.0	173.0	13.0							748.0	4.8				6.0		8.5	2.3
2	SEC-1			13.0	109.0	<1	85.0	35.0			17.0			15.0	118.0	16.0	130.0	12.0							481.0	3.5				7.0		7.5	3.7
2	ATA-2			11.0	256.0	<1	99.0	<20			12.0			30.0	56.0	50.0	172.0	13.0							1250.0	4.2				8.0		8.1	8.8
2	CSN-1			16.0	108.0	17.0	87.0	38.0			22.0			140.0	148.0	32.0	203.0	18.0							838.0	5.8				7.0		13.2	3.7
2	CSN-2			17.0	210.0	17.0	122.0	47.0			21.0			156.0	140.0	33.0	167.0	15.0							1510.0	4.6				<5		10.6	4.4
2	CSN-3			17.0	130.0	18.0	88.0	41.0			22.0			70.0	125.0	27.0	180.0	17.0							526.0	4.9				<5		10.8	3.7
2	MTN-1			8.0	48.0	6.0	30.0	0.0			15.0			129.0	30.0	34.0	508.0	15.0							608.0	12.9				14.0		20.0	4.0
2	XC-20			9.0	54.0	8.0	30.0	0.0			16.0			141.0	80.0	30.0	281.0	13.0							710.0	7.3				14.0		12.0	3.0
2	ESC-100		2.0	4.0	<5	1.0	<20	<20			26.0			218.0	14.0	37.0	220.0	17.0						2.8	605.0	8.5	1.3					16.0	5.1
2	ESC-101		2.0	6.0	10.0	1.0	<20	<20			17.0			134.0	43.0	41.0	169.0	6.0						0.6	469.0	5.8	0.8					19.0	10.0
2	ESC-102		2.0	8.0	18.0	11.0	<20	<20			27.0			2.0	55.0	49.0	706.0	14.0						<0.5	33.0	20.3	1.1					14.1	4.2

XV. Supplementary Data 3

Comparison between different calibrations

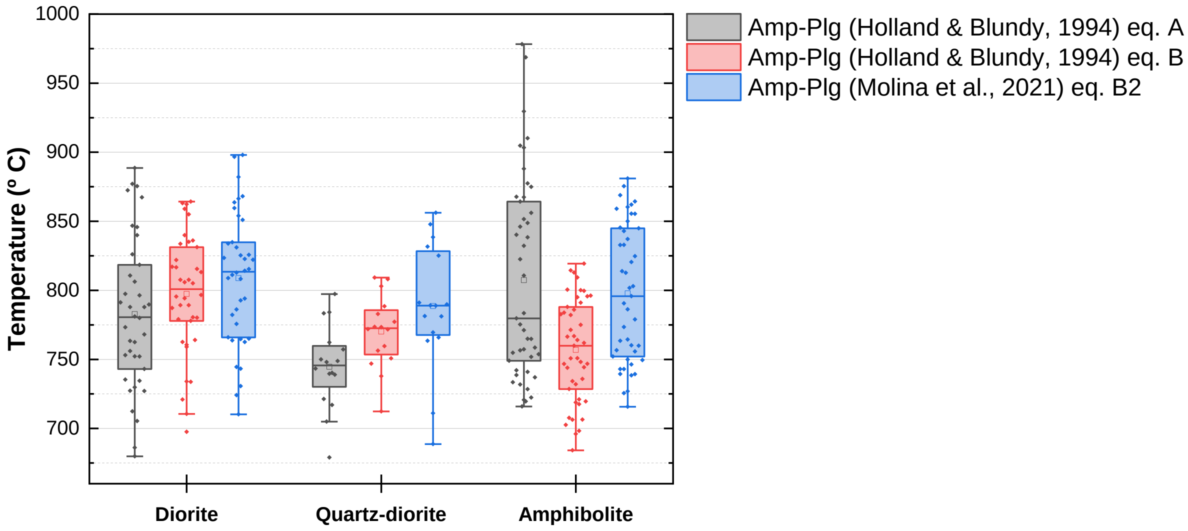

Figure XV-1. Comparison between different calibrations of amphibole-plagioclase equilibria thermometry.

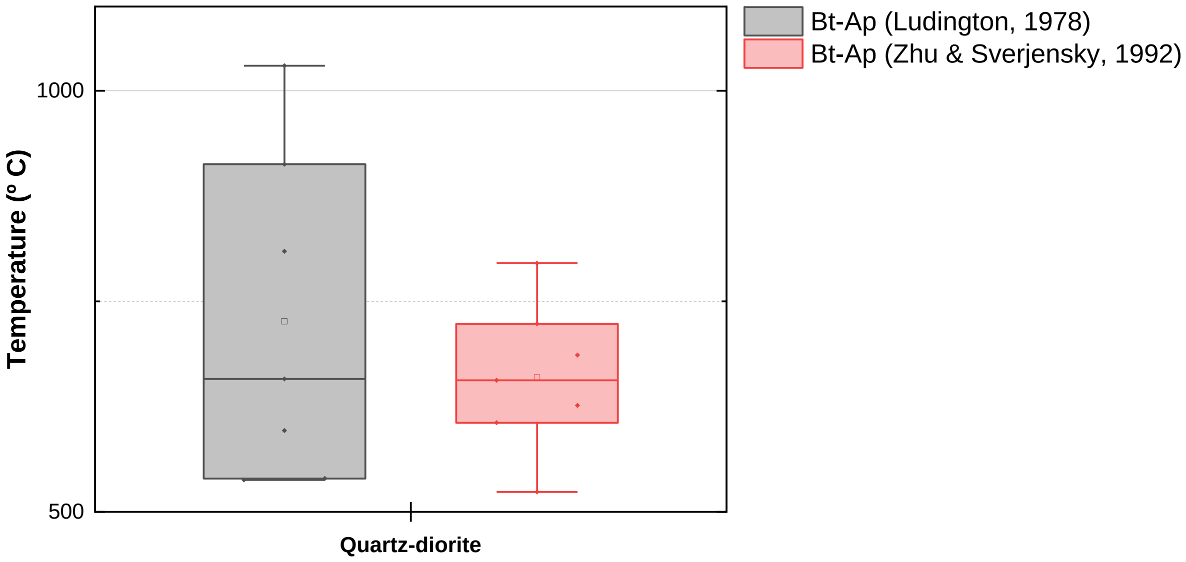

Figure XV-2. Comparison between different calibrations of biotite-apatite equilibria thermometers.

XVI. Supplementary Data 4

Table XVI-1. Bulk partition coefficients of clinopyroxene for relevant elements.

Clinopyroxene	
La	0.0435
Ce	0.0843
Nd	0.1730
Sm	0.2830
Eu	0.3120
Gd	0.3360
Tb	0.3640
Dy	0.3630
Er	0.3510
Yb	0.3130
Lu	0.2650
Cs	0.13
Rb	0.0047
Ba	0.0006
Th	0.003
U	0.04
K	0.0072
Nb	0.0027
Ta	0.013
Sr	0.0963
Zr	0.1210
Ti	0.1
Y	0.4380

Table XVI-2. Bulk partition coefficients of magnetite for relevant elements.

Magnetite	
La	1.5
Ce	1.3
Nd	1
Sm	1.1
Eu	0.60
Gd	0
Tb	1
Dy	0
Er	0.25
Yb	0.90
Lu	0
Cs	0.39
Rb	0.01
Ba	0.01
Th	0.1
U	0.012
K	0.01
Nb	0
Ta	0
Sr	0.1
Zr	0
Ti	9
Y	0.64

Table XVI-3. Bulk partition coefficients of olivine for relevant elements.

Olivine	
La	0.0006
Ce	0.0005
Nd	0.0010
Sm	0.0013
Eu	0.0016
Gd	0.0015
Tb	0.0015
Dy	0.0017
Er	0.0015
Yb	0.0015
Lu	0.0015
Cs	0.0004
Rb	0.0020
Ba	0.0020
Th	0.04
U	0.0450
K	0.013
Nb	0.0017
Ta	0
Sr	0.0022
Zr	0.0045
Ti	0.011
Y	0.0038